TOR VERGATA
UNIVERSITÀ DEGLI STUDI DI ROMA

MACROAREA DI SCIENZE MM. FF. NN.

DOTTORATO DI RICERCA IN FISICA

XXXII CICLO

Search for a beyond the standard model resonance decaying to top quark pair in the dilepton final state with the ATLAS experiment

Candidato:

Maurizio De Santis

Docente:

Prof. Lucio Cerrito

Coordinatore:

Prof. Roberto Benzi

Anno Accademico 2018/2019

Abstract

Name of the student: **Maurizio De Santis** Roll No: **0239136**

Degree for which submitted: **PhD**

Department: **Department of Physics**

Thesis title: **Search for a beyond the standard model resonance decaying to top quark pair in the dilepton final state with the ATLAS experiment**

Thesis supervisor: **Prof. Lucio Cerrito**

Month and year of thesis submission: **November 30, 2019**

Top quark pair production ($t\bar{t}$) can be studied at the LHC with unprecented statistics. In this thesis, studies performed at the ATLAS experiment exploiting the dilepton channel, i.e. events where both top quarks decaying to $t \to Wb$ have a subsequent $W^{\pm} \to \ell^{\pm}\nu$ ($\ell^{\pm} = e^{\pm}, \mu^{\pm}$) decay, are presented. A search for a Beyond Standard Model (BSM) resonance is perfomed considering the full pp collision dataset collected by ATLAS at $\sqrt{s} = 13$ TeV, using two different invariant mass variables ($m_{\ell\ell bb}$ and $m_{t\bar{t}}^{NW}$), each combined with a spin-sensitive variable ($\Delta\phi^{\ell\ell}$). Expected mass limits for three different BSM models, at 95% confidence level, are obtained. A neutral heavy gauge boson Z' with a mass smaller than 1.8 TeV (1.85 TeV) can be excluded if using $m_{\ell\ell bb}$ ($m_{t\bar{t}}^{NW}$). A Randall-Sundrum graviton G, with a mass smaller than 0.8 TeV (0.8 TeV) can be excluded if using $m_{\ell\ell bb}$ ($m_{t\bar{t}}^{NW}$). A Kaluza-Klein gluon g_{KK}, with a mass smaller than 3.1 TeV (3.25 TeV) can be excluded if using $m_{\ell\ell bb}$ ($m_{t\bar{t}}^{NW}$).

Acknowledgements

Non sono mai stato un fenomeno nei ringraziamenti, soprattutto quelli seri e chi mi conosce sa benissimo quale scoglio mi trovo davanti, quindi provo a scrivere qualcosa.

First of all, thanks to my supervisor Lucio, because without him this thesis would not exist. Many thanks to the ATLAS resonance group to help me to unreveal doubts during my work.

Un profondo ringraziamento a Michele che da compare di analisi mi ha sempre saputo dare una mano ed ottimi consigli. Ringrazio anche tutti i miei colleghi del gruppo NPTEV perchè anche loro, in maniere a volte inaspettate, mi hanno saputo consigliare.

Ringrazio la mia famiglia, che mi è sempre stata vicina quando, in effetti, facevano prima a darmi in adozione per quanto sia rompi scatole. Ringrazio i miei amici perchè ridendo e scherzando (con anche una sana dose di prese in giro) mi hanno sempre supportato (e sopportato).

Infine ringrazio tutti coloro che mi hanno insegnato qualcosa nella vita, perchè nel bene o nel male si impara sempre qualcosa di nuovo.

Ok non sono mai stato bravo con le parole, ma sappiate che anche se non scrivo o dico molto dentro c'è un fiume di emozioni che non saprei descrivervi. Grazie di tutto!

Contents

Introduction

In this thesis the search for a heavy resonance decaying to top quark pair in the dilepton final state (where both the W boson decay leptonically, $t\bar{t} \to W^+W^-b\bar{b}$ and $W^\pm \to \ell^\pm\nu$) will be described. Despite the fact is not possible to effectively reconstruct the full resonance, due to the fact that neutrinos are invisible, the dilepton channel is very useful to search Beyond Standard Model phenomena, because this channel is sensitive to the correlation between the spins of the leptons from the $W^\pm$ bosons, and various signals of new physics modify such correlation.
In Chapter 1 the Standard Model (SM) is described, in addition with the three BSM theoretical models under consideration: the neutral heavy gauge boson Z', the Randall-Sundrum graviton G and the Kaluza-Klein gluon g_{KK}.
Chapter 2 describes the ATLAS detector at LHC with its components: the Inner Detector, the calorimeters (electromagnetic and hadronic), the muon spectrometer, the magnetic system and other sub-detectors.
In Chapter 3, the definition of the objects used for the selection of the events (electrons, muons, hadronic jets and missing transverse momentum) is given.
Chapter 4, Chapter 5 and Chapter 6 present my original work. Chapter 4 describes the detailed study on the efficiency in reconstructing muons close to hadronic jets; this is particularly relevant for the signatures considered in this search, as muons and jets arising from a possible new particle tend to be close-by. Similarly, electrons arising from the decay of a new physics particle might be close to other visible objects in the event. Chapter 5 presents a detailed study on the electron isolation and on the procedure to remove overlaps between objects. Chapter 6 describes the core of this analysis: a search for a Beyond Standard Model heavy resonance in the dilepton final state. This part includes the event selection, the analysis strategy, the studies carried out to estimate SM background contributions, control regions

and signal regions in addition to the systematic uncertainties. The expected mass limits are presented in this thesis, obtained combining two different invariant mass variables ($m_{t\bar{t}}^{NW}$ and $m_{\ell\ell bb}$) and the spin-sensitive variable ($\Delta\phi(\ell\ell)/\pi$).
In Chapter 7, the conclusions of the work will be illustrated.

Chapter 1

Theory

1.1 The Standard Model of Particle Physics

The Standard Model (SM) [1] describes the interaction of the matter particle (such as quarks and leptons) and their interactions through three of the four fundamental forces: electromagnetic, weak and strong forces based on the principle of local gauge invariance, e.g. invariance under phase transformation depending on the space-time coordinates.
The predictions of the SM have been largely confirmed (the latest confirmation was the discovery of the Higgs boson in 2012) with very good precision, however, the SM does not yet represent a complete theory of fundamental interactions it leaves a number of open questions at high energy (described in section 1.2).
In the Standard Model the particles are divided in two categories: fermions and bosons. The fermions are spin $\frac{1}{2}$ particles and compose the matter; these include leptons and quarks. The bosons are integer-spin particles and they are responsible for fundamental interactions: the photon γ mediates the electromagnetic force, 8 *gluons* mediate the strong force and the $Z, W^{\pm}$ bosons mediate the weak force. Finally, the Higgs boson, with null spin and charge, is the responsible of the particles mass (fully described in Section 1.1.4). Fig. 1.1 shows the SM of fundamental particles.

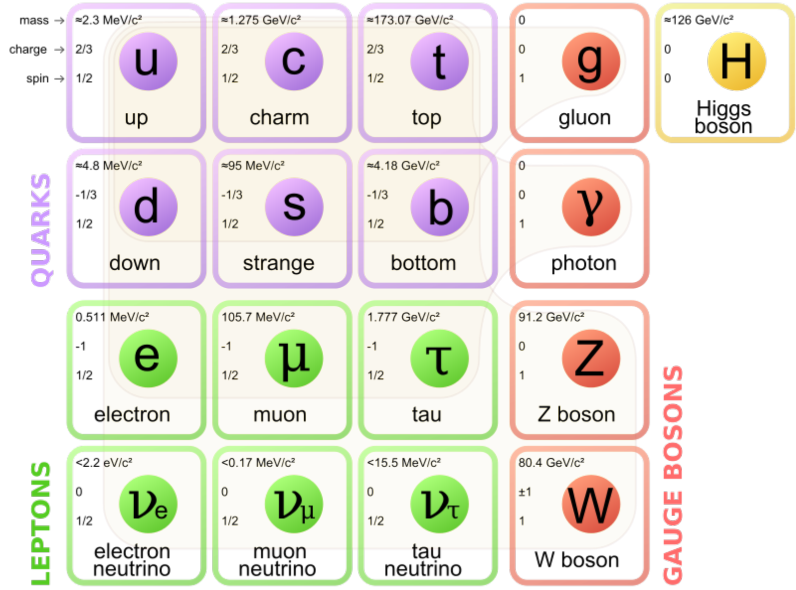

FIGURE 1.1: Scheme of SM fundamental particles: quarks in purple, leptons in green, bosons in red and the Higgs boson (yellow). The quark masses shown are the "naked" ones, that is without taking into account the gluons and quarks of the sea which increase their mass.

Quarks (q) are divided in three families, each composed of a doublet of electric charge $\frac{2}{3}$ and $-\frac{1}{3}$ (in the anti-matter case, the charge have opposite values); these particles have a quantum number, the color charge, that is always preserved in the SM interactions. Each quark flavor may exist in three different colors: red (R), blue (B) or green (G); the anti-quarks, instead, have the anti-colors (anti-red, anti-blue and anti-green).

Quarks cannot exist alone but only together with other quarks, exclusively forming states with no color charge [1] (quarks properties are fully described in section 1.1.5). These bound states are called hadrons, and they are divided in barions and mesons: barions are triplet quark bound states (for example the proton is a bound state uud) and have neutral color charge; mesons are quark anti-quark bound states ($q\bar{q}$) with neutral color charge and must be $R\bar{R}$, $B\bar{B}$ or $G\bar{G}$. Another quantum number is important to define quarks, the *barionic number* (B), and it is always preserved; this number is +1 for barions and −1 for anti-barions, that is quarks have $B = \frac{1}{3}$ while the anti-quarks $B = -\frac{1}{3}$.

In addition to the valence quarks (q_v) that contribute to quantum numbers, hadrons contain virtual quark−antiquark ($q\bar{q}$) pairs called sea quarks. Sea quarks are formed when a gluon from the hadron's color field divides; this process also works in reverse

in the sense that the annihilation of two sea quarks produces a gluon. The result is a constant flow of divisions of gluons and creations. Sea quarks are much less stable than their valence counterparts, and typically annihilate each other within the hadron.
There are also more exotic situations of quarks bound states, like tetra-quarks or penta-quarks, composed of 4 or 5 quarks, respectively.
Leptons (ℓ), as quarks, are divided in three families composed of doublets with a charged lepton and a flavor neutrino; for each lepton family there is a leptonic number (L), that is +1 for leptons and −1 for anti-leptons; this quantum number is always preserved in the Standard Model.

The world we know is composed exclusively of the first quarks (up and down) and leptons (electron and electronic neutrino) family, the second and third families are unstable and decay in lighter families.
From a theoretical point of view, the SM is a quantum field theory that is described by $U(1)_Y \otimes SU(2)_L \otimes SU(3)_C$, which has $8 + 3 + 1 = 12$ generators and gauge fields: the electromagnetic and weak interaction are described by the the $U(1)_Y \otimes SU(2)_L$ symmetry group and $SU(3)_C$ is the symmetry group associated to the strong interaction of Quantum Chromodynamics (QCD). The SM Lagrangian is:

$$\mathcal{L} = -\frac{1}{4}W_{\mu\nu} \cdot W^{\mu\nu} - \frac{1}{4}B_{\mu\nu} \cdot B^{\mu\nu} - \frac{1}{4}G^a_{\mu\nu} \cdot W^{\mu\nu}_a \tag{1.1}$$

$$+\bar{L}\gamma^\mu(i\partial_\mu - \frac{1}{2}g\tau \cdot W_\mu - \frac{1}{2}g'YB_\mu)L + \bar{R}\gamma^\mu(i\partial_\mu - \frac{1}{2}g'YB_\mu)R \tag{1.2}$$

$$+|i\partial_\mu - \frac{1}{2}g\tau W_\mu - \frac{1}{2}g'YB_\mu\phi|^2 - V(\phi) \tag{1.3}$$

$$-(g_1\bar{L}\phi R + g_2\bar{L}\tilde{\phi}R + H.C.) \tag{1.4}$$

$$+\frac{1}{2}g_s(\bar{\psi}^j_q\gamma^\mu\lambda^a_{jk}\psi^k_a)G^a_\mu \tag{1.5}$$

Where: (1.1) is the kinetic energy and auto-interaction of $W^\pm, Z$ bosons and γ; (1.2) is the kinetic energy of the fermions and their interaction with the weak bosons and the photon; (1.3) are the weak bosons, photon and Higgs boson ([2], [3]) masses and couplings; (1.4) is the masses of fermions and their coupling with H and (1.5) is the quark-gluon coupling. Moreover, L is the fermionic doublet left-handed and R is the singlet right-handed; $\phi(h.c.)$ represent the Higgs doublet and ψ is the quarks color field; finally, g and g' are, respectively, $g = e(sin(\theta_w))^{-1}$ and $g' = e(cos(\theta_w))^{-1}$, with θ_w the mixing angle of Weinberg.

1.1.1 Electromagnetic force: QED

The electromagnetism is described by the Quantum Electrodynamics (QED), based on $U(1)_Y$ symmetry group; the photon γ is the mediator of the electromagnetic force, it has spin 1, no mass, no electric charge and it only couples to electrically charged particles. The coupling constant is $\alpha = \frac{1}{137}$ and it is called $fine\ structure\ constant$.

1.1.2 Weak nuclear force

The weak interaction is based on $SU(2)_L$ symmetry group. All fermions have the weak charge quantum number and this means that they can have weak interaction. The weak nuclear force is mediated by three massive bosons: the two charged $W^{\pm}$ bosons, with mass of ∼80 GeV/c^2 and the neutral Z boson, with mass of ∼91 GeV/c^2 and all bosons have spin 1. This means that, for example, quarks and leptons interact via $W^{\pm}$ boson. The $W^{\pm}$ bosons interact only with left-handed fermions and right-handed anti-fermions.
The neutral current interactions take place via the Z boson. The $W^{\pm}$ and Z bosons can interact with each other and, moreover, the $W^{\pm}$ boson, that is charged electrically can interacts with photons.
In the SM the Weak and Electromagnetic interactions are unified in the "Electroweak theory" and to describe them a new quantum number was introduced, the weak isospin T (that will be described in the next subsection).

1.1.3 Electroweak theory

The electroweak interaction is a unified description of the electromagnetic and weak force of the SM of particle physics. Although the two interactions seem to be different at low energies, beyond the unification energy of ∼100 GeV, they are merged together into one force. The electroweak theory was introduced because it was seen that the Z boson is not the neutral partner of $W^{\pm}$ bosons but it mediate a more complex interaction. In this theory the photon and the weak neutral Z boson are a linear combination of weak isospin states and it was introduced by Weinberg and Salam.

This unification is accomplished under an $SU(2)_L \otimes U(1)_Y$ non-abelian gauge symmetry, where Y is the hyper-charge operator and it is defined as $Y = 2(Q - T^3)$ and T is the weak isospin operator. The quantum number T was introduced in the theory, where left-handed quarks and leptons formed a weak doublet that can transform each other through the absorption or emission of a charged boson $W^{\pm}$ (as described in subsection 1.1.2). The value of T associated to them is $T = \frac{1}{2}$ with the third component $T_3 = \pm\frac{1}{2}$; the right-handed fermions are a weak singlet with $T = T_3 = 0$ and they don't have a coupling with the $W^{\pm}$ boson.

To require the conservation of T_3 in the charged current interaction, we need that:

$$T_3(W^+) = +1 \quad \text{and} \quad T_3(W^-) = -1 \tag{1.6}$$

For this reason a third state must exist, to obtain a triplet; this state is identified as W^0 with $T = 1$ and $T_3 = 0$, but this is not the Z boson because the coupling depends on the electric charge; therefore a singlet state must exist with $T = T_3 = 0$, identified as B^0. The W^0 and B^0 states couple with fermions without changing their weak isospins. The photon and the Z boson can be written as the linear combination of the two weak states [4]:

$$\begin{pmatrix} \gamma \\ Z \end{pmatrix} = \begin{pmatrix} cos\theta_w & sin\theta_w \\ -sin\theta_w & cos\theta_w \end{pmatrix} \begin{pmatrix} B^0 \\ W^0 \end{pmatrix} \tag{1.7}$$

The linear combination is expressed by the rotation of the mixing angle θ_w. The link between the mixing angle, the weak charges g and g' and the electric charge e, is obtained by requiring that the photon couples with the left-handed or right-handed fermions but not with the neutrinos. The angle-charge relations are:

$$tan\theta_w = \frac{g'}{g} \quad ; \quad sin\theta_w = \frac{g'}{\sqrt{g^2 + g'^2}} \quad ; \quad cos\theta_w = \frac{g}{\sqrt{g^2 + g'^2}} \quad \text{and} \quad e = g \cdot sin\theta_w \tag{1.8}$$

The mixing angle θ_w is one of the SM parameters (described in section 1.2). It is experimentally measured to be $sin\theta_w = 0.2319 \pm 0.0005$, as predicted by the SM.

1.1.4 Spontaneous symmetry breaking: Brout-Englert-Higgs mechanism

The Standard Model, as a renormalizable theory, does not predict mass terms for the particles in the Lagrangian; instead, we know that the weak bosons have a mass. To resolve this problem a spontaneous symmetry breaking mechanism has been hypothesized, where the ground state of the vacuum is asymmetric [1].
In the Brout-Englert-Higgs (BEH) mechanism ([5],[6]), the bosons mass $W^{\pm}$ and Z are explained in the following: at a sufficiently ($\sim$100 GeV) high temperature (energy) the weak boson don't have a mass like the photon; below a threshold energy there is a transition phase, and the masses are produced by the Higgs fields. The mechanism description can be divided into three steps.
$First\ step$: the Lagrangian of a spin 0 and mass m particle with the motion equation $\partial_\mu \partial^\mu \phi + m\phi^2$, can be written:

$$\mathcal{L} = \frac{1}{2}(\partial_\mu \phi)(\partial^\mu \phi) - \frac{1}{2} m\phi^2 \tag{1.9}$$

Consider now the Lagrangian:

$$\mathcal{L} = \frac{1}{2}(\partial_\mu \phi)(\partial^\mu \phi) - \frac{1}{2}\mu^2\phi^2 - \frac{1}{4}\lambda\phi^4 \tag{1.10}$$

where the potential is written in terms of λ, μ and ϕ, with $\lambda\mu = const$ and $\mu^2 < 0$, $\lambda > 0$.
This Lagrangian has a reflection symmetry (invariant under the transformation $\phi \rightarrow -\phi$). By the condition $\mu^2 < 0$ we cannot interpret ϕ^2 as a mass term, because it

could be imaginary; we use the Feynman rules to rewrite the Lagrangian, where the field perturbation is treated as oscillation around the minimum of energy (vacuum). In this case $\phi = 0$ is not the ground state; to find it, we take the potential:

$$V(\phi) = \frac{1}{2}\mu^2\phi^2 + \frac{1}{4}\lambda\phi^4 \quad \text{with a minimum} \quad \frac{\partial V}{\partial\phi} = \phi(\mu^2 + \lambda\phi^2) = 0 \tag{1.11}$$

where we have three minimums: $\phi = 0$ and $\phi = \pm v$, where $v = \sqrt{-\mu^2/\lambda}$.
Using the minimum $\phi = +v$ and introducing a new field $\chi(x)$, the original field can be written as $\phi(x) = v + \chi(x)$; $\chi(x)$ represents the fluctuation around the ground state $\phi = +v$ and the Lagrangian can be written as:

$$\mathcal{L} = \frac{1}{2}(\partial_\mu\chi)(\partial^\mu\chi) - \lambda v^2\chi^2 - \lambda v\chi^3 - \frac{1}{4}\lambda\chi^4 + \frac{1}{4}\lambda v^4 \tag{1.12}$$

In the new Lagrangian, the second term can be seen as a mass term; the mass obtained by the field $\chi(x)$ is:

$$m_\chi = \sqrt{2\lambda v^2} = \sqrt{-2\mu^2} \tag{1.13}$$

That leads a field χ asymmetry (a spontaneous symmetry breaking).

Second step: the idea is to have a spontaneous breaking of a continuous symmetry (using the Goldstone theorem [1]). Take now a continuum 2-dimensional field, the Lagrangian will be:

$$\mathcal{L} = (\partial_\mu\phi)\cdot(\partial^\mu\phi) - \mu^2\phi\cdot\phi - \lambda(\phi\cdot\phi)^2 \tag{1.14}$$

that is symmetric in U(1) (it is invariant under rotation $\phi \to \phi' = e^{i\alpha}\phi$) and with $\phi = \frac{1}{\sqrt{2}}(\phi_1 + i\phi_2)$. Using ϕ_1 and ϕ_2 terms, the Lagrangian will be:

$$\mathcal{L} = \frac{1}{2}(\partial_\mu\phi_1)^2 + \frac{1}{2}(\partial_\mu\phi_2)^2 - \frac{1}{2}\mu^2(\phi_1 + \phi_2) - \frac{1}{4}\lambda(\phi_1^2 + \phi_2^2)^2 \tag{1.15}$$

The last two terms are $-V(\phi_1, \phi_2)$ if $\mu^2 < 0$ and $\lambda > 0$. $V(\phi_1, \phi_2)$ has a minimum in the circumference $\phi_1^2 + \phi_2^2 = v^2$ with $v = \sqrt{-\mu^2/\lambda}$.
Choosing a ground state with $\phi_1 = v$ and $\phi_2 = 0$ and introducing two fields $\chi_1(x)$ and $\chi_2(x)$ so that:

$$\begin{cases} \phi_1 = v + \chi_1(x) \\ \phi_2 = \chi_2(x) \end{cases} \tag{1.16}$$

then:

$$\phi(x) = \frac{1}{\sqrt{2}}(v + \chi_1(x) + i\chi_2(x)) \tag{1.17}$$

We can see the two fields $\chi_1(x)$ and $\chi_2(x)$ as fluctuation around the ground state $\phi_1 = v$ and $\phi_2 = 0$. In field terms, the Lagrangian becomes:

$$\begin{aligned} \mathcal{L} = & \left[\frac{1}{2}(\partial_\mu \chi_1)(\partial^\mu \chi_1) - \lambda v^2 \chi_1^2\right] + \left[\frac{1}{2}(\partial_\mu \chi_2)(\partial^\mu \chi_2)\right] + \\ & - \left[\lambda v(\chi_1^3 + \chi_1 \chi_2^2) + \frac{\lambda}{4}(\chi_1^4 + \chi_2^4 + 2\chi_1^2\chi_2^2)\right] + \frac{\lambda}{4} v^4 \end{aligned} \tag{1.18}$$

The second term describes a scalar field with a quantum field without mass. The oscillation of χ_2 around the minimum of the potential can be seen as a Goldstone boson. This is an example of the *Goldstone theorem*, which establishes that the spontaneous breaking of a global continuum symmetry leads to one or more scalar bosons without mass.

Third step: We need to extend the analysis to a spontaneous local symmetry breaking $SU(2)_L \otimes U(1)_Y$. We are familiar to the fact that the space is filled with electromagnetic fields where photons are emitted and absorbed. Like it, in the BEH mechanism everywhere in space, the fluctuation of the vacuum could be seen as the absorption or emission of a Higgs boson that have null spin and electric charge, is a color singlet and that it carries weak ipercharge and isospin.

The BEH mechanism is the Goldstone model with the addition of the electromagnetic interaction term. For this reason a vectorial field $A_\mu(x)$ is added and the field can be transformed as $A_\mu \rightarrow A'_\mu = A_\mu - \partial_\mu \Lambda$. With the introduction of the Goldstone potential the Lagrangian like (1.10), becomes:

$$\mathcal{L} = (\partial_\mu - iqA_\mu)\phi \cdot (\partial^\mu - iqA^\mu)\phi - \mu^2 \phi \cdot \phi - \lambda(\phi \cdot \phi)^2 - \frac{1}{4}F_{\mu\nu}F^{\mu\nu} \tag{1.19}$$

With $F_{\mu\nu} = \partial_\mu A_\nu - \partial_\nu A_\mu$. Adding two complex scalar field like Eq.(1.16) the Lagrangian becomes:

$$\begin{aligned}\mathcal{L} = &\left[\frac{1}{2}(\partial_\mu \chi_1)(\partial^\mu \chi_1) - \lambda v^2 \chi_1^2\right] + \left[\frac{1}{2}(\partial_\mu \chi_2)(\partial^\mu \chi_2)\right] + \\ &+ \frac{1}{2}q^2 v^2 A_\mu A^\mu - qvA_\mu \partial^\mu \chi_2 - \frac{1}{4}F_{\mu\nu}F^{\mu\nu} + I.T.\end{aligned} \tag{1.20}$$

where I.T. indicates "interaction terms".
In this case the Goldstone field acquires a mass $m_A = qv$, but there is a problem: now there is a mixed term that brings up a Goldstone boson. To remedy the problem, the filed is parameterized as:

$$\phi(x) = \frac{1}{\sqrt{2}}(v + H(x))exp\left[\frac{i\theta(x)}{v}\right] \tag{1.21}$$

with $H(x)$ and $\theta(x)$ real:

$$\begin{cases} A'_\mu(x) = A_\mu(x) + \frac{1}{qv}\partial_\mu \theta(x) \\ \phi'(x) = \frac{1}{\sqrt{2}}[v + H(x)] \end{cases} \tag{1.22}$$

And the Lagrangian becomes:

$$\begin{aligned}\mathcal{L} = &\left[\frac{1}{2}(\partial_\mu H)^2 - \lambda v^2 H^2\right] + \frac{1}{2}q^2 v^2 A_\mu A^\mu + \frac{1}{2}q^2 A_\mu A^\mu H^2 + \\ &+ q^2 v A_\mu A^\mu H - \lambda v H^3 - \frac{\lambda}{4}H^4 - \frac{1}{4}F_{\mu\nu}F^{\mu\nu} + \frac{\lambda}{4}v^4\end{aligned} \tag{1.23}$$

and the dependence by $\theta(x)$ in the field disappear.

To apply the BEH mechanism to the model, a complex scalar field doublet is introduced:

$$\phi = \begin{pmatrix} \phi^+ \\ \phi^0 \end{pmatrix} = \begin{pmatrix} \phi_1 + i\phi_2 \\ \phi_3 + i\phi_4 \end{pmatrix} \tag{1.24}$$

Choosing the vacuum in one direction of the SU(2) space: $\phi^0 = \left(\begin{smallmatrix} 0 \\ v \end{smallmatrix}\right)$ and choosing an arbitrary field $\phi(x) = \left(\begin{smallmatrix} 0 \\ v+H(x) \end{smallmatrix}\right)$, the Lagrangian becomes:

$$\mathcal{L} = \left[\frac{1}{2}(\partial_\mu H)^2 - \lambda v^2 H^2\right] + \frac{g^2 v2}{8}(W^1_\mu W^{1\mu} + W^2_\mu W^{2\mu}) + \frac{v^2}{8}(gW^3_\mu - g' B_\mu)(gW^{3\mu} - g' B^\mu) \tag{1.25}$$

with the addition of kinetic terms for the Z and $W^\pm$ fields.
The W^1_μ and W^2_μ have mass terms but W^3_μ and B_μ terms are associated to γ and Z of Eq.(1.7).
With these new terms, the free Lagrangian can be written as:

$$\begin{aligned} \mathcal{L} = \frac{1}{2}(\partial_\mu H)^2 - \lambda v H^2 + \\ -\frac{1}{4}(\partial_\mu W^1_\nu - \partial_\nu W^1_\mu)(\partial^\mu W^{1\nu} - \partial^\nu W^{1\mu}) + \frac{g^2 v^2}{8}(W^1_\mu W^{1\mu}) + \\ -\frac{1}{4}(\partial_\mu W^2_\nu - \partial_\nu W^2_\mu)(\partial^\mu W^{2\nu} - \partial^\nu W^{2\mu}) + \frac{g^2 v^2}{8}(W^2_\mu W^{2\mu}) + \\ -\frac{1}{4}(\partial_\mu Z_\nu - \partial_\nu Z_\mu)(\partial^\mu Z^\nu - \partial^\nu Z^\mu) + \frac{v^2}{8}(g^2 + g'^2)(Z_\mu Z^\mu) + \\ -\frac{1}{4}(\partial_\mu A_\nu - \partial_\nu A_\mu)(\partial^\mu A^\nu - \partial^\nu A^\mu) \end{aligned} \tag{1.26}$$

where the mass terms are:

$$m_H = \sqrt{2\lambda v^2} = \sqrt{-2\mu^2} \quad ; \quad m_W = \frac{1}{2}gv \quad ; \quad m_Z = \frac{1}{2}\sqrt{g^2 + g'^2} = \frac{m_W}{cos\theta_w} \quad \text{and} \quad m_\gamma = 0 \tag{1.27}$$

This model introduced a new particle (the Higgs Boson), but it has not defined its mass.

Fig. 1.2 shows the form of the Higgs potential in the $Re(\phi)$,$Im(\phi)$ plane.

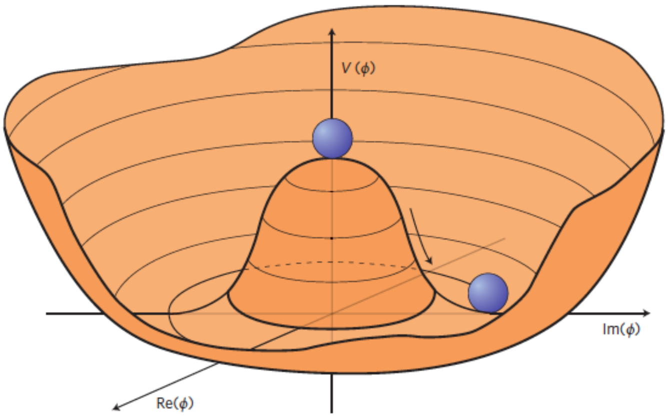

FIGURE 1.2: Higgs potential in $Re(\phi)$,$Im(\phi)$ plane.

An indirect relation between the mass of the Higgs boson and the other SM particles can be derived from the W mass by the equation:

$$\begin{aligned} m_W = 80.364 - 0.0579 ln\left(\frac{m_H}{100GeV}\right) - 0.008 ln^2\left(\frac{m_H}{100GeV}\right) + \\ -0.5098\left[\frac{\Delta\alpha(m_Z)}{0.02761} - 1\right] + 0.525\left[\left(\frac{m_t}{172GeV}\right)^2 - 1\right] - 0.085\left[\frac{\alpha_s(m_Z)}{0.118} - 1\right] \end{aligned} \tag{1.28}$$

Precise measurements of these parameters ($\Delta\alpha$, m_W, m_Z, m_t and α_s) led to various constraints on the mass of the Higgs boson and the subsequently discovery ([2], [3]).

1.1.5 Strong nuclear force: Quantum Chromodynamics (QCD)

The Quantum Chromodynamics QCD is the theory of the strong interaction and it is a non-abelian gauge theory with symmetry group $SU(3)_C$. The particles affected by

the strong coupling require an additional charge to preserve the Pauli-like principle in QCD, the *color* charge.
In order to compensate for the local gauge transformations, eight additional fields, which are associated to eight gluons, must be included into the QCD Lagrangian. The additional fields must be included in the strong Lagrangian, and can be written as:

$$\mathcal{L} = -\frac{1}{4}G^a_{\mu\nu}G^{\mu\nu}_a + \sum_{i=1}^{N_c}\sum_{f=1}^{N_f}\bar{q}_{f_i}(i\gamma^\mu D_\mu - m_f)q_{f_i} \tag{1.29}$$

where the sums run over the color states N_c and the quark flavors N_f. The first term of the Lagrangian is also called $Yang-Mills$ term and describes the dynamics of the gluon fields A_μ.

$$\mathcal{L}_{YM} = -\frac{1}{2}Tr(G^a_{\mu\nu}G^{\mu\nu}_a) \tag{1.30}$$

where $G^a_{\mu\nu}$ is the gauge invariant gluon field strength tensor:

$$G^a_{\mu\nu} = \partial_\mu G^a_\nu - \partial_\nu G^a_\mu + g f_{abc} G^b_\mu G^c_\nu \tag{1.31}$$

where f_{abc} are the structure constants of $SU(3)_C$.
The Quantum Chromodynamics has two properties:

- $Confinement$: the force between quarks does not diminish as they are separated, but it gets stronger. Quarks are bound into hadrons;
- $Asymptotic\ freedom$: the interaction between particles become asymptotically weaker as the energy scale increases and the corresponding length scale decreases.

The strength of the strong force is represented by α_s and it can be expressed as:

$$\alpha_s = \frac{g_s^2}{4\pi} \tag{1.32}$$

where g_s is the QCD gauge coupling.
The α_s exhibits a different trend in the low and high energy regimes; this dependence of the energy scale is called *running coupling*. At the Leading Order (LO) α_s is:

$$\alpha_s(Q^2) = \frac{12\pi}{(33 - 2N_f)ln(\frac{Q^2}{\Lambda^2_{QCD}})} \tag{1.33}$$

where Λ_{QCD} represents the QCD scale and it has been experimentally determined to be $\Lambda_{QCD} \sim 200MeV$.
In the limit of asymptotic freedom, when the coupling constant is very small, calculation of cross section can be expanded perturbatively in powers of α_s; in the limit of confinement, α_s tends to be infinity.
In Fig. 1.3 is shown the running coupling of α_s as a function of Q, together with several measurements.

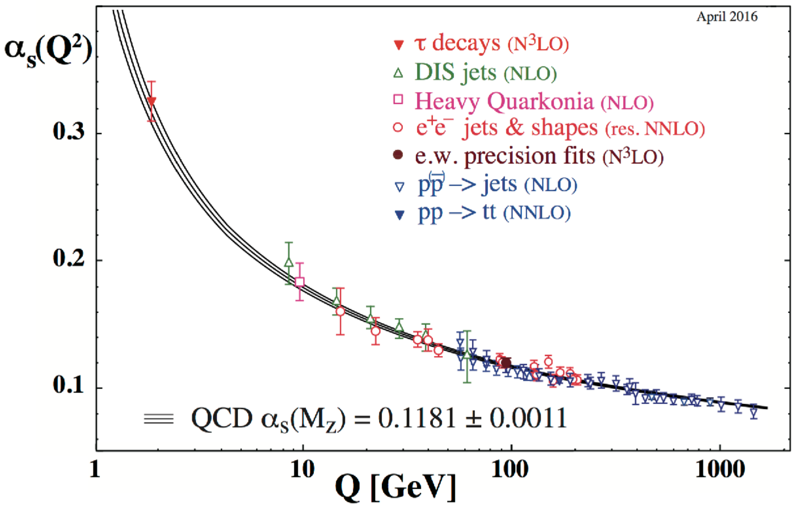

FIGURE 1.3: Measurements of α_s as a function of Q.

1.2 Open questions of the Standard Model

The SM of particle physics has been extremely successful in predicting and explaining particle physics phenomenology so far [7]. Nonetheless, it presents several limitations and it is considered an effective theory valid at low energy $O(100GeV)$. A number of theories, defined as *Beyond Standard Model* (BSM) have been developed to extend the SM. Below are listed and briefly described some of the phenomena not described by Standard Model:

- *Gravity*: the SM does not explain the gravitational force, one of the four known fundamental interactions; the hypothetical carrier of the gravitational force, the spin-2 graviton, has never been observed and a quantum-relativistic theory of gravity has not yet been formulated;
- *Dark matter* and *Dark energy*: cosmological observations indicate that the SM explains the 5% of the total energy in the universe; of the remaining part ∼25% is composed of *dark matter* that seems to interacts weakly or not at all with the SM fields, and the SM does not provide any fundamental particle candidate to be dark matter [8]; the remain percentage seems to be composed by *dark energy*, of which we do not know the nature;
- *Neutrino masses*: in the SM the neutrinos do not have masses, but we know from experiments of neutrino oscillation ($\nu_e \to \nu_\mu$ or $\nu_\mu \to \nu_\tau$) [9] that these particles have a mass, though very small;
- *Matter−antimatter asymmetry*: the universe is composed almost exclusively of matter, but it is reasonable to think that in its first moments of life, the quantity of matter and antimatter was the same. There is no mechanism in the SM that sufficiently explains this asymmetry [10].

In addition to these problems, there are additional aspects of the SM that cause concern:

- *Hierarchy problem*: the Standard Model introduces the particle mass through the BEH mechanism; but large corrections due to the presence of virtual particles (for example top quark loops) are needed and these corrections are bigger than the Higgs boson mass; this implies that the bare mass of the Higgs boson must be renormalized in order to delete these corrections and a fine tuning is needed [11];
- *Number of the parameters*: the Standard Model is based on 19 numerical parameters known from the experiments, but whose theoretical origins are still

unknown. The Standard Model parameters are: the fine structure constant α, the weak mixing angle θ_W, the coupling constant g_s of the strong interaction, the electroweak symmetry breaking energy scale v, the Higgs mass m_H, the QCD vacuum angle θ_{QCD}, the three mixing angles θ_{12}, θ_{23} and θ_{13} and the CP-violating phase δ_{13} of the Cabibbo-Kobayashi-Maskawa (CKM) matrix and nine Yukawa coupling constants that determine the masses of the nine charged fermions (six quarks, three charged leptons).

These and other unsolved problems have led physicists to look for theories that go beyond this model, such as new symmetries or other dimensions. Some of these theories will be described in Section 1.4.

1.3 The top quark

This analysis is done with the dilepton decay of the $t\bar{t}$ resonance because is more sensitive to variations of spin correlation and various signals of new physics change the spin correlation near the resonance.
The top quark is the heaviest particle in the Standard Model [12]. Being heavier than a W boson, it is the only quark that decays to a real W boson and a b quark. The unexpectedly large mass ($\sim$ 173 GeV) of the top quark also places it close to the Electroweak symmetry breaking scale of 246 GeV; so it is strongly coupled to the SM Higgs via Yukawa mechanism. This makes it the main contributor to the quadratic divergences of the SM Higgs mass.
For these reasons, the top quark plays a special role in the Standard Model and in many extensions thereof. An accurate knowledge of its properties (mass, couplings, production cross section, decay branching ratios, etc.) can bring key information on fundamental interactions at the electroweak symmetry-breaking scale and beyond.

1.3.1 Top quark production

In hadron collision, the main top quark production modes are the quark-antiquark annihilation ($q\bar{q} \rightarrow t\bar{t}$) and the gluon-gluon fusion ($gg \rightarrow t\bar{t}$), as shown in Fig. 1.4.

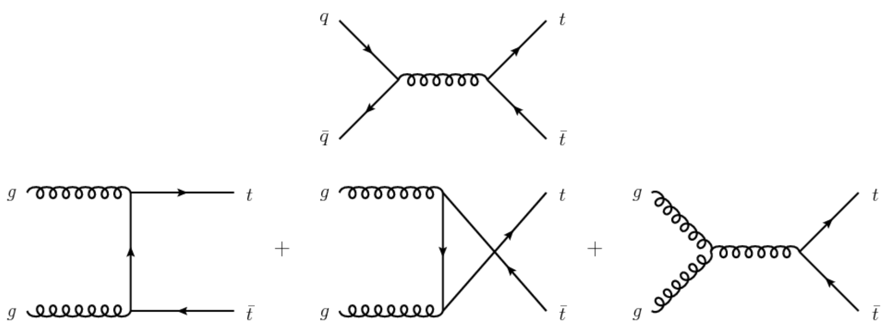

Figure 1.4: Lowest order diagrams contributing to top quark pair production at hadron colliders. Top quarks are produced via strong interaction, either in quark-antiquark annihilation (top) or gluon-gluon fusion (bottom).

Approximately 85% of the production cross section at the Tevatron ($p\bar{p}$ at 1.96 TeV) was from quark-antiquark annihilation, with the remainder from gluon-gluon fusion, while at LHC (pp) energies ($\sqrt{s} = 14$ TeV) about 90% of the production is from the latter process (~ 80 % at $\sqrt{s} = 7$ TeV).

The decay width of the top quark is given by:

$$\Gamma_t = [|V_{td}|^2 + |V_{ts}|^2 + |V_{tb}|^2]\frac{g^2}{64\pi}\frac{m_t^3}{m_W^2}\left(1 - \frac{m_W^2}{m_t^2}\right)^2\left(1 + 2\frac{m_W^2}{m_t^2}\right) \tag{1.34}$$

where $V_{t(d,s,b)}$ are the CKM quark-mixing matrix, with $V_{td} \sim 0.0087$, $V_{ts} \sim 0.04$ and $V_{tb} \sim 0.9991$, according to the latest experiments, g is the strong coupling constant, m_W is the W boson mass and m_t the top quark mass. It follows that the branching ratio for top decay via $t \to bW^+$ ($\bar{t} \to \bar{b}W^-$) is $\sim 99.8\%$.
The $W^\pm$ bosons may decay leptonically ($W^\pm \to l^\pm\nu(\bar{\nu})$) or hadronically ($W^\pm \to q\bar{q}'$); this lead to three classifications of a $t\bar{t}$ event:

- *Fully hadronic* when both the W bosons decay hadronically (both $W^\pm \to q\bar{q}'$) and the branching ratio of process is 45.7%;
- *Lepton + jets* when one W boson decay hadronically and the second one leptonically ($W^\pm \to q\bar{q}'l^\pm\nu(\bar{\nu})$, this final state is 43.8%;
- *Dileptonic* when both W bosons decay leptonically ($W^\pm \to l^+\nu l^-\bar{\nu}$) and the branching ratio of this final state is 10.5%

A summary of the branching ratio is shown in Fig. 1.5.

At Leading-Order (LO), the partial decay width of the W boson to leptons and to quarks, accounting for the color factor and unitarity of the CKM matrix, is:

$$\Gamma(W \to l\nu) = \frac{g_W^2 m_W}{48\pi} \quad \text{and} \quad \Gamma(W \to qq') = 6\Gamma(W \to l\nu) \tag{1.35}$$

Predictions for the top-quark total production cross sections are now available at next-to-next-to leading order (NNLO) with next-to-next-to-leading-log (NNLL) soft

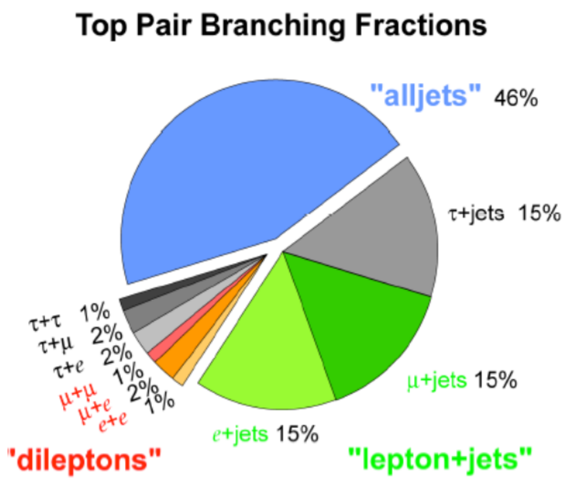

FIGURE 1.5: Pie chart of the top pair production branching fractions.

gluon resummation [13]. At the LHC, taking into account a top quark mass of 172.5 GeV/c^2, the cross sections are [12]:

- $\sigma_{t\bar{t}} = 177.3^{+4.6+9.0}_{-6.0-9.0}$ pb at $\sqrt{s}$ 7 TeV;
- $\sigma_{t\bar{t}} = 252.9^{+6.4+11.5}_{-8.6-11.5}$ pb at $\sqrt{s}$ 8 TeV;
- $\sigma_{t\bar{t}} = 831.8^{+19.8+35.1}_{-29.2-35.1}$ pb at $\sqrt{s} = 13$ TeV;

where the first uncertainty is statistical and the second is systematic.
At the Tevatron, the t-channel and s-channel cross sections of top and antitop are identical, while at the LHC they are not, due to the fact that dominant production is the gluon fusion.

1.3.2 Top quark asymmetries

In addition to standard kinematic variables, it is possible to use the spatial and spin asymmetries to assist the search for possible Beyond Standard Model phenomena. Asymmetries are, in general, defined as:

$$A = \frac{N_a - N_b}{N_a + N_b} \tag{1.36}$$

where N_a and N_b are two exclusive categories of the total events N.

1.3.2.1 Forward-Backward asymmetry

The forward-backward asymmetry is constructed by splitting the detector in two hemispheres and taking the difference between the number of events where the top or antitop quarks are detected on either side, as:

$$A_{FB} = \frac{N(\Delta y > 0) - N(\Delta y < 0)}{N(\Delta y > 0) + N(\Delta y < 0)} \tag{1.37}$$

where $\Delta y = y_t - y_{\bar{t}}$ is the rapidity [1] difference between the top and antitop quarks. A forward-backward asymmetry in $t\bar{t}$ production is measured in $p\bar{p}$ colliders (like Tevatron), because the asymmetry start to be not negligible at order α_S^3 in QCD from the interference between $q\bar{q} \to t\bar{t}$ with 1-loop box production diagrams and between diagrams with gluon radiation in initial and final state; in this case the z direction is very correlated with the incoming quark direction, and the contribution due to an interaction between a sea quark from the antiproton and a sea antiquark from the proton is negligible.

At the LHC the $t\bar{t}$ production is given by pp collision, where the incoming quark has the same probability of coming from either proton and each event receive an equal contribution from both configurations; at center-of-mass energy $\sqrt{s} = 13$ TeV the main mechanism is the charge-symmetric gluon-gluon fusion. In this case is preferential to define a variable dependent on the difference between the absolute value of the rapidity of the top and antitop, $\Delta|y| = |y_t| - |y_{\bar{t}}|$ and the charge asymmetry is defined as:

$$A_C = \frac{N(\Delta|y| > 0) - N(\Delta|y| < 0)}{N(\Delta|y| > 0) + N(\Delta|y| < 0)}, \tag{1.38}$$

The values of A_C has been measured by both ATLAS and CMS collaborations using *lepton + jets* and *dilepton* final state events. For the lepton+jets channel, the asymmetry is $A_C^{t\bar{t}} = 0.009 \pm 0.005$, measured by ATLAS at $\sqrt{s} = 8$ TeV [14]; for the dilepton channel the asymmetry is $A_C^{t\bar{t}} = 0.021 \pm 0.016(stat + syst)$ measured by ATLAS at $\sqrt{s} = 8$ TeV [15] and $A_C^{t\bar{t}} = (0.33 \pm 0.26(stat) \pm 0.33(syst))\%$ measured by CMS at $\sqrt{s} = 8$ TeV [16].

[1] The definition of rapidity y is described in Chapter 2

1.3.2.2 Spin asymmetry

An interesting propriety of the top quark is the fact that it is heavy and has a very short lifetime, such that the particle decays prior to hadronise. For this reason the informations like the spin configuration are retained in the angular distributions of its decay products. Top quark pair production in QCD is parity invariant and hence the top quarks are not expected to be polarised in the SM, so new physics phenomena can be seen from a discrepancy of this top quark pair property.
The spin correlation asymmetry, or double spin asymmetry (A_{LL}), measures the net spin correlation of the top and antitop quarks by subtracting events with aligned and antialigned helicities:

$$A_{LL} = \frac{[N(\uparrow\uparrow) + N(\downarrow\downarrow)] - [N(\uparrow\downarrow) + N(\downarrow\uparrow)]}{[N(\uparrow\uparrow) + N(\downarrow\downarrow)] + [N(\uparrow\downarrow) + N(\downarrow\uparrow)]} \tag{1.39}$$

where the first arrow represents the direction of the top-quark spin along a chosen quantization axis, and the second arrow represents the same for the antitop quark. The spin correlation could be modified by a new $t\bar{t}$ production mechanism such as through SSM Z' boson, the Kaluza-Klein gluons or Randall-Sundrum gravitons.
Spin correlations have been measured at the LHC by both the ATLAS and CMS collaborations. In the dominant gluon fusion production mode for $t\bar{t}$ pairs at the LHC, the angular distribution between the two leptons in $t\bar{t}$ decays to dileptons [17] is sensitive to the degree of spin correlation.

The ATLAS collaboration has measured spin correlations in $t\bar{t}$ production at $\sqrt{s} =$ 13 TeV with 36.1 fb^{-1} of data and the candidate events are selected in the dilepton and lepton+jets topologies. The most sensitive measurement comes from using $\Delta\phi$ in dilepton events and results is $f_{SM} = 1.03 \pm 0.07(stat) \pm^{+0.10}_{-0.14} (scale)$ [18].

1.4 Beyond Standard Model theories

In this section we introduce some models which lead to a $t\bar{t}$ resonance in the dilepton decay mode ($\ell\ell = e^+e^-, \mu^+\mu^-$ and $e^\pm\mu^\mp$). The BSM models under study in this thesis are: the neutral heavy gauge boson Z', the Randall-Sundrum graviton G and the Kaluza-Klein gluon g_{KK}. Representative Feynman diagrams for the production of such particles and their decay to $t\bar{t}$ are shown in Fig. 1.6.

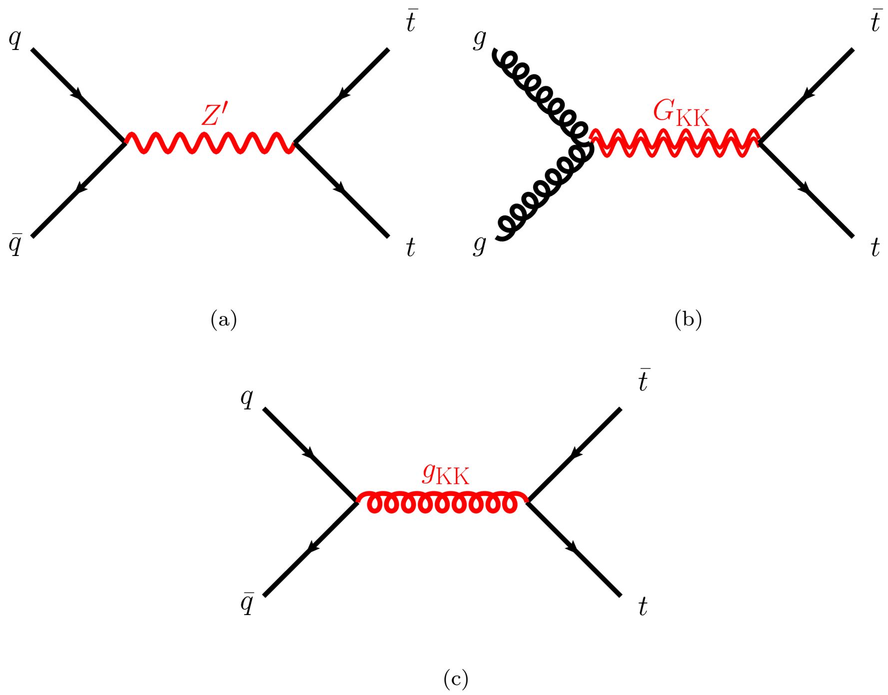

FIGURE 1.6: Schematics of the BSM models in $t\bar{t}$ decay mode: neutral heavy gauge boson Z' (a), Randall-Sundrum graviton G (b) and Kaluza-Klein gluon g_{KK} (c)

1.4.1 Neutral Heavy Gauge Boson (Z'_{SSM})

In the Sequential Standard Model [19], the SSM Z' has the same quantum numbers and coupling to fermions as the SM Z boson and no coupling to the $W^{\pm}$ and Z bosons.

The Z' boson is hence a copy of the SM Z boson, but with a higher mass, it is the simplest extension of the SM. A more theoretically-motivated model is a Grand Unification model in which the E_6 gauge group is broken into $SU(5)$ and two additional $U(1)$ groups [20]. In the extension $SU(2) \otimes U(1)_Y \otimes U(1)'^n$ (with $n \geq 1$) the Lagrangian of the neutral current interaction is:

$$\mathcal{L}_{\mathcal{NC}} = eJ^{\mu}_{em}A_{\mu} + \sum_{\alpha=1}^{n+1} g_{\alpha}J^{\mu}_{\alpha}Z^{0}_{\alpha\mu} \tag{1.40}$$

where g_1, J_1^{μ} and $Z^0_{1\mu}$ are the gauge coupling, boson, and current of the standard model, respectively; similarly g_{α}, J^{μ}_{α} and $Z^0_{\alpha\mu}$, with $\alpha = 2...n+1$, are the gauge coupling, boson, and current of the additional $U(1)'$ symmetry groups, respectively. The lightest linear combination of the corresponding two neutral gauge bosons Z'_{ϕ} and Z'_{χ}, is considered the Z' candidate $Z'(\theta_{E_6}) = Z'_{\psi}cos(\theta_{E_6}) + Z'_{\chi}cos(\theta_{E_6})$, where $-\pi \leq \theta_{E_6} < \pi$ is the mixing angle between the two gauge bosons. The pattern of spontaneous symmetry breaking and the value of θ_{E_6} determine the Z' couplings to fermions. There are six different models that lead to a specific Z' state: Z'_{ψ}, Z'_{N}, Z'_{η}, Z'_{l}, Z'_{S} and Z'_{χ}. In any model considered, the resonances are assumed to have a narrow intrinsic width, meaning the exclusion limits extracted for the widest signal shape can also be used to infer corresponding limits on the other models considered. In Fig. 1.7 is shown the LO predictions of the cross-section times the branching ratio for different Z' models versus pole mass at $\sqrt{s}$ = 13 TeV, the dilepton channel is assumed to be $Z' \to \ell\ell$.

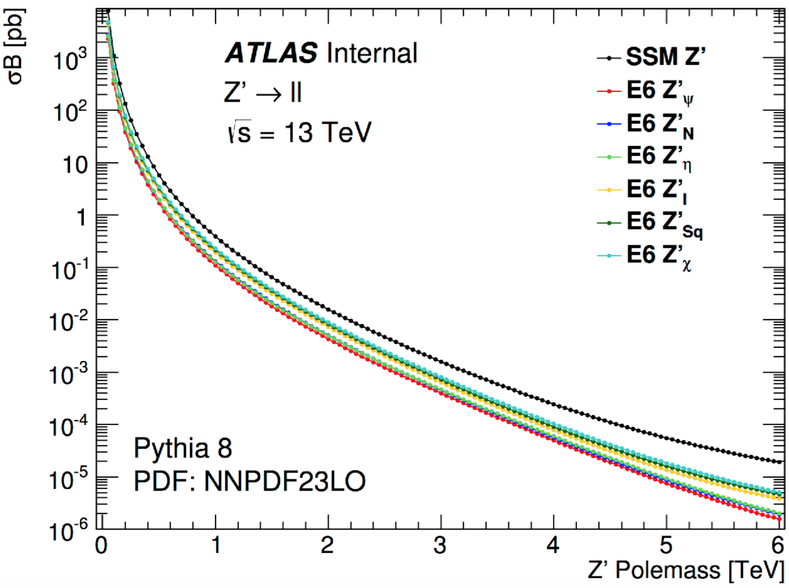

FIGURE 1.7: LO cross-section times branching ratio to a dilepton flavor for various Z' models versus pole mass at $\sqrt{s} = 13$ TeV. [21]

Previous direct searches for Z' have been carried out at the Tevatron experiments and indirect constraints from LEP have resulted in limits on the Z' mass of 1.07

TeV [22] and 1.79 TeV [23], respectively. From the LHC experiment the previous analysis has resulted in limits on mass of 3.0 TeV (expected 2.6 TeV). In this analysis the TC2 benchmark model chosen for this search produces a Z' boson. This is a leptophobic boson, with couplings only to first- and third-generation quarks, referred to as Model IV [24]. The signal hypothesis considered by this analysis is Z' TC2, but as their widths are negligible compared to the experimental resolution, they can be safely compared with SSM models as well (small width as well). The properties of the boson are controlled by three parameters: the topcolour tilting parameter, $cot\theta_H$, which controls the width and the production cross-section, and f_1 and f_2, which are related to the coupling to up-type and down-type quarks, respectively. Here $f_1 = 1$ and $f_2 = 0$, which maximises the fraction of Z' bosons that decay into $t\bar{t}$. In Fig. 1.8 the exclusion limits on cross section times branching ratio versus the expected Z' mass measured in $Z' \rightarrow t\bar{t}$ lepton+jets final state [29] is shown, this analysis excludes a Z' mass below 3 TeV. The CMS collaboration [25], combining $dilepton$, $lepton + jets$ and $full - hadronic$ final states, excludes a narrow Z' mass below 3.8 TeV.

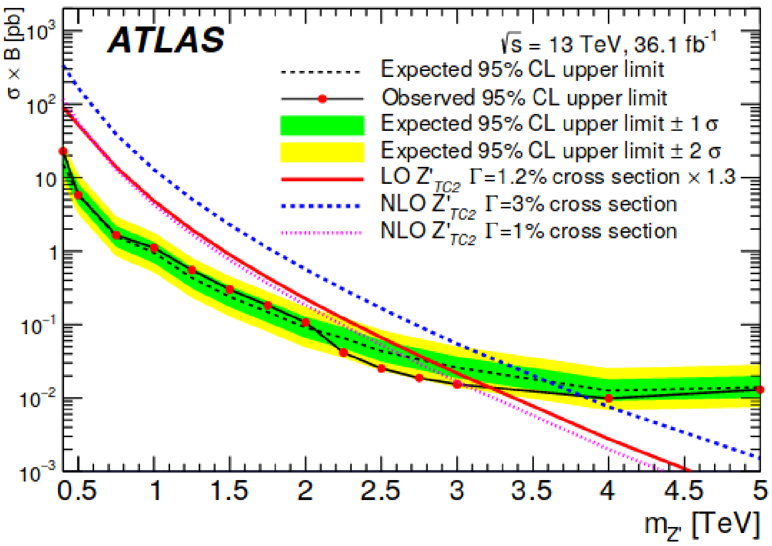

FIGURE 1.8: Exclusion limits on cross section times branching ratio versus the expected Z' mass measured in $Z' \rightarrow t\bar{t}$ lepton+jets final state at center-of-mass energy $\sqrt{s} = 7$ TeV.

1.4.2 Randall-Sundrum Graviton (G)

The gravitons (spin-2 colour-singlet bosons) are produced in models that postulate extra dimensions of space leading to Kaluza–Klein excitations of the graviton. The Randall-Sundrum (RS) model [26] assumes that the universe is an Anti-de Sitter 5-dimensional space and the elementary particles, except for the graviton, are localized on (3+1)-dimensional branes.
This is a *Braneworld* model and it was developed to try to solve the hierarchy problem of the Standard Model; it is a finite 5-dimensional bulk extremely deformed and is composed by two branes: the *Planckbrane*, where the gravity is a relatively strong force; and the *Tevbrane*, where the SM particles are located. In this model, the two branes are separated by a 5th dimension and the space-time is extremely deformed, due to the fact that the Planckbrane has a positive brane-energy and the Tevbrane has a negative brane-energy.
In this deformed space-time the graviton probability function (due to the Kaluza-Klein excitation of the SM fields) is higher in the Planckbrane and decreases exponentially to the Tevbrane only if we assume a 5th dimension; for this reason, gravity is very weak in our universe, bringing the boson (with spin 2) to be detected at the TeV scales.

In the RS model the Einstein equation solution, in a Anti-de Sitter 5-dim space (AdS_5) with a non-factored geometry, can be written as:

$$ds^2 = e^{-2kr_c\phi}\eta_{\mu\nu}dx^\mu dx^\nu + r_c^2 d\phi^2 \tag{1.41}$$

where $k \sim M_{Pl}$ ($M_{Pl} \simeq 10^{19}$ GeV is the Planck mass) is the curvature parameter, r_c is the compactification radius, $\eta_{\mu\nu}$ is the 4-dim metric tensor and ϕ is the parameter of the extra dimension with $0 < \phi < 2\pi$.
If we assumed that the SM fields are confined in the brane located in $\phi = \pi$, any mass parameter m_0 on the visible 3-brane in the fundamental higher-dimensional theory will correspond to a physical mass:

$$m = e^{-kr_c\pi}m_0 \tag{1.42}$$

For example, if we set the Higgs mass (125 GeV), a Planck-scale-mass-order $M_{Pl} \sim 10^{17}$ is reached. In this way, masses of the TeV order can be produced by Planck-scale order parameters; the compactification scale $1/r_c$ is of the M_{Pl}-order so as not to introduce additional hierarchies.
The Lagrangian of the interaction between the graviton and the matter fields, is:

$$\mathcal{L} = -\frac{1}{M_{Pl}} T^{\alpha\beta} h^{(0)}_{\alpha\beta} - \frac{1}{\Lambda_\pi} T^{\alpha\beta} \sum_{n=1}^{\infty} h^{(n)}_{\alpha\beta} \tag{1.43}$$

where $h_{\alpha\beta}$ are the graviton fields, $T^{\alpha\beta}$ is the energy-momentum tensor of the matter field and Λ_π is the coupling parameter.
From the Lagrangian it can be deduced that the coupling between the KK excitation with the matter, is comparable with $\frac{1}{M_{EW}}$, where M_{EW} is the electroweak scale ($\sim 10^3$ GeV).

The RS graviton can decay in all the particles of the Standard Model. Other analyses consider different channels of graviton decay (such as diboson channels [27] and [28]). The leptonic decays are good discovery channels, because electrons and muons can be observed directly in the detectors and the background is small; in the case of hadronic decays, there are many jets and a high QCD background; the di-gamma final state is another good discovery channel, because the photon background is small; the diboson decays have more complicated topologies, as they can generate combinations of leptonic jets and missing energy.
The most stringent results from the ATLAS experiment, in case the graviton G decays into top quark pair, are reported in [29] and set a mass limit of G below 650 GeV, as shown in Fig. 1.9 that shows the cross-section times branching fraction for G production.

1.4.3 Kaluza-Klein Gluon (g_{KK})

In the original model the SM fields were confined to a single brane. However models in which the SM fermions and gauge bosons propagate throughout all five dimensions can have attractive features and allowing gauge coupling unification. The first signal of such a framework should be the resonant production of the Kaluza-Klein (KK)

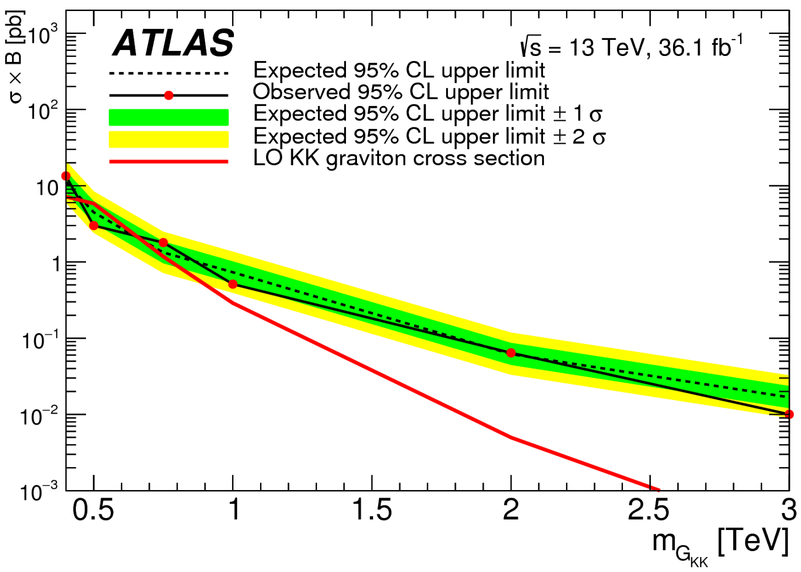

Figure 1.9: Exclusion limits on cross section times branching ratio versus the expected Randal-Sundrum graviton mass measured in $G \to t\bar{t}$ lepton+jets final state (here labeled as G_{KK}) and $\sqrt{s} = 13$ TeV.

excitations of the gauge bosons [30]. Since the KK-gluons are the most strongly coupled of the new KK particles, they have the largest production rate and will likely be the first signal of this model. The KK-gluon is a theoretical particle in the RS model.

Since the KK-gluons are the particles that couple more strongly with the SM particles, in comparison to the other KK-particles, they have the largest production rate and will likely be the first signal of this model. In this model the KK-gluon decay primarily to $t\bar{t}$. In Tab. 1.1 are shown the branching ratios of the KK-gluon decays in quarks pair.

Channel Decay	Branching Ratio
$t + \bar{t}$	92.5%
$b + \bar{b}$	5.5%
$q + \bar{q}$	2%

Table 1.1: Branching Ratios for different kk-gluon channel decay. $q + \bar{q}$ means all lighter quarks-antiquarks pair productions together.

In order to account for the top quark mass, the top quark is likely to be localized towards the TeV brane.
A first study of the $g_{kk} \rightarrow t\bar{t}$ in dilepton channel [31] decay was done with the ATLAS experiment with $\sqrt{s} = 7$ TeV and 1.04 fb^{-1} and a mass range between 0.84 TeV - 0.96 TeV was probed. In Fig. 1.10 the expected and observed limits measured in this preliminary study are shown. Other results in lepton+jets $g_{kk} \rightarrow t\bar{t} \rightarrow \ell\nu qq$ resonance lead to a limit mass expected below 3.2 TeV and observed below 3.7 TeV [29] as shown in Fig. 1.11. The CMS collaboration, combining *dilepton*, *lepton+jets* and $full - hadronic$ final states, excludes a narrow g_{KK} mass below 4.55 TeV [25].

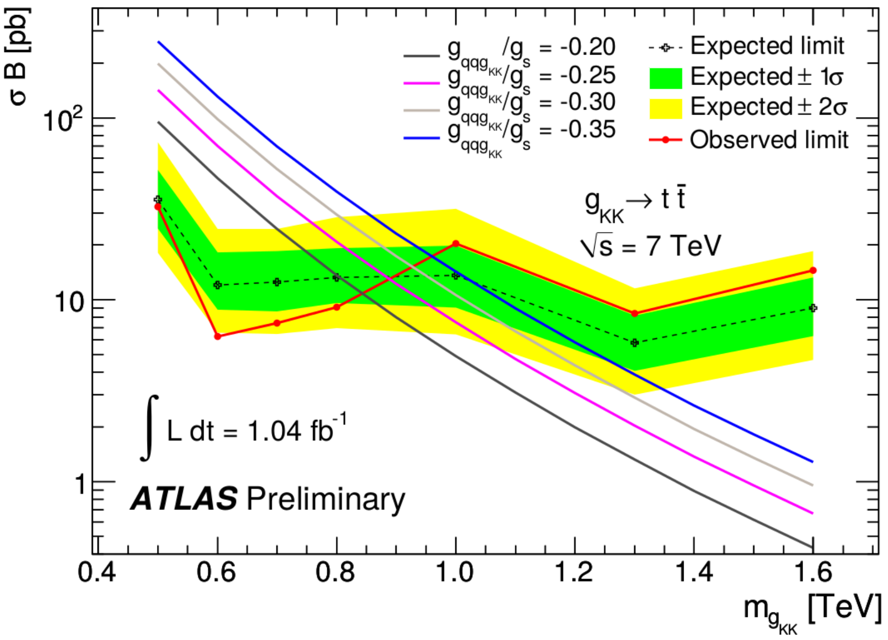

FIGURE 1.10: Exclusion limits on cross section times branching ratio versus the expected kk-gluon mass measured in $g_{kk} \rightarrow t\bar{t}$ dilepton channel and $\sqrt{s} = 7$ TeV.

1.5 Summary

In this chapter was described the Standard Model of particle physics with its fundamental interactions and main open questions. It was described also the top quark particle and the various BSM models connected to the top quark physics with their undirscoved particles, that can explain some of the problems inside the Standard Model.

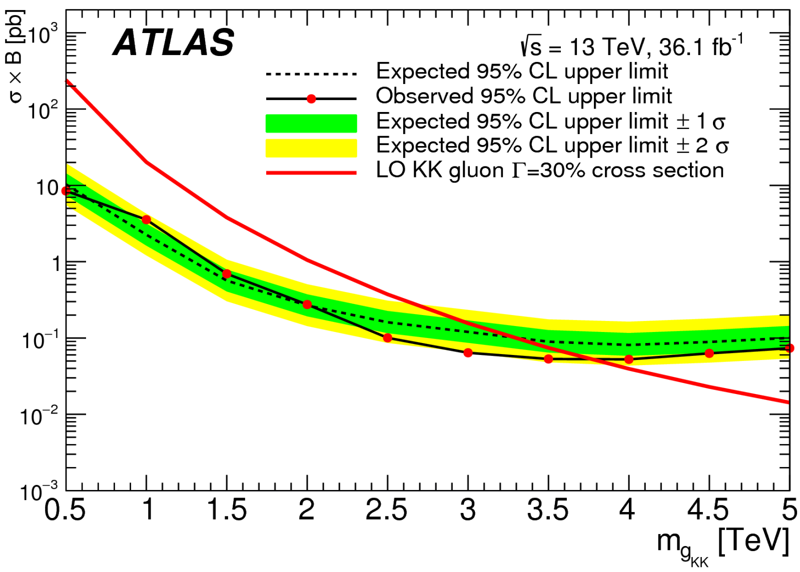

FIGURE 1.11: Exclusion limits on cross section times branching ratio versus the expected kk-gluon mass measured in $g_{kk} \to t\bar{t}$ lepton+jets channel and $\sqrt{s} = 13$ TeV.

Chapter 2

The LHC accelerator and the ATLAS experiment

The Large Hadron Collider (LHC) is the largest energy particle accelerator ever built, with a circumference of 27 km located at CERN, on the border between Switzerland and France, near the city of Geneva.
The main objectives of LHC are the study of the Higgs boson decay, which was discovered in 2012 ([2], [3]), and the research of Beyond Standard Model (BSM) physics at the TeV scale. The ATLAS experiment is located in the interaction point 1 of the LHC ring, as shown in Fig. 2.1. In this chapter, the LHC accelerator complex and its experiments are briefly introduced, followed by a detailed description of the ATLAS experiment and its main components.

2.1 The LHC accelerator

The LHC [32] is a proton-proton (and heavy ions) collider based at CERN in Geneva. Inside the accelerator, two beams of high-energy particles (6.5 TeV for each beam) travel in opposite directions and collide in four points of the ring. The LHC uses proton beams accelerated in pulses and each bunch consists of approximately 10^{11} protons. By design each beam has 2500 bunches, which are separated by 25 ns.
The particle beams are guided along the ring by strong magnetic fields maintained

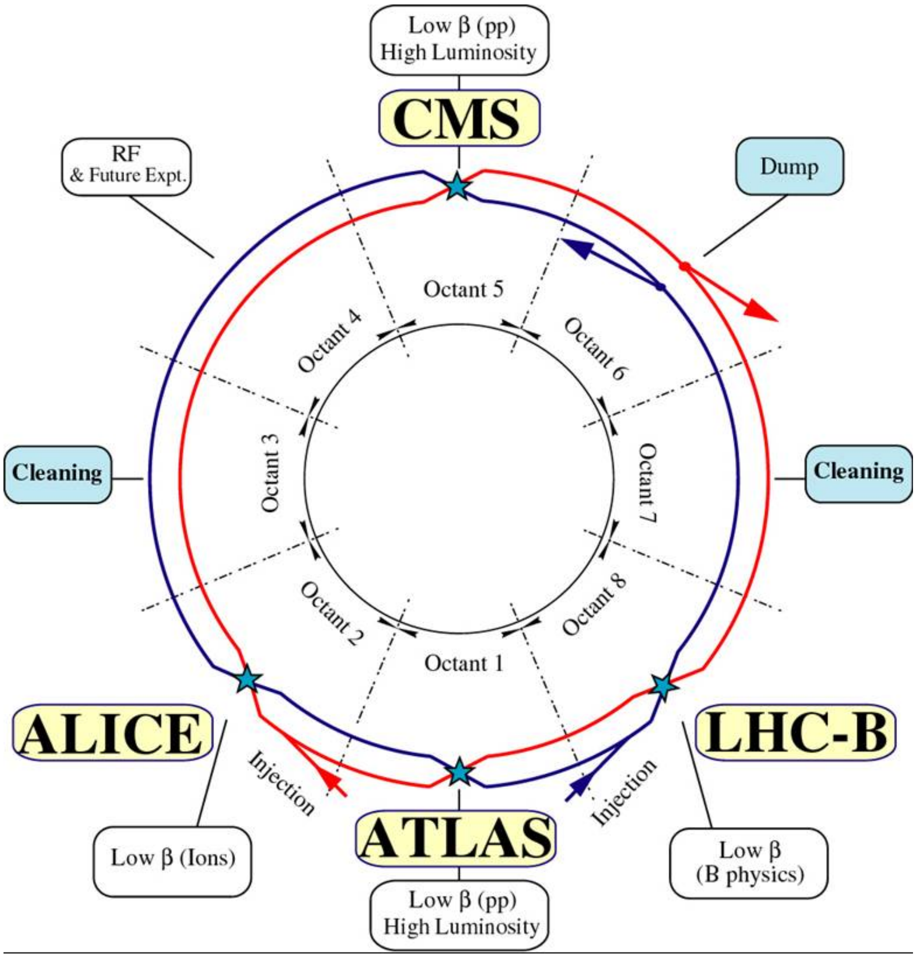

FIGURE 2.1: LHC scheme with its principal experiments: ATLAS, CMS, ALICE and LHCb.

by superconducting electromagnets at very low temperature (around 2 $^{\circ}K$) by a cryostats system with liquid helium.

The magnets used are of various shapes and sizes; 1232 magnetic dipoles of 15 m length are used to guide the particle beams around the ring; 392 magnetic quadrupoles of 5-7 m each are used to focus the beams; just before the collision, another type of magnet is used to reduce the size of the particle bunches, in order to maximize the collision probability and therefore the luminosity.

Before being injected into LHC, the particles are accelerated by a series of accelerators: the first system is a linear accelerator (LINAC2), which takes the beam to an energy of 50 MeV; the protons then go to the Proton Synchrotron Booster (PSB) and reach an energy of 1.4 GeV; after the PSB the protons are injected into the Proton Synchrotron (PS), where they are accelerated to 26 GeV; finally they arrived to the Super Proton Synchrotron (SPS) to increase the beam energy to 450 GeV; from the SPS two transfer lines inject the proton beams into the LHC, that reach an energy of 6.5 TeV for each beam and the instantaneous luminosity of $2{\cdot}10^{34}cm^{-2}s^{-1}$ (described in section 2.1.1). The schemes of the various accelerator are shown in Fig. 2.2.

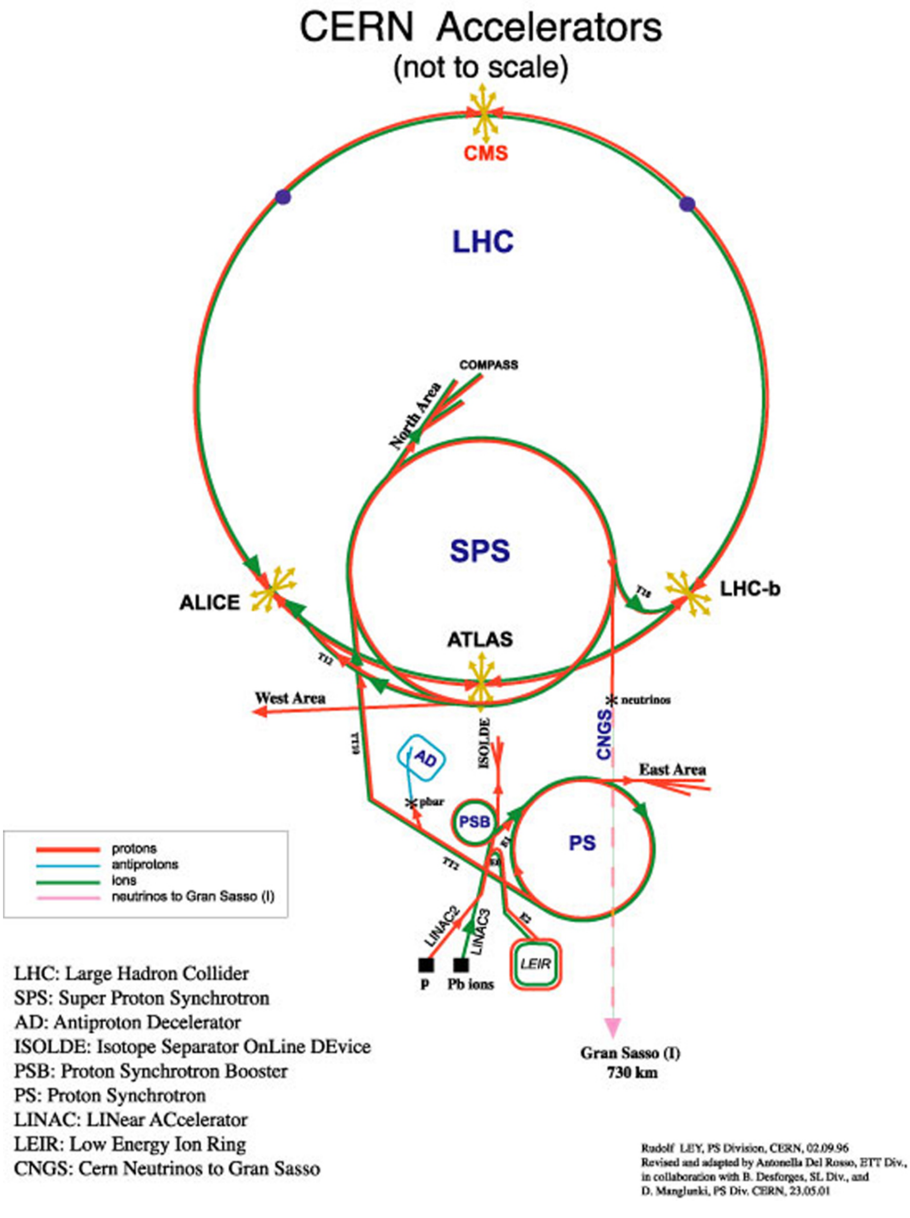

FIGURE 2.2: Schematic layout of the LHC and its accelerators: LINAC2, PSB, PS and SPS.

All the accelerator controls are hosted in the CERN Control Center, in Prevessin (France). The proton beams collide in four points of the ring, which correspond to the position of the four big LHC experiment: ATLAS [33] (A Toroidal LHC ApparatuS) and CMS [34] (Compact Muon Solenoid) are general-purpose experiments and investigate a wide range of physics, from the search for the Higgs boson to extra dimensions and particles that could make up dark matter; the two experiments have the same scientific goals but use different technical solutions and a different magnet-system design. LHCb [35] (Large Hadron Collider beauty) aims to measure the parameters of the CP violation and decays and rare phenomena related to hadrons in which the bottom quark is present. ALICE [36] (A Large Ion Collider Experiment) aims to study condensed matter (for example the quark-gluon plasma) and instead of using pp collisions, it uses lead ions collision (Pb-Pb).

2.1.1 Luminosity

A measurement of the intensity of the beam is "luminosity", which depends only on parameters of the beams and is independent by the experiment. The luminosity is measured as:

$$L = \frac{N_b^2 n_b f_r \gamma_r}{4\pi\epsilon_n \beta^*} \cdot \left(1 + \left(\frac{\theta_c \sigma_z}{2\sigma^*}\right)\right) \tag{2.1}$$

Where: N_b is the number of particles per bunch, n_b is the number of bunches per beam, f_r is the revolution frequency, γ_r is the relativistic gamma factor, ϵ_n is the transverse normalized beam emittance, β^* is the Lorentz factor at the collision point, θ_c is the crossing angle between the beams, σ_z is the Root Mean Square (RMS) of the bunch length and σ^* is the RMS of the beam size at the interaction point. All these parameters have been optimized to ensure maximal luminosity.
During running in 2010 and 2011 the pp energy was $\sqrt{s} = 7$ TeV, increasing to $\sqrt{s} =$ 8 TeV by 2012. In the 2015, following the first long shut-down in 2013 and 2014, the LHC began operating with stable collisions at $\sqrt{s} = 13$ TeV and this energy has continued to be employed until 2018. Previously, up to 2012, the LHC was operated using a 50 ns bunch spacing achieving a peak instantaneous luminosity of $7.7 \cdot 10^{33} cm^{-2} s^{-1}$ and an integrated luminosity of 21 fb^{-1}.
Tab. 2.1 shows the beam parameters of the LHC in pp collision in Run2 (2015-2018). Since this thesis focuses on the 13 TeV data, I present the parameters only for Run2.

Parameter	2015	2016	2017	2018
Beam Energy [TeV]	6.5	6.5	6.5	6.5
Bunch Spacing [ns]	25	25	25	25
Bunch intensity [x 10^{11}p]	1.2	1.1	1.25	1.15
Number of bunches n_b	2200	2200	1900	2500
Emittance ϵn [μm]	3.5	2.5	2.0	2.2
β^* [m]	0.8	0.4	0.3	0.3
Crossing angle [μrad]	290	280	300	300
Peak luminosity [10^{34} $cm^{-2}s^{-1}$]	0.5	1.5	1.5	2.0
Delivered integrated luminosity [fb^{-1}]	4.2	38.5	50.2	63.3

TABLE 2.1: Design parameters of LHC in Run2.

The number of events generated for a specific process can be written as:

$$N_{event} = \sigma_{event} \cdot L \cdot A \cdot \epsilon \tag{2.2}$$

Where σ_{event} is the cross section of the considered process, L is the integrated luminosity over time, A is the geometrical acceptance and ϵ is the efficiency of the detector. The full Run2 luminosity of the experiment ATLAS is shown in Fig. 2.3.

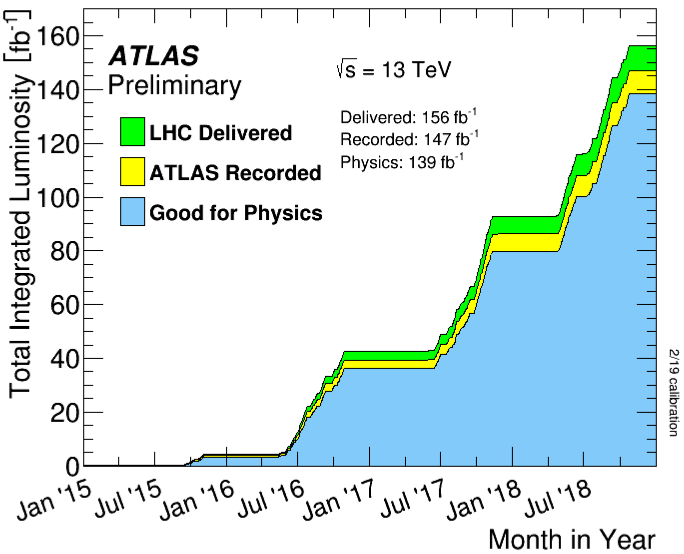

FIGURE 2.3: Cumulative luminosity versus time delivered to ATLAS (green), recorded by ATLAS (yellow), and certified to be good quality data (blue) during stable beams for pp collisions at 13 TeV centre-of-mass energy in 2015-2018.

2.2 The ATLAS experiment

The ATLAS detector is 22 meters high and 44 meters long and has an onion-like structure, as shown in Fig. 2.4.

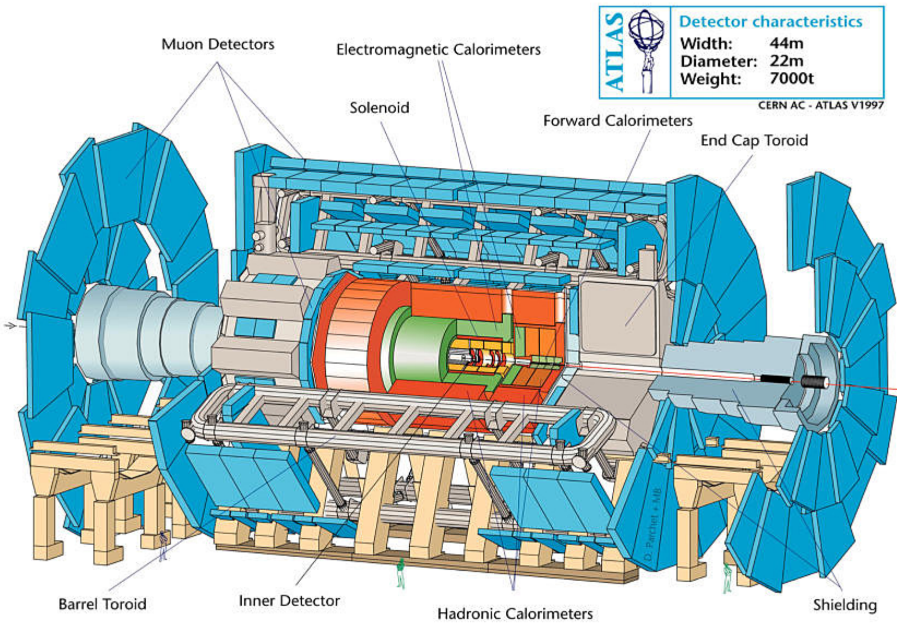

FIGURE 2.4: Internal structure of the ATLAS experiment.

The ATLAS detector consists of a concentric cylinder shape (4π coverage) with the interaction point as a center, where the proton beams collide. It can be divided into five main parts:

- Magnet System;
- Inner Detector (ID);
- Electromagnetic calorimeter (ECAL);
- Hadronic calorimeter (HCAL);
- Muon Spectrometer (MS).

The central part around the beam line is called the "barrel" and the wheels perpendicular to the beam axis in the forward parts are called "end-caps".

The main systems are complementary: the solenoid magnet and the inner tracker measure the charged particles momentum and reconstruct their trajectories precisely, the calorimeters measure the energy deposited and the muon spectrometer measures the trajectory and momentum of the muons.
The only stable particles that are impossible to detect directly are the neutrinos, in fact their presence is deduced from apparent violations of the conservation of momentum during a collision. To carry out this task, the detector must be "hermetic", i.e. it must allow the measurement of all particles, without dead zones.

2.2.1 Coordinate system

The coordinate system used in the ATLAS detector is a right-handed coordinate [1]. The z-axis define the beam direction and the x-y plane is transverse to the beam-pipe, as shown in Fig. 2.5.

The transverse energy E_T and transverse momentum p_T are defined in the x-y plane. The rapidity is defined as:

$$y = \frac{1}{2} log\left(\frac{E + P_z}{E - P_Z}\right) \tag{2.3}$$

but the main coordinate used is the pseudo-rapidity, defined as:

$$\eta = -log\left(tan\frac{\theta}{2}\right) \tag{2.4}$$

where θ is the polar angle; a diagram of how η is directed is shown in Fig. 2.6. The choice is driven by the fact that the total momentum of the initial system along the z-axis is unknown; a difference of pseudo-rapidity of two particles, does not depend on Lorentz boosts along the beam axis. Moreover, when the speed of the

[1] ATLAS uses a right-handed coordinate system with its origin at the nominal interaction point (IP) in the centre of the detector and the z-axis along the beam pipe. The x-axis points from the IP to the centre of the LHC ring, and the y axis points upward. Cylindrical coordinates (r, ϕ) are used in the transverse plane, ϕ being the azimuthal angle around the beam pipe.

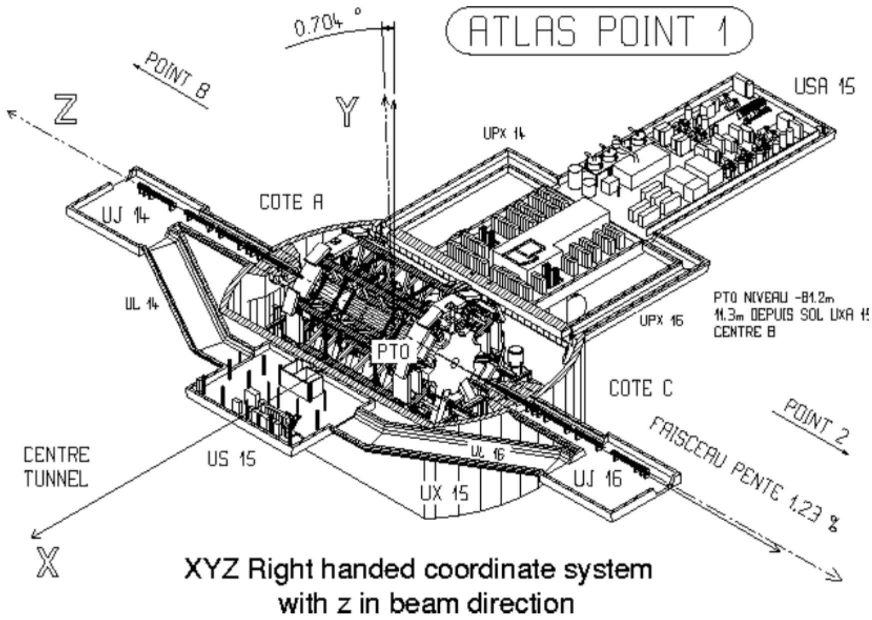

FIGURE 2.5: The coordinate system of the ATLAS experiment.

particle tend to the light, or in the approximation that the mass is negligible, the pseudo-rapidity tends to the definition of rapidity. Distances in the (η, ϕ) plane are measured in units of $\Delta R = \sqrt{\Delta\eta^2 + \Delta\phi^2}$.

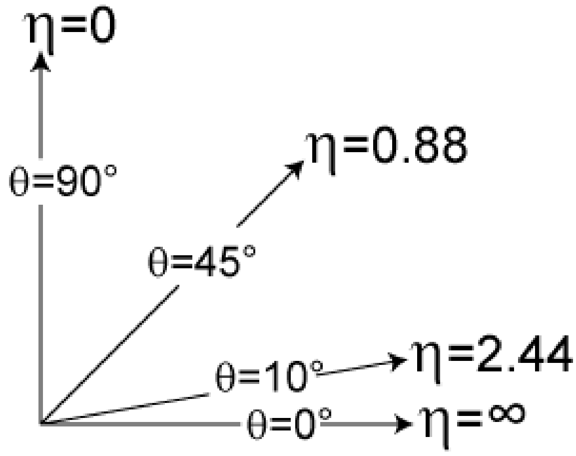

FIGURE 2.6: The pseudo-rapidity tend to infinite when the angle tend to zero. The angle is measured respect the beam axis.

2.2.2 Magnet System

The magnetic system is fundamental to reconstruct the transverse momenta of all charged particles. The ATLAS detector is made up by three different kind of superconducting magnets, as shown in Fig. 2.7: the central solenoid is placed around the Inner Detector (ID) and provides a magnetic field of ≈ 2 T ; the solenoid is located along the beam axis inside the Inner Detector and it is placed before the ECAL; the barrel toroid consists of eight coils assembled radially and provides a peak field of 3.9 T; finally, the end-cap toroids is composed by two air-core toroids and provide ~ 1 T inside the toroid muon spectrometer.
The magnetic field is not completely uniform and the superposition of the magnetic fields of the barrel and end-cap results in a region where the bending power is poorer. This region, in η range $1.3 < |\eta| < 1.6$, is defined as "transition region".

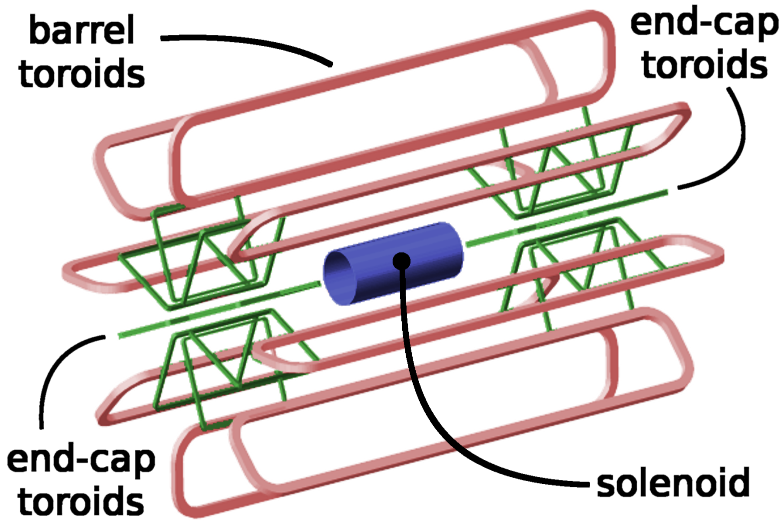

FIGURE 2.7: Magnetic system scheme of the ATLAS detector.

2.3 Inner Detector

The Inner Detector ([37],[38]) is the most central part of the ATLAS detector and has the function of tracking precisely the charged particles that come from the intersection region and go to the ECAL. The ID, which is 6.2 m long and 2.1 m wide, is located inside a solenoid of 2 T that curves the trajectory of the charged particles based on their momentum and electric charge. A scheme of the ID is shown in Fig. 2.8.

The ID is made of three systems based on different technologies which provide complementary information for tracking: PIXEL detector, SemiConductor Tracker (SCT) and Transition Radiation Tracker (TRT).

Passive material in the ID must be minimized in order to avoid inducting particle shower, causing the object to loose energy before the calorimeter. The resolution of the tracking is:

$$\frac{\sigma(p_T)}{p_T} = a \cdot p_T \oplus b \tag{2.5}$$

where a is the intrinsic resolution of the detector, b arises from multiple scattering, dominating the resolution at low momentum and $\oplus$ is the sum in quadrature.

When a particle interacts with one of the sub-detector layers, it deposits part of its energy to the sensor, that will be converted in signal to read-out.

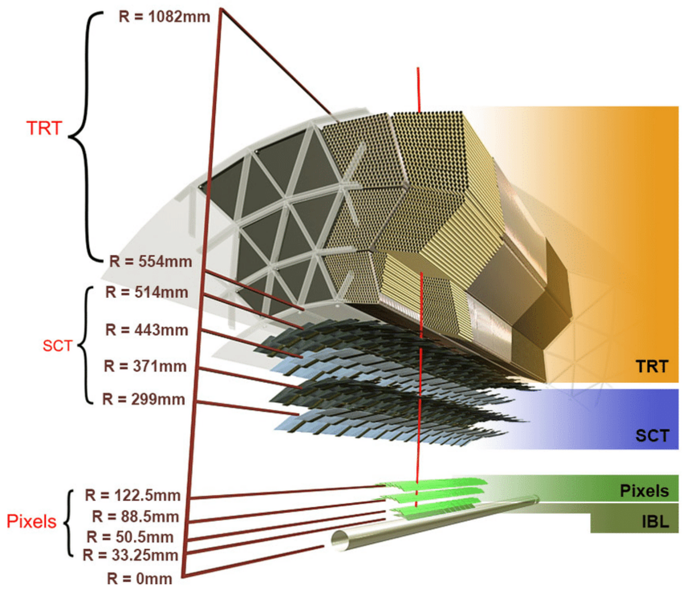

FIGURE 2.8: Inner Detector section. It is composed by: PIXEL detector, Semi-Conductor Tracker (SCT) and Transition Radiation Tracker (TRT).

2.3.1 Pixel detector

The Pixel detector [39] is the component closest to the beam pipe and must cope with a higher particle flux than any other detector in ATLAS.
The detector is composed by silicon modules and consists of three barrel layers and three end-cap disks on each side; an additional barrel, referred as Insertable B-layer (IBL), was installed at the end of run 1, covering the same region $|\eta| < 2.5$, to help improve the vertex resolution and b-tagging efficiency.
The Pixel detector can be seen as a cylinder composed of 1744 modules resulting an active area of $\sim$1.7 m^2 and $\sim 80 \cdot 10^6$ readout channels. Each module contains 46080 pixels with a size of 50·400 μm^2, with the thickness of $\sim$250 μm. The space points are in a 3-dimensional shape and they are used to reconstruct the trajectory of the particles, to identify the primary point of interaction. Each pixel corresponds to an area in read-out chips that contains an amplifier and a discriminator; the information on the pixels is read by a circuit that store it, waiting for the trigger to accept them or not. If the trigger accepts the inputs, the chips collect the data of a single bunch cross from the buffer and store them. The structure of the Pixel detector is shown in Fig. 2.9.

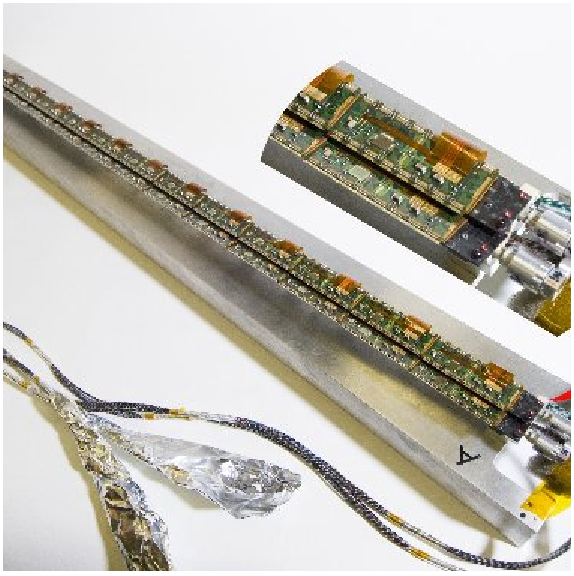

FIGURE 2.9: half-shell structure of the ATLAS pixel detector.

2.3.2 SemiConductor Tracker

Outside the Pixel there is the SemiConductor Tracker (SCT) [40]. It is built around the Pixel detector and is designed to provide eight precision measurements per track in the intermediate radial range, contributing to the measurements of momentum, impact parameter and vertex position.
The SCT is made of silicon strip detectors, with strips spaced apart from each other by 80 μm. Each module is composed of two pairs of silicon detectors, composed in turn by 128 strips. The SCT consists of 2112 tubes, covering a pseudo-rapidity $|\eta|$ <1.4, the modules are organized in four concentric cylinders (with radius, respectively, of 30, 37.3, 44.7 and 52 cm); the end-cap structures are composed by two cylinders divided into nine disks, positioned at the end of each barrel.
To improve the efficiency of the area covered by the silicon strips, the modules are arranged so that the particle must pass through the four layers of the detector and with a minimum cover over $|\eta| = 2.5$.
A scheme of the SCT is shown in Fig. 2.10.

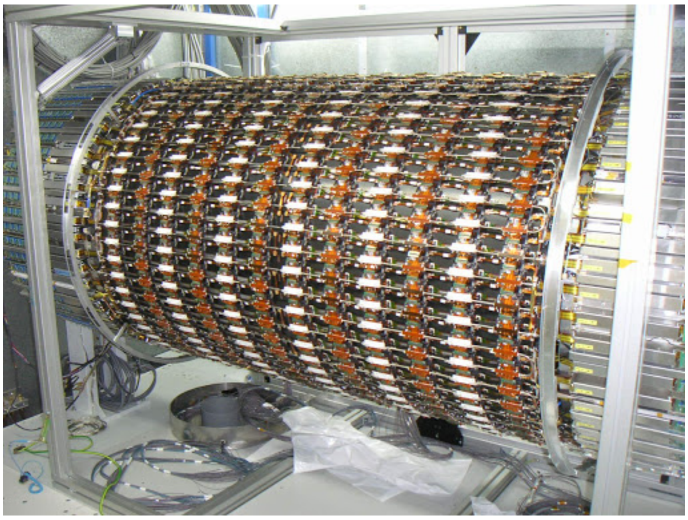

FIGURE 2.10: A view of the ATLAS SCT barrel module.

2.3.3 Transition Radiation Tracker

The TRT [41] is the outermost part of the Inner Detector. It is a gas tubes detector, in which detection occurs when a particle passes through the gas (where there is a

electrical field) generating a current in a wire located at the center of the tube. The detector is composed of 50,000 small tubes arranged axially and 160,000 arranged transversely in each end-cap, so that the particle must pass through 34 tubes.
The gas tubes are cave with a diameter of 4 mm and with a $30\mu m$ W-Re (Tungsten-Rhenium) wire in the center, where the high voltage is applied. The tubes are filled with a mix of gas: the Xenon (70%), which captures the x-rays produced by transitional radiation; CF_4 (10%) that increases the speed of the gas and the CO_2 (20%) that is used to stabilize the high voltage mixture.
The peculiarity of the TRT detector is the ability to distinguish the electrons and positrons by their X radiation when they pass through two mediums with different refraction index and this is determined by the structure of the plastic medium (polypropylene or polyethylene). Moreover, the emission of transition radiation is much more likely for electrons than for charged hadrons. This allows for a discrimination of those particle types which is important, especially for an efficient separation between $\pi^{\pm}$ and $e^{\pm}$ tracks. The total number of readout channels in the TRT is $\sim 351 \cdot 10^3$; the barrel part covers pseudo-rapidities with $|\eta| < 1.1$ and including the end-caps the total range extends to $|\eta| < 2.0$.

2.3.4 Tracking reconstruction

The main parameters that are used in the ATLAS detector are the azimuthal angle ϕ, the transverse impact parameter d_0, which is the distance to the beam axis in the x-y plane, the longitudinal impact parameter z_0, which is the distance to the coordinate system origin in z-direction.
In ATLAS the tracks of primary charged particles are built using inside-out track finding [42]; this algorithm is based on the information of the innermost layer of the Pixel detector and follows the direction of the outer layer of the ID to build the track candidates. In the last step the tracks are extended in the TRT and their hits are fit together with tracks from the silicon detectors.
Track passing basic quality criteria are considered for the reconstruction of vertices. When there is an interesting process (defined by the analysis) the tracks are associated to vertex candidates and fits are performed to determinate the vertex position [43]; the hard scattering vertex is chosen as the primary vertex with the highest $\sum p_T^2$ (often associated to the position of the pp interaction).

The vertex reconstruction efficiency rises from 83% for vertices with two tracks to almost 100% for vertices with at least five tracks.

2.4 Calorimeters

Outside the Inner Detector are located the calorimeters [44],[45] which cover the range $|\eta|$ <4.9, have a total diameter of $\sim$ 8.5 m and length $\sim$ 13.5 m. Their task is to identify and measure the energy of particles (charged or neutral) and jets; there are two kind of calorimeters: the ECAL, that is the inner one and is used to detect the particles that interact electromagnetically ($\gamma, e^{\pm}$) and part of some hadrons (like pions or kaons) and the HCAL that is used to detect the particle that interact hadronically.

ATLAS has separate ECAL and HCAL up to $|\eta| < 3.2$ and a special combined electromagnetic and hadronic calorimeter covers the range $3.1 < |\eta| < 4.9$. The operating principle of the two calorimeter is the same: the incident particle interacts with the absorber (lead, steel, copper and tungsten), thus producing a shower of secondary particles, that are directed to the detecting material. The method for detection is: in the Liquid Argon (LAr) the ionizing particle produce positive and negative ions that are measured by the front-end; the sensitive element in the calorimeter is the scintillator, where the ionizing particles produce photons that are detected by a set of photomultipliers. The size of the output signal is proportional to the incident particle energy, taking into account a calibration made on the basis of the known particles. The layout of the calorimeters is shown in Fig. 2.11

2.4.1 Electromagnetic calorimeter

The ECAL is a sampling calorimeter made of LAr as scintillating material and lead as absorber, providing complete ϕ symmetry with its accordion shape, as shown in Fig. 2.12, such as to minimize the gaps between the various layers of the detector.

The total depth of the ECAL exceeds 22 radiation lengths (X0) in the barrel and 24 in the end-cap- The resolution provided by the calorimeter is:

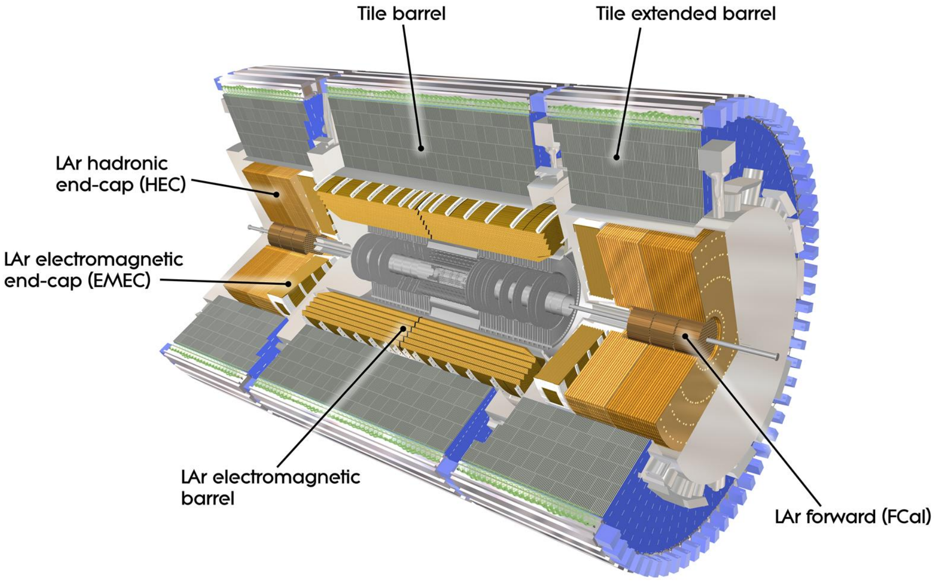

FIGURE 2.11: Layout of the ECAL and HCAL of the ATLAS experiment.

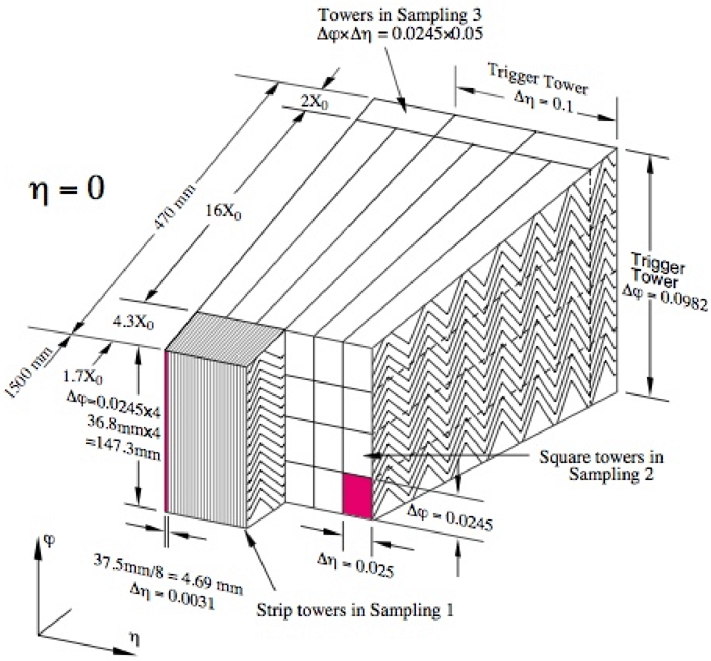

FIGURE 2.12: Accordion shape of the barrel ECAL and its read-out granularity.

$$\frac{\sigma(E)}{E} = \frac{10\%}{\sqrt{E}} \oplus 0.3\% \tag{2.6}$$

where E is expressed in GeV. In the region $|\eta| < 2.5$, the ECAL is segmented in three layers: the L1 has a very high segmentation in η and permits a precise measurement of the shower position and good rejection of photons from π^0 decay; the L2 is the largest and allows the collection of a larger fraction of the energy of the incoming particle, providing the most precise measurement in ϕ; the L3 is the last layer and is dedicated to the measurement of the tails of the particle showers; moreover, an additional pre-sampler layer covering the $|\eta| < 1.8$ region is used to correct for fluctuations in energy loss of particles before they reach the calorimeter.

2.4.2 Hadronic calorimeter

The outer calorimeter is the HCAL, which is divided in Tile Calorimeter (TileCal), the Hadronic End-cap Calorimeter (HEC) and the Forward Calorimeter (FCal). The active material of the HCAL is LAr. The TileCal covers the region $|\eta| < 1.7$ and it is made with steel as the absorber with plastic scintillator plates, the HEC works like the ECAL and is composed by LAr as active material and copper as the absorber and measure the particle energy in the region $1.5 < |\eta| < 3.2$ with resolution given by:

$$\frac{\sigma(E)}{E} = \frac{50\%}{\sqrt{E}} \oplus 3\% \tag{2.7}$$

where E is in GeV. The FCal covers the region $3.1 < |\eta| < 4.9$ and it is installed to improve the measurement of the missing transverse energy, with LAr as active material and copper-tungsten alloy as absorber. The energy resolution is:

$$\frac{\sigma(E)}{E} = \frac{100\%}{\sqrt{E}} \oplus 10\%. \tag{2.8}$$

2.5 Muon spectrometer

Muons are very penetrating particles, so for this reason the Muon Spectrometer (MS) is placed in the outer part of ATLAS, surrounding the calorimeters, as shown in Fig. 2.13.

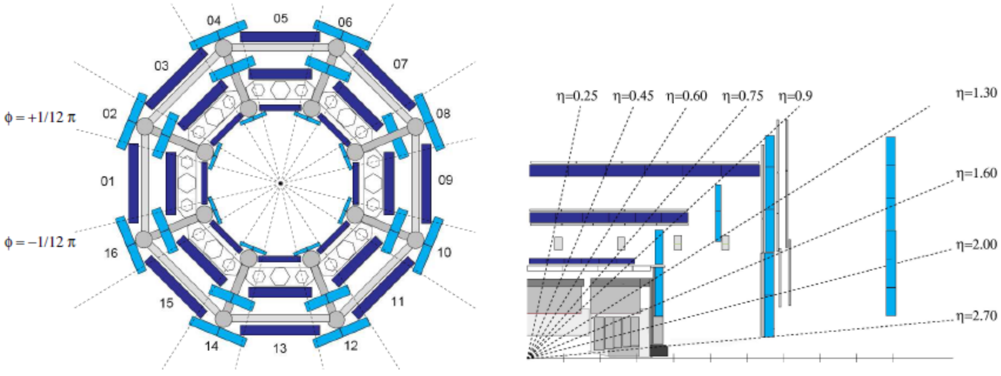

(a) ϕ-binning (b) η-binning

FIGURE 2.13: Left: layout of the MS in the x-y plane (ϕ binning). Right: layout of the MS in the z axis (η binning).

The MS is immersed in a toroidal magnetic field of approximately 0.5 T and 1 T, in the barrel region and end-cap region, respectively. It is designed to be capable of a stand-alone measurement of the transverse momentum of the muons.
There are two different functions that muon chambers must accomplish: triggering and high precision tracking. The trigger system covers the region $|\eta| < 2.4$ and is composed by Resistive Plate Chambers (RPC) in the barrel and Thin Gap Chambers (TGC) in the end-caps. The triggering system provides bunch-crossing identification, well defined p_T thresholds and a measurement of the muon coordinate in the direction orthogonal to the chambers dedicated to precision tracking. The tracking is performed by the Monitored Drift Tubes (MDT) and by Cathode Strip Chambers (CSC) at large pseudo-rapidity.
The momentum resolution of the muon system is approximately:

$$\frac{\sigma(p_T)}{p_T} = 3\% \quad \text{at 50 GeV and} \quad \frac{\sigma(p_T)}{p_T} = 10\% \quad \text{at 1 TeV} \tag{2.9}$$

The muon track in the MS is reconstructed in two steps: in the first step the muons are triggered in the RPC/TGC and local track segments are defined in each layer of chambers; in the second step, the local track segment from different layers are combined through a χ^2-fit forming a full MS track. To reduce the probability of backgrounds tracks, the fitted tracks of the muon candidates are required to point towards the interaction point.

2.5.1 Monitored Drift tube Chambers

The MDT chambers are made of drift tubes witha diameter of 30 mm and a tungsten-rhenium wire of 50 μm in diameter is located at the center of the tube; the tubes are filled with a mix of Argon and CO_2 at an absolute pressure of 3 bar. When a muon passes through a tube it ionizes the gas, the electrons from the ionization drift towards the wire with a maximum drift time of 700 ns when drifting from the wall to the wire. The position of the muon can be determined by the relationship between the non-linear space and time in the tube. The spatial resolution of the MDT tube is $\sim$80 μm.

2.5.2 Cathode Strip Chambers

The CSC is a multi-wire proportional chamber with the wires oriented in the radial direction. The cathodes are segmented, one with the strips perpendicular to the wires and the other parallel to the wires providing the transverse coordinate; the position of the track is obtained by interpolation of the charge induced on the segmented cathode by the avalanche created on the anode wire.

2.5.3 Resistive Plate Chambers

The RPC are muon trigger chambers placed in the outer part of the detector and they are used because have good spatial and time resolution and also an adequate rate capability. The RPCs are a gaseous parallel electrode-plate detector, operated with a mixture of $C_2H_2F_4$ (94.7%), Iso-C_4H_{10} (5%) and SF_6 (0.3%) and are very useful for their relatively low operating voltage while providing a good plateau for safe avalanche operation. The RPC contains two resistive plates made of phenolic-melaminic plastic laminate, that are parallel to each other at a distance of 2 mm. Insulating spacers and the electric field between them allows avalanches to form alog the ionizing tracks towards the anode. The signal is read out via capacitive coupling to metallic strips, which are mounted on the outer faces of the resistive plates.

2.5.4 Thin Gap Chambers

The TGCs are used in the end-cap region for their good time resolution and rate capability. Moreover, the TGCs provide a second azimuthal coordinate to complement the measurement of the MDTs in the bending direction. The TGC is a multi-wire proportional chamber operated in a highly quenching gas mixture of CO_2 and n-C_5H_{12}. This cell geometry allows for operation in a quasi-satured mode.

2.6 Forward Detectors

There are two frontal detectors: LUCID and ZDC ([46]).
The "Luminosity measurement Using Cherenkov Integrating Detector" (LUCID) is the main luminosity provider of the ATLAS experiment and the only one able to provide a reliable luminosity determination in all beam configurations, luminosity ranges and at bunch-crossing level. The detector is composed by two modules located at $\pm$ 17 m from the beams interaction point and covers a range of $5.5 < |\eta| < 5.9$. Each LUCID detector is a symmetric array 1.5 m long composed by aluminum tubes that surrounding the beam pipe and point towards the ATLAS interaction point, so that they have the maximum Cherenkov emission by the charged particles. Each LUCID tube has a diameter of 1.5 mm and is filled with C_4F_{10} gas at a pressure of 1.2-1.4 bar, with a Cherenkov light threshold of 2.8 GeV for the pions and 10 MeV for the electrons. LUCID is located in the high radiation area and is estimated that it receives a dose of $\sim$7 Mrad per year at the maximum luminosity.
The "Zero Degree Calorimeter" (ZDC) is a detector sensitive to neutral particles produced both in *pp* and in Heavy Ions collisions. The detector covers the region $|\eta| > 8.3$ and is located at $\pm$ 140 m from the interaction point. The ZDC detector is composed by three calorimeter hadronic modules, made of 11 tungsten plates, with faces facing perpendicular to the beam direction; the detector is composed by vertical layers for the energy measurement and the horizontal barrels for the position information.

2.7 Trigger System

The trigger system [47] is very important in the collider experiments, because the rate of events containing interesting physics is a small fraction of the total events. Due to the constraints from data storage capacity it is impossible to store all the events; for this reason, the trigger is employed to rapidly decide interesting events. The proton-proton collision at the LHC takes place every 25 ns (40 MHz) with $\sim$ 23 interaction per crossing. These regimes can give in total 40 Tb/s which is too much for the modern computer technology. The goal is to reduce the rate from 40 MHz to 100 Hz without a loss of information. To reduce the amount of data, the online event selection has to decide whether a collision looks interesting or not and for that it employs several strategies. In Run2 the trigger system consists of two levels of event selection: the Level-1 trigger (L1), that it reduces the rate to 100 kHz and a High-Level Trigger (HLT) further reducing event rate to 1 kHz. The L1 trigger is implemented as hardware devices in the detector structure, while the HLT is a software trigger. The ATLAS Trigger and Data Acquisition (TDAQ) system is shown in Fig. 2.14.

The Level-1 trigger is composed by three subsystem: one is the L1 calorimeter trigger (L1Calo), which uses calorimeter information for reduced granularity to trigger electrons, photons, hadronic tau decays, jets and missing energy transverse; the other system with a direct detector interface is the L1 muon trigger (L1Muon), which primarily uses TGC and RPC information to make fast decisions on muon items; then there is the L1 topological trigger (L1Topo) that combines information from multiple L1Calo and L1Muon objects as well as their kinematics; then the Central Trigger Processor (CTP) makes the final decision.
When the events are accepted by the L1 trigger, they are passed to the HLT [48]. The HLT runs on a conventional computer cluster and has about 0.2 s on average to decide. The target average HLT rate is 1 kHz; the trigger items may be prescaled, e.g. a specified fraction of positive trigger decision is randomly ignored, which makes it possible to use triggers whose unprescaled rates are too high to record their events. Another important pending upgrade will improve the granularity of calorimeter information available to L1Calo and will therefore also benefit tau trigger; it will be

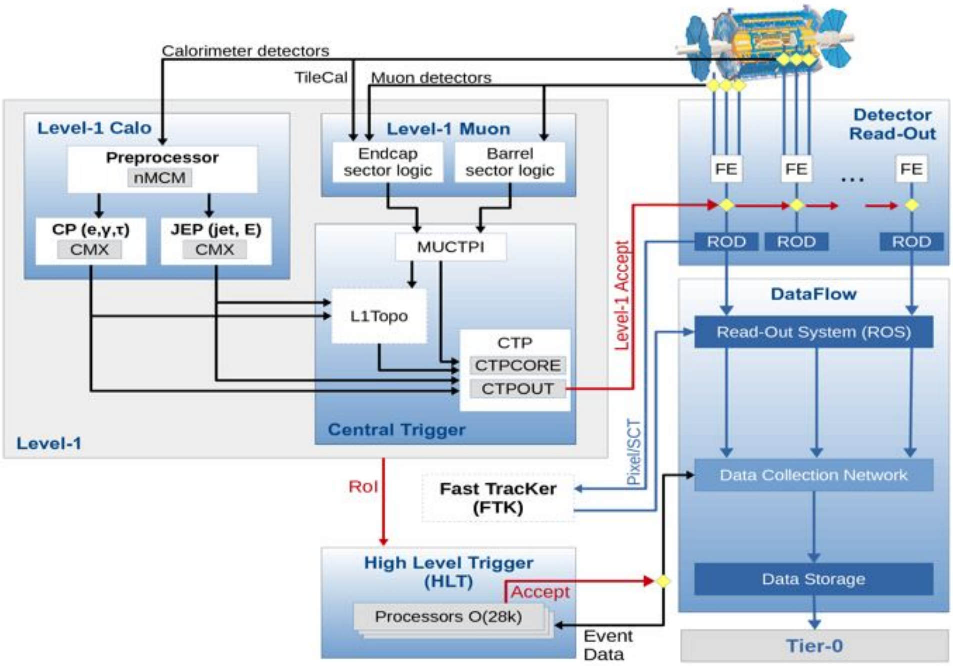

FIGURE 2.14: ATLAS TDAQ system in Run2 with emphasis on the components relevant fo trigging.

installed during the Long Shut-down 2 (between 2018 and 2020).

2.8 Data Quality

The data analyses need selections to have events which are not affected by beam background. In order to avoid these defects, the data stored for the analyses are then measured taken into account the *Good Run List* (GRL). A GRL is a list of luminosity blocks, spanning 1-2 minutes of data-taking, in which the LHC is circulating stable colliding beams and all critical detector components are functioning properly. In particular, the inner detector, the electromagnetic and hadronic calorimeters, and the muon spectrometers must deliver data of high quality to ensure that electrons, muons, jets, and missing transverse energy are measured accurately.

An important effect in accelerator particle physics is the *pileup*, a situation where a particle detector is affected by several collision events at the same time [49]. The

Monte Carlo (MC) simulated samples also include pileup effects. To take into account differences in the pileup profiles in data and MC a *Pileup Reweighting* (PRW) procedure is used. The PRW procedure is used in order to correct MC samples (simulated events that recreate the real one) to the relative pileup profiles in the 2015+2016 (referred as $mc16a$), 2017 ($mc16d$) and 2018 ($mc16e$) data.

Chapter 3

Object reconstruction in the ATLAS experiment

The raw data from the ATLAS detector is a series of readout signals; the task of the offline reconstruction software is to translate this stream of readout signals into the information necessary to perform physics analysis.
Reconstruction of physics objects such as leptons and jets begins with the reconstruction of basic objects such as tracks and vertex and calorimeter clusters. The reconstruction of physics objects such as electrons, muons and jets begin with the reconstruction of the tracks in the Inner Detector and calorimeter clusters. This chapter will describe the reconstruction and identification algorithms of these objects, in addition to the missing transverse energy and the Overlap Removal (OR) procedure, that are relevant for the analysis presented in this thesis.

3.1 Low level objects and primary vertex

Tracks, primary and decay vertices and the calorimeter clusters define the low-level object reconstruction. The Inner Detector hits that are associated to form tracks, are used to reconstruct the trajectories of charged particles.
Important track information induces the transverse (z_0) and longitudinal (d_0) impact parameters, already described in Chapter 2.

The input to the vertex reconstruction is a collection of reconstructed tracks. The procedure to reconstructs the primary vertex is divided into two steps: vertex finding (described in Chapter 2) and vertex fitting.
The vertex fitting step can be divided in different steps: first of all, a set of tracks satisfying the selection criteria is defined; then a seed position for the first vertex is selected. Finally, the tracks and the seed now are used to estimate the best vertex position with a fit following an iterative procedure; in each iteration, less compatible tracks are down-weighted and the vertex position is recomputed and the procedure stops when the best track position compatible is found and it is associated to the primary vertex.
All vertices with at least two associated tracks are retained as valid primary vertex candidates. The output of the vertex reconstruction algorithm is a set of three dimensional vertex positions and their covariance matrices.

3.2 Leptons

This section focuses on the reconstruction and identification of electrons (muons will be described in a dedicated chapter, Chapter 4).In this section the tau ($\tau^{\pm}$) leptons [50] will not be described, because final states with hadronically decaying taus are not considered in this thesis. This is because in such final states the QCD background would decrease the sensitivity of the analysis.

3.2.1 Electrons

The combination of the information between ECAL [51] and ID is very important for the electron reconstruction; because a good reconstruction is crucial to reject the large background typically originating from jets, leading to fake electrons.
The first step, referred to as "cluster reconstruction", is the identification of energy clusters deposited in the EM calorimeter. These clusters are reconstructed using a dedicated $sliding - window$ algorithm [52]. After the selection of a local maximum in the transverse energy ($E_T > 2.5$ GeV), this energy deposit is treated as a seed cluster, which has to match with one or more tracks coming from the reconstruction

in the ID; this procedure takes into account also the energy losses by high-energy electrons, which can change the path of the particles and so modify the track.
The track fitting and extrapolation is done with the *Gaussian Sum Filter* (GSF) algorithm, which takes care of bremsstrahlung energy losses and experimental noise (derived from TRT and ECAL) [53]. The trajectory of an electron can be approximated as a weighted sum of Gaussian functions. The GSF divides the experimental noise and bremsstrahlung energy losses into individual Gaussian components and then it processes each one of them using a "Kalman Filter" algorithm [54]. The GSF algorithm finds all the electron candidate tracks (with $p_T > 400$ GeV and $|\eta| < 2.5$) which are fitted again, because the tracks obtained by this fit procedure are used to compute the electron 4-momentum and match the clusters found in the EM calorimeter.
The electron measurements are performed by requiring the track associated with the electron to be compatible with the primary vertex of the hard collision. There are also other conditions to take into account: $d_0/\sigma_{d_0} < 5$ and $|z_0 sin\theta| < 0.5$ mm, where d_0, z_0 and θ are already described in Chapter 2 and σ_{d_0} is the estimated uncertainty of the d_0 parameter.
The efficiency of these requirements in data and Monte Carlo simulation is estimated together with the efficiency of the various identification operating points. In the following the reconstruction and the identification steps are described. Tab. 3.1 shows the main parameters requirement for this analysis.

Electron kinematics
$p_T > 400$ GeV
$\lvert\eta\rvert < 2.5$
$d_0/\sigma_{d_0} < 5$
$\lvert z_0 sin\theta\rvert < 0.5$ mm

TABLE 3.1: Electron main parameters requirement.

3.2.1.1 Electron reconstruction

The electron reconstruction and trigger efficiencies are measured with the $Tag-and-Probe$ method [55] based on $Z \to e^+e^-$, $W \to e\nu$ and $J/\Psi \to e^+e^-$ data and simulated samples: one lepton is selected using the standard cuts (*tag*), while for

the second candidate (*probe*) a looser set of cuts is applied.
The energy is corrected for non-uniformity of the detector response and by using a multivariate regression algorithm trained on MC simulation to correct for loss of energy outside the calorimeter of the clusters. To account for small differences of the calibration between simulation and data, both the energy scale (in data and MC) and resolution (in MC simulation) are adjusted based on the correction measured in $Z \to e^+e^-$ events.
The resolution is depending on the pseudorapidity and energy of the electron. In the central $\eta < 0.5$ region, it ranges from 2.5% for 25 GeV to 0.5% for 1 TeV and for larger η it rises up to 10% for low energy electrons. For most of the pseudorapidity range the reconstruction efficiency is above 97% [56] and increases with the energy of the reconstructed electron. An example of the reconstruction efficiency versus the p_T and η is shown in Fig. 3.1, where it is possible to see the decrease of the efficiency in the transition region ($1.37 < |\eta| < 1.52$). Fig. 3.2 shows the algorithm flow diagram for the electron reconstruction.

3.2.1.2 Electron identification and isolation

After the electron object reconstruction, using EM calorimeter and tracking system information, a cut-based approach is employed to identify the electrons in the $|\eta| < 2.47$ region (the transition region between the barrel and endcap calorimeters, i.e $1.37 < |\eta| < 1.52$, is excluded). This step is called electron identification.
Three different selections, optimized in bins of η and E_T are defined, according to the quality of the reconstruction, providing different electron efficiency versus jet rejection working points: loose, medium and tight.

- *Loose*: The loose identification criteria use only information from the calorimeters. Selections are applied on the hadronic leakage (the ratio of the E_T in the first compartment of the HCAL and in the whole ECAL) and on shower shape variables (lateral shower shape and width) based on the second layer of the ECAL. This set of requirements provides excellent identification efficiency and low background rejection.
- *Medium*: This selection improves the quality by adding requirements on both the ECAL and the tracking variables. The fine longitudinal segmentation

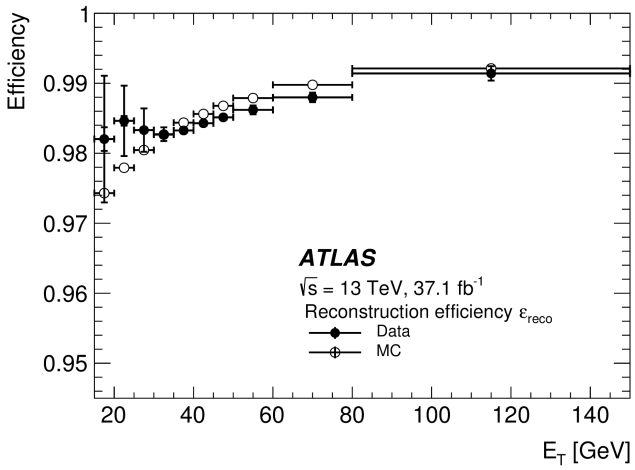

(a)

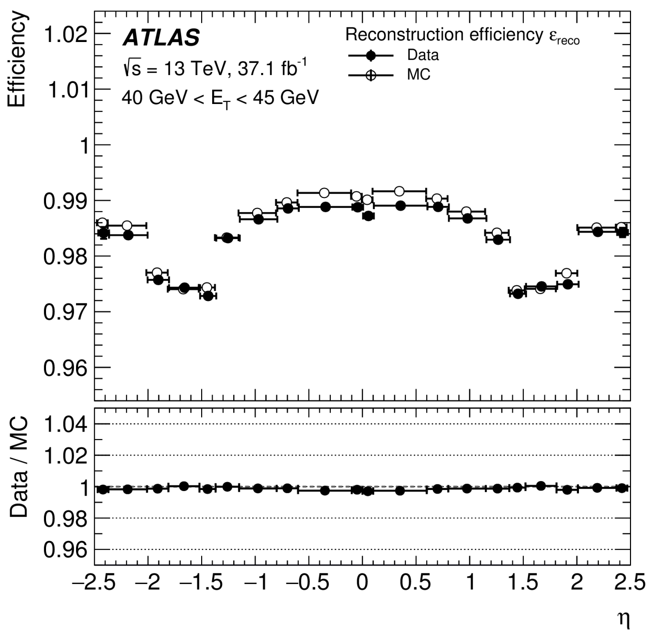

(b)

FIGURE 3.1: Electron reconstruction efficiency from $Z \rightarrow e^+e^-$ as a function of E_T (a) and η (b) for E_T between 40 to 45 GeV.

of the first layer of the ECAL is exploited, in particular to reject photons from neutral pion decays, which result into very close deposits of energy; this selection increases the jet rejection by a factor 3-4 with respect to the loose identification and reduces the selection efficiency by $\sim 10\%$.

- *Tight*: This set of selections makes use of all the particle identification tools;

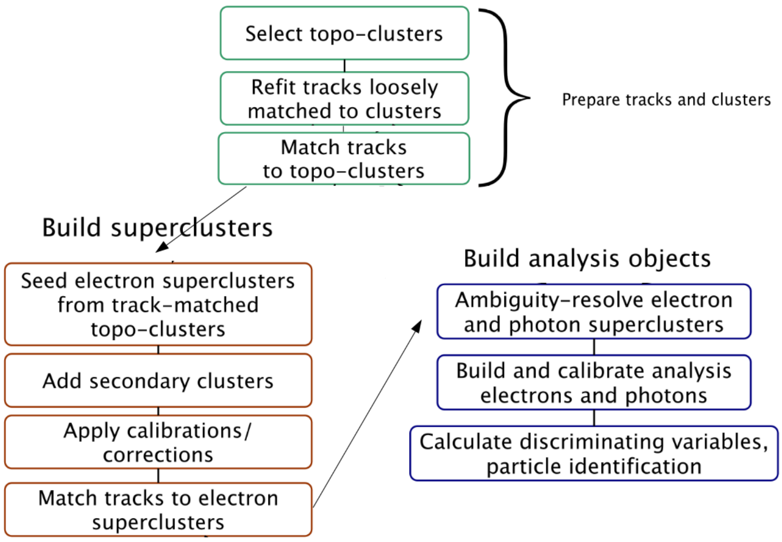

FIGURE 3.2: Algorithm flow diagram for the electron reconstruction.

further requirements are applied on the tracking variables and, in addition, an energy (and momentum) isolation cut is applied to the cluster using all cell energies within a cone of $\Delta R < 0.2$ (and 0.3) around the electron candidate. This selection provides the highest isolated electron identification and rejection against jets.

Some corrections are applied to MC simulation in form of efficiency scale factors, in order to match isolation and trigger efficiency in data.
These corrections are obtained by comparing MC predictions to $J/\Psi \to e^+e^-$ and $Z \to e^+e^-$ data samples using the tag-and-probe method. In Fig. 3.3 the various electron identifications are shown.

The electron energy scale and the inter-calibration of the different parts of the EM calorimeter are obtained from $Z \to e^+e^-$, $J/\Psi \to e^+e^-$ and $W \to e\nu$. The relative alignment of the calorimeter components with respect to the inner detector has been measured using electron candidates, compatible with the ones coming from W and Z decays. These correction factors have the effect of widening the MC Z-peak indicating that the simulated resolution was originally too narrow.

For the dilepton analysis configuration the *Tight* electron identification is used.

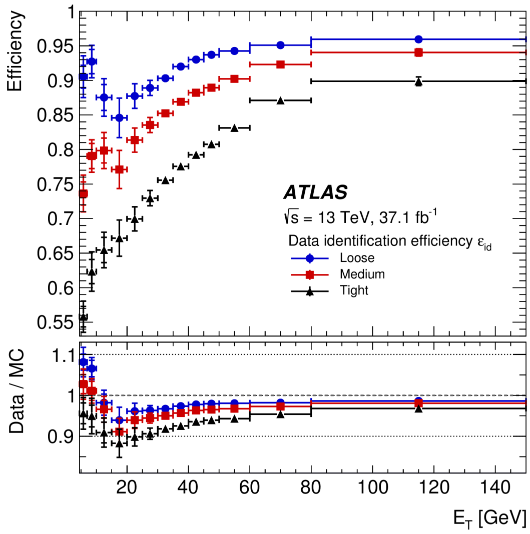

(a)

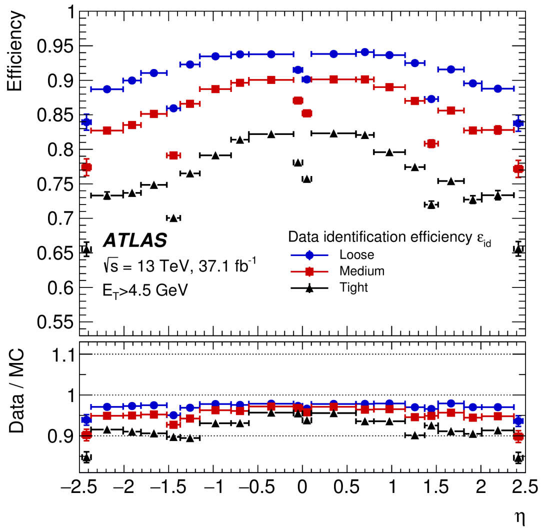

(b)

FIGURE 3.3: Measured electron-identification efficiencies in $Z \to e^+e^-$ events for the Loose (blue circle), Medium (red square), and Tight (black triangle) operating points as a function of E_T (top) and η (bottom). The vertical uncertainty bars (barely visible because they are small) represent the statistical (inner bars) and total (outer bars) uncertainties. The data efficiencies are obtained by applying data-to-simulation efficiency ratios that are measured in $J/\Psi \to e^+e^-$ and $Z \to e^+e^-$ events to the $Z \to e^+e^-$ simulation. For both plots, the bottom panel shows the data-to-simulation ratios.

It is the best choice for the electrons close to jets measurements and useful for the Overlap Removal procedure, as shown in Chapter 5.

The activity near the electrons can be quantified from the energy deposit in the calorimeters or from the tracks of nearby charged particles. An accurate electron isolation description is in Chapter 5.

3.3 Hadronic jets

Jets are hadronic clusters [57] and they are defined locally in the (η, ϕ) plane using electromagnetic and hadronic calorimetry. Due to high particle density in a jet, each cell may contain deposits due to multiple particles. A set of (η, ϕ, p_T) calorimeter objects parameterised are used to define the distances between these objects, and are defined by:

$$\Delta d_{ij} = min(p_{T,i}^{2\alpha} - p_{T,j}^{2\alpha}) \cdot \frac{\Delta R_{ij}^2}{R^2} \tag{3.1}$$

where

$$\Delta R_{ij} = \sqrt{(\eta_i - \eta_j)^2 + (\phi_i - \phi_j)^2} \tag{3.2}$$

and R is a chosen constant. Jets are constructed via an algorithm that combines these objects over the full grid, beginning with the pair that minimises d. These final objects define the set of jets. There are a variety of cone jet algorithms corresponding to different values of R and α.
The Eq. 3.1 satisfies these criteria for all values of α, and a value of α = -1 is suggested. This anti-k_t algorithm [58] causes objects with high p_T to gather surrounding low p_T objects, resulting in smooth round jets in the (η, ϕ) plane. The value of R is selected to balance two factors: the loss of jet p_T due to radiation outside the cone, and the absorption of soft hadrons from the hard scattering. The correction depends on the p_T and η of each jet, and accounts for pileup effects. In this analysis a value of $R = 0.4$ is used.
The process to define if a jet contains a b-hadron is defined as "b-tagging". It is vital for the ATLAS analyses that need information about heavy flavor jets and it is useful for suppressing backgrounds containing only light-flavor jets. The basic

b-tagging algorithms use charged particle tracks to produce a set of variables which discriminate between different jet flavor. ATLAS uses three distinct basic b-tagging algorithms, fully described in [59], but the recommended algorithm in Run 2 is called MV2. MV2 is a multivariate algorithm that is performed on jets from $t\bar{t}$ events with b-jets being considered as signal and c- and light-flavor jets being considered as background. The kinematic properties of the jets (p_T and $|\eta|$) are included in the training in order to take advantage of the correlations with the other input variables.
In this analysis the jets are b-tagged using the MV2c20 algorithm with a working point chosen has approximately 77% efficiency for such jets to contain a b-hadron in simulated SM $t\bar{t}$ events.
Finally, the algorithm "$Jet\ Vertex\ Tagger$" (JVT) [60] is used to reject jets from pileup. The JVT algorithm combines two track-based variables, which are sensitive to the vertex origin of jet, in a likelihood discriminant. Jets with $p_T < 50$ GeV and $|\eta| < 2.4$ are rejected if they have a JVT output of less than 0.641. This corresponds to an expected efficiency of about 92% for jets from the hard-scatter and a 2% efficiency for pileup jets. The JVT selection is close to 100% efficient for b-tagged jets.

3.4 Missing Transverse Energy (E_T^{miss} or MET)

The interaction probability for neutrinos with the material of the detector is close to zero. Therefore, they can be reconstructed only indirectly from the total energy balance of the event. Neutrino information are very important for several analyses such as BSM, because MET might arise also from new physics particles. The longitudinal component of the energy in hadron-hadron collisions is unknown, since the colliding partons carry only a fraction of the energy of the hadrons. But the initial transverse component is zero and the transverse energy balance can be used to reconstruct at least the transverse energy of neutrino, so-called E_T^{miss}.
The missing transverse energy E_T^{miss} is the module of the projection to the transverse plane of the vectorial sum of the transverse momenta (taking into account that the neutrinos are massless) of all visible particles (photons, leptons and jets), changed sign:

$$E_T^{miss} = \left| - \left(\sum_{\gamma} p_{T,\gamma} + \sum_{\ell} p_{T,\ell} + \sum_{j} p_{T,j} \right) \right| \tag{3.3}$$

The soft term is reconstructed from detector signal objects not associated with any object passing the above selection cuts. These can be ID tracks (track-based soft term) or calorimeter signals (calorimeter-based soft term) [61].

3.5 Overlap Removal between leptons and jets

Objects can satisfy both the jet and lepton selection criteria and, as such, a procedure called "overlap removal" is applied, in order to associate objects to a unique hypothesis. This procedure has an enormous impact on signal retention in this analysis, as true top- granddaughter leptons often fall inside the jet of the true top-daughter b-quark for signal events.

3.5.1 Electrons

In a reconstructed event, when a jet and an electron are found very close to each other, there are three different possibilities that have occurred: the same electron calorimeter deposit has been reconstructed once as an electron and once as a jet; the b-jet and the electron from the leptonic top or antitop decay have overlapping energy deposits in the calorimeters and the reconstructed jet cone contains the electron cluster; a b-jet decay has produced a non-prompt electron.
An electron-jet overlap removal procedure is used to prevent the double counting of electrons as jets as well as to remove non-prompt electrons, to reduce the rate of events with mis-reconstructed or non-prompt electrons. The main variable used to achieve this is the angular distance $\Delta R(el, jet)$, measured for all electron-jet combinations in each event. The procedure depends to the type of particle:

- Jets are removed if the angular distance is $\Delta R < 0.2$;
- Electrons are removed if the angular distance is $0.2 < \Delta R < 0.4$.

As a consequence, the electron and the b-jet from a leptonic top or antitop decay are both kept in the event only if $\Delta R > 0.4$. A schematic view of the OR procedure is shown in Fig. 3.4.

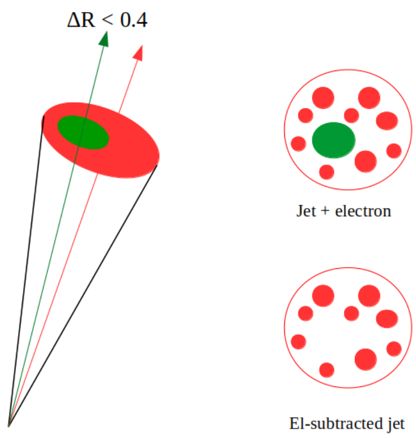

FIGURE 3.4: Schematic of the electron overlap removal procedure. The electron 4-momentum (green) is subtracted from the jet cone (red).

3.5.2 Muons

Normally the overlap removal procedure, used by the ATLAS Top analysis group, is done with $\Delta R(\mu, jet) > 0.4$ combining the isolation criteria, to increase the rejection of the bad events.

The lepton-jet overlap-removal procedure for muons is similar to that for electrons, but the situation for muons is simpler, as it is less likely for an isolated muon to produce an energy cluster in the calorimeters reconstructed as a jet.

There are different ways in which a muon can be overlapping with a jet: the pileup, where a muon and a jet can be produced in the same area of the detector but can be reduced requiring that the tracks must be in the primary vertex; the light meson decays ($\pi^{\pm}$ or $K^{\pm}$) that can be reduced requiring an high transverse momentum of the muon, combining the muon isolation and a vertex requirement; the heavy-flavor hadron decays (charm or beauty quarks) that can give rise to muons, the techniques are the same of the light flavor, but in this case the secondary vertex and the primary one are very close; the final state radiation (FSR), in this case a photon and a muon are produced very close and can be reconstructed as a muon and jet in the EM calorimeter; the bremsstrahlung where the muon at very high energy will loose energy in the calorimeter.

3.6 Monte Carlo simulation

MC samples [62] are simulated events that reflect our physics knowledge about interaction and production in particle accelerators and the comparison between these simulations and the acquired data can help the search of new physics phenomena. The simulation of the events inside a particle accelerator can be divided in different aspects:

- *Hard interaction*: many LHC processes of interest involve large momentum transfers, such as the production of heavy particles or jets with high transverse momenta. In this case the matrix element must be calculated and also the phase space integration must be performed. Moreover, the parton distribution functions of incoming partons are taken into account and perturbation theory is used.

- *Parton showering*: because the partons carry color charge, they can radiate additional gluons and these bosons radiate themself, creating a shower of soft gluons. The MC generator simulates this shower, evolving in terms of a certain variables (such as the relative transverse momentum) from the hard scattering to a cutoff scale, determined by the hadronisation scale.

- *Hadronisation*: it refers to the specific model used in an event generator for the transition from the partonic "final" state to a complete representation of the actual hadronic final state, in order to form bound states. Several MC generators use different models to reconstruct the the process.

- *Underlying events*: this kind of events are due to not-hard-scattering processes, that contribute to the total observed activity in hadron-hadron collisions, and can be exist also from lower energy collisions from the remnants of the beams.

- *Unstable particle decay*: the hadronisation taken into account the stable particles, but can exist also unstable resonances and they are calculated using known decay information and branching ratios.

The MC generators consist to a set of simulated events with defined particles and with known kinematics information. In this case the relation between particles are well described, from mother particles to decay products, referred as "truth level". The generators are chosen from their parameters (such as hadronisation or parton showering) and the optimisation of these parameters is called "tuning".
In the ATLAS experiment the generators used for the Matrix Element are POWHEG [63], MadGraph_aMC@NLO [64], HERWIG7 [65] and SHERPA [66]; instead, about the parton showering PYTHIA8 [67], HERWIG7 and SHERPA are chosen. The MC samples used for this analysis processes are described in Section 6.4.

Chapter 4

Reconstruction efficiency of muon close to jets

The first part of my work involved the study of the reconstruction efficiency for muons close to jets.
Muons close to jets are a key to some analysis that use muon information inside jets, such as the $t\bar{t}$ resonance analysis, due to the high $t\bar{t}$ invariant mass, because the Lorentz boost, the muons will be close to the b-jets. Specific and dedicated measurements of the reconstruction efficiency of muons as a function of the distance with respect to jets is fundamental for these kind of measurements. So, the measurement of the reconstruction efficiency, as well as of the momentum scale and resolution is mandatory. The reconstruction efficiencies are determined using the Tag-and-Probe method with J/Ψ samples and the Combined Muon reconstruction (described in this chapter) type is used.
After introducing the ATLAS muon reconstruction and identification algorithms, this chapter describes the performance of muon close to jets reconstruction using the LHC dataset recorded at $\sqrt{s} = 13$ TeV in 2016. Using a sample of $J/\Psi \to \mu^+\mu^-$ decay, reconstruction efficiencies and scale factors are compared with the recommended ones by the Muon Combined Performance (MCP) ATLAS group [68]. MCP Scale factors are used to correct the simulation to improve the agreement with data and to minimise the systematic uncertainties in physics analyses; my study confirms that MCP setup recommendations are applicable to the dilepton analysis.

4.1 Muon Reconstruction

Muon reconstruction is performed [68] indipendently in the Inner Detector (ID) and in the Muon Spectrometer (MS), and this information is combined to form the muon tracks.
The combined ID–MS muon reconstruction is performed according to various algorithms based on the information provided by the ID, MS, and calorimeters. The muon system allows the identification of muons with a p_T above 3 GeV. Muons with momenta lower than that are difficult to reconstruct since they do not reach the spectrometer, loosing too much energy in the calorimeter and/or do not leave a significant signal over the noise in the muon spectrometer.
Four muon types are defined depending on which sub-detectors are used in the reconstruction:

- *Combined muon* (CB): the track reconstruction is performed independently in the ID and the MS and a combined track is formed by a global refit that uses the hits from both the ID and MS subdetectors. During the global fit procedure, MS hits may be added to or removed from the track to improve the fit quality;
- *Segment−tagged muon* (ST): a track in the ID is classified as a muon if, once extrapolated to the MS, it is associated with at least one local track segment in the MDT or CSC chambers;
- *Calorimeter − tagged muon* (CT): a track in the ID is identified as a muon if it can be matched to an energy deposit in the calorimeter compatible with a minimum-ionizing particle. This type has the lowest purity of all the muon types but it recovers acceptance in the region where the ATLAS MS is only partially instrumented to allow for cabling and services to the calorimeters and ID;
- *Extrapolated muon* (ME): the muon trajectory is reconstructed based only on the MS track and a loose requirement on compatibility with originating from the ID. The parameters of the muon track are defined at the interaction point, taking into account the estimated energy loss of the muon in the calorimeters.

Overlaps between different muon types are resolved before producing the collection of muons used in physics analyses. When two muon types share the same ID track, preference is given to CB muons, then to ST, and finally to CT muons. The overlap with ME muons in the muon system is resolved by analyzing the track hit content and selecting the track with better fit quality and larger number of hits.

In this analysis the Combined Muon reconstruction is used. For CB muons, the variables used in muon identification are:

- q/p significance: defined as the absolute value of the difference between the ratio of the charge and momentum of the muons measured in the ID and MS divided by the sum in quadrature of the corresponding uncertainties;
- ρ': defined as the absolute value of the difference between the transverse momentum measurements in the ID and the MS divided by the p_T of the combined track;
- normalised χ^2 of the combined track fit.

4.2 Muon Identification

Muon identification [68] is performed by applying quality requirements that suppress background, mainly from pion and kaon decays, while selecting prompt muons with high efficiency and/or guaranteeing a robust momentum measurement.
Muon candidates originating from in-flight decays of charged hadrons in the ID are often characterized by the presence of a distinctive "kink" topology in the reconstructed track. As a consequence, it is expected that the fit quality of the resulting combined track will be poor and that the momentum measured in the ID and MS may not be compatible.
In a similar way to the electrons (described in Chapter 3) the muon tracks are done using a Kalman Filter algorithm. Moreover, some requirements on the number of hits in the ID and MS are used in order to have a good momentum measurement. For the ID, the quality selections require at least one Pixel hit, at least five SCT hits, fewer than three Pixel or SCT holes, and that at least 10% of the TRT hits

originally assigned to the track are included in the final fit (the TRT measurements are included in the track fits for tracks with $|\eta| < 2.0$).
Four muon identification selections (Medium, Loose, Tight and High-p_T) are provided to address the specific needs of different physics analyses. Loose, Medium, and Tight are inclusive categories in that muons identified with tighter requirements are also included in the looser categories.
In dilepton analysis a muon configuration that minimises the systematic uncertainties is needed, because it improves the signals sensitivity significantly.

- *Medium Muons* (MM): The Medium identification criteria provide the default selection for muons in ATLAS. This selection minimises the systematic uncertainties associated with muon reconstruction and calibration. Only CB and ME tracks are used. The former are required to have ≥ 3 hits in at least two MDT layers, except for tracks in the $|\eta| < 0.1$ region, where tracks with at least one MDT layer but no more than one MDT hole layer are allowed.

- *Tight Muons* (TM): Tight muons are selected to maximise the purity of muons at the cost of some efficiency. Only CB muons with hits in at least two stations of the MS and satisfying the Medium selection criteria are considered. The normalised χ^2 of the combined track fit is required to be < 8 to remove pathological tracks. A two dimensional cut in the ρ' and q/p significance variables is performed as a function of the muon p_t to ensure stronger background rejection for momenta below 20 GeV where the misidentification probability is higher.

- *Loose Muons* (LM): The Loose identification criteria are designed to maximise the reconstruction efficiency while providing good-quality muon tracks. They are specifically optimised for reconstructing Higgs boson candidates in the four-lepton final state. All muon types are used. All CB and ME muons satisfying the Medium requirements are included in the Loose selection. CT and ST muons are restricted to the $|\eta| < 0.1$ region.

- $High - p_T$ *Muons* (HM): The High-p_T selection aims to maximise the momentum resolution for tracks with transverse momentum above 100 GeV. The selection is optimised for searches for high-mass Z' and W' resonances. CB muons passing the Medium selection and having at least three hits in three

MS stations are selected. Specific regions of the MS where the alignment is suboptimal are vetoed as a precaution. Requiring three MS stations, while reducing the reconstruction efficiency by about 20%, improves the $p_T$resolution of muons above 1.5 TeV by approximately 30%.

The MM identification criteria is used as default selection for muons in ATLAS and it minimises the reconstruction and calibration uncertainties. Some corrections are applied to MC simulations in form of efficiency scale factors (SF), in order to match isolation and trigger efficiency in data.
In this analysis the Medium Muon selection is used because, it aims to lower systematics in high-p_T region, where the muons are close to jets. These corrections are obtained by comparing MC predictions to large samples of $J/\Psi \to \mu^+\mu^-$ and $Z \to \mu^+\mu^-$ data events using the tag-and-probe method, as shown in the next sections.

4.3 Muon Isolation

The measurement of the activity around a muon candidate, called *muon isolation* [68], is useful for those muons that come from semileptonic decays of b-hadrons, which are embedded in jets.
Two variables are defined to assess muon isolation, defined before:

- $p_T^{varcone30}$ is the track-based isolation variable, it is defined as the scalar sum of the transverse momenta of the tracks with $p_T > 1$ GeV in a cone of size $\Delta R = min(10\ GeV/p_T^{\mu}, 0.3)$ around the muon of transverse momentum p_T^{μ} , excluding the muon track itself;
- $E_T^{topocone20}$ is the calorimeter-based isolation variable, it is defined as the sum of the transverse energy of the topological clusters [70] in a cone of size $\Delta R = 0.2$ around the muon, after subtracting the contribution from the energy deposit of the muon itself and correcting for pileup effects.

Where the pileup is a situation where a particle detector is affected by several events at the same time that are not in the center-of-mass.

For the muon isolation performance, seven isolation selection criteria, or "working point", are defined and each one is optimised for different physics analysis; the isolation criteria are determined using the relative isolation variables, which are defined as the ratio between the track-based or the calorimeter-based isolation variables and the transverse momentum of the muon.
Tab. 4.1 lists the seven isolation working point with the definitions and discriminating variables. For the first five working points, cuts are provided in bins of p_T and η of the muon; they are tuned aiming for a uniform efficiency in all bins. The $LooseTrackOnly$ and the $FixedCutTightTrackOnly$ working points are exclusively defined by cuts on the relative track based isolation variable only. The other working points are defined by cuts applied separately on both track and calorimeter-based relative isolation variables.

Isolation WP	Discriminating variables	Definition
LooseTrackOnly	$p_T^{varcone30}/p_T^{\mu}$	99% eff. constant in η and p_T
Loose	$p_T^{varcone30}/p_T^{\mu}$,$E_T^{topocone20}/p_T^{\mu}$	99% eff. constant in η and p_T
Tight	$p_T^{varcone30}/p_T^{\mu}$,$E_T^{topocone20}/p_T^{\mu}$	96% eff. constant in η and p_T
Gradient	$p_T^{varcone30}/p_T^{\mu}$,$E_T^{topocone20}/p_T^{\mu}$	$\geq$ 90(99)% eff. at 25(60) GeV
GradientLoose	$p_T^{varcone30}/p_T^{\mu}$,$E_T^{topocone20}/p_T^{\mu}$	$\geq$ 95(99)% eff. at 25(60) GeV
FixedCutTightTrackOnly	$p_T^{varcone30}/p_T^{\mu}$	$p_T^{varcone30}/p_T^{\mu} < 0.06$
FixedCutLoose	$p_T^{varcone30}/p_T^{\mu}$,$E_T^{topocone20}/p_T^{\mu}$	$p_T^{varcone30}/p_T^{\mu} < 0.15$, $E_T^{topocone20}/p_T^{\mu} < 0.30$

TABLE 4.1: Definition of the seven isolation working points for the muon isolation performance.

The efficiencies for the isolation working points are measured with $Z \rightarrow \mu^+\mu^-$ decays, in data and simulation, using the Tag-and-Probe method. To avoid probe muons near to jets, a $\Delta R > 0.4$ is required, where ΔR is the angular difference between the muon and its nearest jet, that is reconstructed using anti-k_t algorithm [58] with radius parameter 0.4 and with the transverse momentum $p_T > 20$ GeV.
Fig. 4.1 shows the isolation efficiencies for medium muons measured in data and Monte Carlo simulation, as a function of the transverse momentum of the muon for the $LooseTrackOnly$ and $GradientLoose$ working points; the respective data/MC ratios are shown in the bottom panel of each plot. The blue bar is the statistical uncertainty and the yellow bar is both statistical and systematic uncertainties, where the systematic uncertainty is evaluated in the $Z \rightarrow \mu^+\mu^-$ analysis by taking the

maximum variation of the transfer factor T when estimated with a simulation-based approach as described in [69]. In the low-p_T region the uncertainties are due to the background estimation and the mass window variation; the high-p_T region is dominated by statistical uncertainty in data and simulation. The efficiency decreases, between 40 GeV and 80 GeV for *LooseTrackOnly* and between 30 GeV and 60 GeV for *GradientLoose*, This is due to the dependence of the selection on the transverse momentum. Moreover, the main uncertainty in both p_T regions arises from having neglected the η dependence of the Scale Factors (SFs), shows in Section 4.6, which are usually provided as a function of η and p_T (SFs will be fully describe in Section 4.5).

In this analysis, the *FixedCutTightTrackOnly* isolation is used because it is only track-dependent; so it implies an higher amount of simulated signal events, increasing the signal/background ratio as shown in Section 5.3.

4.3.1 Muon energy scale and resolution

The muon momentum scale and resolution are studied using $J/\Psi \to \mu^+\mu^-$ and $Z \to \mu^+\mu^-$ decays. Although the simulation contains an accurate description of the ATLAS detector, the level of detail is not enough to describe the muon momentum scale to the per mille level and the muon momentum resolution to the percent level. A set of corrections is applied to the simulated muon momentum in order to obtain the data/MC agreement.

To improve the precision, the p_T and η distributions of the Z and J/Ψ resonances in simulation are reweighted to the distributions observed in data, as shown in Fig. 4.2, for the invariant mass distribution of the $Z \to \mu^+\mu^-$. The invariant mass window for the two muons to result form a Z decay is $75-105$ GeV. After correction, the line-shape of the Z resonance in simulation (red solid line) agrees with the data within the systematic uncertainties, demonstrating the overall effectiveness of the p_T calibration. A better demonstration of the effectiveness of the momentum calibration is obtained by comparing, in data and simulation, the measurement of the position $m_{\mu\mu}$ and resolution $\sigma_{\mu\mu}$ of the dimuon mass peaks, extracted in bins of η and p_T from fits to the $J/\Psi \to \mu^+\mu^-$ and $Z \to \mu^+\mu^-$ invariant mass distributions.

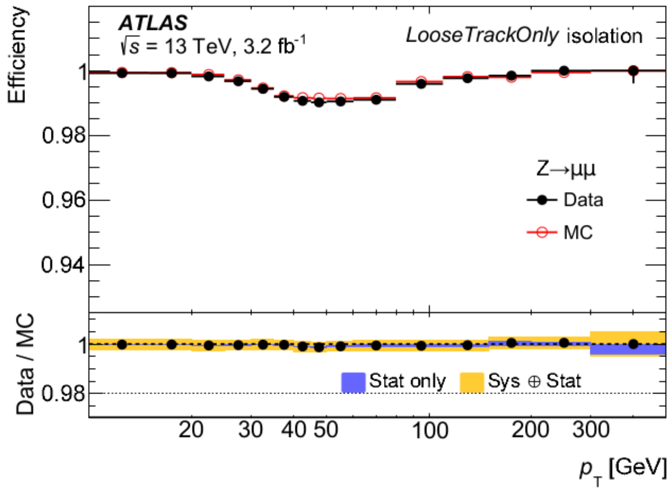

(a)

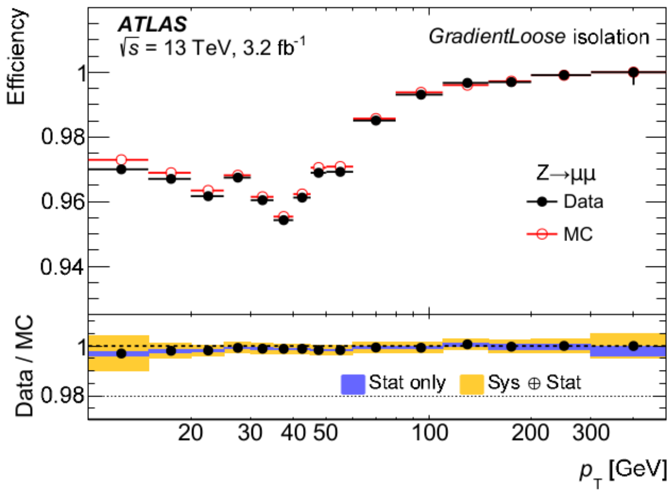

(b)

FIGURE 4.1: Isolation efficiencies for *LooseTrackOnly* (a) and *GradientLoose* (b) working points. The black dots are data and the red dots are the simulation, measured in $Z \rightarrow \mu^+\mu^-$ samples using Tag-and-Probe method. The uncertainties shown on the efficiency are statistical only. The bottom panels are the data/MC ratio; blue is the statistical uncertainty only and yellow are both statistical and systematic [68].

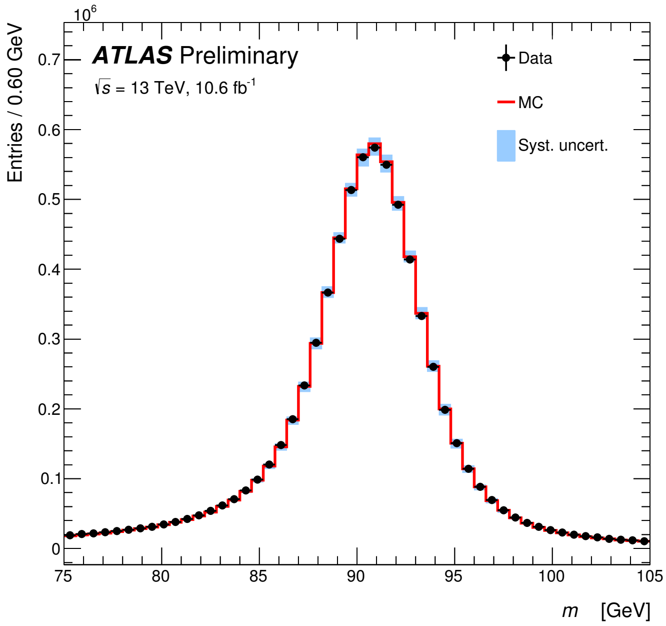

FIGURE 4.2: Dimuon invariant mass distribution of $Z \to \mu^+\mu^-$ events reconstructed with combined muons. The points show the data. The continuous line corresponds to the simulation with the momentum corrections applied. The band represents the effect of the systematic uncertainties on the momentum corrections. Simulation is normalised to data.

4.4 Tag-and-Probe method with $J/\Psi \rightarrow \mu^+\mu^-$ sample

As the muon reconstruction in the ID and MS detectors is performed independently, a precise determination of the muon reconstruction efficiency in the region $|\eta| < 2.5$ is obtained with the tag-and-probe method.
The Tag-and-Probe method is employed to measure the efficiency of the muon identification selections within the acceptance of the ID ($|\eta| < 2.5$). The method is based on the selection of an almost pure muon sample from $J/\Psi \rightarrow \mu^+\mu^-$ events, requiring one leg of the decay (tag) to be identified as a Medium muon that fires the trigger and the second leg (probe) to be reconstructed by a system independent of the one being studied. Tag and probe tracks are extrapolated to the MS trigger surfaces and the extrapolated positions are required to be $\Delta R > 0.2$ far apart. The invariant mass requirement on the dimuon pair to select the J/Ψ is 2.75 GeV $< m_{\mu\mu} <$ 3.5 GeV.

In this work, two kind of efficiencies are measured:

- Efficiency for Medium muons with Calo muon as probes (CP);
- Efficiency for ID tracks with MS muon as probes (MS).

The Calo muons are the ID tracks tagged as muons by the calorimeter deposit. Calo muons allow a measurement of the efficiency in the MS, while MS tracks are used to determine the complementary efficiency of the muon reconstruction in the ID.
The efficiency measurement for Medium muons consists of two stages. First, the efficiency $\epsilon(Medium|CP)$ of reconstructing these muons assuming a reconstructed ID track is measured using a CP muon as probe; then this result is corrected by the efficiency $\epsilon(ID|MS)$ of the ID track reconstruction, measured using MS probes:

$$\epsilon(Medium) = \epsilon(Medium|CP) \cdot \epsilon(ID|MS) = \epsilon(Medium|ID) \cdot \epsilon(ID) \qquad (4.1)$$

A similar approach is used when using ID probe tracks for cross-checks.
This approach is valid if two assumptions are satisfied. First, the ID track reconstruction efficiency is independent from the muon spectrometer track reconstruction $\epsilon(ID) = \epsilon(ID|MS)$; then the use of a CP muon as a probe instead of an ID track does not affect the probability for Medium reconstruction $\epsilon(Medium|ID) = \epsilon(Medium|CP)$.
The level of agreement of the measured efficiency, $\epsilon^{Data}(Medium)$ with the efficiency measured with the same method in simulation, $\epsilon^{MC}(Medium)$, is expressed as the ratio of these two numbers, called "efficiency scale factor" (SF):

$$SF = \frac{\epsilon^{Data}(Medium)}{\epsilon^{MC}(Medium)} \tag{4.2}$$

This quantity describes the deviation of the simulation from the real detector behaviour, and it is useful to physics analyses, which use it to correct the simulation. The efficiency and SF measurements for medium muons are shown in section 4.6.

4.5 Non-isolated muon reconstruction efficiency with $J/\Psi \rightarrow \mu^+\mu^-$

MCP ATLAS group provides official SFs calculated for isolated muons; so additional studies are requested in order to provide the efficiency and SF for muon close to jets.

4.5.1 Event selection

Events are selected by requiring muon pairs with an invariant mass between 2.7 GeV and 3.5 GeV; a transverse momentum of at least 4 GeV and $|\eta| < 2.5$ for each muon. The tagged muon is required to satisfy Medium muon identification selection and to have triggered the read-out of the events. A difference $|z_0^{tag} - z_0^{probe}| < 5$ mm is required and $\Delta R(jet, probe) < 0.4$, where $\Delta R = \sqrt{\Delta\eta^2 + \Delta\phi^2}$ is the angular difference between the muon and its nearest jet.
ATLAS dataset 2016 belonging to the Good Run List (GRL) is used; Monte Carlo

samples are used for the Calo muons and the MS probes. Events used to measure the muon reconstruction efficiency are selected according to a trigger list containing a mixture of unprescaled single muon trigger and special muon+track triggers designed for efficiency measurements (a three-muon trigger with a J/Ψ mass window, HLT_muX_bJpsi_Trkloose with X = 4, 6, 10 and 18 GeV). Tab. 4.2 shows the triggers list.
The list of sample and trigger names are listed in Appendix A.

μ trigger
HLT_mu4
HLT_mu6
HLT_mu6_idperf
HLT_mu4_bJpsi_Trkloose
HLT_mu6_bJpsi_Trkloose
HLT_mu10_bJpsi_Trkloose
HLT_mu18_bJpsi_Trkloose

TABLE 4.2: List of muon triggers used for this study about the efficiency for muons close to jets.

4.5.2 Reconstruction efficiency

Selected tag-and-probe pairs are grouped in two independent samples: pairs in which the probe is matched to the muon type (matched sample) and pairs in which the probe is not matched (unmatched sample). The matching is performed requiring a distance $\Delta R < 0.005$ between the probe and the matched object. The reconstructed muons of a given type (in the following Medium Muons) are considered the probes that are angularly matched to that selected muon; CP muons are the ones that are considered to be reconstructed so that the efficiency is obtained by calculating:

$$\frac{N_{matched} - N_{unmatched}}{N_{matched} + N_{unmatched}} \tag{4.3}$$

The efficiency is derived by a simultaneous log-likelihood fit of the two statistically independent distributions of the invariant mass. The fits are performed in the seven p_T bins and nine η bins of the probe:

- p_T: [5-6,6-7,7-8,8-10,10-12,12-15,15-20] GeV;
- η: ($\pm$0.1, $\pm$ 1.05, $\pm$ 1.3, $\pm$ 2 and $\pm$ 2.5)

The signal is modelled with a Crystal Ball function with a single set of parameters for the two independent samples. Separate first-order polynomial fits are used to describe the background shape for matched and unmatched probes.
Fig. 4.3 shows examples of the J/Ψ fits, in this case using CP muons to measure the reconstruction efficiency for medium muons, for probes with ratio $p_T^{varcone30}/p_T > 0.06$ (non-isolated muons).

After the fits, a study on the reconstruction efficiencies is done for different regions of isolation ($p_T^{varcone30}/p_T(probe)$ and $E_T^{topocone20}/p_T(probe)$) of the calo muon probes that are matched to medium muons and $\Delta R(jet, \mu)$ between the medium muon and its nearest jet. An example of the reconstruction efficiency, for data 2016 in a precise bin in η and in the two regions of isolation for muons close to jets, is shown in Fig. 4.4.
All the plots are presented in Appendix A.

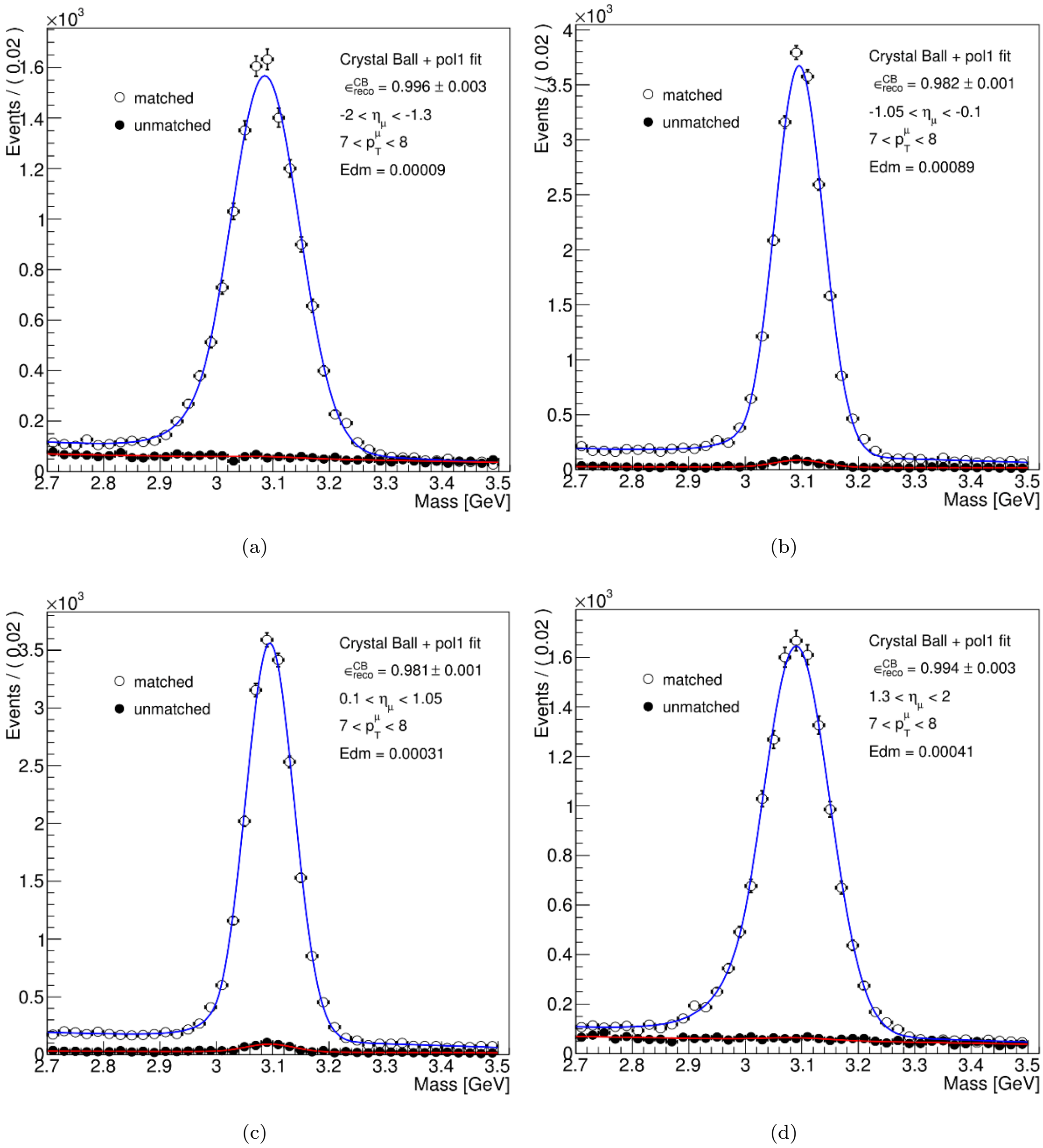

FIGURE 4.3: Invariant mass distributions for the calorimeter-tagged probes matched (empty circles) and unmatched (full circles) to Medium muons from data with the corresponding fits reported as continuos lines. The $\eta - p_T$ intervals are specified on each figure. The probes are CP muons passing an isolation requirement $p_T^{varcone30}/p_T > 0.06$.

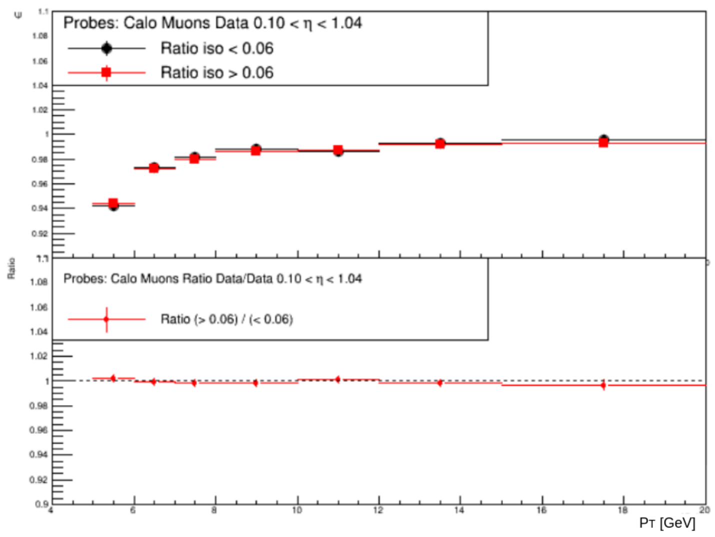

(a)

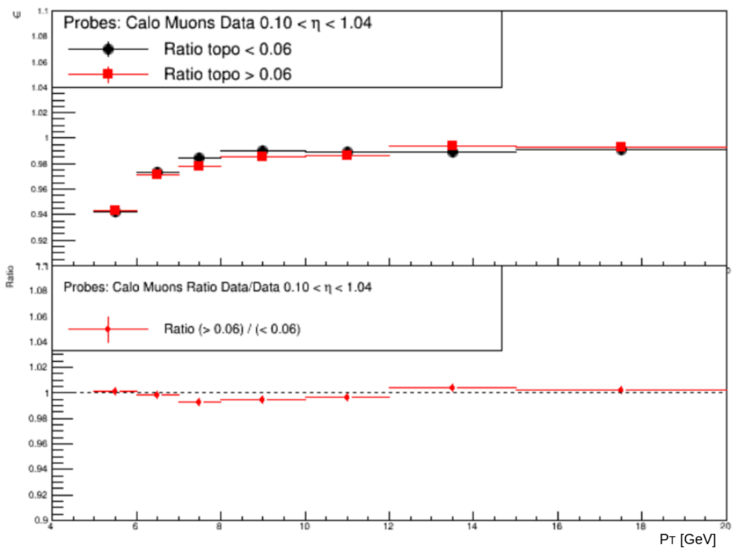

(b)

FIGURE 4.4: (a): medium muon efficiency, using data samples, with calo muons as probes in the region of isolation $p_T^{varcone30}/p_T(probe) > 0.06$. (b): medium muon efficiency, using data samples, with calo muons as probe in the region of isolation $E_T^{topocone20}/p_T(probe) > 0.06$. η bin $0.1 < \eta <$1.05 . Bottom panels show ratio between the non isolated muon efficiencies and the isolated muon efficiencies.

The cuts are applied to the muon p_T for both the track and calorimeter-based isolation variables; Fig. 4.5 shows the distribution of this variables in muons in non-isolated regions $p_T^{varcone30}/p_T(probe) > 0.06$ and $E_T^{topocone20}/p_T(probe) > 0.06$. Fig. 4.6 shows the distribution of the ΔR variable and a zoom in the no-isolated region ($\Delta R < 0.4$), splitted in two sub-regions, in order to measure SFs for muon close to jets ($0.2 < \Delta R < 0.4$) and very close to jets ($0 < \Delta R < 0.2$).

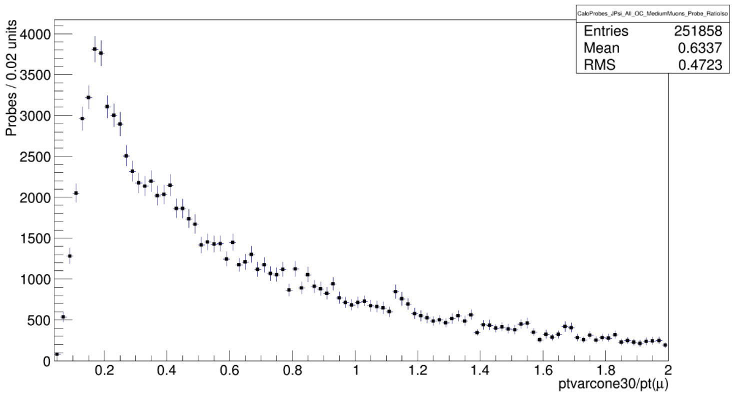

(a)

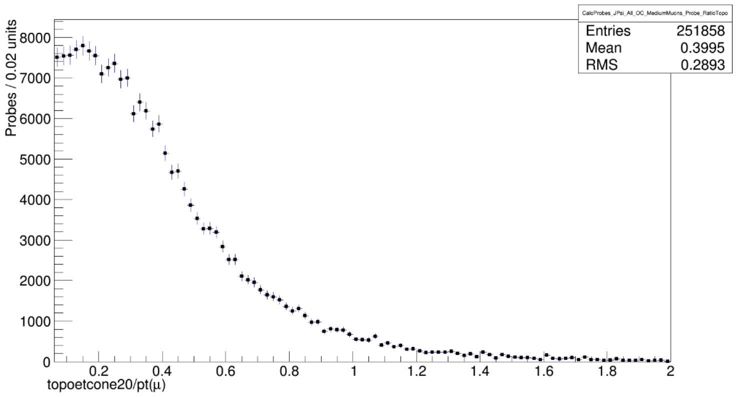

(b)

FIGURE 4.5: Track-based (a) and calorimeter-based (b) isolation variables divided by the transverse momentum of the muon in no-isolated regions: $p_T^{varcone30}/p_T(probe) > 0.06$ and $E_T^{topocone20}/p_T(probe) > 0.06$.

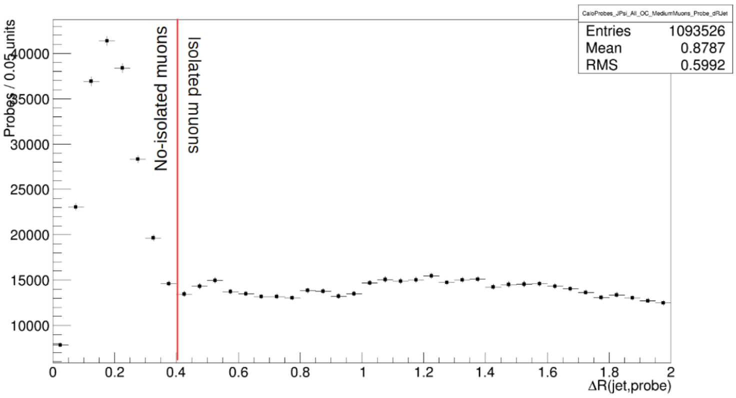

(a)

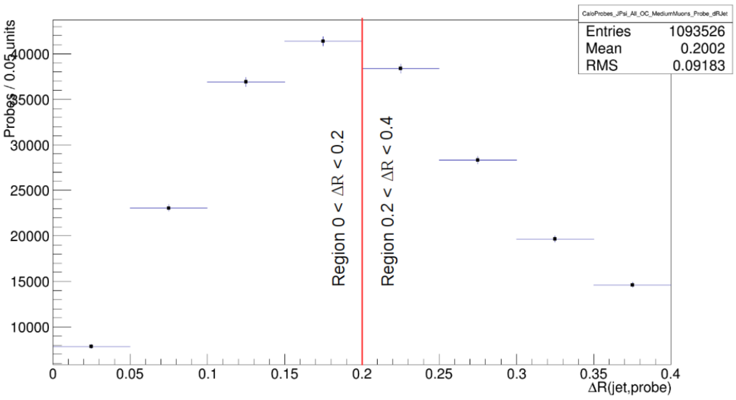

(b)

FIGURE 4.6: Distribution of the ΔR variable (a) and a zoom in the no-isolated region ($\Delta R < 0.4$), splitted in two sub-regions (b).

4.5.3 Results

In this section the results of the reconstruction efficiencies and Scale Factors (SFs) are shown.
Figure 4.7 (a) shows the muon reconstruction efficiency in different η regions measured from $J/\Psi \rightarrow \mu^+\mu^-$ events for Medium muon selection in the no-isolated-region $p_T^{varcone30}/p_T(probe) > 0.06$. Within each η region, the efficiency is measured in seven p_T bins (5-6,6-7,7-8,8-10,10-12,12-15 and 15-20 GeV). The resulting values are plotted as distinct measurements in each η bin and with p_T increasing from 5 to 20 GeV going from left to right. The error bars on the efficiencies indicate the statistical uncertainty. The panel at the bottom shows the ratio of the measured to predicted efficiencies, the SFs are close to unity within the uncertainties. Figure 4.7 (b) shows the efficiency SFs total uncertainty as a function of the η regions and the increasing p_T bins; the combined uncertainty is the sum in quadrature of the individual contributions. It is possible to see that in this region of isolation ($p_T^{varcone30}/p_T(probe)$) the largest component of the uncertainty is referred to as *truth closure*. This arises from possible biases in the tag-and-probe method, such as biases due to different kinematic distributions between reconstructed probes and generated muons or correlations between ID and MS efficiencies. The truth closure is estimated in simulation by comparing the efficiency measured with the tag-and-probe method with the "true" efficiency given by the fraction of generator-level muons that are successfully reconstructed.
Figure 4.8 (a) shows the muon reconstruction efficiency in different η regions measured in $J/\Psi \rightarrow \mu^+\mu^-$ events for Medium muon selection, in the region $E_T^{topocone20}/p_T(probe) > 0.06$. The panel at the bottom shows the ratio of the measured to predict efficiencies, the SFs are close to unity within the uncertainties. Figure 4.8 (b) shows the total uncertainty in the efficiency SFs as a function of the η regions and the increasing p_T bins. It is possible to see that in this region of isolation the dominant uncertainty is the truth closure.
Figure 4.9 (a) shows the muon reconstruction efficiency in different η regions measured in $J/\Psi \rightarrow \mu^+\mu^-$ events for Medium muon selection, in the region $0 < \Delta R < 0.2$. The panel at the bottom shows the ratio of the measured to predict efficiencies, the SFs are close to unity within the uncertainties. Figure 4.9 (b) shows the total uncertainty in the efficiency SFs as a function of the η regions and the increasing p_T

bins. It is possible to see that in this region the dominant uncertainty is statistic, because there are very few events in this ΔR region.
Figure 4.10 (a) shows the muon reconstruction efficiency in different η regions measured in $J/\Psi \rightarrow \mu^+\mu^-$ events for Medium muon selection, in the region $0.2 < \Delta R < 0.4$. The panel at the bottom shows the ratio of the measured to predict efficiencies, the SFs are close to unity within the uncertainties. Figure 4.10 (b) shows the efficiency SFs total uncertainty as a function of the η regions and the increasing p_T bins. It is possible to see that in this region $0.2 < \Delta R < 0.4$ the dominant uncertainty is statistic and truth closure.

The scale factors measured in the Tag-and-Probe study, within the statistical uncertainty, are close to the official SFs calculated by the MCP group, referred in [68].

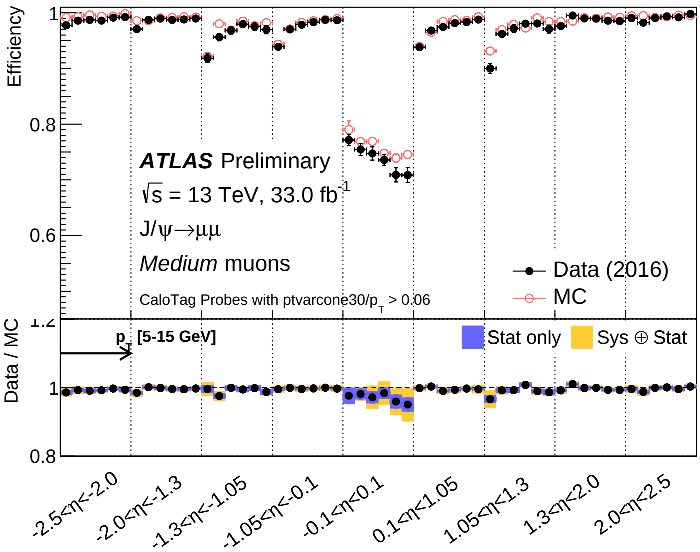

(a)

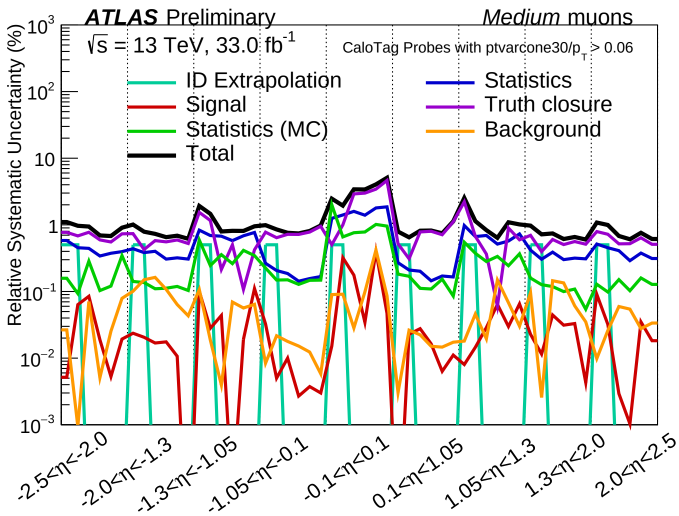

(b)

FIGURE 4.7: (a): Muon reconstruction efficiency in different η regions measured in $J/\Psi \rightarrow \mu^+\mu^-$ events for Medium muon selection, in the region $p_T^{varcone30}/p_T(probe) > 0.06$. (b): Total uncertainty in the efficiency scale factor for medium muons as a function of η obtained by $J/\Psi \rightarrow \mu^+\mu^-$ sample in the region $p_T^{varcone30}/p_T(probe) > 0.06$.

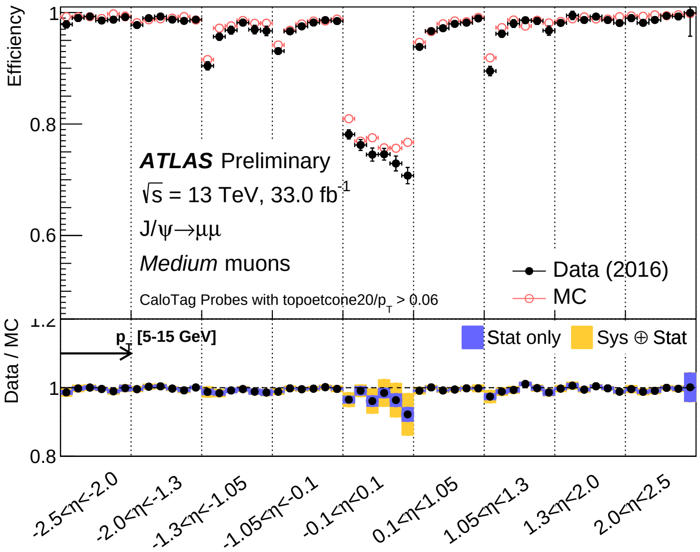

(a)

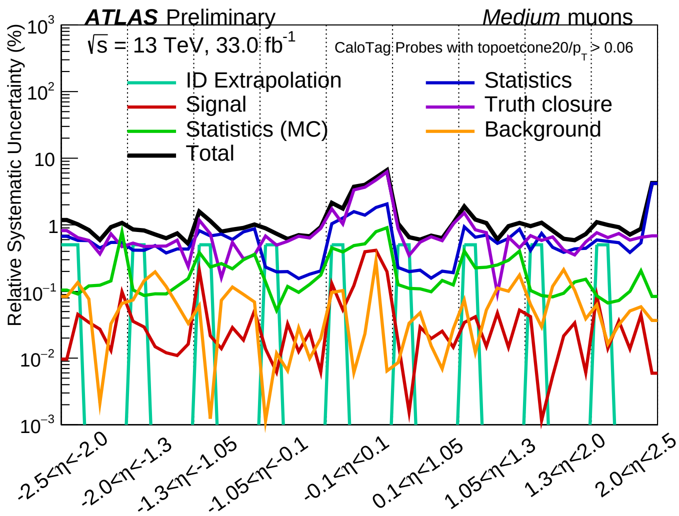

(b)

FIGURE 4.8: (a): Muon reconstruction efficiency in different η regions measured in $J/\Psi \rightarrow \mu^+\mu^-$ events for Medium muon selection, in the region $E_T^{topocone20}/p_T(probe) > 0.06$. (b): Total uncertainty in the efficiency scale factor for medium muons as a function of η obtained by $J/\Psi \rightarrow \mu^+\mu^-$ sample in the region $E_T^{topocone20}/p_T(probe) > 0.06$.

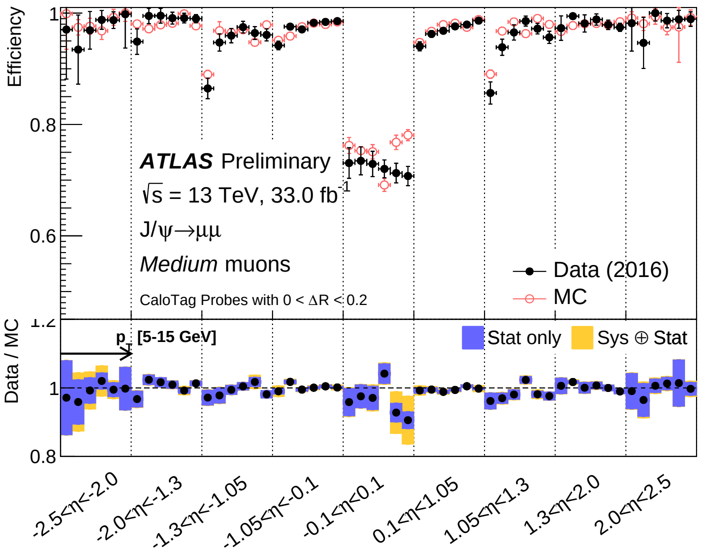

(a)

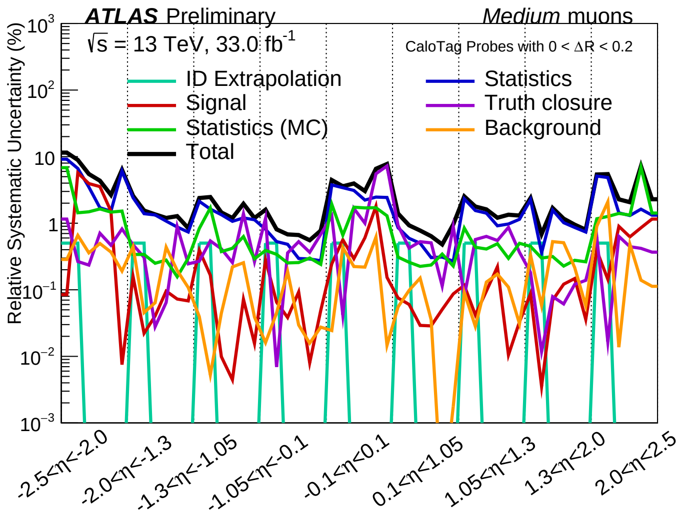

(b)

FIGURE 4.9: (a): Muon reconstruction efficiency in different η regions measured in $J/\Psi \to \mu^+\mu^-$ events for Medium muon selection, in the region $0 < \Delta R < 0.2$. (b): Total uncertainty in the efficiency scale factor for medium muons as a function of η obtained by $J/\Psi \to \mu^+\mu^-$ sample in the region $0 < \Delta R < 0.2$.

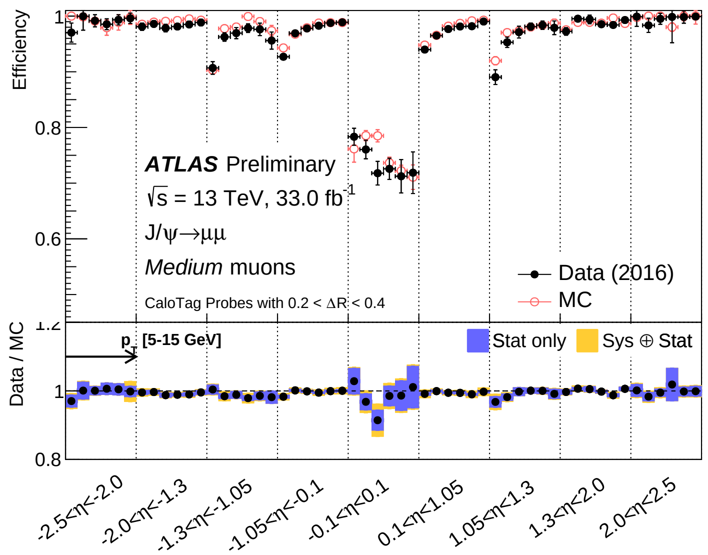

(a)

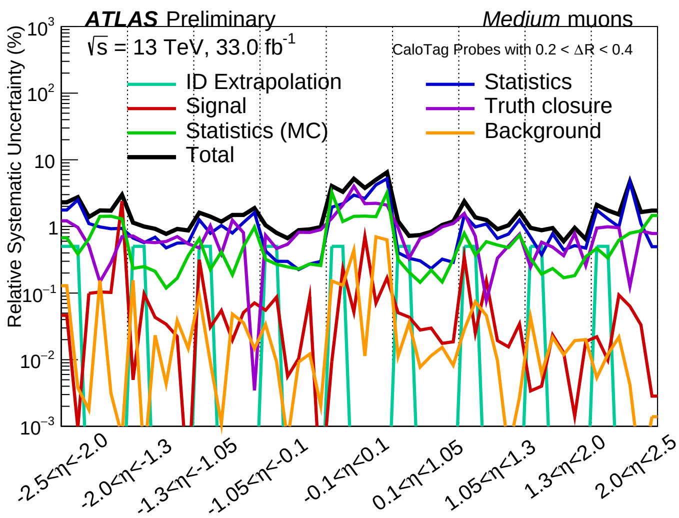

(b)

FIGURE 4.10: (a): Muon reconstruction efficiency in different η regions measured in $J/\Psi \rightarrow \mu^+\mu^-$ events for Medium muon selection, in the region $0.2 < \Delta R < 0.4$. (b): Total uncertainty in the efficiency scale factor for medium muons as a function of η obtained by $J/\Psi \rightarrow \mu^+\mu^-$ sample in the region $0.2 < \Delta R < 0.4$.

A comparison between SF measurements for muon close to jets and official MCP SFs in the pseudorapidity bin $0.1 < \eta < 1.05$ for the isolation and ΔR variables are shown in Fig. 4.11 and Fig. 4.12. All SF plots are shown in Appendix A.

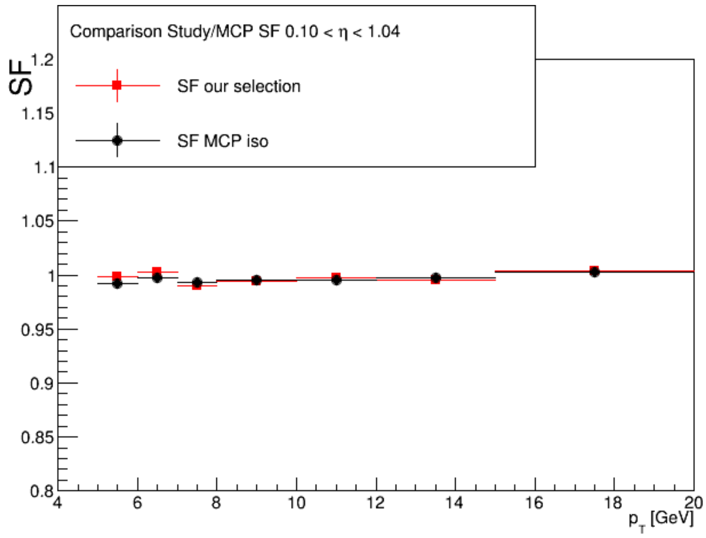

(a)

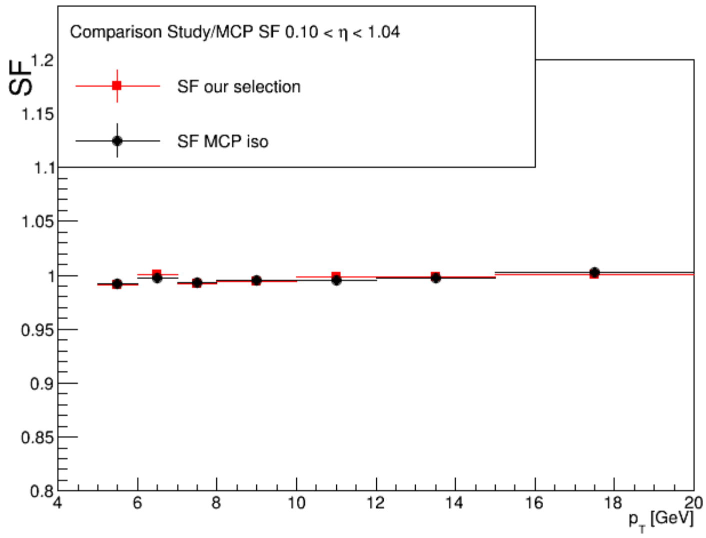

(b)

FIGURE 4.11: Comparison between SFs measured in this analysis (Red) and the default MCP SFs (Black) in the two regions of isolation for muons close to jets in η bin $0.1 < \eta < 1.05$. (a): $p_T^{varcone30}/p_T(probe) > 0.06$; (b): $E_T^{topocone20}/p_T(probe) > 0.06$.

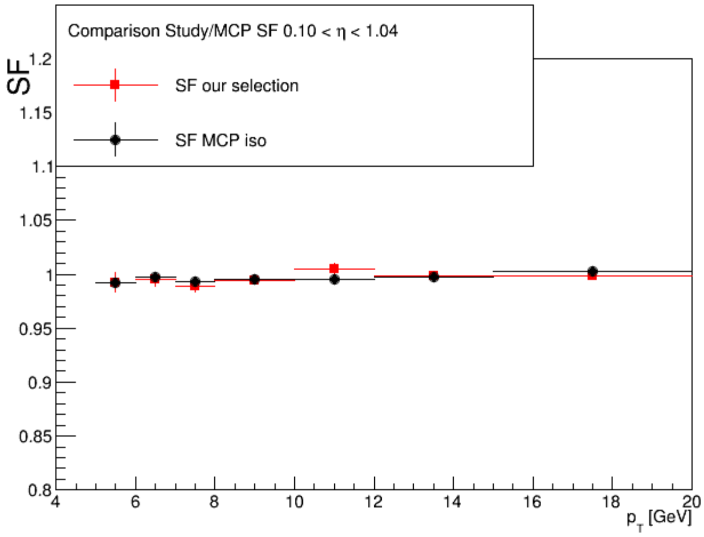

(a)

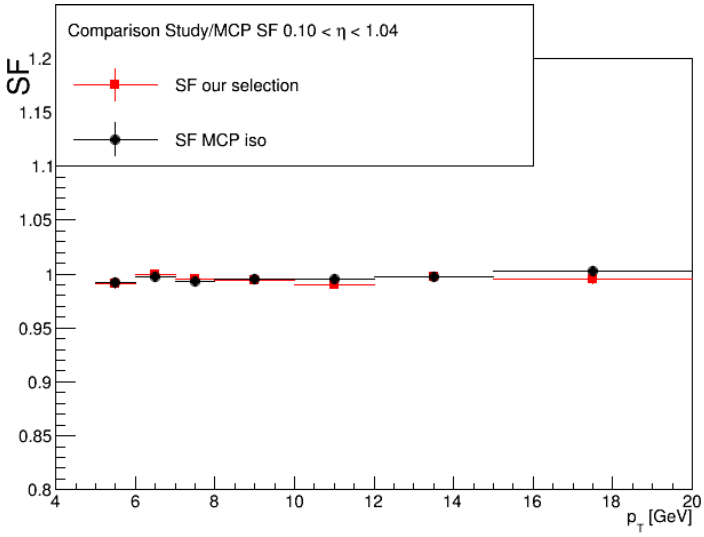

(b)

FIGURE 4.12: Comparison between SFs measured in my analysis (Red) and the default MCP SFs (Black) in the two regions of ΔR between muon and it's nearest jet: (a): $0 < \Delta R < 0.2$; (b): $0.2 < \Delta R < 0.4$ in η bin $0.1 < \eta < 1.05$.

Finally, a χ^2 test has been done for all bins in p_T and η, between our SFs and the official MCP SFs; all $P(\chi^2)$ of these exceeded the 5% which confirmed the compatibility, Tab. 4.3 shows the measured $P(\chi^2)$ between SFs measurement for muons close to jets and the official MCP SFs for isolated muons, both are related to medium muons.

Region	$P(\chi^2)$
$p_T^{varcone30}/p_T(probe) > 0.06$	0.74
$E_T^{topocone20}/p_T(probe) > 0.06$	0.32
$0 < \Delta R < 0.2$	0.36
$0.2 < \Delta R < 0.4$	0.83

Table 4.3: Measured $P(\chi^2)$ between my SFs done for muons close to jets and the official MCP SFs for isolated muons, both are related to medium muons.

In conclusion, the SFs measured for muon close to jets are compatible to the default MCP SFs measured for isolated muons within the global uncertainties, so they are added in MCP recommendations; this can be observed seeing the SFs plots and the $P(\chi^2)$ table.
Many analysis that use the information from muon close to jets will benefit from this additional SFs; such as, the $t\bar{t}$ resonances in dilepton final state. Moreover, as described in the following chapters, such recommendations will be followed in the setup concerning muons.

Chapter 5

Electron isolation efficiency and overlap removal extension

The second part of my work involved detailed studies on the electron isolation efficiency and the Overlap Removal (OR) needed for electron and muon candidates. This study has been produced in collaboration with the $t\bar{t}$ Resonance group of the ATLAS experiment. The main motivation for this work is similar to the muon case:the request of electron isolation and how the choice can be improved are very useful if I want to get a very sensitive measurement for the BSM signals.
In this analysis, the different isolation working points and the extension of the OR procedure were compared, to find the best setup, because the leptons from $X \rightarrow t\bar{t}$, for X sufficiently heavy, will have a good chance of being close to a jet (specifically the b-jet from the top and antitop decays) and therefore the normal requirements of isolation of the leptons are in some cases inappropriate, reducing signal efficiency.

5.1 Electron Isolation

In this section the different isolation working points were compared. The study was done using the *Tight* electron quality.
The isolation study is based on the measurement of two classes of electron isolation

variables [51] (similar to the muon isolation variables described in Chapter 4). The main variables are the following:

- $p_T^{varcone20}$: is the track isolation variable, defined as the sum of transverse momenta of all tracks, satisfying quality requirements, within a cone of $\Delta R = \min(0.2, 10 \text{ GeV}/E_T)$ around the candidate electron track and originating from the reconstructed primary vertex of the hard collision, excluding the electron associated tracks;
- $E_T^{topocone20}$: is the calorimetric isolation, defined as the sum of transverse energies of topological clusters, calibrated at the electromagnetic scale, within a cone of $\Delta R = 0.2$ around the candidate electron cluster. Only clusters with reconstructed positive energy are considered in the sum. The E_T contained in a rectangular cluster of size $\Delta\eta$ x $\Delta\phi = 0.125$ x 0.175 centered around the electron cluster barycentre is subtracted.

The implementation of isolation criteria is a trade off between a highly efficient identification of prompt electron and a good rejection of electrons from heavy flavor decay or light misidentified hadrons. Tab. 5.1 shows different electron isolation working points. The working points can be defined in two ways: targeting a fixed value of efficiency or with fixed cuts on the isolation variables.

Working Point	Calo. Isolation	Track Isolation
Gradient	$\epsilon = 0.1143$ x $p_T + 92.14\%$	$\epsilon = 0.1143$ x $p_T + 92.14\%$
GradientLoose	$\epsilon = 0.057$ x $p_T + 95.57\%$	$\epsilon = 0.057$ x $p_T + 95.57\%$
FCHighPtCaloOnly	$E_T^{cone20} < \max(0.015$ x p_T,3.5GeV)	-
FCLoose	$E_T^{cone20}/p_T < 0.2$	$p_T^{varcone20}/p_T < 0.15$
FCTight	$E_T^{cone20}/p_T < 0.06$	$p_T^{varcone20}/p_T < 0.06$
FCTightTrackOnly	-	$p_T^{varcone20}/p_T < 0.06$

TABLE 5.1: Definition of the electron isolation working points. In the Gradient and GradientLoose working point definitions the unit of p_T is GeV.

The Gradient working point has an efficiency of 90% at $p_T = 25$ GeV and 99% at $p_T = 60$ GeV; the GradientLoose working point has an efficiency of 95% at $p_T = 25$ GeV and 99% at $p_T = 60$ GeV.

5.1.1 Electron Isolation in the $t\bar{t}$ resonance analysis

This study is done using the ATLAS Top analysis framework. Only Monte Carlo referred to 2015+2016 dataset (36.1 fb^{-1}) simulated samples are used: the $t\bar{t}$ dilepton sample as the main background; the $t\bar{t}$ no all hadronic sample ($t\bar{t}$ events for which at least one of the W bosons decays leptonically) as fakes (described later); Z', g_{KK} and G as simulated signals.

Electron candidates are required to have transverse momentum $p_T > 25$ GeV and $|\eta| < 2.5$. The region $1.37 \leq |\eta| \leq 1.52$ is excluded because it corresponds to a transition region between the barrel and end-cap calorimeters that has a degraded energy resolution. The electrons are required to satisfy the $Tight$ quality selection. Jets are reconstructed using the anti-k_t algorithm (R = 0.4). Only jets with $p_T >$ 25 GeV and $|\eta| < 2.5$ are considered.
In the standard configuration used for the ATLAS analyses the working point *Gradient* or *GradientLoose* are used, but there are other four working points (listed in Tab. 5.1) that are recommended from the Electron-Gamma ATLAS group: *FCLoose*, *FCTight*, *FCHighPtCaloOnly* and *FCTightTrackOnly*. For this reason, I compared the performance of using electrons selected with different working points, to find the best setup for my analysis.
The comparison was made observing the isolation efficiency (defined as the ratio between the electrons that pass the isolation and the total number of electrons) versus the leading lepton p_T of the various samples described before. Given that the ΔR distance between the electron and its nearest jet is a key variable for the search I presented in this thesis, this variable is also shown in the following.
Fig. 5.1 and Fig. 5.2 show, for *eμ-channel* and *ee-channel* respectively, the isolation efficiencies as obtained considering electrons object selected with different working points, for the samples used: the main background $t\bar{t}$ dilepton, the events where there is a non-reconstructed lepton or where a light jet is reconstructed as a lepton (referred as *fakes*) and some examples of signals samples (all isolation efficiency plot for the signal samples are shown in Appendix B.
The plots show that the *FCTightTrackOnly* working point has the better isolation efficiency ($\sim 99\%$) in all p_T range of leading electron. Despite the performance for electrons selected using the *FCTightTrackOnly* working point being slightly better,

the no-isolated electron is used for the analysis. This is a compromise between careful evaluation of the performance and uncertainties and readiness of the complete study at the time of the publication of this analysis.

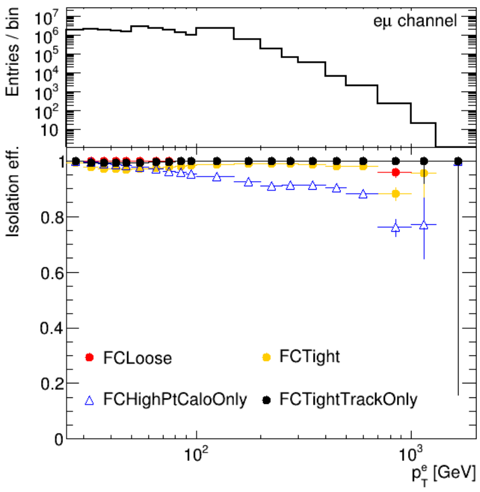

(a)

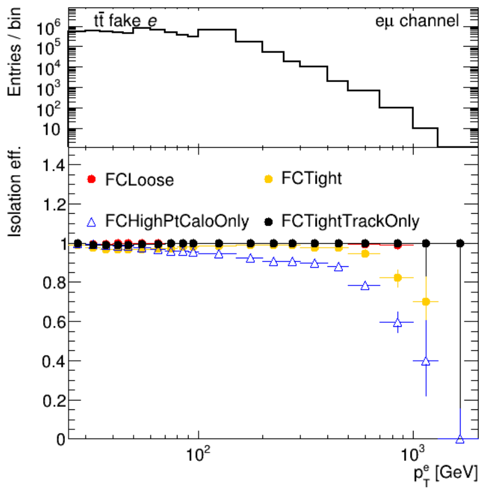

(b)

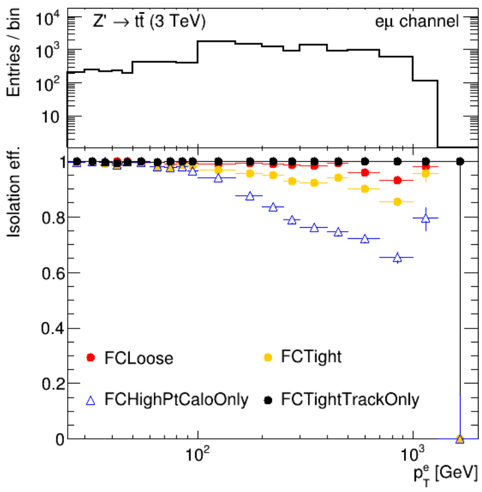

(c)

FIGURE 5.1: Comparison between different isolation efficiencies, for the *eμ-channel*, for $t\bar{t}$ dilepton (a), $t\bar{t}$ fake (b), SSM Z' with a mass of 3 TeV (c). The upper part of the plots show the trend of the events.

In addition, the isolation efficiency of the other working points in the plots decreases at high p_T, especially for signal models characterised by a high mass of the Z' boson. So it is not useful in a high-p_T region analysis.

In this analysis I chose not to use any isolation requirement for the electrons. This choice introduces some more background events but the amount of them is negligible

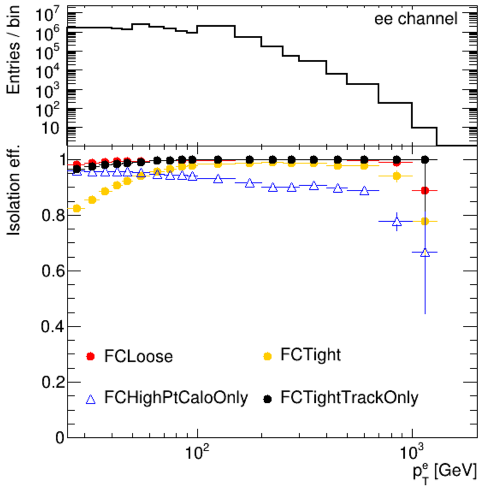

(a)

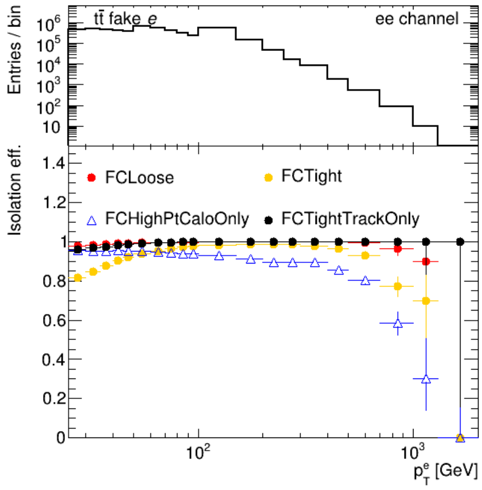

(b)

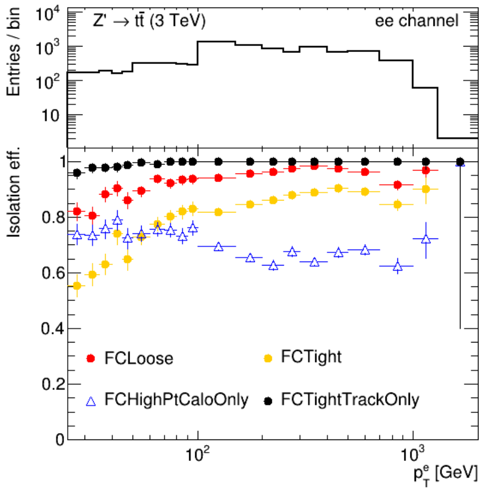

(c)

FIGURE 5.2: Comparison between different isolation efficiencies, for the *ee-channel*, for $t\bar{t}$ dilepton (a), $t\bar{t}$ fake (b), SSM Z' with a mass of 3 TeV (c). The upper part of the plots show the trend of the events.

in the dilepton channel, so it is a good compromise for my setup. Moreover, the increase in the signal acceptance is shown in Fig. 5.3. These plots are related to the leading electron in the $ee - channel$. Signal events are multiplied by a factor of 10000 only to aid observation in the plots.

Finally, the effectiveness of the choice is confirmed from the increase of the signal/background ratio in Tab. 5.2, that shows the comparison between the standard configuration and the configuration used in my dilepton analysis. The background

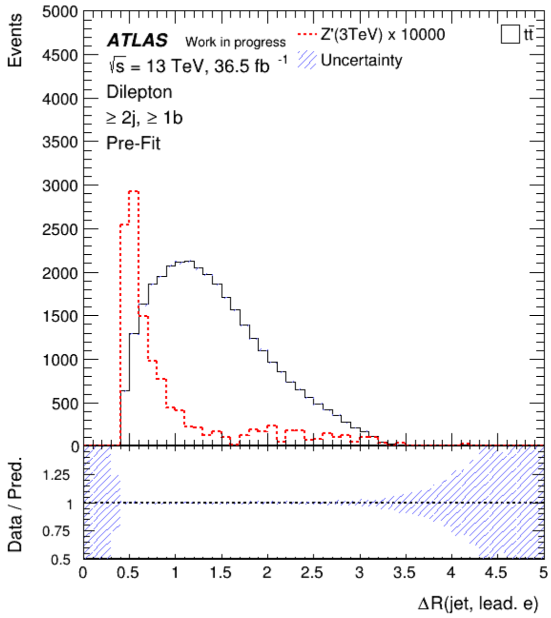

(a)

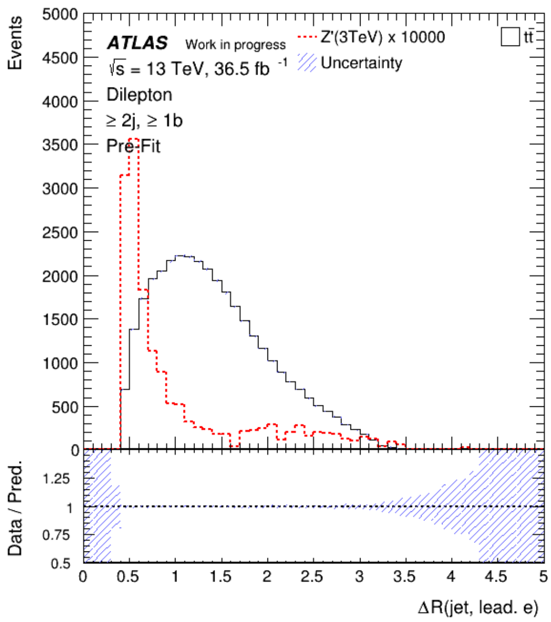

(b)

FIGURE 5.3: Comparison between the standard isolation working point configuration (a) and my setup without any electron isolation (b). The main background $t\bar{t}$ dilepton is in white and the dashed red is the Z' signal sample. Only statistical uncertainty.

under study was only the SM $t\bar{t}$ and the fakes come from $t\bar{t}$ events; the QCD multi-jet background was not taken into account because, in the dilepton analysis, events with two or more fake leptons are negligible.

	$Gradient$	$No-isolation$
$t\bar{t}$ background	504411	568199
Z' (3 TeV)	661	950
$\frac{S}{\sqrt{S+B}}$	0.93	1.26

TABLE 5.2: Comparison of background and signal sample and the signal-background ratio between the standard isolation configuration (using *Gradient* working point) and the setup configuration used in this analysis (without any electron isolation).

5.2 Extension of the Overlap Removal procedure

After finding the best setup for the electron isolation, the next step was to extend the Overlap Removal (OR) procedure [72] in my analysis. The overlap removal studies for electrons have been carried on specifically in the dilepton-channel analysis context, while in the case of muons the outcomes of previous studies performed for the lepton + jet channel analysis [29] have been considered and applied.
The standard configuration in the top pair measurements rejects electrons close to jets ($\Delta R_{el,jet} < 0.4$), but for this analysis I need a different requirement because in the high p_T-region the electrons tend to be close to jets and I want to keep electrons information. In this section I will describe the Overlap Removal extension procedure for the electrons close to jets ($0.2 < \Delta R_{el,jet} < 0.4$). The OR procedure was fully described in Section 3.5.

5.2.1 Electrons

In this analysis, since many signal events are in a boosted regime, where the lepton originating from the top-quark decay tends to be close to the b-jet, we want to keep precisely both the lepton and the jet, recovering electrons in the region $0.2 < \Delta R < 0.4$ but without double-counting their energy and that of their close-by jet.
As mentioned in the beginning of this section, I investigated the OR procedure to verify any improvements for the analysis. The modified jet-in-electron OR procedure is described in the following.
If an electron is reconstructed within $\Delta R < 0.4$ from a jet, the electron four-momentum is subtracted from the jet one. If the jet p_T after the subtraction is below a certain threshold, the reconstructed jet is assumed to come from the energy deposit of the electron itself, and the jet is removed from the event [1]. If the jet survives this selection, the ΔR between the electron and the corrected jet is recalculated: if $\Delta R < 0.2$, the electron is removed from the collection, because it is interpreted as a non-prompt electron from a heavy-flavor hadron decay, and its four-momentum is re-added to the jet one; otherwise, both the electron and the reduced jet are recognised as independent and are kept in the analysis. Such OR

[1] The threshold is not zero, because of the difference in the particle calibrations. Moreover, if the el-subtracted jet p_T is below the p_T threshold, the jet is rejected

procedure is expected to improve the acceptance for $X \to t\bar{t}$ events with large $m_{t\bar{t}}$ values, by keeping a larger fraction of high-p_T electron-b-jet pairs coming from a single high-p_T top quark.

This procedure is applied in order to keep or remove the electrons and jets with $\Delta R < 0.4$ in $t\bar{t}$ events; for each jet if there is an electron within a radius of $\Delta R < 0.4$ it is subtracted from the four-momentum jet to obtain a subtracted-jet-four-momentum: if this subtracted jet fails the p_T cut is removed, if the jet passes the p_T cut and the angular distance is ΔR(electron, subtracted jet) > 0.2 then both the electron and the jet are recognised as independent and are kept in the measurements; instead, if the jet passes the p_T cut but the angular distance is ΔR(electron, subtracted jet) < 0.2, it assumed that the electron is a b-jet decay product and is not counted as a prompt electron.
To improve the measurements presenting in this thesis, the OR procedure I developed is compared with the standard one used in $t\bar{t}$ cross-section measurements. I extended the procedure by including the electron-in-jet subtraction described before. The results of these studies will be described in section 5.3.

5.2.2 Muons

In the dilepton analysis the information about muons close to jets is needed (for the $\mu\mu-channel$ and the muon in $e\mu-channel$); for this reason the $BoostedSlidingDrMu$ procedure is used, as explained in the following: the ΔR depends on the muon p_T and tends to be zero for high-p_T muons; with this procedure, in a similar way described before for the electron case, the region $\Delta R(\mu, jet) < 0.4$ (where the muon is really close to the jet or b-jet) is taken into account and the muon is not rejected from the collection. Moreover, the effectiveness of the procedure is confirmed by the reconstruction efficiencies measured for muons close to jets, described in Chapter 4. This part was performed by the $lepton + jets$ analysis and this study confirms that also in the dilepton analysis the $BoostedSlidingDrMu$ procedure works better than the standard procedure.

5.3 Isolation and overlap removal studies for electrons and muons: results

This study is done using the ATLAS Top analysis framework. Only Monte Carlo referred to 2015+2016 dataset (36.1 fb^{-1}) simulated samples are used: the $t\bar{t}$ dilepton sample as the main background, the $t\bar{t}$ no all hadronic sample as fakes and Z' with $m_{Z'} = 3$ TeV as simulated signals.

The simulated samples are listed in Appendix B.
In the ATLAS top pair measurements there are some standard setup: the *Gradient* working point for both electron and muons is used and also the standard overlap removal, as described above, is done for $\Delta R(\ell, jet) > 0.4$.
In my analysis, instead, lepton closest to jets information are relevant, for this reason a comparison between the standard configuration and the dilepton analysis configuration is done.
As in the previous study about the isolation, the electron candidates are required to have transverse momentum $p_T > 25$ GeV and $|\eta| < 2.5$. The region $1.37 \leq |\eta| \leq 1.52$ is excluded. The electrons are required to satisfy the *Tight* quality selection. Moreover, muon candidates are required to have transverse momentum $p_T > 25$ GeV and $|\eta| < 2.5$. The muons are required to satisfy the *Medium* quality selection. The *FixedCutTightTrackOnly* isolation criteria was used. Jets are reconstructed using the anti-k_t algorithm (R = 0.4). Only jets with $p_T > 25$ GeV and $|\eta| < 2.5$ are considered.

The differences between the standard configuration, defined by:

- *Gradient* isolation working point both for electrons and muons;
- Default Overlap Removal ($\Delta R > 0.4$) procedure both for electrons and muons;

and the configuration used for the dilepton analysis, defined by:

- No electron isolation;

- $FixedCutTightTrackOnly$ working point muon isolation;
- $El - in - jet - subtraction$ OR ($0.2 < \Delta R < 0.4$) procedure for electrons;
- $BoostedSlidingDRMu$ OR ($\Delta R < 0.4$) procedure for muons;

are shown in Fig. 5.4, Fig. 5.5, Fig. 5.6 and Fig. 5.7 for $ee - channel$, $\mu\mu - channel$ and electrons and muons in $e\mu - channel$, respectively. Signal events are multiplied by a factor of 1000 only to aid observation in the plots.
The samples used for this study and shown in the plots are the SM $t\bar{t}$ dilepton and Z' $m_{Z'} = 3$ TeV. In all plots the error is only statistical.
The ΔR distribution for electrons in the $ee-channel$ and $e\mu-channel$ shows a double peak. The second peak contains events where the electron is correctly matched. The first peak, instead, is connected with different effects: the first effect is that the presence of the jet disturbs the electron identification and therefore there is a loss of efficiency; the second effect is that the electron-in-jet-4-momentum subtraction, even if the jet survives, causes a recalculation of the ΔR.

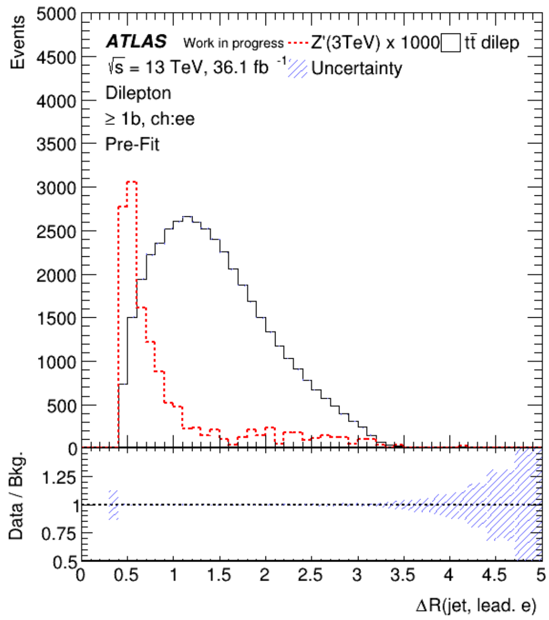

(a)

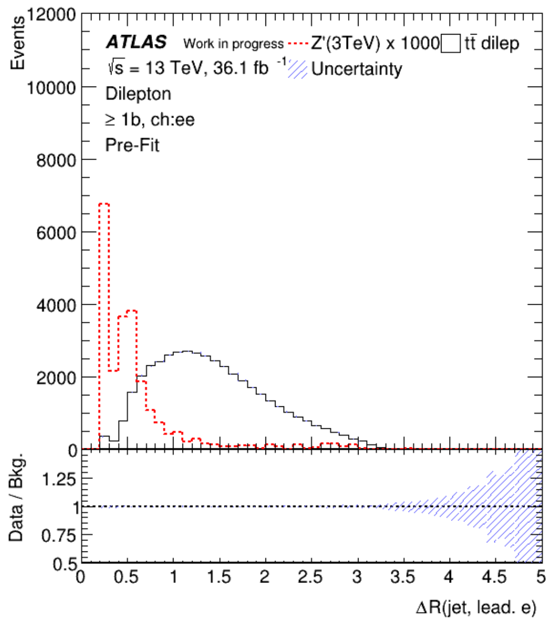

(b)

FIGURE 5.4: Comparison between the standard configuration (*Gradient* isolation and standard OR for electrons) (a) and this analysis configuration (No electron isolation and $Electron-in-Jet-subtraction$ OR for electrons) (b). In white the $t\bar{t}$ dilepton background and in dashed red the signal (Z' with $m_{Z'} = 3$ TeV). The plots are for $ee-channel$ of the leading electron. Only statistical uncertainty.

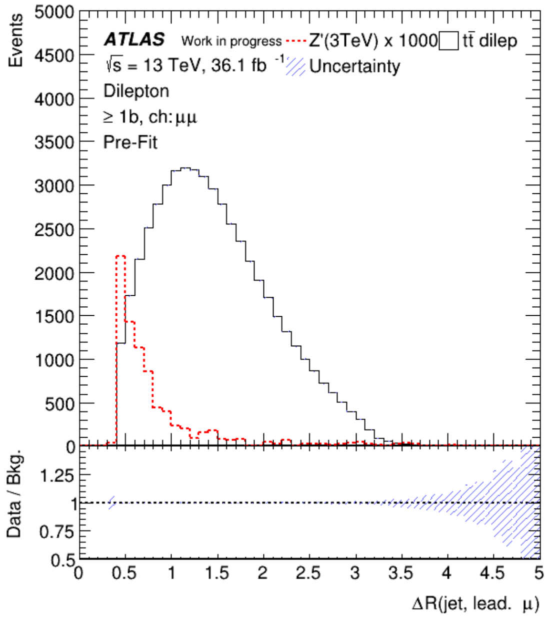

(a)

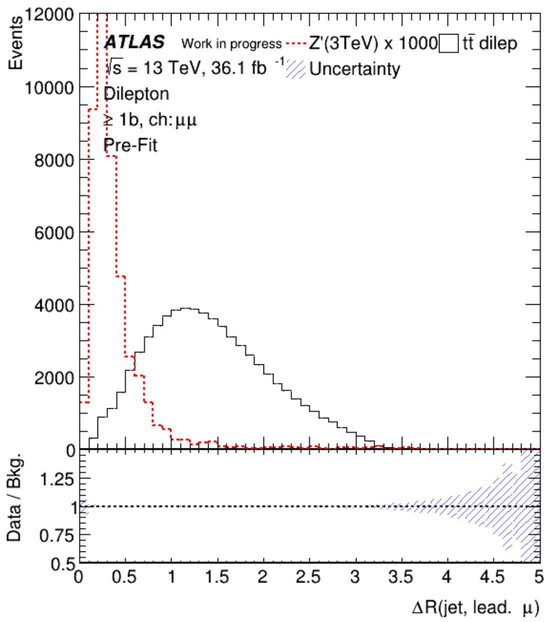

(b)

FIGURE 5.5: Comparison between the standard configuration (*Gradient* isolation and standard OR for muons) (a) and this analysis configuration (*FixedCutTightTrackOnly* muon isolation in addition to *BoostedSlidingDrMu* OR for muons) (b). In white the $t\bar{t}$ dilepton background and in dashed red the signal (Z' with $m_{Z'} = 3$ TeV). The plots are for $\mu\mu-channel$ of the leading muon. Only statistical uncertainty.

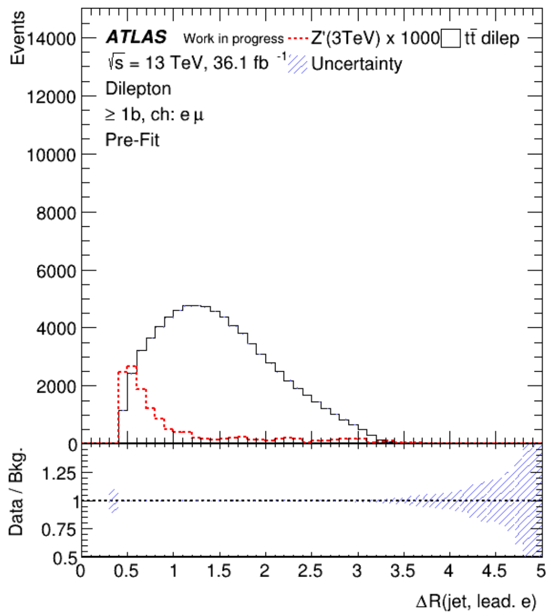

(a)

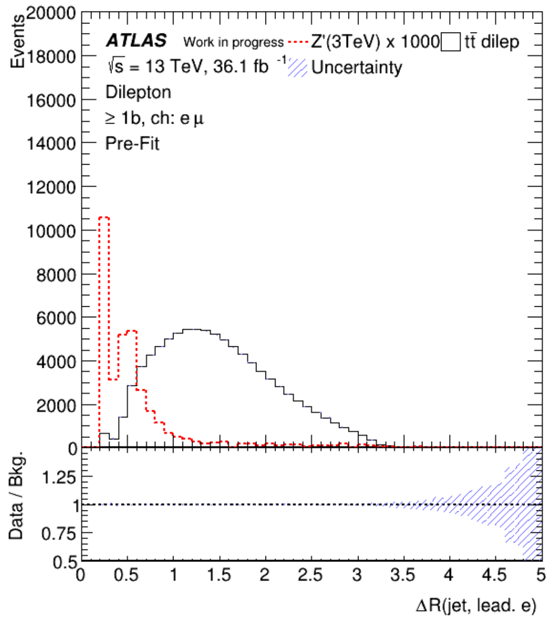

(b)

FIGURE 5.6: Comparison between the standard configuration (*Gradient* isolation and standard OR for both electrons and muons) (a) and this analysis configuration (No electron isolation and *FixedCutTightTrackOnly* muon isolation in addition to $Electron - in - Jet - subtraction$ and *BoostedSlidingDrMu* for electron and muons, respectively) (b). In white the $t\bar{t}$ dilepton background and in dashed red the signal (Z' with $m_{Z'} = 3$ TeV). The plots are for the electron in $e\mu - channel$. Only statistical uncertainty.

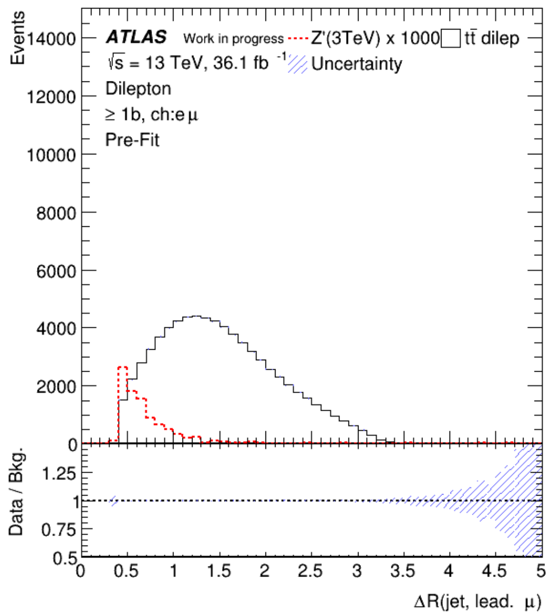

(a)

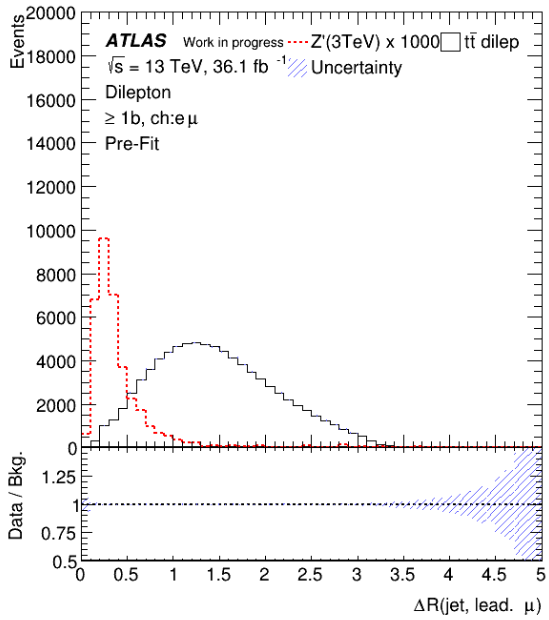

(b)

FIGURE 5.7: Comparison between the standard configuration (*Gradient* isolation and standard OR for both electrons and muons) (a) and this analysis configuration (No electron isolation and *FixedCutTightTrackOnly* muon isolation in addition to $Electron - in - Jet - subtraction$ and $BoostedSlidingDrMu$ for electron and muons, respectively) (b). In white the $t\bar{t}$ dilepton background and in dashed red the signal (Z' with $m_{Z'}$ = 3 TeV). The plots are for the muon in $e\mu - channel$. Only statistical uncertainty.

These plots show that the configuration used for my analysis can recover many events in the lepton-close-to-jet region. The effectiveness of my configuration can be confirmed in Tab. 5.3, that shows the signal/background ratio between the two different configurations. It is possible to see also that there is a satisfying increase of the signal sample events using this analysis configuration, specially in the $\mu\mu - channel$.

Channel:	Z' events	$t\bar{t}$	Fake	$\frac{S}{\sqrt{S+B}}$
$ee - channel$	$m_{Z'} = 3$ TeV			
Default OR	777	2082918	594265	0.47
Dilepton OR	1277	2349108	697985	0.73
$e\mu - channel$	$m_{Z'} = 3$ TeV	$t\bar{t}$	Fake	$\frac{S}{\sqrt{S+B}}$
Default OR	1113	4634558	1317518	0.45
Dilepton OR	3435	5503025	1614445	1.29
$\mu\mu - channel$	$m_{Z'} = 3$ TeV	$t\bar{t}$	Fake	$\frac{S}{\sqrt{S+B}}$
Default OR	416	2538907	720284	0.23
Dilepton OR	2325	3192341	926846	1.15

TABLE 5.3: Number of Z' signal events, the $t\bar{t}$ dilepton and fake backgrounds and the signal-background ratio for the three channels decay and in two different configuration: the standard configuration and the analysis configuration, referred as "Dilepton".

Finally, also the fake information is taken into account. Fig. 5.8 shows the comparison between the two different configuration for the leading electron in $ee - channel$. It is possible to see that in all these plots, the fake quantity increases with the dilepton analysis configuration; this is not a problem because the fake rate is not so big and, moreover, other background cuts will be applied (as will be described in Chapter 6). All these studies, confirmed from the tables, assert that this configuration is the best choice for the subsequent steps regarding the measurement of invariant masses and signal limits.

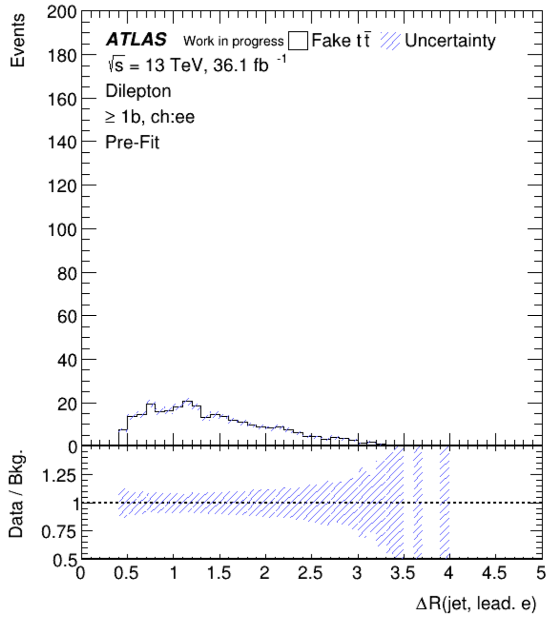

(a)

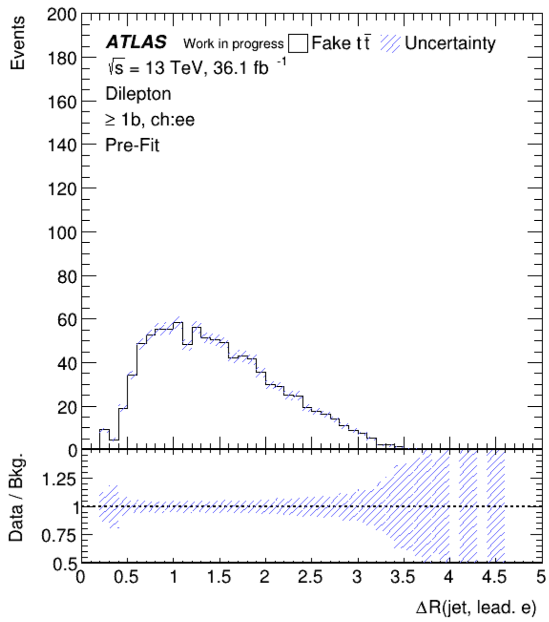

(b)

FIGURE 5.8: Comparison between the standard configuration (*Gradient* isolation and standard OR for electrons) (a) and this analysis configuration (No electron isolation and $Electron - in - Jet - subtraction$ OR for electrons) (b) for fake events. The plots are for $ee - channel$ of the leading electron. Only statistical uncertainty.

Chapter 6

Search for a $t\bar{t}$ resonance in the dilepton channel

In this chapter the last part of my analysis is shown. A search for $t\bar{t}$ resonances is described, performed in the dilepton final state and considering the full pp collision dataset collected by ATLAS at $\sqrt{s} = 13$ TeV, corresponding to 139 fb^{-1} of integrated luminosity. The analysis strategy is based on the combination of two observables, one carrying information on the $t\bar{t}$ invariant mass (either the complete reconstructed invariant mass or a partial invariant mass variable, referred to as "invariant mass proxy" in the following) and one sensitive to the $t\bar{t}$ spin correlation (e.g. the angular separation between the two charged leptons in the transverse plane, $\Delta\phi^{\ell\ell}$). In the dilepton final state, high-mass resonances tend to produce leptons close to b-jets, making the setup described in the previous two chapters for muon and electron selection essential for the sensitivity of the analysis to multi-TeV signals. As described in Chapter 1, the BSM models under study in this are the neutral heavy gauge boson Z', the Randall-Sundrum graviton G and the Kaluza-Klein gluon g_{KK}.

This chapter will describe the event selection, the used Monte Carlo simulations, the analysis strategy, the considered systematic uncertainties and finally the expected sensitivity evaluation. Exclusion limits are set on the production cross-section times branching ratio for hypothetical Z' bosons, Randall-Sundrum graviton and Kaluza-Klein gluons, that decay into top quark pairs. Only expected exclusion limits obtained from simulation are reported at the end of the chapter, because at the moment of the writing of this thesis the data are still blinded, so the data in the relevant signal regions cannot be used in any of the steps of the analysis, until all the aspects of the analysis setup are finalised.

6.1 Event selection

The event selection is used to maximize the signal sensitivity and in order to be complementary to other $t\bar{t}$ resonance channels [29] [73]. The $t\bar{t}$ final state is quite complex. The top quarks decay nearly 100% of times in a W boson and a bottom quark. The W boson decays into a lepton and neutrino pair or in a quark anti-quark pair. Requiring dilepton $t\bar{t}$ decays, we expect exactly two leptons and missing transverse energy due to two escaping neutrinos and jets. The decay products should have high transverse momenta, because the mass of the resonance particles is of the order of several top quark masses. I consider only reconstructed electrons and muons. To select the reconstructed objects (jets, lepton and E_T^{miss}), the following criteria have been applied.
As first criterion, events of interest are required to have exactly two opposite-sign charged leptons (electrons or muons). Of this two, at least one is required to match, within $\Delta R < 0.05$, the lepton with the same flavour reconstructed by the trigger algorithm.
The main backgrounds are: the SM $t\bar{t}$ dilepton, the $Z + jets$, the $diboson$, and the $single - top$ processes. A fully description about these backgrounds is described in Section 6.4. Tab. 6.1 shows the amount of event backgrounds for each channel before the selections.

TABLE 6.1: Percentage of the event backgrounds in each channel before the selection cuts.

channel	ee $\geq$ 1 b [%]	e$\mu \geq$ 1 b [%]	$\mu\mu \geq$ 1 b [%]
$t\bar{t}$ dilep.	~39.4	~94	~37.2
Single top	~1.8	~4.2	~1.7
Z+jets	~56.5	~0.2	~59.3
Diboson	~1.4	~0.3	~1.4
$t\bar{t} + V$	~0.3	~0.2	~0.2
Fakes	~0.6	~0.8	~0.1

In both ee and $\mu\mu$ channels, the dilepton invariant mass ($m_{\ell\ell}$) must be above 15 GeV, to reject Drell-Yan processes and outside the Z-boson mass window 80-100 GeV, to reduce the Z+jets background. A single lepton trigger is used and the lepton (both electron and muon) passes the threshold if $p_T > 27$ GeV.
Moreover, the Z+jets background is further reduced throught a cut in the Missing Transverse Energy, MET > 45 GeV.

Electron candidates are required to:

- satisfy transverse momentum $p_T > 25$ GeV;
- satisfy pseudorapidity $|\eta| < 2.5$. The region $1.37 \leq |\eta| \leq 1.52$ is excluded because it corresponds to a transition region between the barrel and end-cap calorimeters that has a degraded energy resolution;
- satisfy the $Tight$ quality selection;
- not pass any electron isolation criterion;
- the electron-in-jet-subtraction OR procedure is used (electron in $0.2 < \Delta R(el, jet) < 0.4$ region).

Muon candidates are required to:

- satisfy transverse momentum $p_T > 25$ GeV;
- satisfy pseudorapidity $|\eta| < 2.5$;
- Be within $d_0/\sigma_{d_0} < 3$ and $|z_0 sin\theta| < 0.5$ cm;
- satisfy the $Medium$ quality selection;
- passes the $FixedCutTightTrackOnly$ isolation criteria (only the track isolation requirement $p_T^{varcone30}/p_T < 0.06$);
- The $BoostedSlidingDRMu$ OR procedure was used (muon in $\Delta R < 0.4$ region).

Jets are reconstructed using the anti-k_t algorithm (R = 0.4) and satisfy the quality and kinematic criteria discussed in Chapter 3. These jets are then calibrated to the hadronic energy scale [74], using p_T and η dependent correction factors obtained during simulation. The jet position is corrected to the primary vertex. Only jets with $p_T > 25$ GeV and $|\eta| < 2.5$ are considered. In this analysis a multivariate b-tagging with a 77% tagging efficiency (mv2c10 @77%) is used and requires ≥1 b-jet.
The Jet Vertex Tagger (JVT) tool, to discard jets with 20 GeV $< p_T <$ 50 GeV, is used; this tool is useful to suppress jets from pileup interactions and it guarantees a valid measurement of the E_T^{miss}.

A summary of the event selection is shown in Tab. 6.2.

Table 6.2: Summary of the object selection.

Object	Kinematics	Type/Quality
Electron	$p_T > 25$ GeV $\|\eta\| < 2.5$ exclude $1.37 \leq \|\eta\| \leq 1.52$	$No-isolation$ $Tight$ $el-in-jet$ subtraction
Muon	$p_T > 25$ GeV $\|\eta\| < 2.5$	$FCTightTrackOnly$ $Medium$ $BoostedSlidingDRMu$ subtraction
Jet	$p_T > 25$ GeV $\|\eta\| < 2.5$ ≥ 1 b-jet	anti-k_t R = 0.4 JVT 20 GeV $< p_T <$ 50 GeV mv2c10 @77%
MET	$E_T^{miss} > 45$ GeV	

6.2 Analysis strategy and setup

Following the event selection, a two-dimensional scan is performed on an observable correlated with invariant mass of the $t\bar{t}$ system ($m_{t\bar{t}}$) and an observable sensitive to the $t\bar{t}$ spin correlation. Data are compared to the SM expectation resulting from MC simulated events for the main expected background ($t\bar{t}$, single-top, Z/W+jets and diboson). In the absence of significant excesses, limits are set on the cross-section times branching ratio to $t\bar{t}$ for new physics resonances according to the different signal models discussed in Chapter 1.
The considered $t\bar{t}$-spin-correlation sensitive variable is $\Delta\phi^{\ell\ell}$, the angular separation

between the two selected charged leptons in the transverse plane. The variable is computed in the laboratory frame.

The considered proxies for the $m_{t\bar{t}}$-related observable are: the invariant mass of the two charged leptons and the two b-jets (m_{llbb}); the transverse invariant mass of the two charged leptons, the two b-jets and the MET ($M_{T,t\bar{t}}$); finally, the invariant mass of the $t\bar{t}$ system ($m_{t\bar{t}}^{NW}$) reconstructed through the neutrino weighting method [75]. These variables will be further described in the following sections.
The exclusion limits are derived from a 2-dimensional fit: the considered invariant-mass variable is divided into a number of bins and in each of these bins the $\Delta\phi^{\ell\ell}$ distribution is exploited, effectively performing a simultaneous fit of 10 $\Delta\phi^{\ell\ell}$ distributions. The chosen bin number and size are based on the available simulated sample and expected data sample statistics (as shown in the next sections). Tab. 6.3, Tab. 6.4 and Tab. 6.5 show the various signal simulations used in this analysis; they are related to seven mass regions of Z', nine mass regions of g_{KK} and five mass regions of G, respectively. The number of events are considered before the different selections and selections carried in the analysis setup.
This analysis is done using the ATLAS Top analysis framework with full Run2 data (from 2015 to 2018) produced by LHC with a center-of-mass energy of $\sqrt{s} = 13$ TeV, and Monte Carlo simulated samples referred to the full Run2 dataset, representing a total integrated luminosity of 139 fb^{-1}. The MC samples are splitted because each distribution is simulated with pileup conditions similar to those in the corresponding dataset.

TABLE 6.3: List of Z' MC signal samples.

DSID	Process	Generator	Signal mass [TeV]	Events
301323	$Z' \to t\bar{t}$	PYTHIA8	$m_{Z'} = 0.5$	200000
301324	$Z' \to t\bar{t}$	PYTHIA8	$m_{Z'} = 0.75$	200000
301325	$Z' \to t\bar{t}$	PYTHIA8	$m_{Z'} = 1$	300000
301327	$Z' \to t\bar{t}$	PYTHIA8	$m_{Z'} = 1.5$	200000
301329	$Z' \to t\bar{t}$	PYTHIA8	$m_{Z'} = 2$	200000
301333	$Z' \to t\bar{t}$	PYTHIA8	$m_{Z'} = 3$	300000
301334	$Z' \to t\bar{t}$	PYTHIA8	$m_{Z'} = 4$	200000

TABLE 6.4: List of g_{KK} MC signal samples.

DSID	Process	Generator	Signal mass [TeV]	Events
307522	$g_{KK} \to t\bar{t}$	PYTHIA8	$m_{g_{KK}} = 0.5$	58051
307523	$g_{KK} \to t\bar{t}$	PYTHIA8	$m_{g_{KK}} = 1$	67772
307524	$g_{KK} \to t\bar{t}$	PYTHIA8	$m_{g_{KK}} = 1.5$	72268
307527	$g_{KK} \to t\bar{t}$	PYTHIA8	$m_{g_{KK}} = 2$	74804
307528	$g_{KK} \to t\bar{t}$	PYTHIA8	$m_{g_{KK}} = 2.5$	75699
307529	$g_{KK} \to t\bar{t}$	PYTHIA8	$m_{g_{KK}} = 3$	75248
307530	$g_{KK} \to t\bar{t}$	PYTHIA8	$m_{g_{KK}} = 3.5$	74694
307531	$g_{KK} \to t\bar{t}$	PYTHIA8	$m_{g_{KK}} = 4$	73840
307532	$g_{KK} \to t\bar{t}$	PYTHIA8	$m_{g_{KK}} = 4.5$	72800

TABLE 6.5: List of G MC signal samples.

DSID	Process	Generator	Signal mass [TeV]	Events
305012	$G \to t\bar{t}$	MADGRAPH+PYTHIA8	$m_G = 0.4$	60492
305013	$G \to t\bar{t}$	MADGRAPH+PYTHIA8	$m_G = 0.5$	67311
305014	$G \to t\bar{t}$	MADGRAPH+PYTHIA8	$m_G = 0.75$	75887
305015	$G \to t\bar{t}$	MADGRAPH+PYTHIA8	$m_G = 1$	78697
305016	$G \to t\bar{t}$	MADGRAPH+PYTHIA8	$m_G = 2$	88066

6.3 Top pair invariant mass reconstruction

As mentioned before, different alternative observables carrying information on the $t\bar{t}$ invariant mass can be used. The presence of two undetected neutrinos from the leptonic decays of the two top quarks makes the reconstruction of such invariant mass non-trivial: either special reconstruction techniques have to be used to obtain the missing information on the two neutrinos (such as the neutrino weighting, described in Section 6.3.1), or only a partial invariant mass observable can be used.

6.3.1 Neutrino weighting

The full invariant mass reconstruction of the $t\bar{t}$ system ($m_{t\bar{t}}^{NW}$) uses information about the charged leptons, the b-jets and the two neutrinos. While for charged leptons and b-jets one can rely on the precisely measured four-momenta from the detector, the only information about neutrinos comes from the measurement of the MET and its direction in the transverse plane. To reconstruct the neutrino information the Neutrino Weighting (NW) method is used.

Taking into account that the three particles (lepton, bottom and neutrino) must be reconstructed with the vertex towards their top quark, some constraints are applied to measure the invariant $t\bar{t}$ mass:

$$(\ell_1 + \nu_1)^2 = m_{W,1}^2 \quad \text{and} \quad (\ell_1 + \nu_1 + b_1)^2 = m_{t,1}^2 \tag{6.1}$$

$$(\ell_2 + \nu_2)^2 = m_{W,2}^2 \quad \text{and} \quad (\ell_2 + \nu_2 + b_2)^2 = m_{t,2}^2 \tag{6.2}$$

where $\ell_{1,2}$ represent the four-momenta of the two charged leptons, $b_{1,2}$ represent the four-momenta of the two b-jets, $\nu_{1,2}$ represent the four-momenta of the two neutrinos, $m_W = 80.4$ GeV is the W boson mass and $m_t = 172.5$ GeV is the top quark mass. The other constraints, required for $\nu_{1,2}$, are the pseudorapidities of the neutrino (anti-neutrino) $\eta(\nu)$ ($\eta(\bar{\nu})$) and, being these quantities unknown, a scale in

0.2 increments between -5 and 5 is used and only real solutions without imaginary terms are taken into consideration.
At this point, the E_T^{miss} terms measured by the NW tool are compared with the observed events and, subsequently, is applied a weight to quantify the agreement:

$$w = exp\left(\frac{-\Delta E_x^2}{2\sigma_x^2}\right) \cdot \left(\frac{-\Delta E_y^2}{2\sigma_y^2}\right) \tag{6.3}$$

where ΔE_x (ΔE_y) is the difference between the x (y) component of the missing transverse momentum computed from the neutrino four momenta and the observed one; σ_x (σ_y) is a fixed scale related to the resolution of the E_T^{miss} observed in the detector in the x (y) axis, based on Z boson events [76]. To reconstruct the top and antitop quarks the highest weights of $\eta(\nu)$ and $\eta(\bar{\nu})$ are used.
Some selected events contain more than two b-jets and this may lead to combinatorial problems; in such cases, the two b-jets are chosen among those with the highest weights measured by the b-tagging algorithm.

Unfortunately, the equation 6.1 cannot always be solved, due to a mis-measurement of the input objects four-momenta. This effect causes inefficiency in the invariant mass reconstruction, as shown in Fig. 6.1, where different signals and the $t\bar{t}$ dilepton SM sample are compared; in the first bin, that defines the mis-reconstruction, the inefficiency increases when the signal mass rises.

Tab. 6.6 shows the inefficiency of the invariant mass reconstruction using the neutrino weighting. For example, the efficiency ranges from ~60% for a Z' with mass of 4 TeV to ~88% for the same model with mass of 500 GeV.

6.3.2 Invariant mass proxies

The viable alternative approach to a full reconstruction of the $t\bar{t}$ system is to rely on observables that retain sensitivity to the mass of a signal by combining only transverse and/or directly detectable particle kinematic variables. In addition to the m_{tt}^{NW} other two invariant mass proxies are being studied:

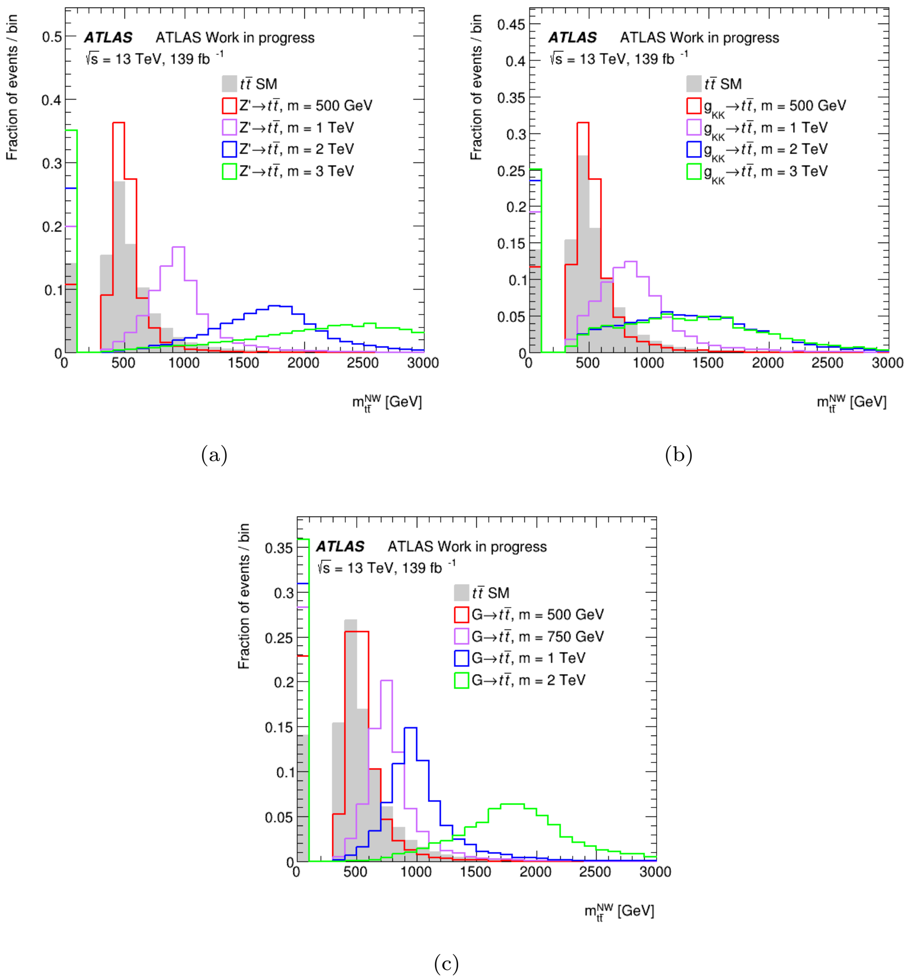

FIGURE 6.1: Invariant mass m_{tt} comparison between $t\bar{t}$ dilepton background and different mass signals: Z' (a), KK-gluon (b) and RS-Graviton (c).

- $m_{\ell\ell bb}$: the invariant mass of the system built using the two charged leptons and the two highest-p_T b-tagged jets, ordered in p_T;
- $M_{T,t\bar{t}}$: the transverse mass of the system built using the same object as for $m_{\ell\ell bb}$ plus the missing transverse momentum.

The first proxy, $m_{\ell\ell bb}$, is the momenta and energies of the two charged leptons and the two b-jets. The $m_{\ell\ell bb}$ can be written as:

$$m^2_{\ell\ell bb} = (E_{\ell_1} + E_{\ell_2} + E_{b_1} + E_{b_2})^2 - (\overrightarrow{p}_{\ell_1} + \overrightarrow{p}_{\ell_2} + \overrightarrow{p}_{b_1} + \overrightarrow{p}_{b_2})^2 \tag{6.4}$$

TABLE 6.6: Mis-measurement of reconstructed events using the neutrino weighting, compared with different simulated signal samples.

Sample	Mis-measurement [%]
SM $t\bar{t}$ dilepton	15
Data (full Run2)	15
Z' 500 GeV	12.5
Z' 750 GeV	19.2
Z' 1 TeV	22.8
Z' 2 TeV	29.4
Z' 3 TeV	35.6
Z' 4 TeV	40.2
G 400 GeV	20.9
G 500 GeV	24.8
G 750 GeV	31.8
G 1 TeV	34.1
G 2 TeV	39.1
g_{KK} 500 GeV	13.4
g_{KK} 1 TeV	21.9
g_{KK} 1.5 TeV	24.8
g_{KK} 2 TeV	25.9
g_{KK} 2.5 TeV	26.8
g_{KK} 3 TeV	27.4
g_{KK} 3.5 TeV	27.5
g_{KK} 4 TeV	27.5
g_{KK} 4.5 TeV	27.5

where E_{ℓ_1} ($\overrightarrow{p}_{\ell_1}$) is the energy (three-momentum) of the first charged lepton, E_{ℓ_2} ($\overrightarrow{p}_{\ell_2}$) is the energy (three-momentum) of the second charged lepton, E_{b_1} ($\overrightarrow{p}_{b_1}$) is the energy (three-momentum) of the first b-jet and E_{b_2} ($\overrightarrow{p}_{b_2}$) is the energy (three-momentum) of the second b-jet; moreover, in the case of events with only one b-tagged jet, this one and the highest-p_T non-b-tagged jet (because not always the jets are b-tagged as well) are taken into account to reconstruct the mass variable.
The second proxy $M_{T,t\bar{t}}$ tries to add to the previous variable some information about the escaping neutrinos, by incorporating the missing trasverse energy. The $M_{T,t\bar{t}}$ can be written as:

$$M^2_{T,t\bar{t}} = (E_{T,\ell_1}+E_{T,\ell_2}+E_{T,b_1}+E_{T,b_2}+E_T^{miss})^2-(\overrightarrow{p}_{T,\ell_1}+\overrightarrow{p}_{T,\ell_2}+\overrightarrow{p}_{T,b_1}+\overrightarrow{p}_{T,b_2}+\overrightarrow{p}_T^{miss})^2 \tag{6.5}$$

Holding information about neutrinos (from E_T^{miss}), $M_{T,t\bar{t}}$ proxy is prone to count in additional systematic uncertainties regarding MET which have to be taken into consideration.

These three variable masses are then used in the systematics measurements and signal research, in order to reconstruct the best expected signal mass limits.

6.4 Signal and background modelling

Signal and background predictions after the event selection are obtained through Monte Carlo simulated samples.
The dominant background is the Standard Model $t\bar{t}$ and it is simulated using POWHEG+PYTHIA8 [63] [67]. This is an irreducible background, with final states that is identical to those from BSM signal processes. In order to improve the prediction of highly boosted top quark kinematics, which can improve the agreement between the MC predictions and the data, a top p_T correction is applied to the simulated sample (as shown in the next subsection).
The second main background, in $ee-channel$ and $\mu\mu-channel$, is the $Z+jets$ and is simulated using SHERPA2.2.1 NLO [66]. It is a reducible background because the Z boson decay produces two charged leptons without MET; in this analysis the $Z+jets$ background was reduced through different methods, further described in the following section.
The other sources of backgrounds are: the *diboson* process (ZZ, W^+W^- and $ZW^{\pm}$), simulated using SHERPA2.2.1 NLO; the $single-top$ process simulated with POWHEG+PYTHIA8, and including the three production channels, $t-channel$, $s-channel$ and Wt (using the diagram-removal scheme to avoid double counting of $t\bar{t}$) [71]. The $W+jets$ is simulated with SHERPA2.2.1 NLO; finally, the $t\bar{t}+V$ background ($t\bar{t}Z$, $t\bar{t}W$, tZ and tWZ samples) is simulated with MADGRAPH5_aMC@NLO+PYTHIA8 [64].
The "fake lepton background", or simply "fakes", are events with only one prompt charged lepton (from a W or Z decay) with a non-prompt lepton that pass the dilepton event selection, and they are treated separately in the following. This category

includes the entire $W + jets$ and single-top s- and t- channels, as well as single-lepton $t\bar{t}$ and single top Wt events. Events with two non-prompt or fake leptons are negligible.

The Z' signal samples are simulated using PYTHIA8 for all the seven samples ($m_{Z'}$ = 500 GeV, 750 GeV, 1 TeV, 1.5 TeV, 2 TeV, 3 TeV and 4 TeV). The Kaluza-Klein gluon g_{KK} samples are simulated using PYTHIA8 for all the nine samples ($m_{g_{KK}}$ = 500 GeV, 1 TeV, 1.5 TeV, 2 TeV, 2.5 TeV, 3 TeV, 3.5 TeV, 4 TeV and 4.5 TeV). The Randall-Sundrum graviton G samples are simulated using MADGRAPH5_aMC@NLO+PYTHIA8.1 for all the five samples (m_G = 400 GeV, 500 GeV, 750 GeV, 1 TeV and 2 TeV).

6.4.1 Top p_T correction to NNLO-QCD + NLO-EW predictions

Recently, more and more accurate theoretical predictions have been released for the $t\bar{t}$ differential cross-section as a function of several quantities. In particular, calculations performed at NNLO in QCD, including NLO EW [77] effects have been released. These calculations predict a significantly softer top p_T spectrum than the NLO QCD fixed order calculations as well as the various MC "NLO+PS" implementations, like those used for the prediction of the $t\bar{t}$ events in this analysis. In addition, scale and PDF uncertainties on the prediction of the top p_T spectrum from these calculations are smaller than uncertainties of the same quantity derived by comparing different MC setups. Therefore, all $t\bar{t}$ MC simulation samples are corrected to match the parton-level top p_T spectrum as predicted by these calculations.

The reweighting is obtained, for each MC sample, as follows. The top parton four-momentum in $t\bar{t}$ simulation events is obtained from the last top quark replica in the MC record. Then a histogram is built with this top parton p_T for all the generated events, without the application of any event selection. This histogram, normalised to unity, is then compared with the histogram from the normalised differential cross-section prediction (using the prediction for the $p_{T,avg.}$), and the ratio between the two histograms is then used to derive a top-p_T dependent scale factor. This scale-factor is then applied to selected $t\bar{t}$ events according to the value of the top parton

p_T, as just defined. Fig. 6.2 shows the difference of the leading electron p_T before and after the p_T correction. Fig. 6.3, Fig. 6.4 show the leading lepton p_T and the ΔR between the leading lepton and its nearest jet; the variables shown are measured after the p_T correction. In all plots the MC predictions are absolute. All plots are labeled "Pre-Fit", this mean that these variables and their uncertainties are measured before the fit method (that will be described in Section 6.7).
Tab. 6.7 shows the list of all expected events for each background.

TABLE 6.7: Expected events for each background.

channel	ee $\geq$ 1 b [x10^3]	eμ $\geq$ 1 b [x10^3]	$\mu\mu$ $\geq$ 1 b [x10^3]
$t\bar{t}$ dilep.	190 $\pm$ 50	480 $\pm$ 70	287 $\pm$ 9
Single top	8.9 $\pm$ 2.7	22 $\pm$ 7	13 $\pm$ 4
Z+jets	60 $\pm$ 18	0.76 $\pm$ 0.23	100 $\pm$ 30
Diboson	2.6 $\pm$ 1.3	1.8 $\pm$ 0.9	3.9 $\pm$ 2.0
$t\bar{t}+V$	1.11 $\pm$ 0.33	1.07 $\pm$ 0.32	1.5 $\pm$ 0.5
Fakes	2.8 $\pm$ 0.8	3.8 $\pm$ 1.1	0.86 $\pm$ 0.26
Total	270 $\pm$ 50	510 $\pm$ 70	406 $\pm$ 32

In $ee-channel$ and $\mu\mu-channel$ the Z+jets background (orange) and the SM $t\bar{t}$ dilepton (white) are the largest contributions to the total backgrounds; the other backgrounds are single top (blue), diboson (yellow), $t\bar{t}+V$ (green) and the fakes (purple). In $e\mu-channel$ the main backgrounds are the SM $t\bar{t}$ dilepton (white) and the single top contribution (blue). The errors are both statistical and systematics, and the data are in agreement with the simulated predictions.

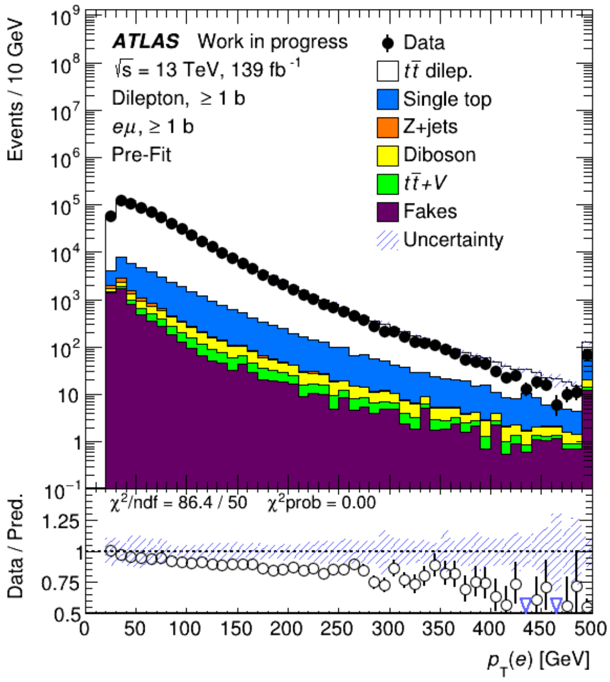

(a)

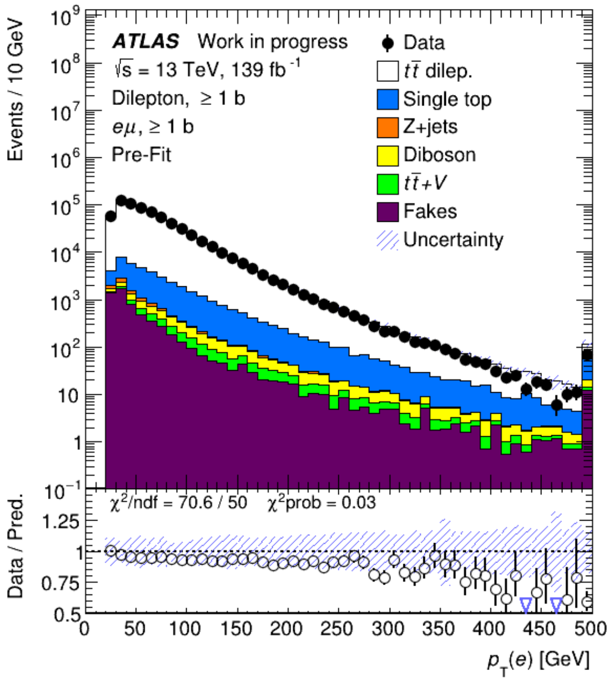

(b)

FIGURE 6.2: Difference in the leading electron p_T in $e\mu-channel$ before (a) and after (b) the p_T correction.

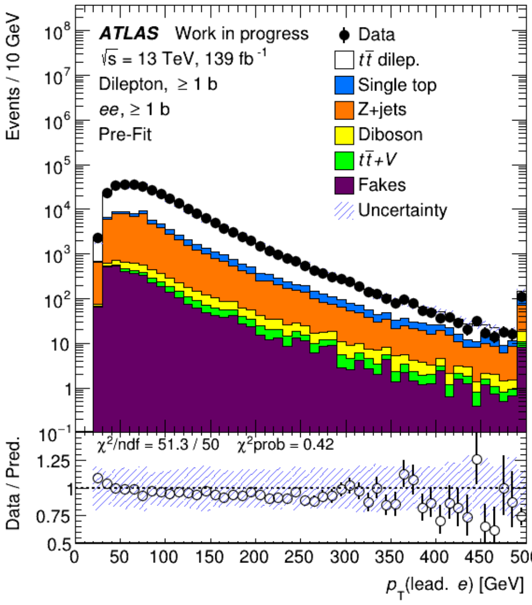

(a)

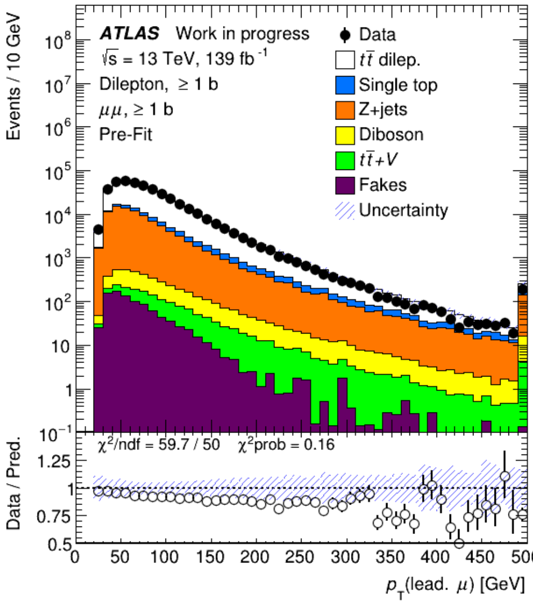

(b)

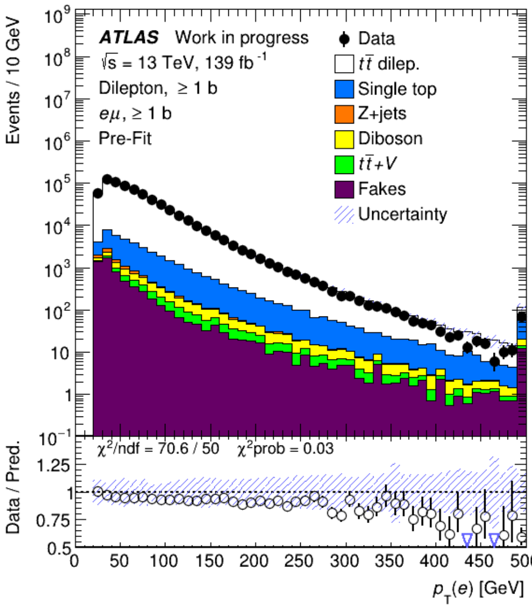

(c)

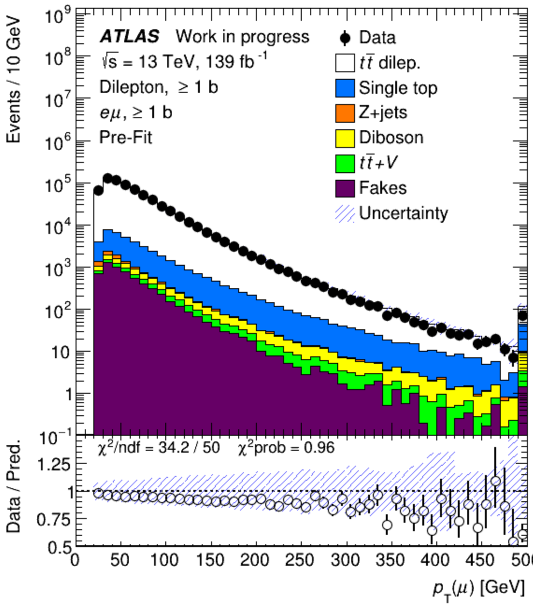

(d)

FIGURE 6.3: Transverse momentum of the leading lepton, after the p_T correction, in $ee-channel$ (a) $\mu\mu-channel$ (b) and $e\mu-channel$: electron (c) and muon(d). Errors are both statistical and systematics.

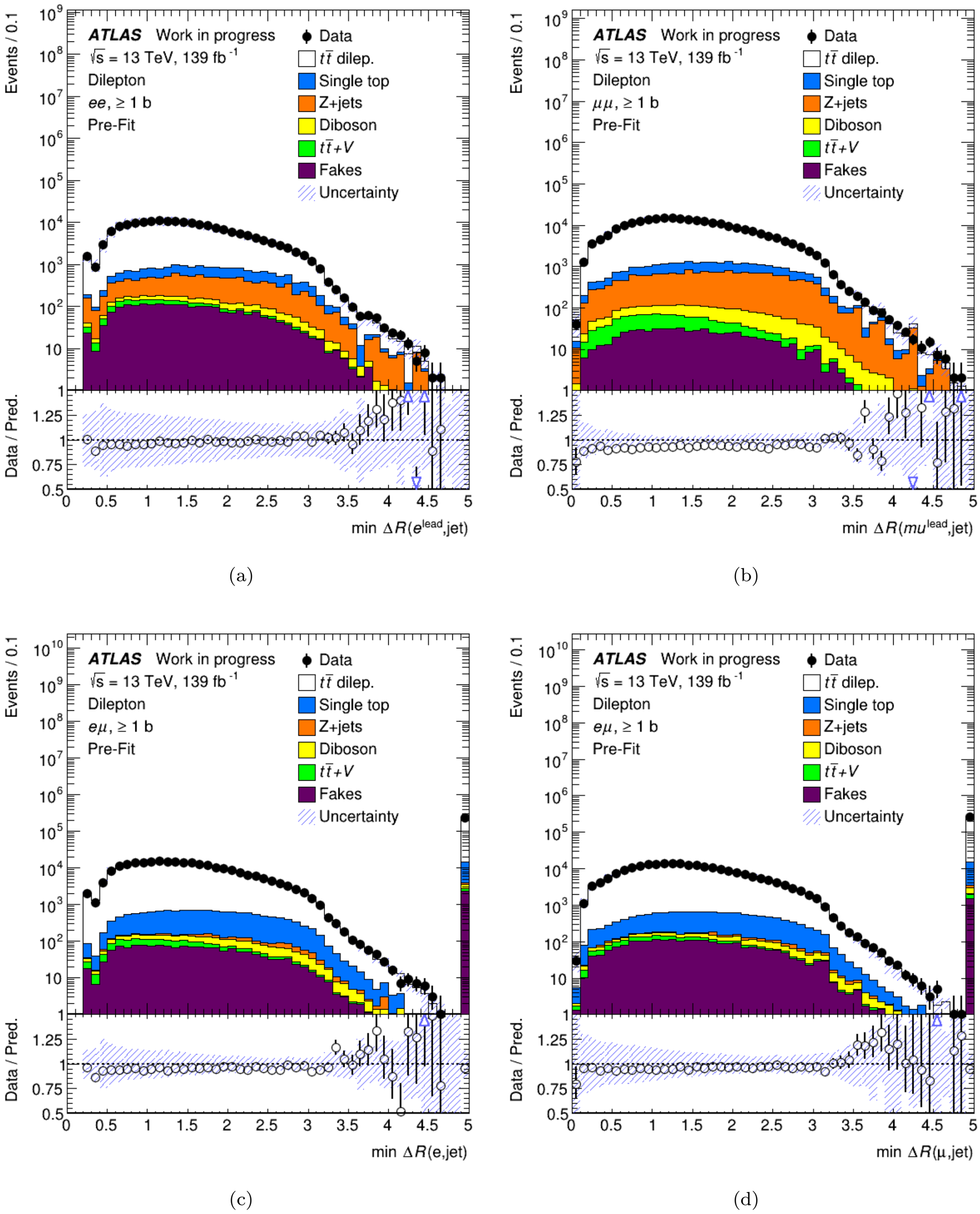

FIGURE 6.4: ΔR between the charged leading lepton and its nearest jet, after the p_T correction, in $ee - channel$ (a) $\mu\mu - channel$ (b) and $e\mu - channel$: electron (c) and muon(d). Errors are both statistical and systematics.

6.5 Control regions and background assessment

Two control regions are defined for the backgrounds coming from Z+jet (only relevant for the $ee - channel$ and $\mu\mu - channel$) events and from single lepton events with a fake or non-prompt lepton from various processes (mainly $t\bar{t}$, single-top and W+jet events). Even if the predictions shown in Fig. 6.3 and Fig. 6.4 are good, further confirmations are made using the Control Regions (CR). These CRs are not currently included in the fit.

6.5.1 Z+jet background

Z+jets is the second main background after the SM $t\bar{t}$ but it can be reduced. Reducing this background is very important, due to the fact that the Z boson can decay in two same-flavor leptons and if jets are mis-measured they could mimic missing transverse momentum.

The Z+jets control region (referred as "CR$_Z$" from now on) is obtained by selecting the ee and $\mu\mu$ events and inverting the Z-mass window cut, i.e. requiring $80 < m_{\ell\ell} < 100$ GeV. Fig. 6.5 shows the $m_{\ell\ell}$ distributions in the ee and $\mu\mu$ channels, without the Z-mass window selection; because the Z+jets background is relevant after signal selection, to reduce it I apply a Missing Energy Transverse MET > 45 GeV cut. Fig. 6.6, Fig. 6.7, and Fig. 6.8 show the leading lepton p_T, the ΔR between the leading lepton and its nearest jet and the leading jet p_T distribution, respectively, in CR$_Z$; in these plots the MET cut is applied. Additional plots are shown in Appendix C.

There is a satisfying agreement between data and Monte Carlo and also the Z peak is well reconstructed; the other backgrounds are SM $t\bar{t}$ dilepton (white), single top (blue), diboson (yellow), $t\bar{t} + V$ (green) and the fakes (purple). The errors are both statistical and systematics. Tab. 6.8 shows the reduction of the Z+jets background event.

Table 6.8: Difference between the expected events for the Z+jets background, before and after the MET cut.

Z + jets	ee $\geq$ 1 b [x10^3]	$\mu\mu \geq$ 1 b [x10^3]
No MET cut	390 $\pm$ 120	630 $\pm$ 190
MET cut	60 $\pm$ 18	100 $\pm$ 30

6.5.2 Fake lepton background

A sample enriched in events with a real prompt lepton and a fake or non-prompt lepton, referred to as "CR$_{\text{fakes}}$" in the following, is obtained by inverting the opposite-sign requirement on the electric charges of the selected leptons, i.e. requiring same-sign dilepton events. Fig. 6.9, Fig. 6.10, and Fig. 6.11 show various distributions in this control region (leading lepton p_T, the ΔR between the leading lepton and its nearest jet and the leading jet p_T, respectively), for the three channels ee, $\mu\mu$ and $e\mu$. The contributions in the fake region are Z+jets (orange), diboson (yellow), $t\bar{t} + V$ (green) and the fakes (purple); furthermore. The SM $t\bar{t}$ dilepton (white) is negligible. This is due to the fact that to have a pair of same sign leptons, the charge of one of the leptons should be mis-reconstructed. The probability of this mis-reconstruction (charge flip) is very low. The errors are both statistical and systematics and the MC predictions are absolute. Additional plots are shown in Appendix C.
The ee and $e\mu$ channels show a significant contribution from $t\bar{t}$ and Z+jets with two real prompt leptons, due to the non-negligible electron charge mis-identification. In all channels, there is a non-negligible contribution from $t\bar{t} + V$, especially from $t\bar{t} + W$. The fake background appear well modelled.

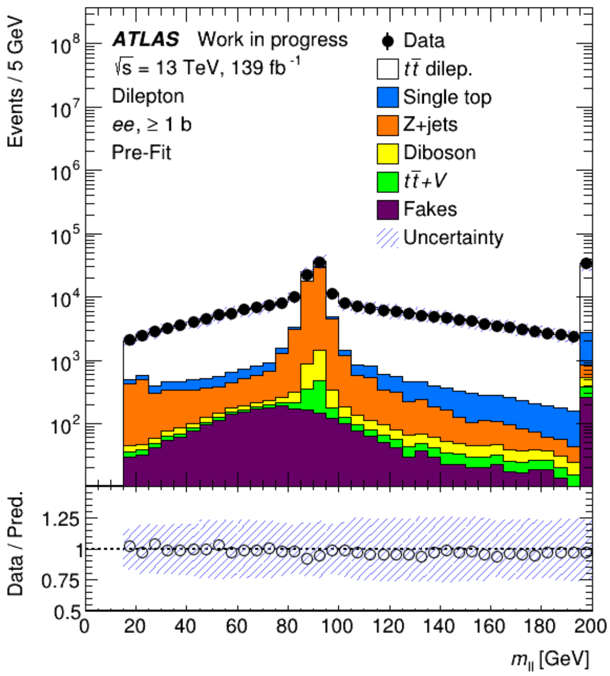

(a)

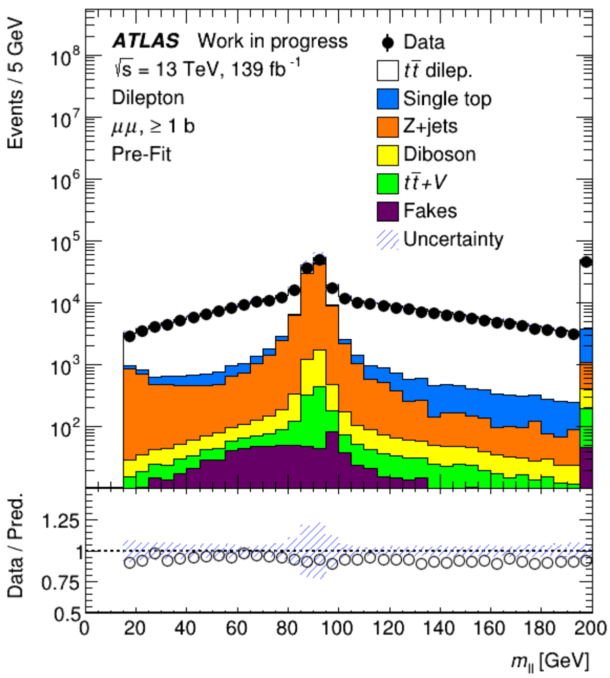

(b)

FIGURE 6.5: Invariant mass of the two charged leptons in $ee - channel$ (a) and $\mu\mu - channel$ (b) in CR$_Z$ region. Errors are both statistical and systematics.

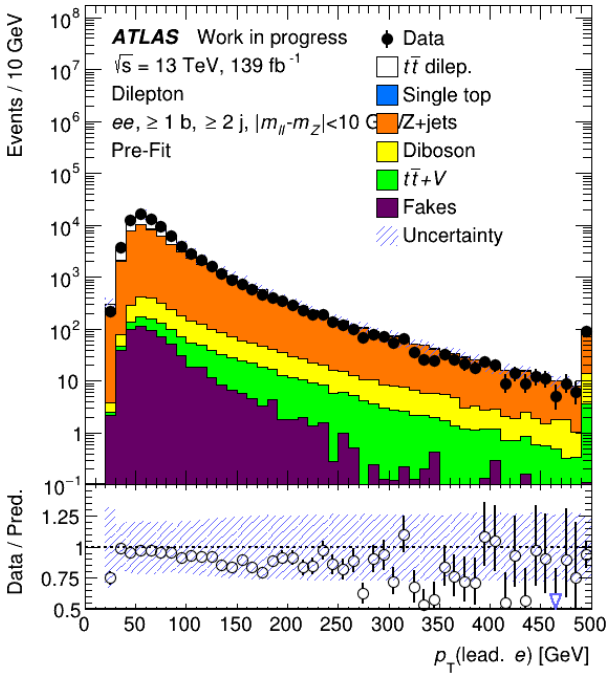

(a)

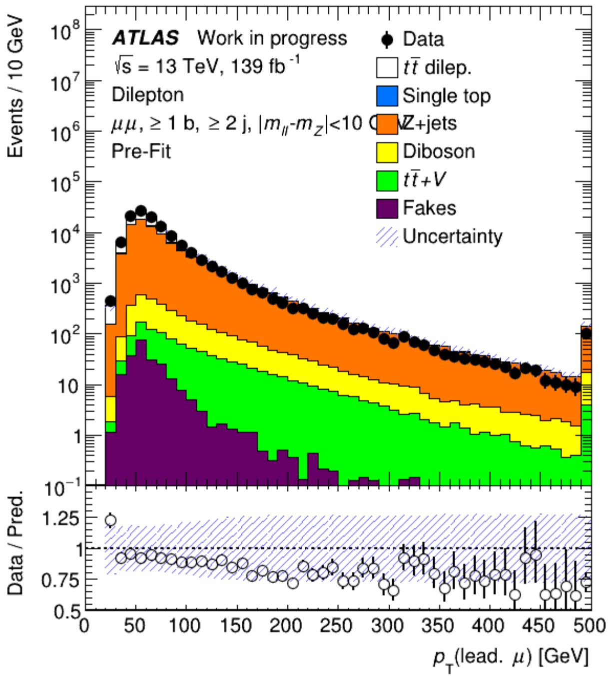

(b)

FIGURE 6.6: Transverse momentum of the leading lepton in $ee-channel$ (a) and $\mu\mu - channel$ (b) in CR_Z region. Errors are both statistical and systematics.

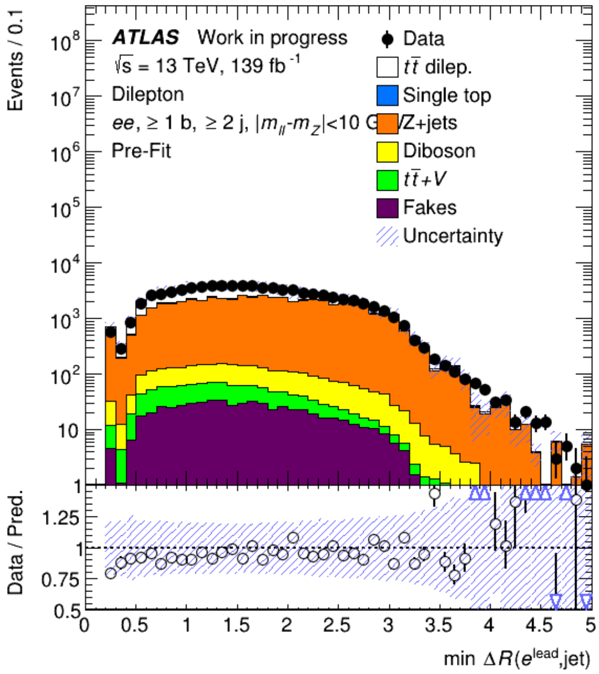

(a)

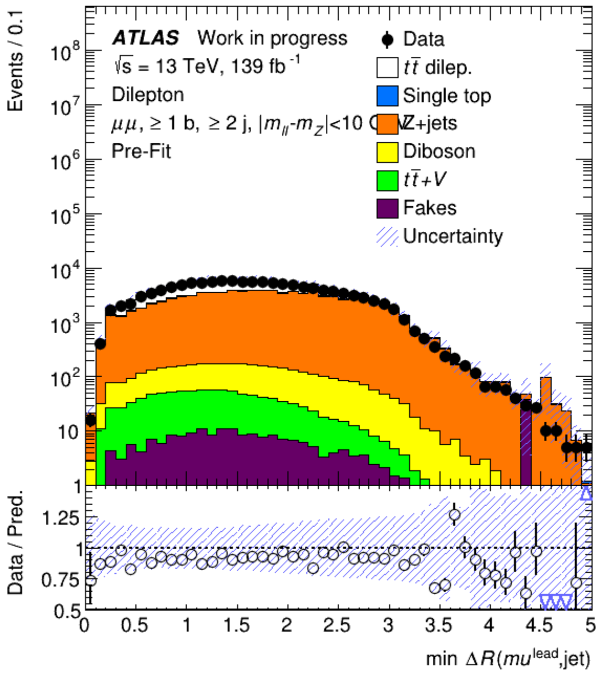

(b)

FIGURE 6.7: ΔR between the charged lepton and its nearest jet in $ee-channel$ (a) and $\mu\mu - channel$ (b) in CR$_Z$ region. Errors are both statistical and systematics.

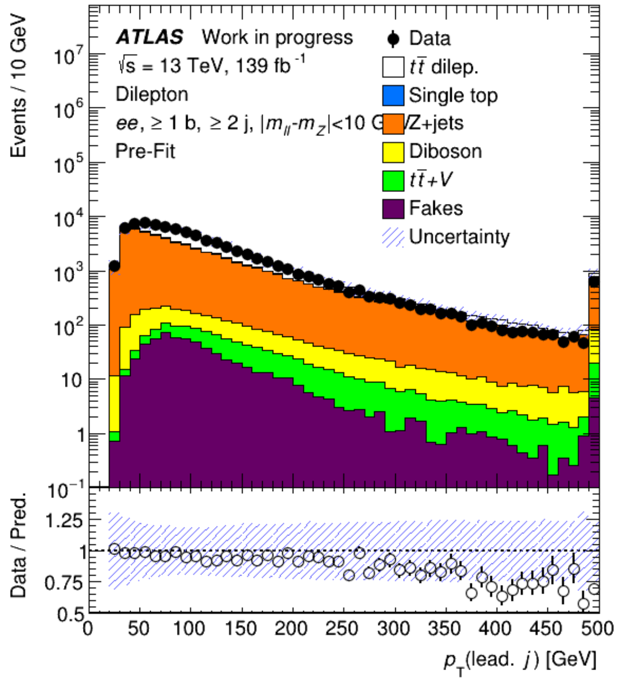

(a)

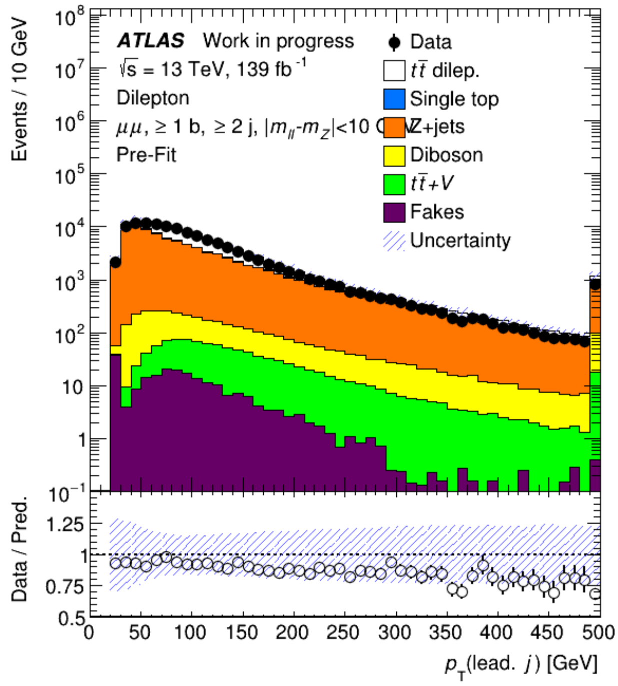

(b)

FIGURE 6.8: Transverse momentum of the leading jet in $ee - channel$ (a) and $\mu\mu - channel$ (b) in CR$_Z$ region. Errors are both statistical and systematics.

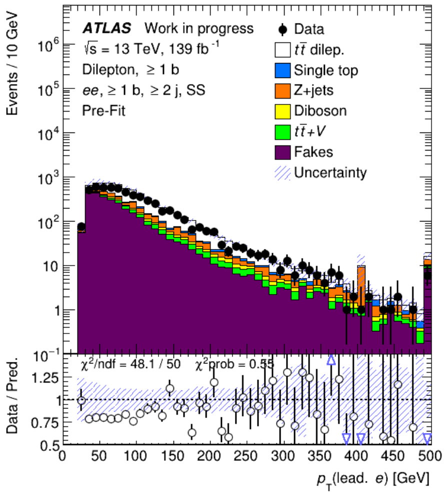

(a)

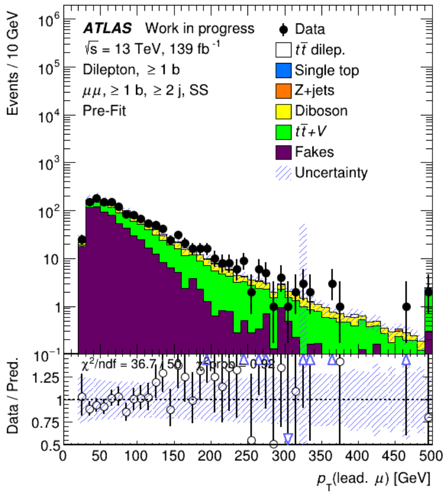

(b)

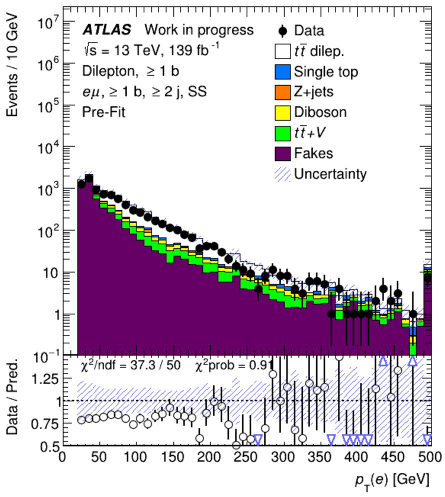

(c)

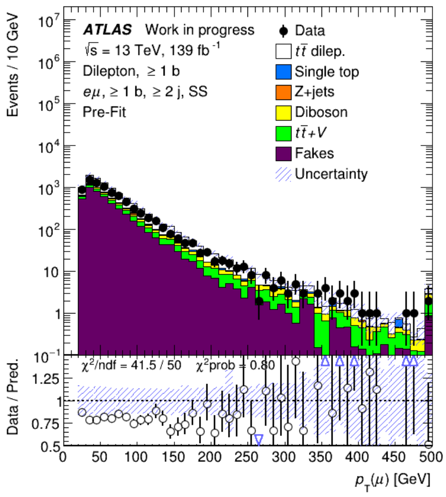

(d)

FIGURE 6.9: Transverse momentum of the leading lepton in $ee-$ *channel* (a) $\mu\mu-$ *channel* (b) and $e\mu-$ *channel*: electron (c) and muon(d) in $\mathrm{CR_{fakes}}$ region. Errors are both statistical and systematics.

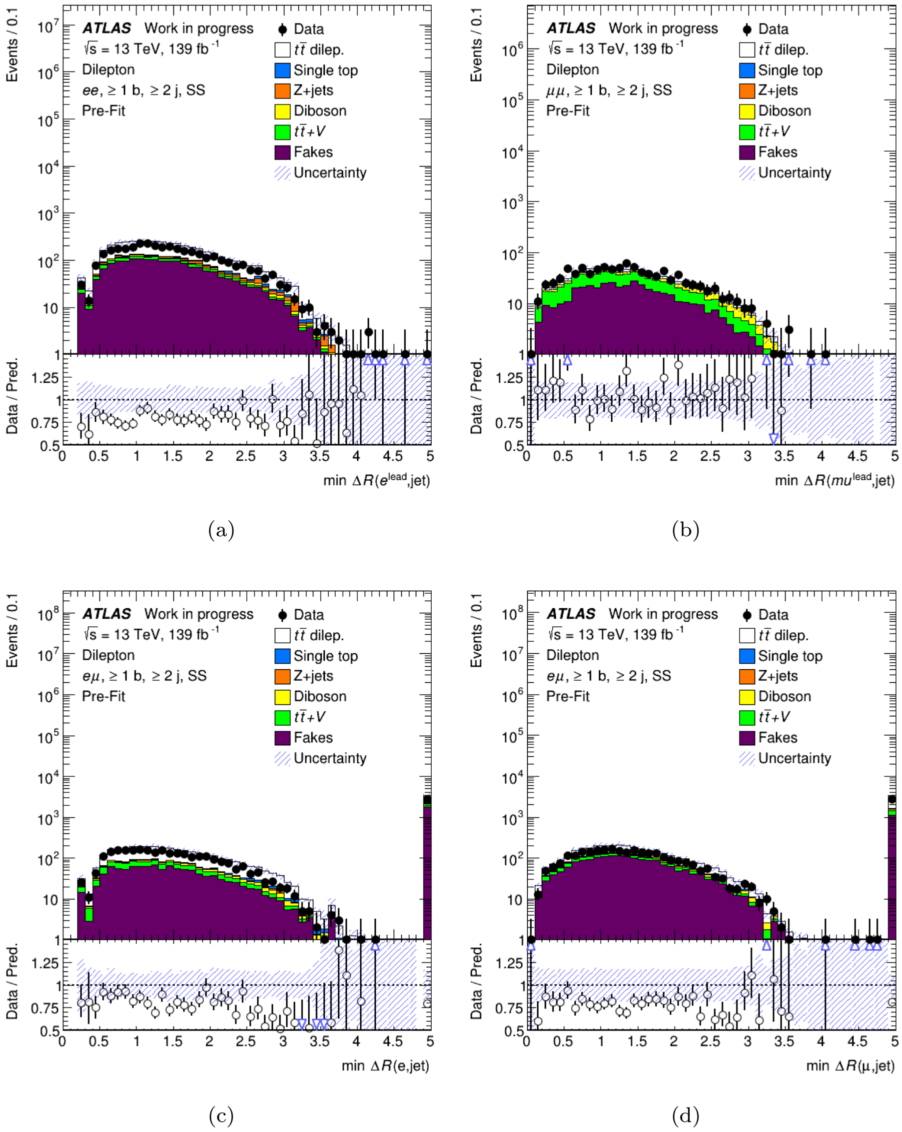

FIGURE 6.10: ΔR between the charged leading lepton and its nearest jet in $ee-channel$ (a) $\mu\mu-channel$ (b) and $e\mu-channel$: electron (c) and muon(d) in $\mathrm{CR_{fakes}}$ region. Errors are both statistical and systematics.

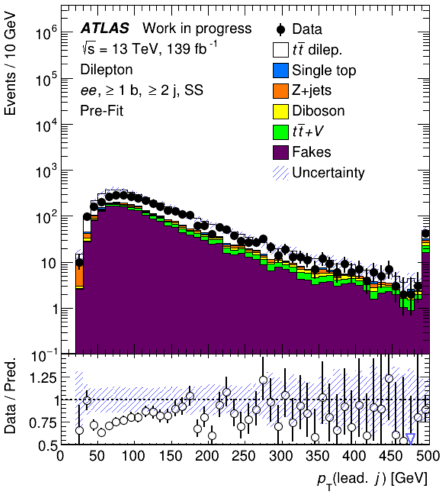

(a)

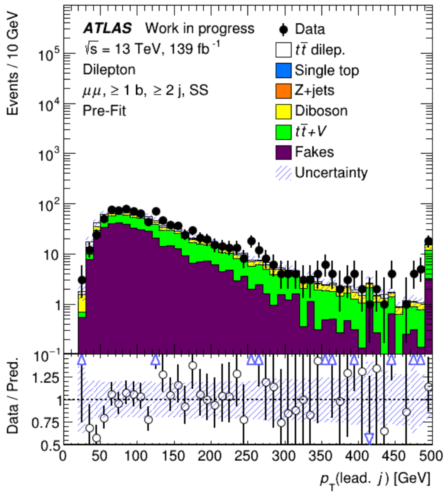

(b)

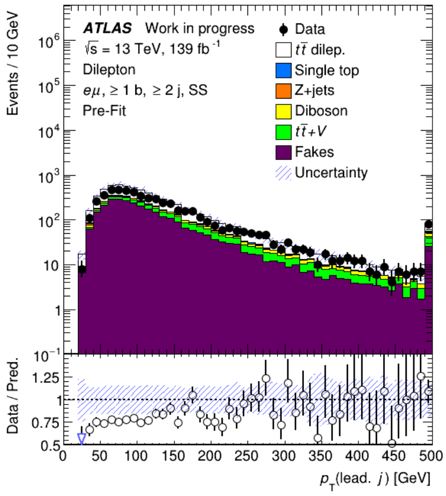

(c)

FIGURE 6.11: Transverse momentum of the leading jet in $ee-channel$ (a) $\mu\mu-channel$ (b) and $e\mu-channel$ (c) in CR$_{\text{fakes}}$ region. Errors are both statistical and systematics.

6.6 Signal regions

Before defining the Signal Region (SR) (or mass region), measurements in the total mass variables ($m_{t\bar{t}}^{NW}$ and $m_{\ell\ell bb}$) and the spin-sensitive variable $|\Delta\phi^{\ell\ell}|$ ranges are shown, to confirm the effectiveness of the distributions. Fig. 6.12 and Fig. 6.13 show the $m_{t\bar{t}}^{NW}$ and $m_{\ell\ell bb}$ inclusive distribution, respectively. Fig. 6.14 shows the $\Delta\phi^{\ell\ell}/\pi$ inclusive distribution. All plots are taken after the selections; moreover, both MC statistical and systematics errors are used. Unfortunately, $M_{T,t\bar{t}}$ systematics errors of the MET information are too high for now to perform a fit and, successively, the limit mass plots, as shown in Fig. 6.15. For this reason it will not show in the final results for now, but future improvements are expected on the reconstruction of this proxy variable aiming to reduce the MET systematics errors.

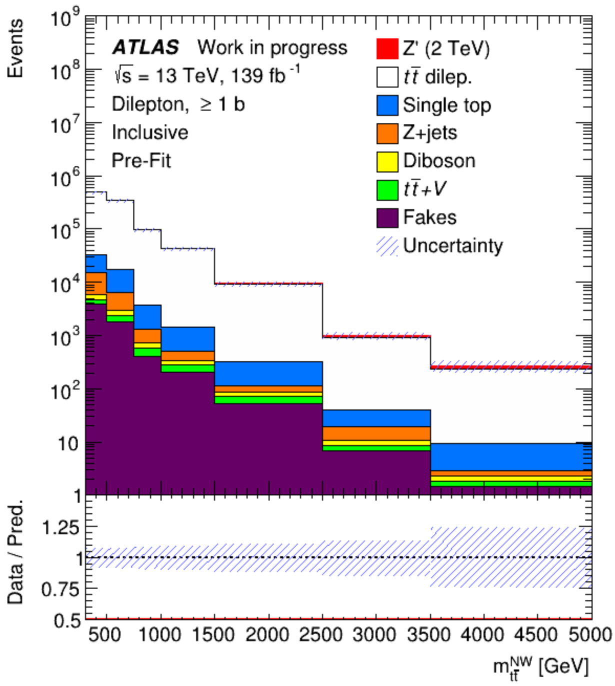

FIGURE 6.12: Distribution of $m_{t\bar{t}}$ invariant mass. The errors are MC statistical and systematics.

A signal region is defined for each bin of the mass variables $m_{t\bar{t}}^{NW}$ and $m_{\ell\ell bb}$, and in each of these regions the spin-sensitive variable $\Delta\phi^{\ell\ell}/\pi$ is considered. In these SRs the signal sensitivity increases in the region of $\Delta\phi^{\ell\ell}/\pi > 0.5$, as shown in the next plots. The number of bins chosen is based on the simulated statistics I have and to

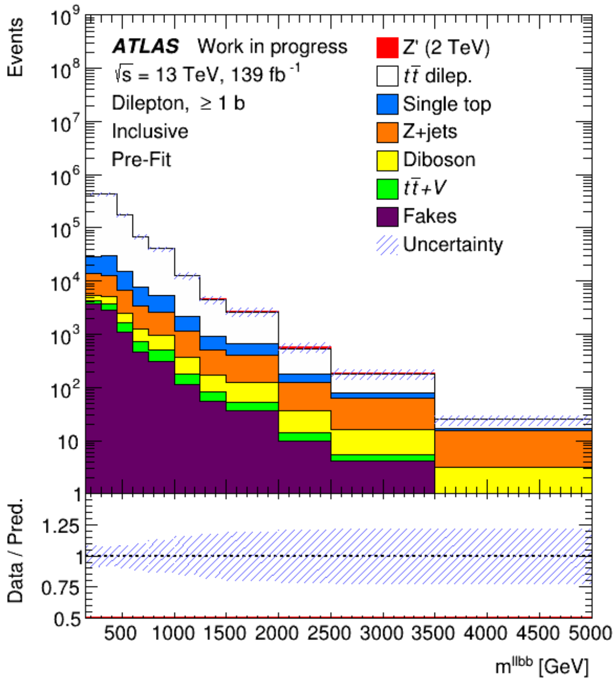

FIGURE 6.13: Distribution of $m_{\ell\ell bb}$ invariant mass. The errors are MC statistical and systematics.

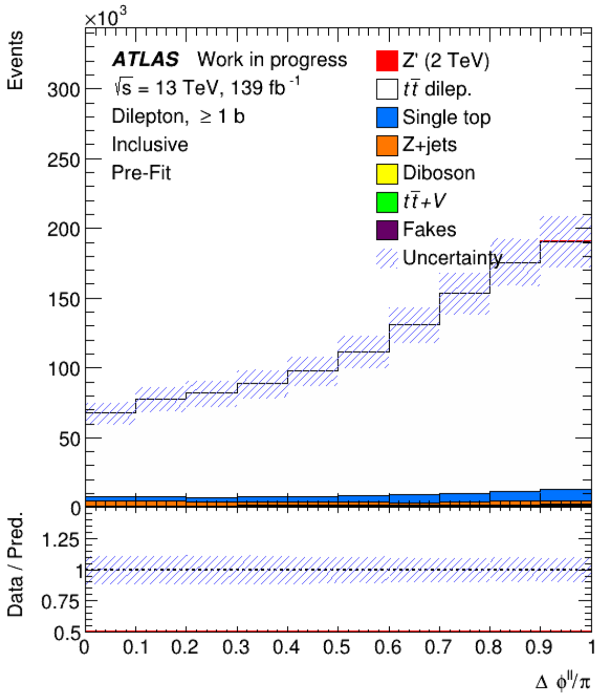

FIGURE 6.14: Distribution of the spin-sensitive variable $\Delta\phi^{\ell\ell}/\pi$. The errors are MC statistical and systematics.

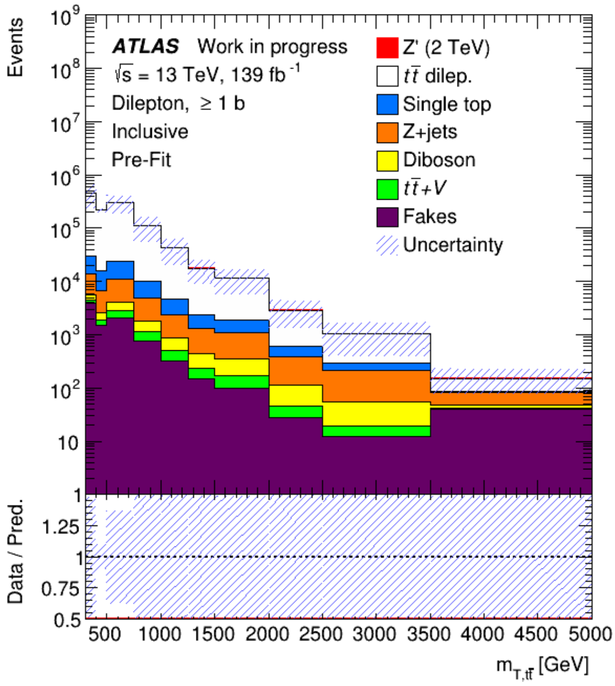

FIGURE 6.15: Distribution of $M_{T,t\bar{t}}$ invariant mass. The errors are MC statistical and systematics.

have enough expected signal statistics in comparison with the total background. Tab. 6.9 summarises the mass region binning for $m_{t\bar{t}^{NW}}$ and $m_{\ell\ell bb}$ distributions.

Fig. 6.16 shows the signal (Z' 2 TeV) in the two mass variables. Mass region between 2 TeV and 2.5 TeV for $m_{t\bar{t}}^{NW}$ and between 1.5 TeV and 2 TeV for $m_{\ell\ell bb}$. Fig. 6.17 shows the $\Delta\phi^{\ell\ell}/\pi$ distribution in two of the ten $m_{t\bar{t}}^{NW}$ mass region bins (0.5 TeV $< m_{t\bar{t}}^{NW} <$ 0.75 TeV and 2 TeV $< m_{t\bar{t}}^{NW} <$ 2.5 TeV, respectively), the second plot shows that in the high mass region the signal tend to be higher in the $\Delta\phi^{\ell\ell}/\pi > 0.5$ region. The signal sample used is Z' 2 TeV (red area). The main background are SM $t\bar{t}$ (white) and single-top (blue).
Fig. 6.18 shows the $\Delta\phi^{\ell\ell}/\pi$ distribution in two of the ten $m_{\ell\ell bb}$ mass region bins (0.5 TeV $< m_{\ell\ell bb} <$ 0.75 TeV and 1.5 TeV $< m_{\ell\ell bb} <$ 2 TeV, respectively), the second plot shows that in the high mass region the signal tend to be higher in the $\Delta\phi^{\ell\ell}/\pi >$ 0.5 region. The signal sample used is Z' 2 TeV (red are). The main background are SM $t\bar{t}$ (white), Z+jets (orange), single-top (blue) and diboson (yellow).
Plots for the other mass bins under study are shown in Appendix C.

TABLE 6.9: Mass region binning for $m_{t\bar{t}^{NW}}$ and $m_{\ell\ell bb}$ distributions.

Variable	Bins [TeV]
$m_{\ell\ell bb}$	0-0.3
	0.3-0.4
	0.4-0.5
	0.5-0.75
	0.75-1
	1-1.25
	1.25-1.5
	1.5-2
	2-2.5
	> 2.5
$m_{t\bar{t}}^{NW}$	0.3-0.5
	0.5-0.75
	0.75-1
	1-1.25
	1.25-1.5
	1.5-2
	2-2.5
	2.5-3
	3-4
	> 4

Finally, Tab. 6.10 shows the Control Regions and Signal Regions selection criteria.

TABLE 6.10: Control Regions and Signal Regions selection criteria.

Region	Use	Selection
CR_Z	Constraint to $Z + jets$ background	$E_T^{miss} > 45$ GeV ≥ 1 b-jet $80 < m_{\ell\ell} < 100$ GeV
$\mathrm{CR}_{\mathrm{fakes}}$	Constraint to fake	$E_T^{miss} > 45$ GeV ≥ 1 b-jet
Inclusive plots	Validation of fit	$E_T^{miss} > 45$ GeV ≥ 1 b-jet inclusive
SR	Signal research	$E_T^{miss} > 45$ GeV ≥ 1 b-jet mass region bins

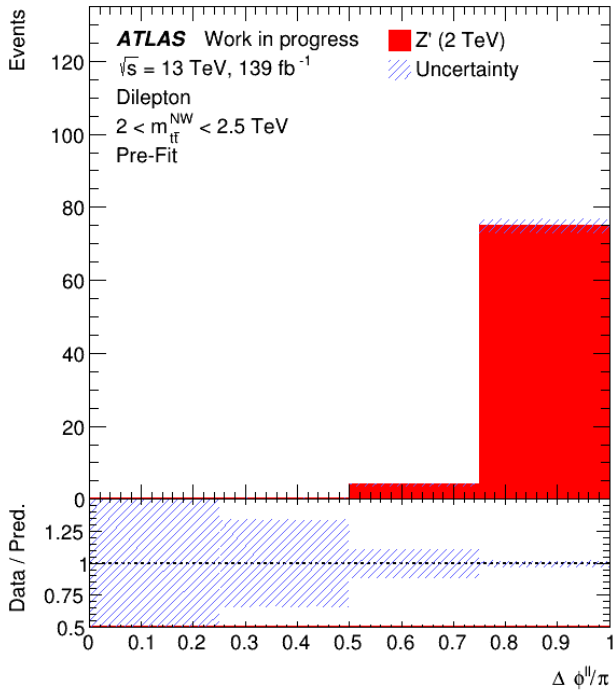

(a)

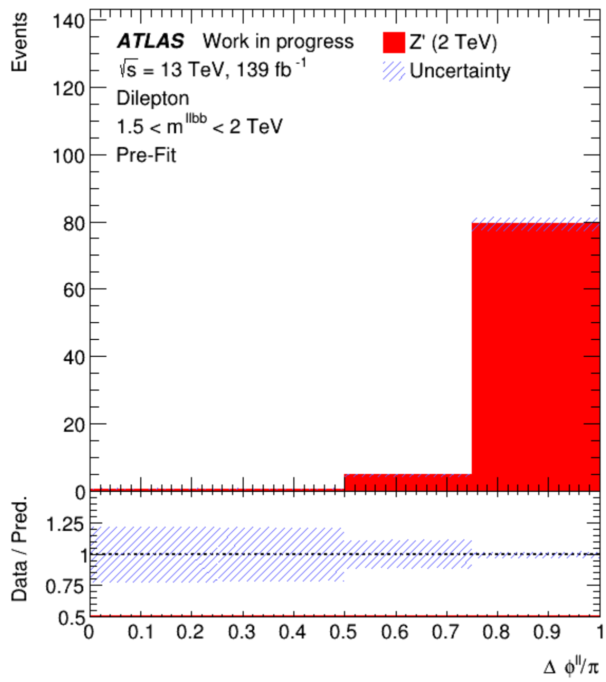

(b)

FIGURE 6.16: $\Delta\phi^{\ell\ell}/\pi$ distribution, only for signal sample Z' with a mass of 2 TeV, in $m_{t\bar{t}}^{NW}$ mass region bin 2 TeV $< m_{t\bar{t}}^{NW} <$ 2.5 TeV (a) and in $m_{\ell\ell bb}$ mas region bin 1.5 TeV $< m_{\ell\ell bb} <$ 2 TeV (b). The errors are MC statistical.

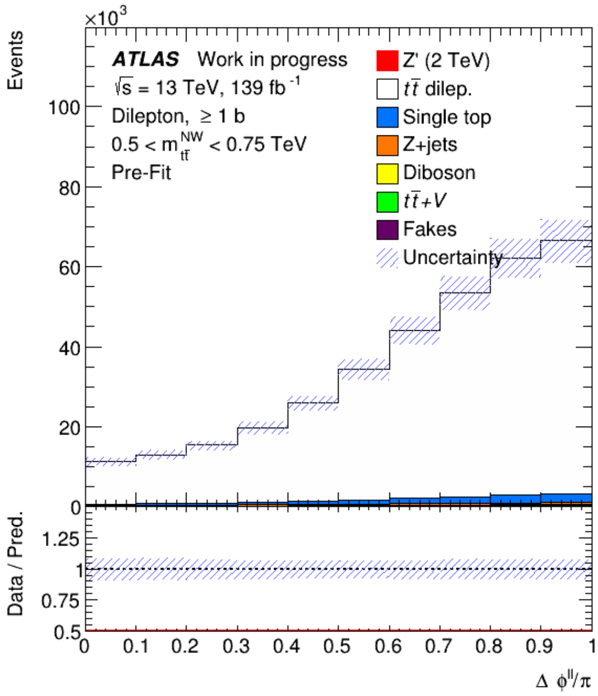

(a)

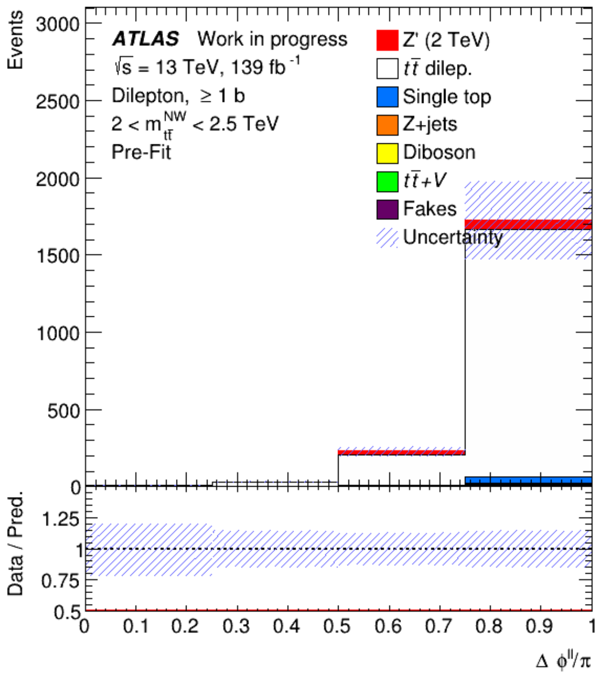

(b)

FIGURE 6.17: $\Delta\phi^{\ell\ell}/\pi$ distribution in $m_{t\bar{t}}^{NW}$ mass region bins for 0.5 TeV $< m_{t\bar{t}}^{NW} <$ 0.75 TeV (a) and 2 TeV $< m_{t\bar{t}}^{NW} <$ 2.5 TeV (b). The errors are MC statistical and systematics.

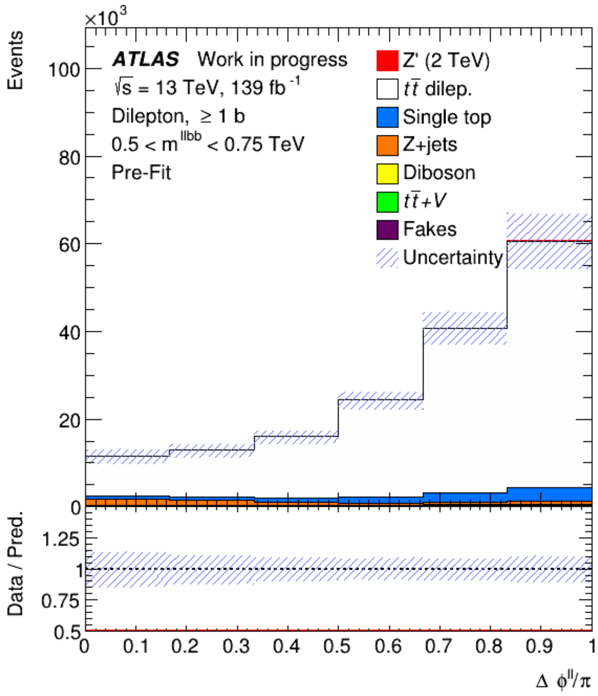

(a)

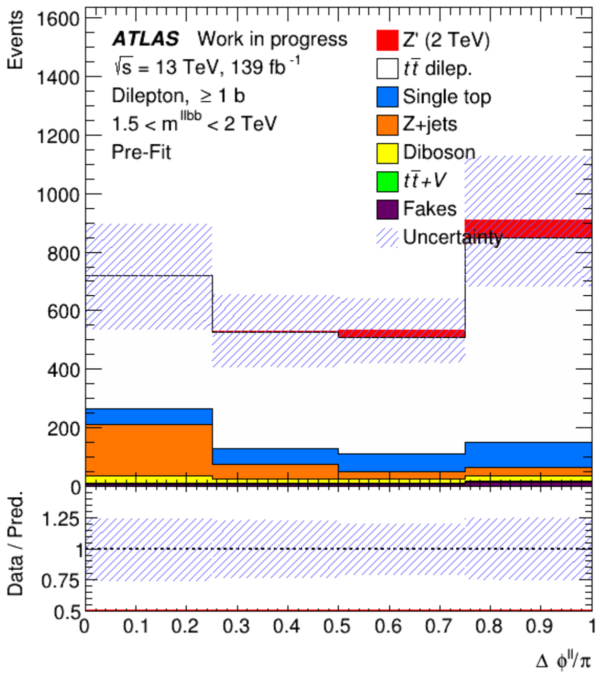

(b)

FIGURE 6.18: $\Delta\phi^{\ell\ell}/\pi$ distribution in $m_{\ell\ell bb}$ mass region bins for 0.5 TeV $< m_{\ell\ell bb} <$ 0.75 TeV (a) and 1.5 TeV $< m_{\ell\ell bb} <$ 2 TeV (b). The errors are MC statistical and systematics.

6.7 2-dimensional Fit and likelihood technique

The two-dimensional fit is described as follows: the two dimensions are the invariant mass ($m_{t\bar{t}}^{NW}$ or $m_{\ell\ell bb}$) and the $\Delta\phi$ (as showed in the SR plots). The mass variable is split in bins and the $\Delta\phi$ distribution in each bin is evaluated; finally, I fit all distributions simultaneously.
The profile likelihood technique is used when fitting models with some parameters of interest (POI, in our case the signal-strength μ for a particular signal hypothesis) and with more than one unknown parameters or nuisance parameters θ (NP, in our case used to encode the effect of systematic uncertainties in the measurement) that are used to define the fit model. The general likelihood function is written as a product of Poisson measurements in all considered bins plus a probability density function (G) for each of the nuisance parameters and it is defined, for binned likelihood, as:

$$L(n, \theta_0|\mu, \theta) = \prod_{i \in bins} P(n_i|\mu, S_i(\theta) + B_i(\theta)) \cdot \prod_{j \in n.p.} G(\theta_j^0|\theta_j) \tag{6.6}$$

where n is the yield, μ is the signal strength, defined as a ratio of the signal production (Z', G or g_{KK}) cross-section times branching ratio in the dilepton final state to its theoretically predicted value, θ_0 is the nominal value of the nuisance parameter θ, S is the predicted signal and B is the predicted background, both for each mass bin, i.
The probability that the background fluctuates creating a signal-like excess is defined as p_0 (p-value) and it is important to assess if an excess is real or it is due to the background fluctuation. The p-value is defined with a test statistic:

$$q_0 \begin{cases} 0 & \text{for } \mu < 0; \\ -2ln\frac{\mathcal{L}(data|0,\theta_0)}{\mathcal{L}(data|\mu,\theta)} & \text{for } \mu \geq 0; \end{cases} \tag{6.7}$$

that is used to reject the background-only hypothesis.
The probability p_0 corresponding to a given experimental observation q_0^{obs} is:

$$p_0 = \int_{q_0}^{\infty} P(q_0|0)dq_0 \quad . \tag{6.8}$$

Normally, the p-values are translated in a scale of $Significance$ Z defined as:

$$Z = \Phi^{-1}(1 - p_0) \tag{6.9}$$

where Φ^{-1} is the inverse of the cumulative function for the normal Gaussian [78]. Such a likelihood is built with all the bins $\Delta\phi^{\ell\ell}$ in all the mass regions (for a particular choice of the mass-sensitive valriable, $m_{t\bar{t}}^{NW}$ or $m_{\ell\ell bb}$). The normalisation of the $t\bar{t}$ background is left free floating (k_{tt}) in the fit. The expected exclusion limits obtained through this technique for the BSM particles will be shown in the result section.

6.8 Systematic uncertainties

In this analysis, information from theoretical models, Monte Carlo simulations, and control regions are all required and each information carries uncertainties.
Several sources of systematic uncertainty are included in the analysis, affecting signal and background process cross sections and event kinematics, as well as the detector response description by the simulation. Each individual source of uncertainty is associated to an independent nuisance parameter in the profile likelihood fit, and its effect on different signal or background samples is treated as fully correlated.
Only $t\bar{t}$ systematics uncertainties are taken into account because in this analysis it is the main background and it is also irreducible. The sources of systematic uncertainties include modelling and experimental uncertainties. The modelling uncertainties are:

- initial and final state radiation (ISR/FSR) variations. These systematic uncertainties on the amount of initial- and final-state QCD radiation, in $t\bar{t}$ dilepton events, are assessed in the following way:

  - ISR *hdamp*: the comparison is done between the nominal simulation and the Powheg+Pythia8 sample, that have the h_{damp} parameter (which controls the p_T of the first additional emission beyond the Born configuration) varied. The nominal h_{damp} parameter is set to $1.5\times m_t$, while the varied h_{damp} parameter is set to $3\times m_t$. In order to relax the constraint for this uncertainty, the normalization and the shape components are splitted. Moreover, a decorrelation of the shape component for each mass bin is applied;

- ISR μ_F: this uncertainty is obtained by comparing the nominal simulation with a simulation where the factorisation scale in the initial-state parton shower process is varied up and down of a factor of 2 and 0.5;

- ISR μ_R: this uncertainty is obtained by comparing the nominal simulation with a simulation where the normalisation scale in the initial-state parton shower process is varied up and down of a factor of 2 and 0.5;

- ISR A14 tune: the comparison is done between the nominal simulation and simulations where the "Var3c" up and down variations of the A14 tune are used;

- FSR: this uncertainty is obtained by comparing the nominal simulation with a simulation where the normalisation scale in the final-state parton shower process is varied up and down of a factor of 2 and 0.5;

- parton shower and hadronisation model (PS) choice: a systematic uncertainty related to the PS choice for the $t\bar{t}$ dilepton simulation is included by comparing the nominal Powheg+Pythia8 sample with a sample produced with Powheg interfaced with Herwig7. In order to relax the constraint for this uncertainty, the normalization and the shape components are splitted. Moreover, a decorrelation of the shape component for each mass bin is applied;

- matrix element generator (ME) choice: a systematic uncertainty associated with the choice of the Monte Carlo simulation of the matrix element at NLO in QCD and of its matching scheme with the parton shower, is evaluated, for the $t\bar{t}$ dilepton process, by comparing the nominal simulation with a sample generated using aMC@NLO interfaced with Pythia8. In order to relax the constraint for this uncertainty, the normalization and the shape components are splitted. Moreover, a decorrelation of the shape component for each mass bin is applied;

- background cross-section uncertainties: a 5% total cross-section uncertainty, obtained from NNLO scale variation, is applied to the $t\bar{t}$ prediction, while for non-$t\bar{t}$ simulated samples larger uncertainties, using $ad-hoc$ numbers (30% for $Z+jets$, $Wt\ single-top$, ttV and $Fake$ backgrounds and 50% for *diboson* background), are applied to take into account acceptance effects without directly including the comparison between different simulation setups;

- top-p_T reweighting: an uncertainty is included in the fit. The systematic is obtained from from the difference between the $t\bar{t}$ dilepton process with and without reweighting. To apply this uncertainty the nominal sample is taken and the weights, described in Section 6.4.1, are applied and added as systematics.

Instead, the instrumental uncertainties are:

- uncertainties in lepton reconstruction, identification and trigger efficiencies;

- jet energy scale (JES) uncertainty: the jet energy scale was derived using information from test-beam data, LHC collision data and simulation and includes uncertainties in the flavor composition of the samples and mis-measurements from close-by jets and pileup. There are 22 parameters associated to the JES uncertainty;

- jet energy resolution (JER) uncertainty: the energy resolution was derived from dijet events and it is important for the measurement top-quark cross-sections, mass measurements and searches involving resonances decaying to jets, and all these effects are associated to separate nuisance parameters;

- uncertainties related to missing transverse energy: beside the fact that uncertainties on energy scale and resolution for jets and leptons are propagated to the MET, specific sources of systematic uncertainty are included for the soft part of the MET calculation (the part not associated with any reconstructed object);

- b-tagging uncertainties: the uncertainties on the determination of the tagging efficiency for b-jets, c-jets and light-flavour jets are propagated from the algorithm calibration in data;

- luminosity uncertainty: a 1.7% luminosity uncertainty is applied to all samples (it is the integrated luminosity uncertainty of full Run2 dataset [79]);
- uncertainty on the efficiency to pass the JVT requirement is evaluated by varying the scale factors within their uncertainties;
- uncertainty on pileup activity is evaluated according to the uncertainty on the average number of interactions per bunch crossing.

In order to minimise numerical instabilities of the fit procedure, the following pruning procedure was applied to neglect irrelevant systematic uncertainty sources:

- a source of systematic uncertainty is not included in the fit for a particular simulated sample (and in a particular selected region) if its effect in all of the bins is smaller than 0.5% of the predicted yield in that bin for that sample;
- some sources can be kept only for some of the samples;
- for some sources only the overall effect in each selected sample is kept, if the shape effect is negligible, applying the criterion explained in the first point to the shape variation induced by the systematic shift;
- similarly, for some sources only the shape effect is kept, if the overall effect of the systematic shift is below 0.5% of the total predicted yield.

Fig. 6.19 shows in a graphical way which systematic uncertainty sources are removed or partially removed from the fit model. The systematics uncertainties are only for $t\bar{t}$, as described before. Only normalization uncertainties for other backgrounds are taken into account.

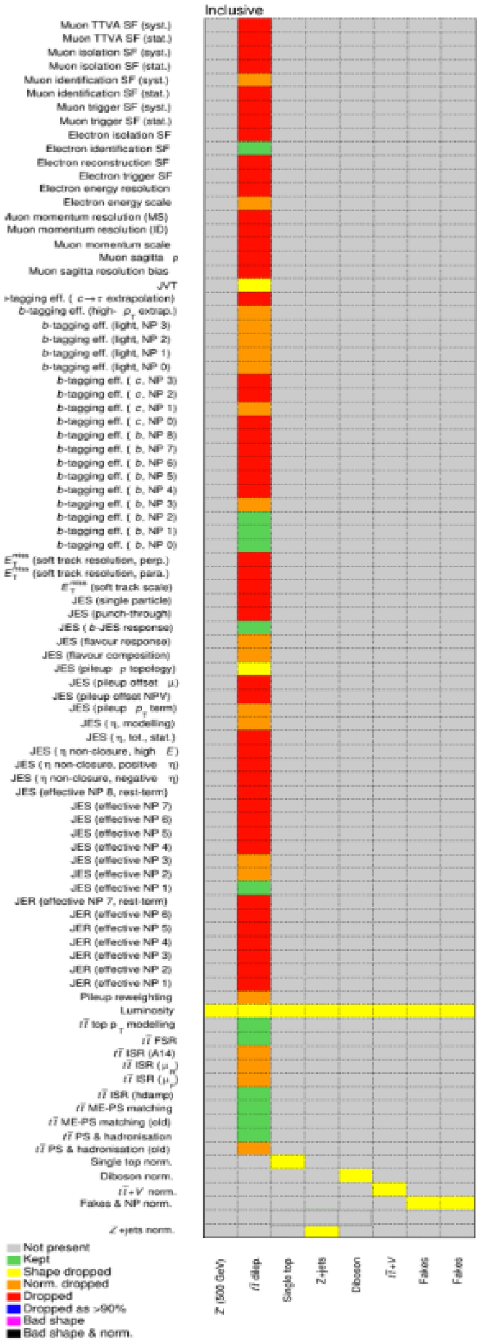

FIGURE 6.19: List of all systematics used in the analysis samples.

The remaining sources of systematic uncertainty after the pruning procedure are the following:

- luminosity, pileup, JVT and background modeling;
- the Jet Energy Scale (JES_EffectiveNP1,JES_EffectiveNP2,JES_EffectiveNP3), JES of the b-jets (JES_BJES_Resp), pseudorapidity modelling (JES_EtaModelling), pileup (JES_Pileup_PtTerm and JES_Pileup_RhoTopology) and flavor composition and respond (JES_Flavor_Comp and JES_Flavor_Resp);
- the b-tagging systematics (btag_b_0,btag_b_1,btag_b_2,btag_b_3,btag_c_1, btag_extrap,btag_light_0,btag_light_1,btag_light_2,btag_light_3);
- the lepton scale factor uncertainties (leptonSF_EL_SF_ID and leptonSF_MU_SF_ID_SYST).

Fig. 6.20 shows example systematics for the $m_{t\bar{t}}^{NW}$ mass variable that survive the pruning step, namely PS hadronisation and pileup JES. Fig. 6.21 shows example systematics for the $m_{\ell\ell bb}$ mass proxy that survive the pruning step, namely PS hadronisation and pileup JES. The black line is the shape of the nominal sample and in red (blue) is the +1% (−1%) of deviation standard from it, the dashed lines are before the symmetrization and smoothing[1] and the continuous lines are after these.

[1]Smoothing techniques can be applied to systematic variations, to wash away or mitigate statistical fluctuations.

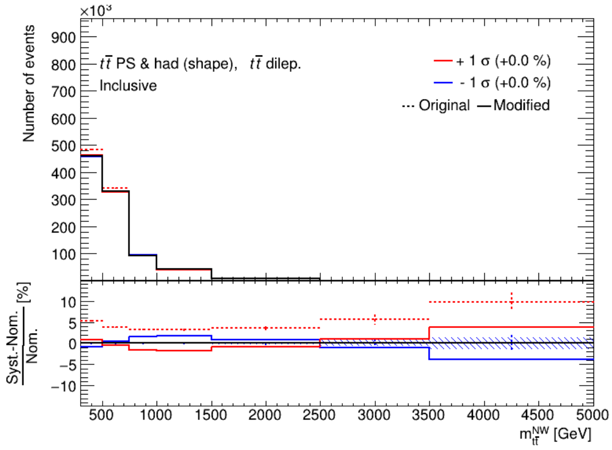

(a)

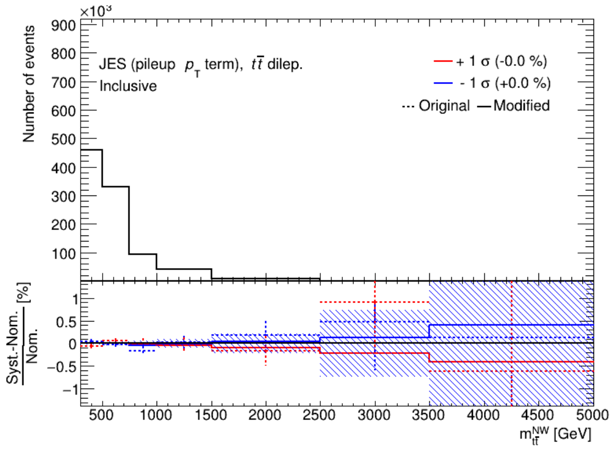

(b)

FIGURE 6.20: Example of JES systematics in $m_{t\bar{t}}^{NW}$: the shape component parton shower (a) and the JES pileup p_T (b).

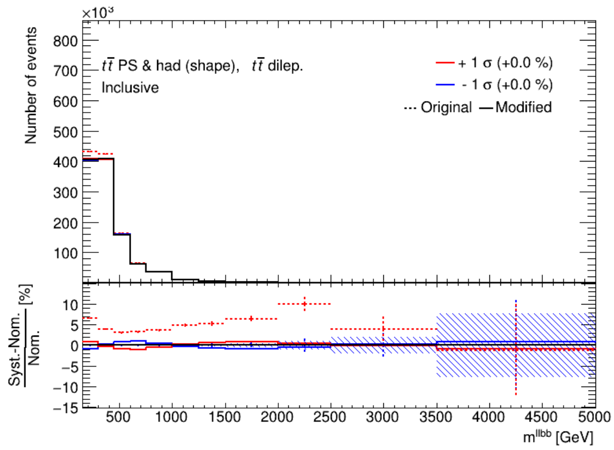

(a)

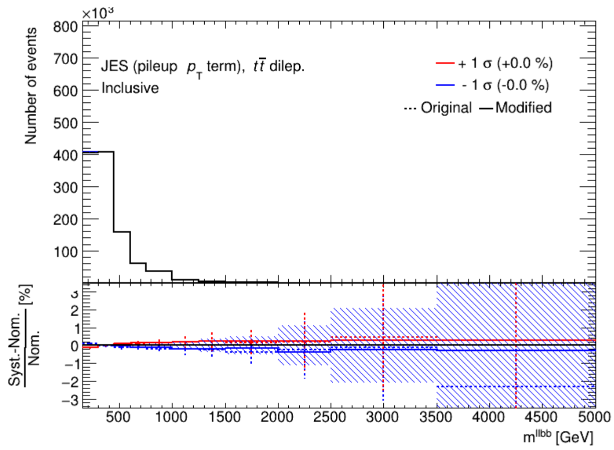

(b)

FIGURE 6.21: Example of JES systematics in $m_{\ell\ell bb}$: the shape component parton shower (a) and the JES pileup p_T (b).

Fig. 6.22 shows the list of surviving nuisance parameter post-fit values and uncertainties when performing a S+B fit to the Asimov dataset, i.e. to a pseudo-data sample where the yields in each bin are set to be exactly equal to the background prediction in that bin. The central values are all equal to zero, indicating the absence of serious numerical instabilities in the fit, and the size of the error bars indicate the level of in-situ reduction of each of systematic uncertainty through the profile likelihood procedure. Systematic uncertainties here described provide in reality just a simplified model, that turned out not to be flexible enough for the final fit to the data. This can be seen from the strong constraints on the nuisance parameters related to some of the $t\bar{t}$ modelling systematic uncertainties, when applying the fit to the Asimov data-set (see Fig. 6.22). This is happening because some of these systematic variations on the $t\bar{t}$ prediction are so large that the data in high-statistics bins of the discriminant distributions (mainly the low part of the $m_{t\bar{t}}$-proxy spectrum) has enough power to constrain the related nuisance parameters, i.e. to restrict their allowed values to intervals significantly smaller than the standard deviation of their Gaussian constraints in the likelihood (the "pre-fit" values of the uncertainties). This effect is dangerous and considered in most cases inappropriate for theory modelling systematic uncertainties, especially for those obtained by varying different things at the same time in the MC simulation, lacking flexibility for an effective "in situ" calibration such as this nuisance-parameter constraining effect. However, in this case the expected limits evaluated with such simplified model can be taken seriously, as it is expected that a more elaborated and flexible systematic uncertainty model, foreseen to be ready for the final analysis of the real data, will include smaller systematic uncertainty variations, eventually with a larger number of associated nuisance parameters controlling different effects, and therefore looser constraints on the nuisance parameters after the fit to the data (or Asimov data). These two effects, i.e. systematic variations being smaller but nuisance parameters being less constrained, would then partially cancel out, for a net effect of a final signal sensitivity roughly equal to the one estimated in this thesis. Fig. 6.23 and Fig. 6.24 show, for different signal samples (Z' 750 GeV, g_{KK} 2 TeV and G 500 GeV) the ranking of $m_{\ell\ell bb}$ and $m_{t\bar{t}}^{NW}$ main systematic uncertainties, including the pulls and the impact of constraining the systematic uncertainties. The leading systematics uncertainties depend from the simulated signal and the mass variable used, as shown in the plots. These uncertainties are only for the $t\bar{t}$ background sample;

simulated signals and other background samples are not taken into account, as described before.

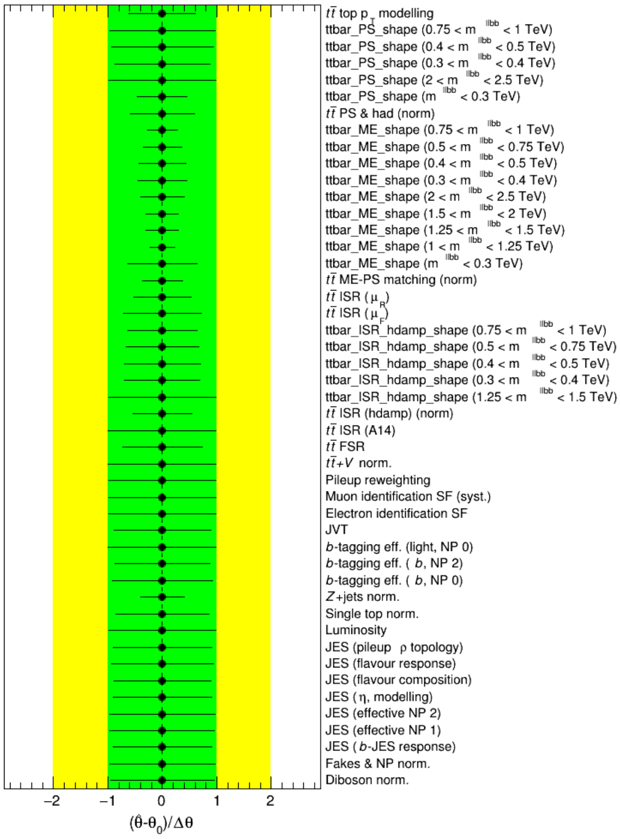

FIGURE 6.22: List of the nuisance parameters under study for a signal sample Z' 2 TeV in $m_{\ell\ell bb}$ variable.

Other plots showing the effect of systematic uncertainties are shown in Appendix C.

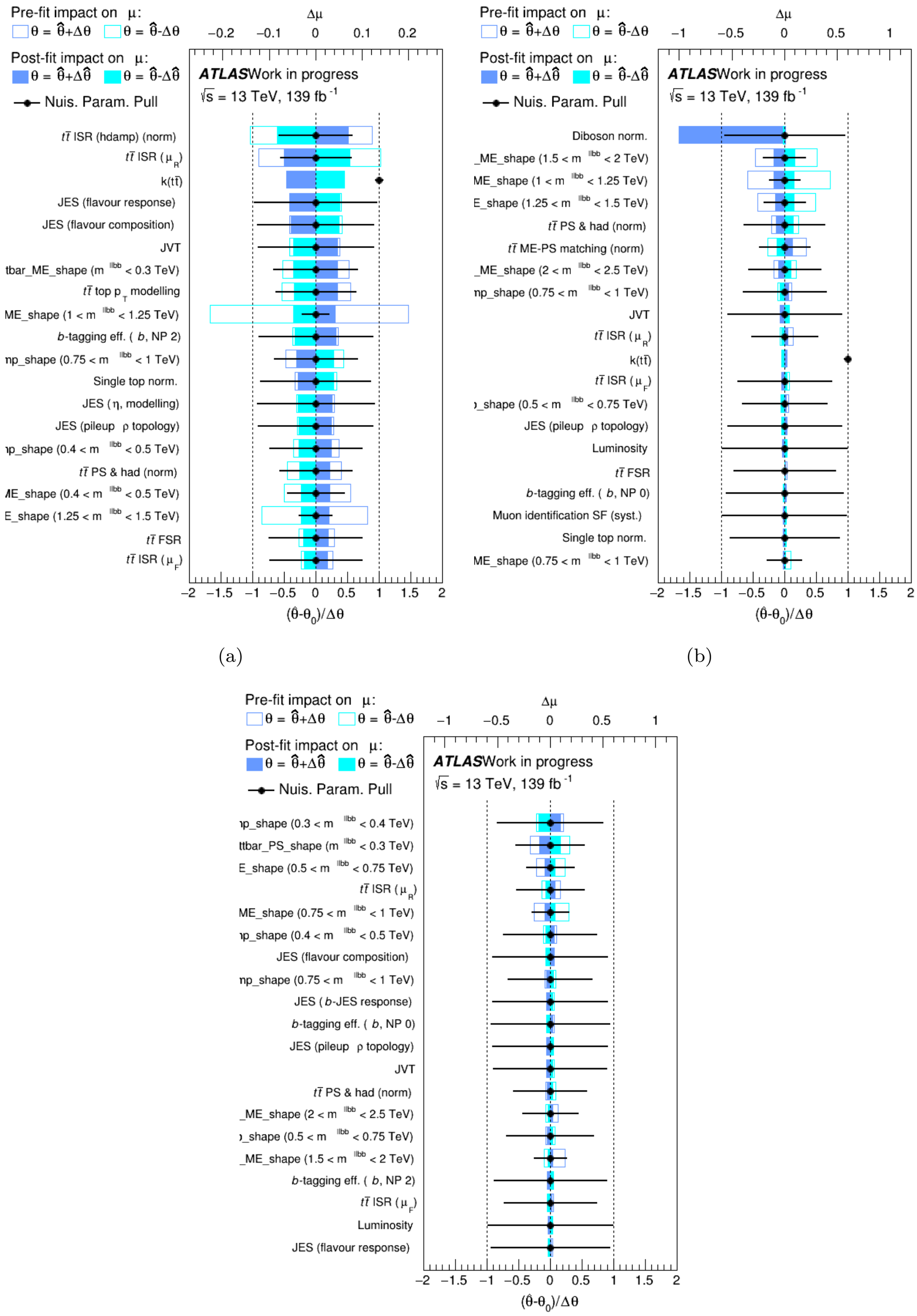

(a) (b) (c)

FIGURE 6.23: Ranking plots for $m_{\ell\ell bb}$: Z' 750 GeV (a), g_{KK} 2 TeV (b) and G 500 GeV (c). Only $t\bar{t}$ systematics uncertainties are taken into account.

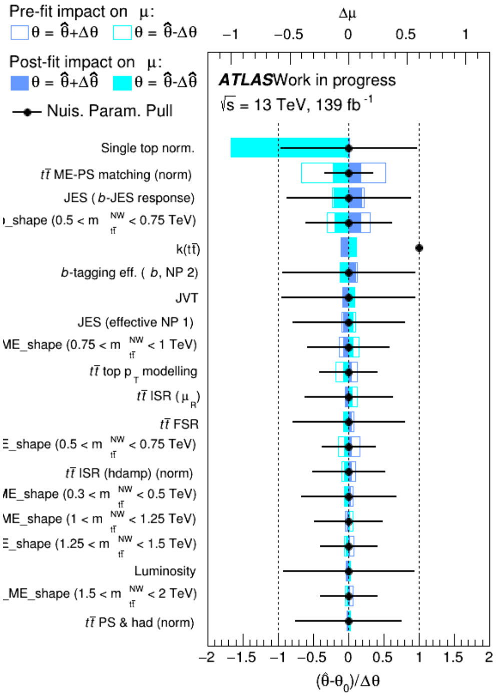

(a)

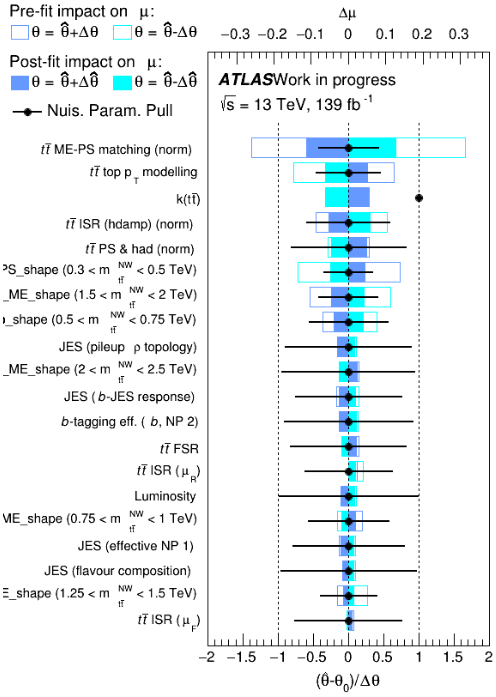

(b)

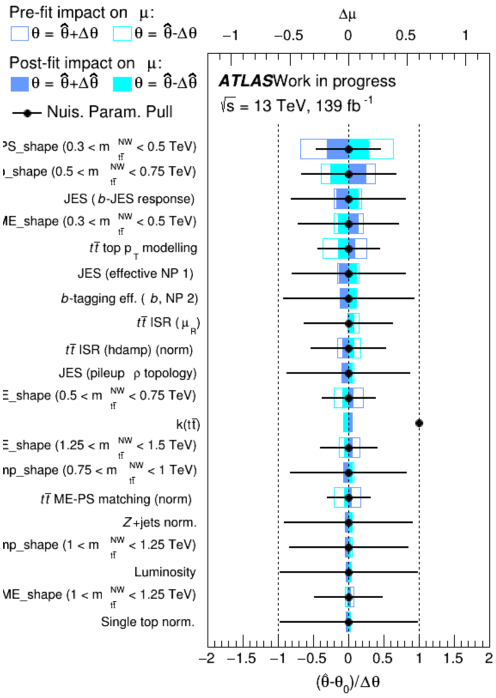

(c)

FIGURE 6.24: Ranking plots for $m_{t\bar{t}}^{NW}$: Z' 750 GeV (a), g_{KK} 2 TeV (b) and G 500 GeV (c). Only $t\bar{t}$ systematics uncertainties are taken into account.

6.9 Results

In this section, the final expected limits on the theoretical models (described in Chapter 1) are shown. To improve the signal sensitivity, the three final states (ee,$\mu\mu$ and $e\mu$) are combined together in each of the two mass variables ($m_{t\bar{t}}^{NW}$ and $m_{\ell\ell bb}$) considered in this analysis.
Limits on cross section times branching ratio as a function of the signal mass are obtained, using a two-dimensional fit of the spin-sensitive variable $|\Delta\phi^{\ell\ell}|/\pi$ versus the mass variable (either $m_{\ell\ell bb}$ or $m_{t\bar{t}}^{NW}$), with the setup described in section 6.6.
Fig. 6.25 shows the 95% C.L. expected exclusion limit on the cross section times branching ratio versus the mass of the Z' signal (from 500 GeV to 4 TeV), Kaluza-Klein gluon g_{KK} signal (from 500 GeV to 4.5 TeV) and Randall-Sundrum graviton G (from 400 GeV to 2 TeV), respectively, using the $\Delta\phi$ scan in the $m_{t\bar{t}}^{NW}$ invariant mass variable. The black dots are the expected limit, the red line is the theory and in green and yellow are $\pm$ 1σ and $\pm$ 2σ standard deviation, respectively. Plots show that the dilepton analysis is sensible to the low-mass region of Z' and G. In particular a Z' mass below 1.85 TeV, a g_{KK} mass below 3.25 TeV and a G mass below 800 GeV can be exluded. In this limits statistical (taken into account from the expected data statistics) and systematics uncertainties are included.
Fig. 6.26 shows the 95% C.L. expected exclusion limit on the cross section times branching ratio versus the mass of the Z' signal (from 500 GeV to 4 TeV), Kaluza-Klein gluon g_{KK} signal (from 500 GeV to 4.5 TeV) and Randall-Sundrum graviton G (from 400 GeV to 2 TeV), respectively, using the $\Delta\phi$ scan in the $m_{\ell\ell bb}$ invariant mass variable. The black dots are the expected limit, the red line is the theory and in green and yellow are $\pm$ 1σ and $\pm$ 2σ standard deviation, respectively. Plots show that the dilepton analysis is sensible to the low-mass region of Z' and G. In particular a Z' mass below 1.8 TeV, a g_{KK} mass below 3.1 TeV and a G mass below 800 GeV can be exluded. In this limits statistical (taken into account from the expected data statistics) and systematics uncertainties are included.
As it is possible to see in the limits plots, comparing the two mass variables, the expected limits obtained from $m_{t\bar{t}}^{NW}$ are slightly worse than the $m_{\ell\ell bb}$, due to the fact that, as described in section 6.3.2, the NW method becomes inefficient in reconstructing top quark pairs produced by high mass resonances.
Tab. 6.11 shows the expected limits obtained with $m_{\ell\ell bb}$ and $m_{t\bar{t}}^{NW}$ for the three

different simulated signal samples. These limits can be compared to the expected limits from different analyses ([25], [29] and [31]), as shown in Tab. 6.12. It is possible to see, using the dilepton analysis, that a very good improvement in the expected limits of the resonance masses is measured. Moreover, in the low mass region (less than 1 TeV) the systematics uncertainties are dominant, instead, the statistical uncertainties are dominant in the higher mass regions; an increasing of the statistics can improve the limits at higher resonance masses. In conclusion, it can be assert that this analysis, comparing it with the old ones, is a good way to search the BSM resonances from the top quark pair decays.

TABLE 6.11: Expected mass limits obtained with the dilepton analysis.

Variable	Z' [TeV]	g_{KK} [TeV]	G [TeV]
$m_{\ell\ell bb}$	1.8	3.1	0.8
$m_{t\bar{t}}^{NW}$	1.85	3.25	0.8

TABLE 6.12: Expected mass limits obtained in different analyses.

Analysis, CoM, Int. Lumi.	Z' [TeV]	g_{KK} [TeV]	G [TeV]
ATLAS $l+jets$, 13 TeV, 36.1 fb^{-1} [29]	2.6	3.2	0.65
ATLAS *Dilepton*, 7 TeV, 1.04 fb^{-1} [31]		0.84	
CMS $All-channels$, 13 TeV, 35.9 fb^{-1} [25]	(Γ/m 1%) 3.8		
	(Γ/m 10%) 5.25		
	(Γ/m 30%) 6.65		
		4.55	

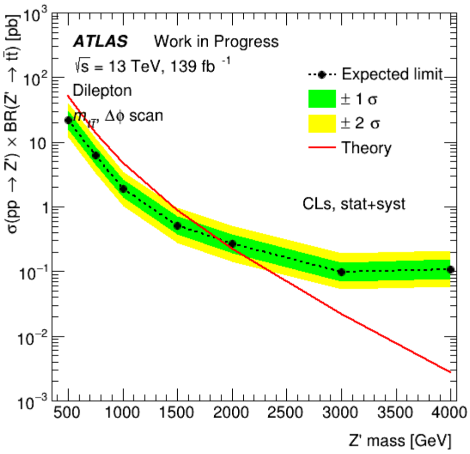

(a)

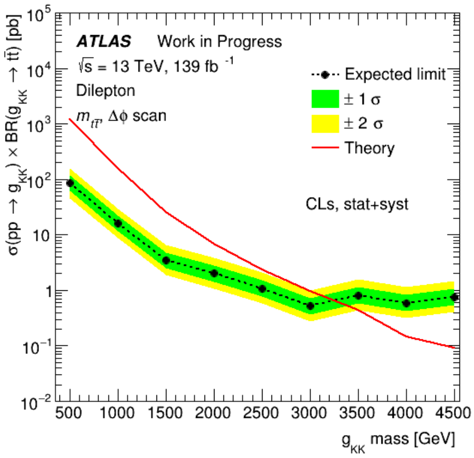

(b)

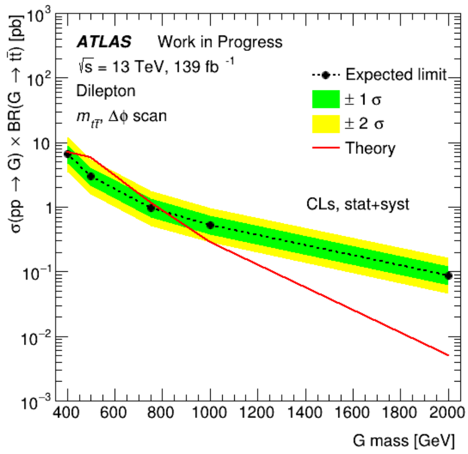

(c)

FIGURE 6.25: Expected limit of the $\Delta\phi$ scan with the $m_{t\bar{t}}^{NW}$ invariant mass variable. The plots are for Z' (a), g_{KK} (b) and G (c). Errors are both statistical and systematics. The limits exclude a Z' mass below 2 TeV, a g_{KK} mass below 3.3 TeV and a G mass below 900 GeV.

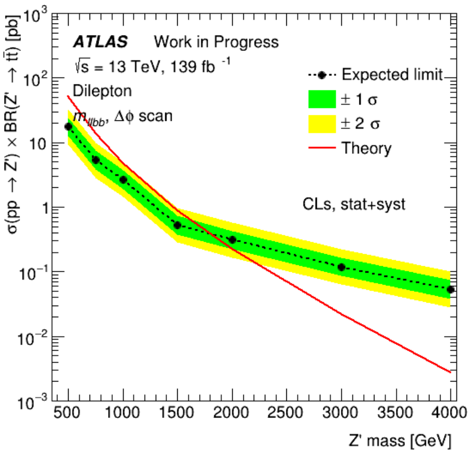

(a)

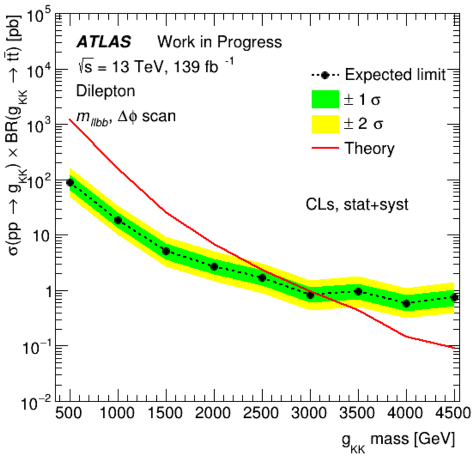

(b)

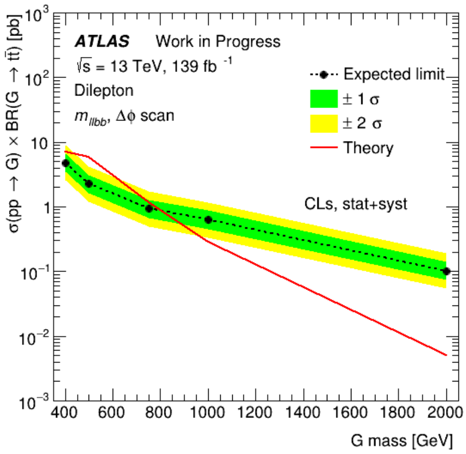

(c)

FIGURE 6.26: Expected limit of the $\Delta\phi$ scan with the $m_{\ell\ell bb}$ proxy variable. The plots are for Z' (a), g_{KK} (b) and G (c). Errors are both statistical and systematics. The limits exclude a Z' mass below 2.35 TeV, a g_{KK} mass below 3.5 TeV and a G mass below 1 TeV.

Chapter 7

Conclusions

Between 2015 and 2018, the LHC delivered proton-proton collisions with a centre-of-mass energy of $\sqrt{s} = 13$ TeV. In this thesis results are shown from the analysis of the high energy collision data recorded by the ATLAS detector.

Three studies covering different aspects of the search for a $t\bar{t}$ resonance in the dilepton final state have been presented. The first part aims to measure the reconstruction efficiency for muons close to jets. This study was done using 2016 data collected from the ATLAS experiment and confirms that the reconstruction efficiency for muons close to jets is unchanged with respect to the isolated muons.

The second part aims to study different electron isolation working points and the extension of the electron overlap removal procedure for the region $0.2 < \Delta R < 0.4$ (electrons close to jets). An increase of the signal over background ratio can be achieved using this setup compared to the default one of the ATLAS experiment Group.

The last part illustrates the analysis performed to targed heavy mass resonances in case the new particle decays into top quark pairs, done with the simulated sample referred to the full Run2 collected by the ATLAS experiment (139 fb^{-1}). The 95% C.L. exclusion limits on the cross section times branching ratio versus the mass of the signal samples are produced in this thesis. The expected limits, using the $m_{\ell\ell bb}$ proxy variable, exclude a Z' mass below 1.8 TeV, a g_{KK} mass below 3.1 TeV and a G mass below 0.8 TeV, respectively. The expected limits, using the $m_{t\bar{t}}^{NW}$ proxy variable, exclude a Z' mass below 1.85 TeV, a g_{KK} mass below 3.25 TeV and a G mass below 0.8 TeV, respectively.

Appendix A

Muon close to jets efficiency Tag-and-Probe study

This appendix shows the additional event selections and plots about the reconstruction efficiencies, discussed in Chapter 4.

About the selection, events are required to be included in good luminosity block; the GRL

data16_13TeV.periodAllYear_DetStatus-v89-pro21-01_DQDefects-00-02-04_PHYS_StandardGRL_All_Good_25ns.xml

For the Monte Carlo simulation we are used two kind of sets:

- group.perf-muons.mc16_13TeV.424108.Pythia8B_A14_CTEQ6L1_Jpsimu6.NTUP_MCP.r9781_r9778_p3374_v047_EXT0, used for information about the Calo muon probes;
- group.perf-muons.mc16_13TeV.424108.Pythia8B_A14_CTEQ6L1_Jpsimu6.NTUP_MCP.r9955_r9315_v047_EXT0, used for information about the MS probes.

Single muon triggers and triggers requiring one muon and an ID track are used in Overlap Removal:

- HLT_mu4,
- HLT_mu6,

- HLT_mu6_idperf.

The following triggers are added to the list when using ID tracks, CaloTagged muons, Loose Muions, Medium muons or Tight muons as probes:

- HLT_mu4_bJpsi_Trkloose,
- HLT_mu6_bJpsi_Trkloose,
- HLT_mu10_bJpsi_Trkloose,
- HLT_mu18_bJpsi_Trkloose.

For the medium muon efficiencies we used seven bin in p_T [5-6,6-7,7-8,8-10,10-12,12-15,15-20] GeV and nine bin in η [-2.5,-2.0,-1.3,-1.05,-0.1,0.1,1.05,1.3,2.0,2.5]. Figure A.1 show the reconstruction efficiency, using only data 2016, for medium muons with calo muons as probes, versus the p_T in two different regions of isolation $p_T^{varcone30}/p_T(probe)$: in black the values of efficiency for isolation smaller than 0.06 (isolated muons), in red the values of efficiency for isolation larger than 0.06 (non-isolated muons). Is possible to see that the shapes are similar and there are not big difference between isolated and non-isolated muons.
Figure A.2 show the reconstruction efficiency, using only data 2016, for medium muons with calo muons as probes, versus the p_T in two different regions of isolation $E_T^{topocone20}/p_T(probe)$: in black the values of efficiency for isolation smaller than 0.06 (isolated muons), in red the values of efficiency for isolation larger than 0.06 (non-isolated muons). Is possible to see that the shapes are similar and there are not big difference between isolated and non-isolated muons.
Figure A.3 show the reconstruction efficiency, using only data 2016, for medium muons with calo muons as probes, versus the p_T in two different regions of ΔR for non-isolated muons: in black the non-isolated muons between $0 < \Delta R < 0.2$, in red the non-isolated muons between $0.2 < \Delta R < 0.4$. Is possible to see that the shapes are similar but there are some difference between the two regions of ΔR for low p_T values when the ΔR is between 0 and 0.2, this is due the fact that there are some background events in the Tag-ad-Probe samples.

For the medium muon efficiencies we used seven bin in p_T [5-6,6-7,7-8,8-10,10-12,12-15,15-20] GeV and nine bin in η [-2.5,-2.0,-1.3,-1.05,-0.1,0.1,1.05,1.3,2.0,2.5]. Figure A.4 show the reconstruction efficiency, using only Monte Carlo, for medium muons with calo muons as probes, versus the p_T in two different regions of isolation $p_T^{varcone30}/p_T(probe)$: in black the values of efficiency for isolation smaller than 0.06 (isolated muons), in red the values of efficiency for isolation larger than 0.06 (non-isolated muons). Is possible to see that the shapes are similar and there are not big difference between isolated and non-isolated muons.
Figure A.6 show the reconstruction efficiency, using only Monte Carlo, for medium muons with calo muons as probes, versus the p_T in two different regions of isolation $E_T^{topocone20}/p_T(probe)$: in black the values of efficiency for isolation smaller than 0.06 (isolated muons), in red the values of efficiency for isolation larger than 0.06 (non-isolated muons). Is possible to see that the shapes are similar and there are not big difference between isolated and non-isolated muons.
Figure A.5 show the reconstruction efficiency, using only Monte Carlo, for medium muons with calo muons as probes, versus the p_T in two different regions of ΔR for non-isolated muons: in black the non-isolated muons between $0 < \Delta R < 0.2$, in red the non-isolated muons between $0.2 < \Delta R < 0.4$. Is possible to see that the shapes are similar but there are some difference between the two regions of ΔR for low p_T values when the ΔR is between 0 and 0.2, this is due the fact that there are some background events in the Tag-and-Probe samples.

Figures A.7, A.8 and A.9 show the scale factors for, respectively, the various regions of isolation $p_T^{varcone30}/p_T(probe)$, ΔR between muon and its nearest jet and isolation $E_T^{topocone20}/p_T(probe)$. For the SF in these regions, within the statistical error there are not big differences. Moreover, a χ^2 test confirms that efficiencies for non-isolated muons are compatible with those of isolated muons.

For the ID muon efficiencies we used eight bin in p_T [4-5,5-6,6-7,7-8,8-10,10-12,12-15,15-20] GeV and nine bin in η [-2.5,-2.0,-1.3,-1.05,-0.1,0.1,1.05,1.3,2.0,2.5]. Figure A.10 show the reconstruction efficiency, using only data 2016, for ID muons with MS muons as probes, versus the p_T in two different regions of isolation $p_T^{varcone30}/p_T(probe)$: in black the values of efficiency for isolation smaller than 0.06, in red the values of efficiency for isolation larger than 0.06. Is possible to see that the shapes are similar

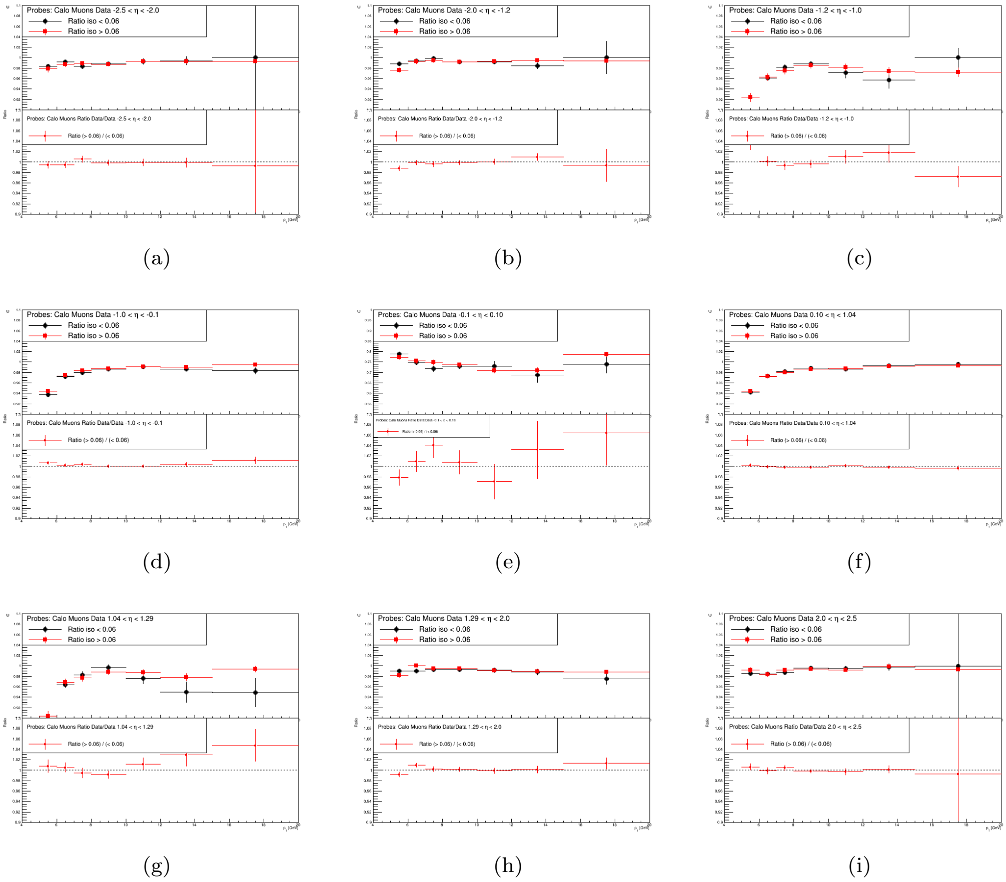

(a) (b) (c)

(d) (e) (f)

(g) (h) (i)

FIGURE A.1: Top of plots: medium muon efficiency, using data samples, with calo muons as probes in two different regions of isolation: Black: $p_T^{varcone30}/p_T(probe) < 0.06$; Red: $p_T^{varcone30}/p_T(probe) > 0.06$. Bottom of plots: ratio between the isolated and non-isolated muons, data only.

and there are not big difference between isolated and non-isolated muons.

Figure A.11 show the reconstruction efficiency, using only data 2016, for ID muons with MS muons as probes, versus the p_T in two different regions of isolation $E_T^{topocone20}/p_T(probe)$: in black the values of efficiency for isolation smaller than 0.06, in red the values of efficiency for isolation larger than 0.06. Is possible to see that the shapes are similar and there are not big difference between isolated and non-isolated muons.

Figure A.12 show the reconstruction efficiency, using only data 2016, for ID muons with MS muons as probes, versus the p_T in two different regions of ΔR: in black the region $0 < \Delta R < 0.2$, in red the isolated muons $0.2 < \Delta R < 0.4$. Is possible to see that the shapes are similar and there are not big difference between the two regions.

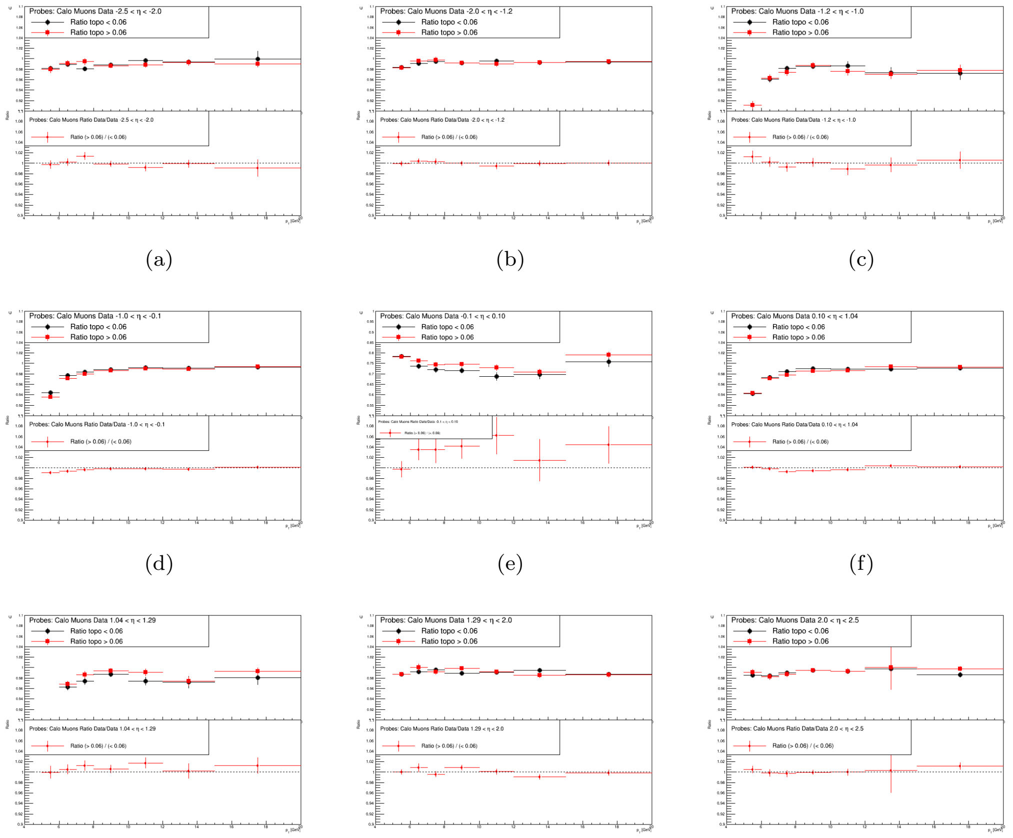

(a) (b) (c)

(d) (e) (f)

(g) (h) (i)

FIGURE A.2: Top of plots: medium muon efficiency, using data samples, with calo muons as probes in two different regions of isolation: Black: $E_T^{topocone20}/p_T(probe) < 0.06$; Red: $E_T^{topocone20}/p_T(probe) > 0.06$. Bottom of plots: ratio between the two regions of isolation, data only.

Figure A.13 show the reconstruction efficiency, using only Monte Carlo, for ID muons with MS muons as probes, versus the p_T in two different regions of isolation $p_T^{varcone30}/p_T(probe)$: in black the values of efficiency for isolation smaller than 0.06, in red the values of efficiency for isolation larger than 0.06. Is possible to see that the shapes are similar and there are not big difference between isolated and non-isolated muons.

Figure A.14 show the reconstruction efficiency, using only Monte Carlo, for ID muons with MS muons as probes, versus the p_T in two different regions of isolation $E_T^{topocone20}/p_T(probe)$: in black the values of efficiency for isolation smaller than 0.06, in red the values of efficiency for isolation larger than 0.06. Is possible to see that the shapes are similar and there are not big difference between isolated and

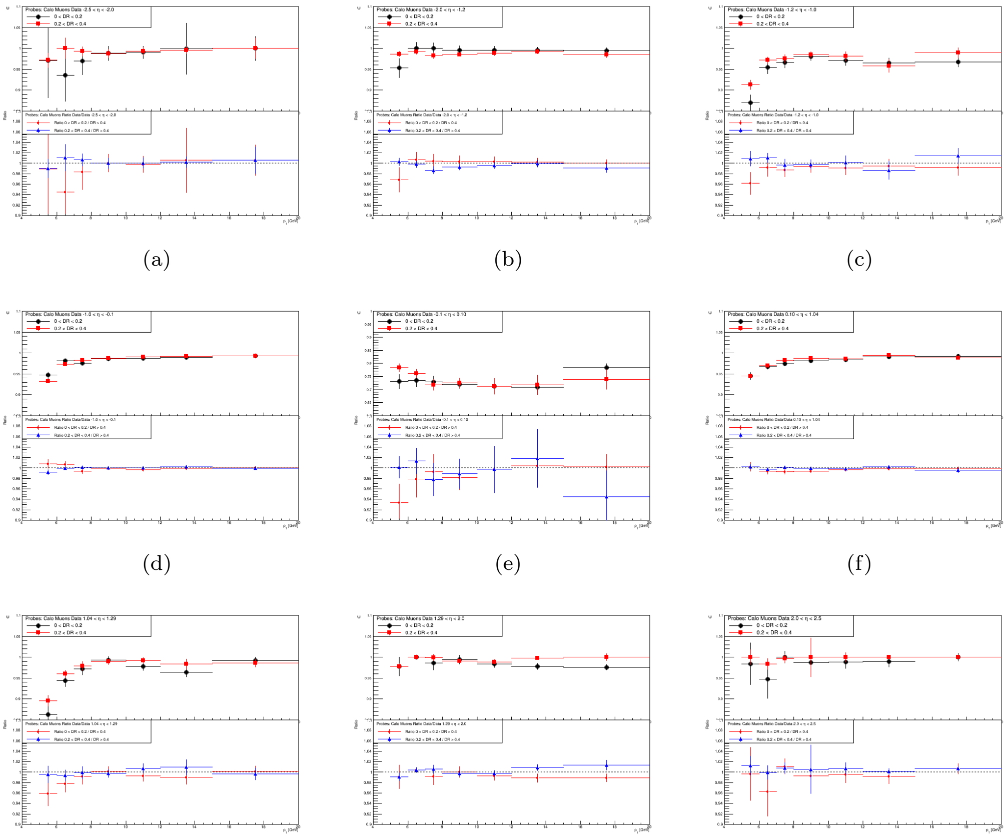

(a) (b) (c)

(d) (e) (f)

(g) (h) (i)

FIGURE A.3: Top of plot: medium muon efficiency, using data samples, with calo muons as probes in two different regions of ΔR: Black: $0 < \Delta R < 0.2$; Red: 0.2 $< \Delta R < 0.4$. Bottom of plots: ratio between the two different regions, data only.

non-isolated muons.

Figure A.15 show the reconstruction efficiency, using only Monte Carlo, for ID muons with MS muons as probes, versus the p_T in two different regions of ΔR: in black the region $0 < \Delta R < 0.2$, in red the isolated muons $0.2 < \Delta R < 0.4$. Is possible to see that the shapes are similar and there are not big difference between the two regions.

Figures A.16, A.17 and A.18 show the scale factors for, respectively, the two regions of isolation $p_T^{varcone30}/p_T(probe)$, the two regions of isolation $E_T^{topocone20}/p_T(probe)$ and the various regions of ΔR between the muon and its nearest jet. All these SFs are close to one.

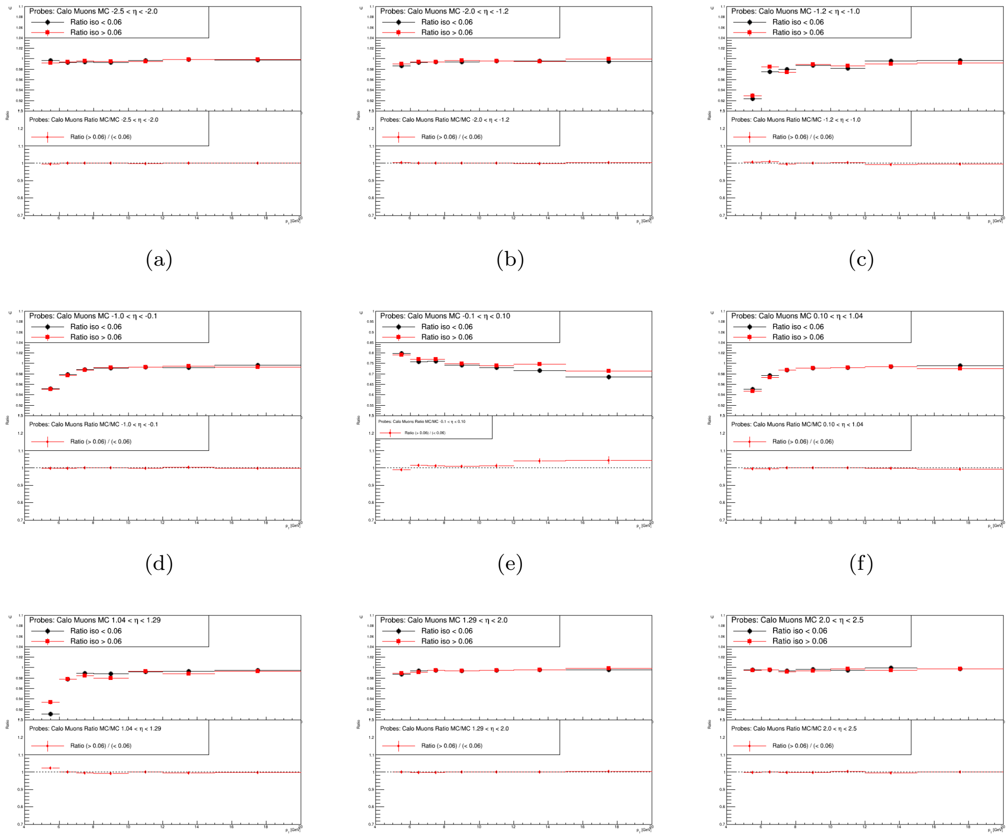

(a) (b) (c) (d) (e) (f) (g) (h) (i)

FIGURE A.4: Top of plots: medium muon efficiency, using MC samples, with calo muons as probes in two different regions of isolation: Black: $p_T^{varcone30}/p_T(probe) < 0.06$; Red: $p_T^{varcone30}/p_T(probe) > 0.06$. Bottom of plots: ratio between the isolated and non-isolated muons, MC only.

Was also made a comparison between my SFs and the official MCP SFs that are show below. In the following plot the SFs are measured as the product of the efficiencies of medium muons with calo muons as probes and the ID tracks with the MS muons as probes.

In all regions of isolation (e.g. the ratio $p_T^{varcone30}/p_T(probe)$ and $E_T^{topocone20}/p_T(probe)$) under study is possible to see a good agreement between the two SFs; for the ΔR regions, instead, there are some differences, this is due to the fact that the MC of the J/Ψ sample does not have enough probes close the jets and in the data there are some background events. But within the statistical errors there is a good agreement between the SFs for muons close to jets and the official MCP SFs.

Figure A.19 show the comparison between the SFs in the region $p_T^{varcone30}/p_T(probe) <$

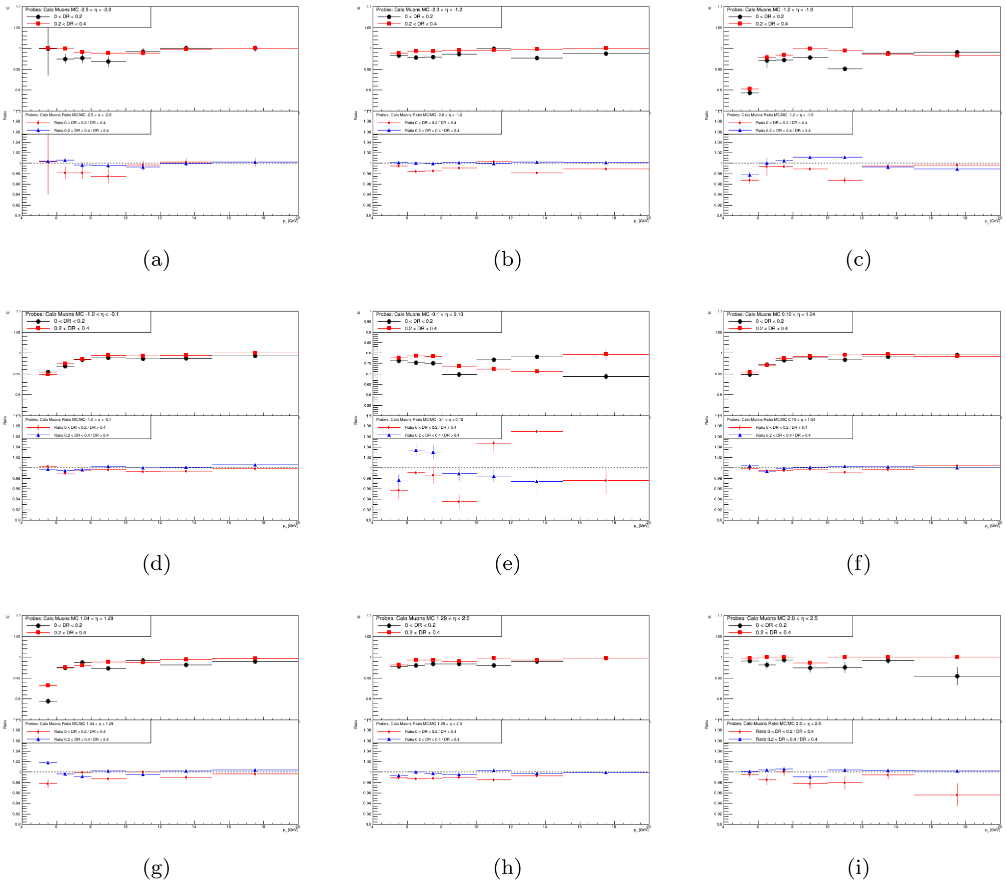

(a) (b) (c)

(d) (e) (f)

(g) (h) (i)

FIGURE A.5: Top of plots: Medium muon efficiency, using MC sample, with calo muons as probes in two different regions of ΔR: Black: $0 < \Delta R < 0.2$; Red: 0.2 $< \Delta R < 0.4$. Bottom of plots: ratio between the two different regions, MC only.

0.06 (red) and the official MCP SFs (black). In some bin of η for values of p_T of the probe around 12-15 and 15-20 GeV there is some difference between the two SFs, this is due to the fact that there are not enough non-isolated muons in this sample. But within the statistical errors, there is a good agreement.

Figure A.20 show the comparison between the SFs in the region $p_T^{varcone30}/p_T(probe) >$ 0.06 (red) and the official MCP SFs (black). In this region there is a good agreement between the SFs measured in this study and the official MCP SFs.

Figure A.21 show the comparison between the SFs in the region $E_T^{topocone20}/p_T(probe) <$ 0.06 (red) and the official MCP SFs (black). In this region there is a good agreement between the SFs measured in this study and the official MCP SFs.

Figure A.22 show the comparison between the SFs in the region $E_T^{topocone20}/p_T(probe) >$ 0.06 (red) and the official MCP SFs (black). In this region there is a good agreement

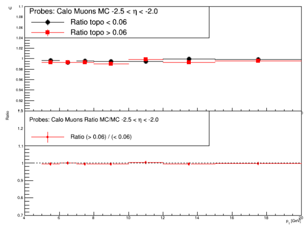

(a)

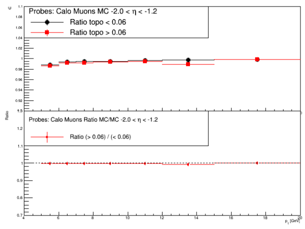

(b)

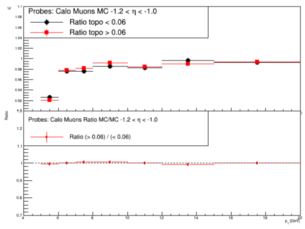

(c)

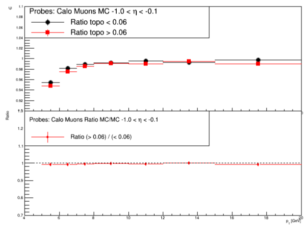

(d)

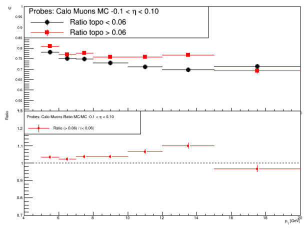

(e)

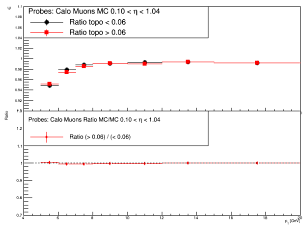

(f)

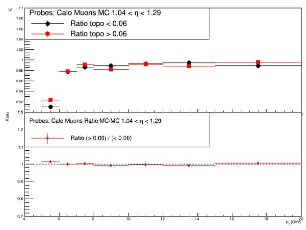

(g)

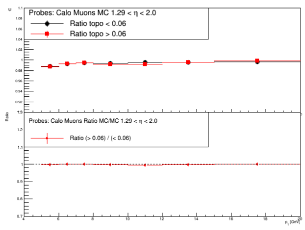

(h)

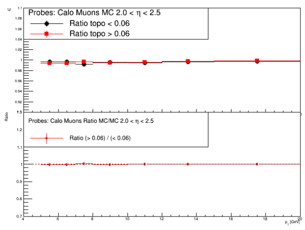

(i)

FIGURE A.6: Top of plots: medium muon efficiency, using MC samples, with calo muons as probes in two different regions of isolation: Black: $E_T^{topocone20}/p_T(probe) < 0.06$; Red: $E_T^{topocone20}/p_T(probe) > 0.06$. Bottom of plots: ratio between the isolated and non-isolated muons, MC only.

between the SFs measured in this study and the official MCP SFs.

Figure A.23 show the comparison between the SFs in the region $0 < \Delta R < 0.2$ (red) and the official MCP SFs (black). Is possible to see a certain difference between the two SFs, is due to the fact that in this region there are not enough probe in the sample, which entails an increase of the statistical error. But within the errors there is a good agreement.

Figure A.24 show the comparison between the SFs in the region $0.2 < \Delta R < 0.4$ (red) and the official MCP SFs (black). Is possible to see a certain difference between the two SFs, is due to the fact that in this region there are not enough probe in the sample, which entails an increase of the statistical error, but the SFs are better than the region $0 < \Delta R < 0.2$. But within the errors there is a good agreement.

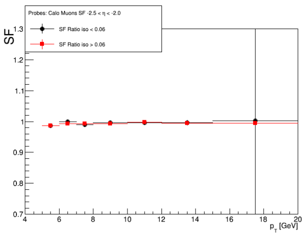

(a)

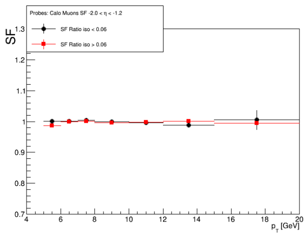

(b)

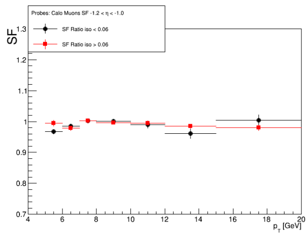

(c)

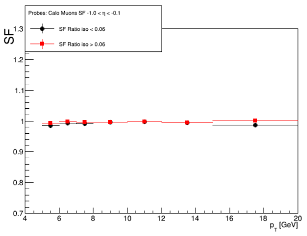

(d)

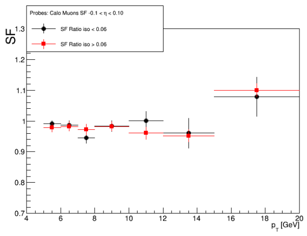

(e)

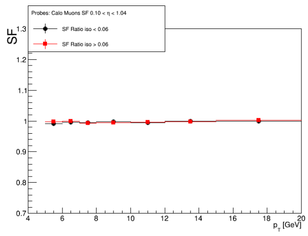

(f)

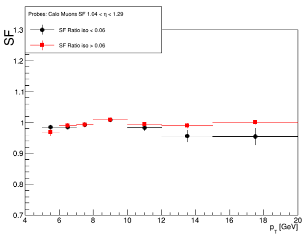

(g)

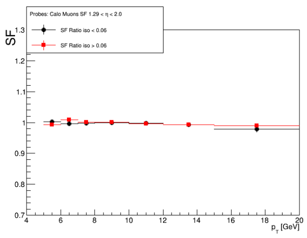

(h)

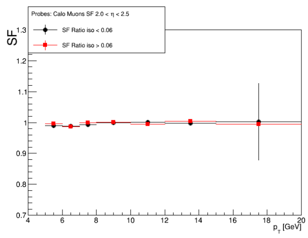

(i)

FIGURE A.7: Scale factor of the two different regions of isolation: Black: $p_T^{varcone30}/p_T(probe) < 0.06$; Red: $p_T^{varcone30}/p_T(probe) > 0.06$.

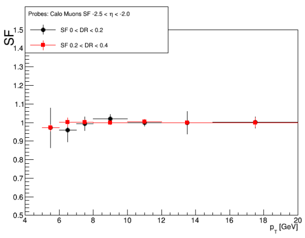

(a)

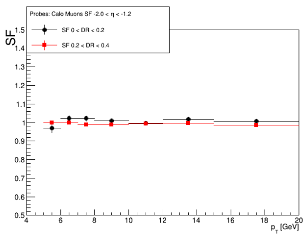

(b)

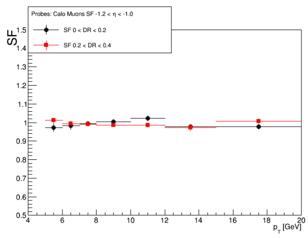

(c)

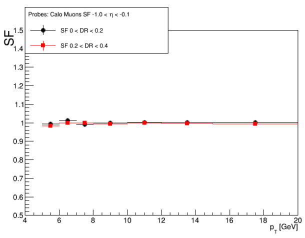

(d)

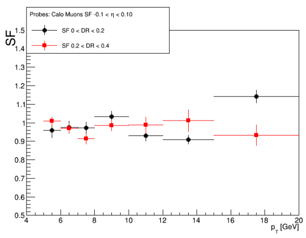

(e)

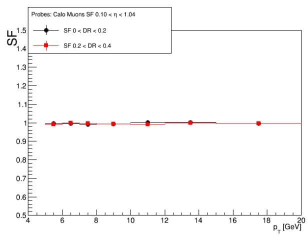

(f)

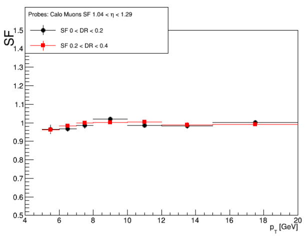

(g)

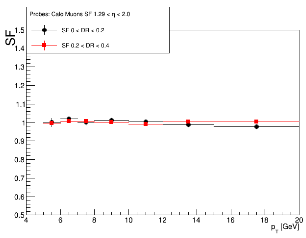

(h)

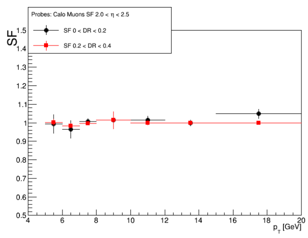

(i)

FIGURE A.8: Scale factor of the two different regions of ΔR: Black: $0 < \Delta R < 0.2$; Red: $0.2 < \Delta R < 0.4$.

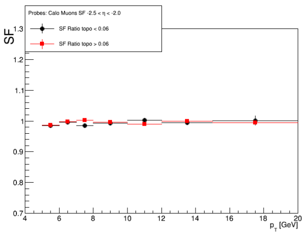

(a)

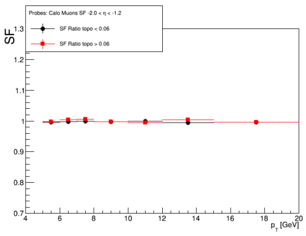

(b)

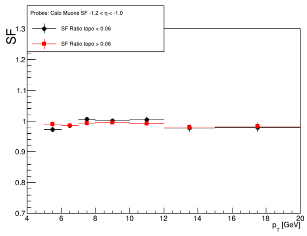

(c)

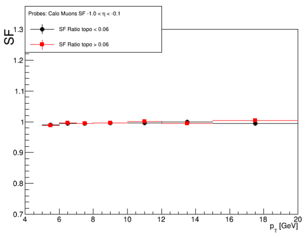

(d)

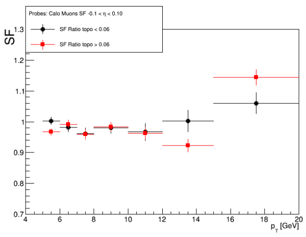

(e)

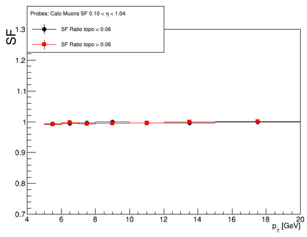

(f)

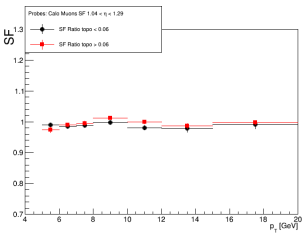

(g)

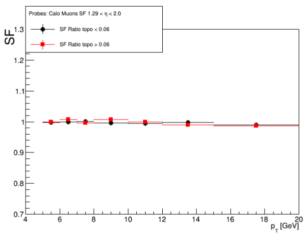

(h)

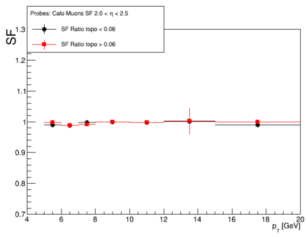

(i)

FIGURE A.9: Scale factor of the two different regions of isolation: Black: $E_T^{topocone20}/p_T(probe) < 0.06$; Red: $E_T^{topocone20}/p_T(probe) > 0.06$.

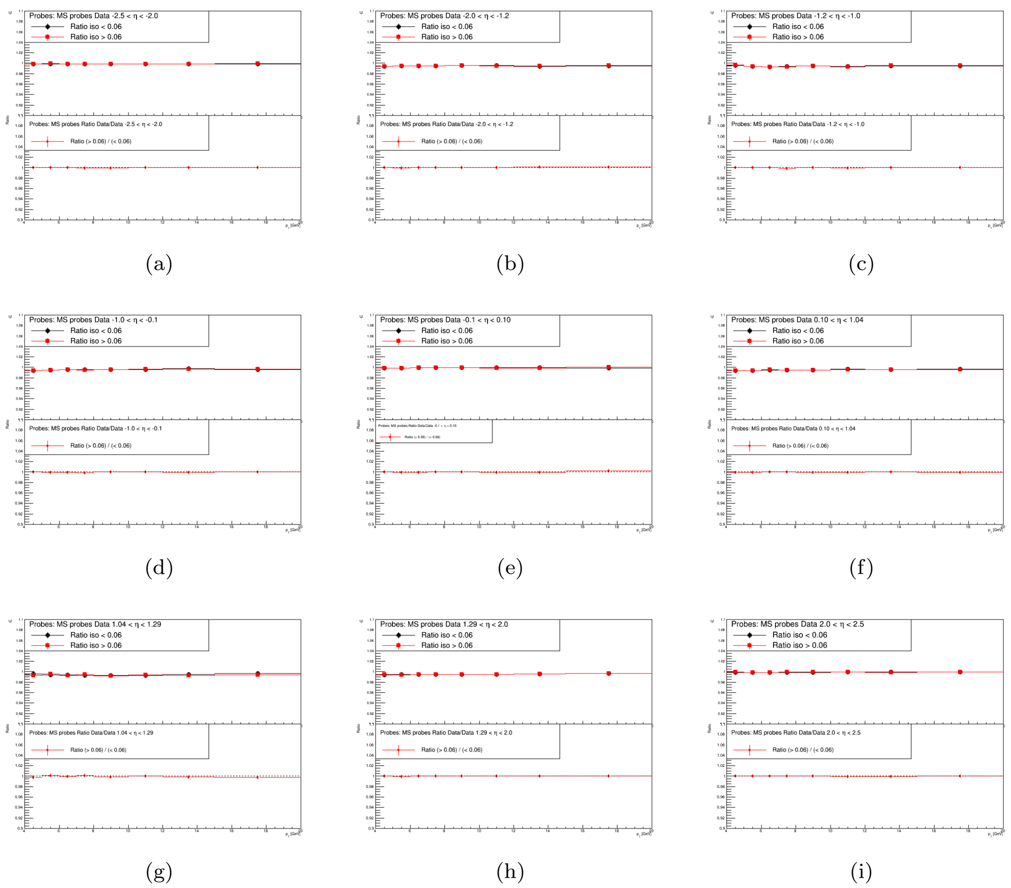

FIGURE A.10: Top of plots: ID muon efficiency, using data samples, with MS muons as probes in two different regions of isolation: Black: $p_T^{varcone30}/p_T(probe) < 0.06$ (isolated muons); Red: $p_T^{varcone30}/p_T(probe) > 0.06$ (non-isolated muons). Bottom of plots: ratio between the two regions of isolation, data only.

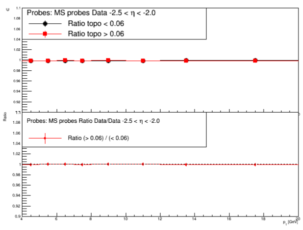

(a)

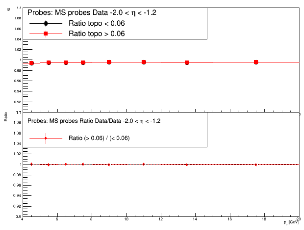

(b)

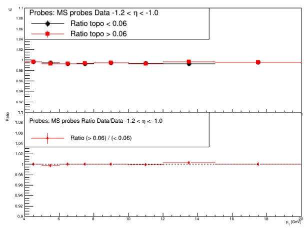

(c)

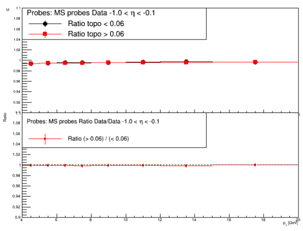

(d)

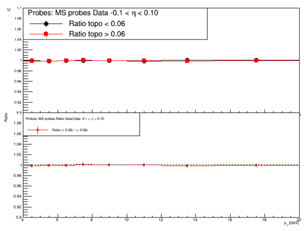

(e)

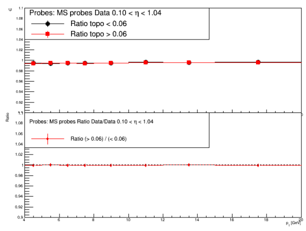

(f)

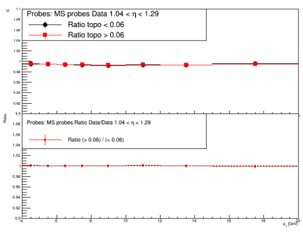

(g)

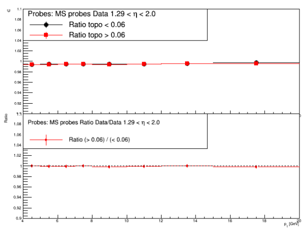

(h)

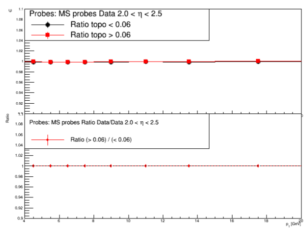

(i)

FIGURE A.11: Top of plots: ID muon efficiency, using data samples, with MS muons as probes in two different regions of isolation: Black: $E_T^{topocone20}/p_T(probe) < 0.06$ (isolated muons); Red: $E_T^{topocone20}/p_T(probe) > 0.06$ (non-isolated muons).Bottom of plots: ratio between the two regions of isolation, data only.

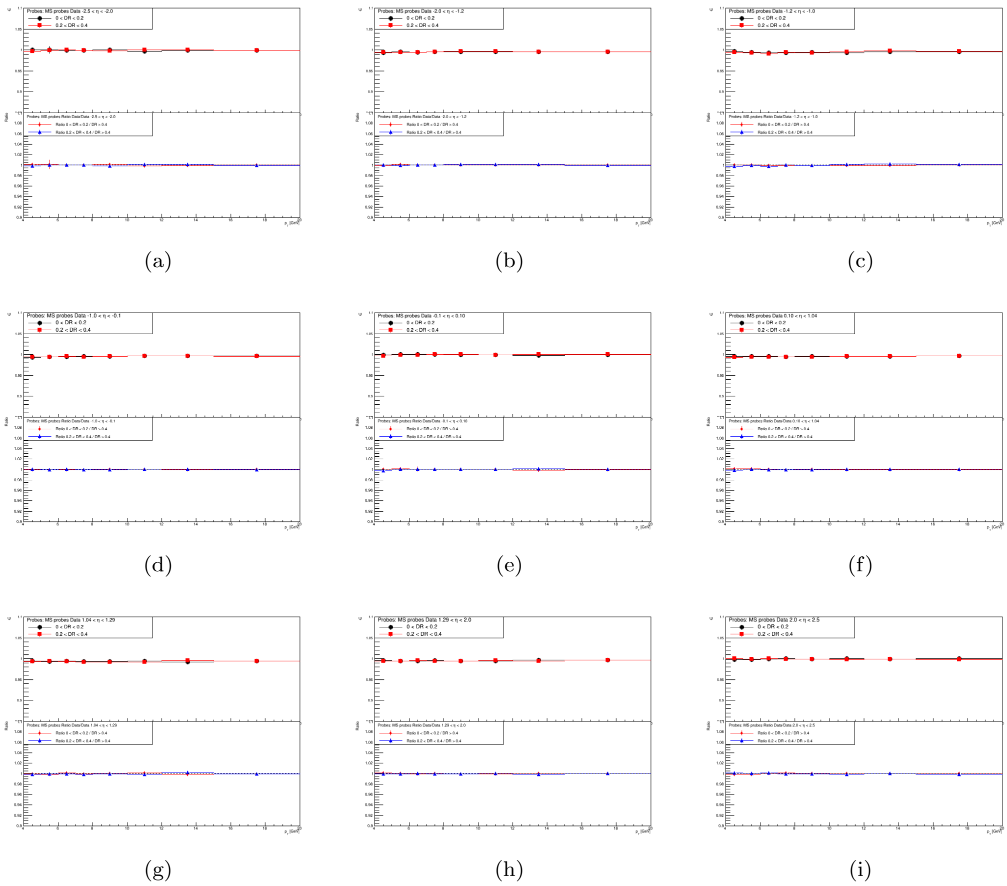

FIGURE A.12: Top of plot: ID muon efficiency, using data samples, with MS muons as probes in two different regions of ΔR: Black: $0 < \Delta R < 0.2$; Red: $0.2 < \Delta R < 0.4$. Bottom of plots: ratio between the two different regions, data only.

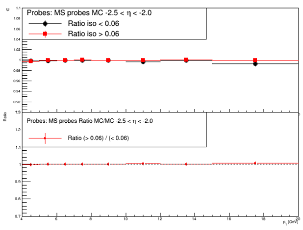

(a)

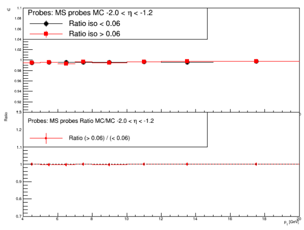

(b)

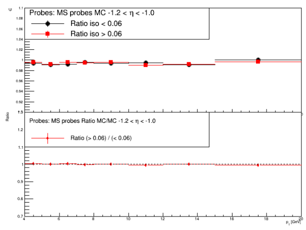

(c)

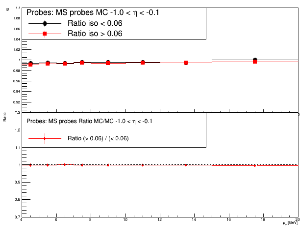

(d)

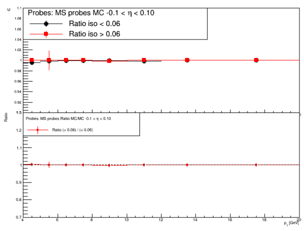

(e)

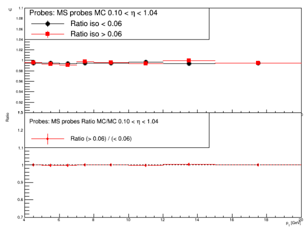

(f)

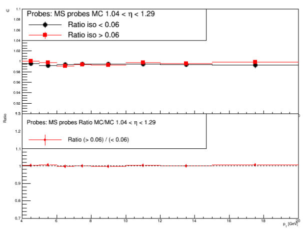

(g)

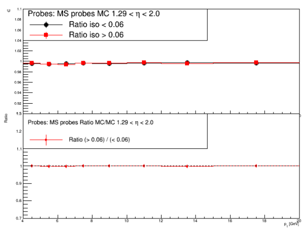

(h)

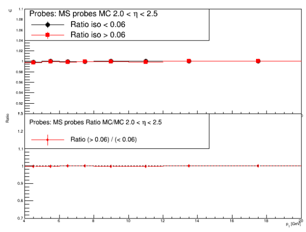

(i)

FIGURE A.13: Top of plots: ID muon efficiency, using MC samples, with MS muons as probes in two different regions of isolation: Black: $p_T^{varcone30}/p_T(probe) < 0.06$ (isolated muons); Red: $p_T^{varcone30}/p_T(probe) > 0.06$ (non-isolated muons). Bottom of plots: ratio between the two regions of isolation, MC only.

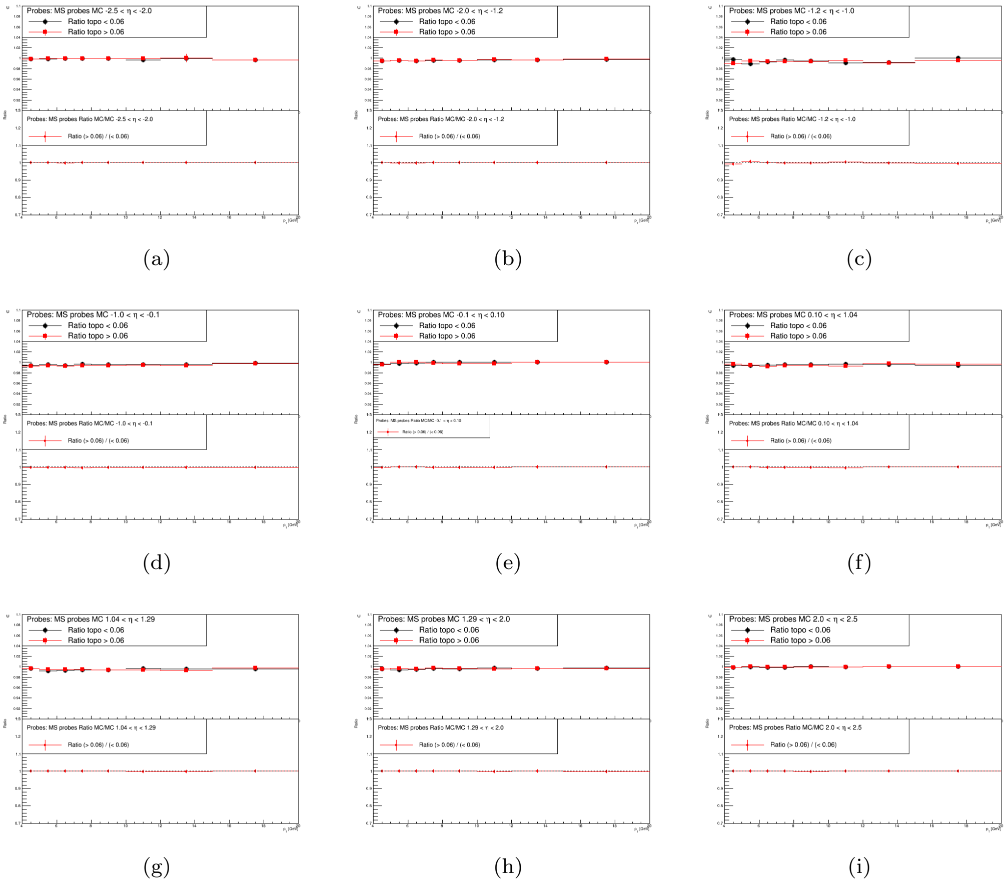

FIGURE A.14: Top of plots: ID muon efficiency, using data samples, with MS muons as probes in two different regions of isolation: Black: $E_T^{topocone20}/p_T(probe) < 0.06$ (isolated muons); Red: $E_T^{topocone20}/p_T(probe) > 0.06$ (non-isolated muons). Bottom of plots: ratio between the two regions of isolation, MC only.

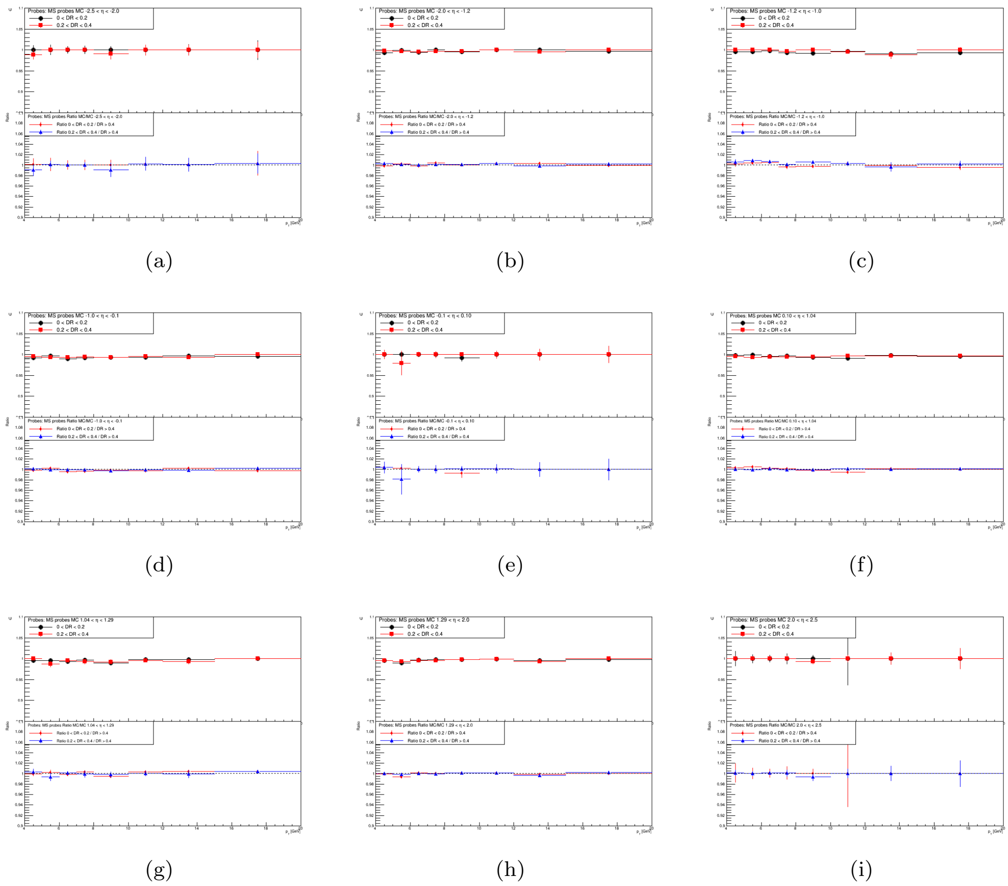

(a) (b) (c)

(d) (e) (f)

(g) (h) (i)

FIGURE A.15: Top of plots: ID muon efficiency, using MC sample, with MS muons as probes in two different regions of ΔR: Black: $0 < \Delta R < 0.2$; Red: $0.2 < \Delta R < 0.4$. Bottom of plots: ratio between the two different regions, MC only.

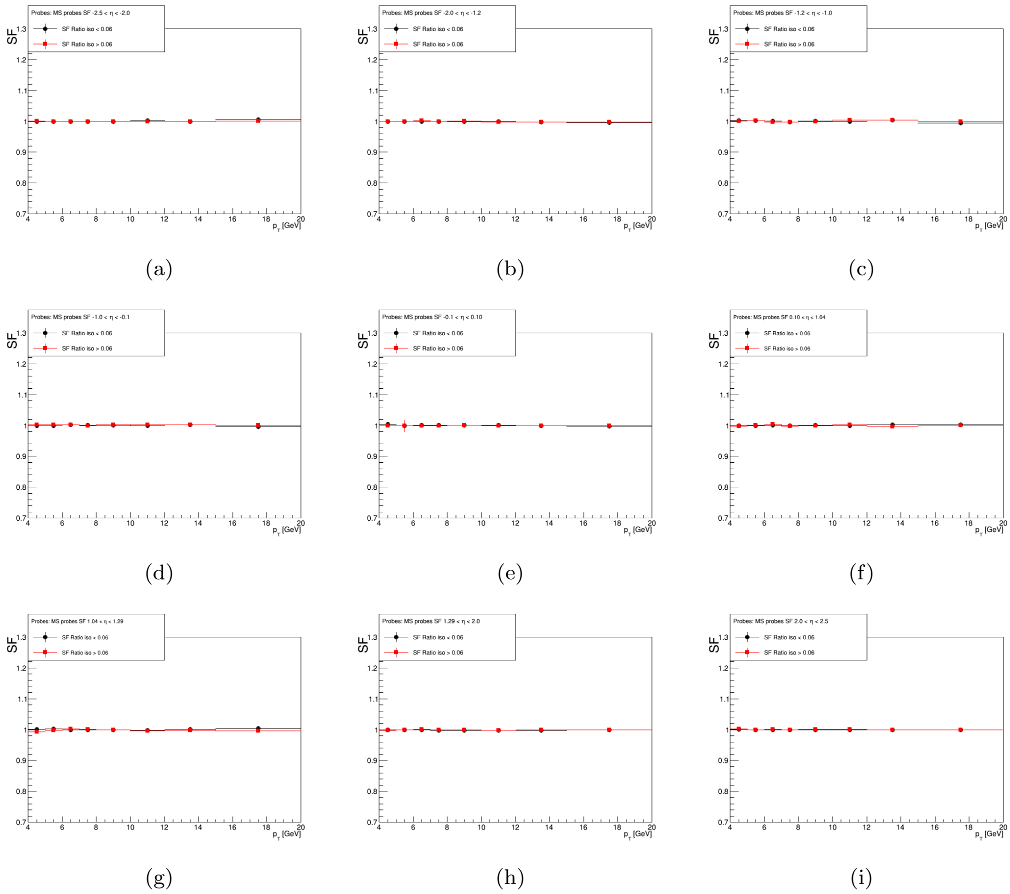

Figure A.16: Scale factor of the two different regions of isolation for ID muons: Black: $p_T^{varcone30}/p_T(probe) < 0.06$; Red: $p_T^{varcone30}/p_T(probe) > 0.06$.

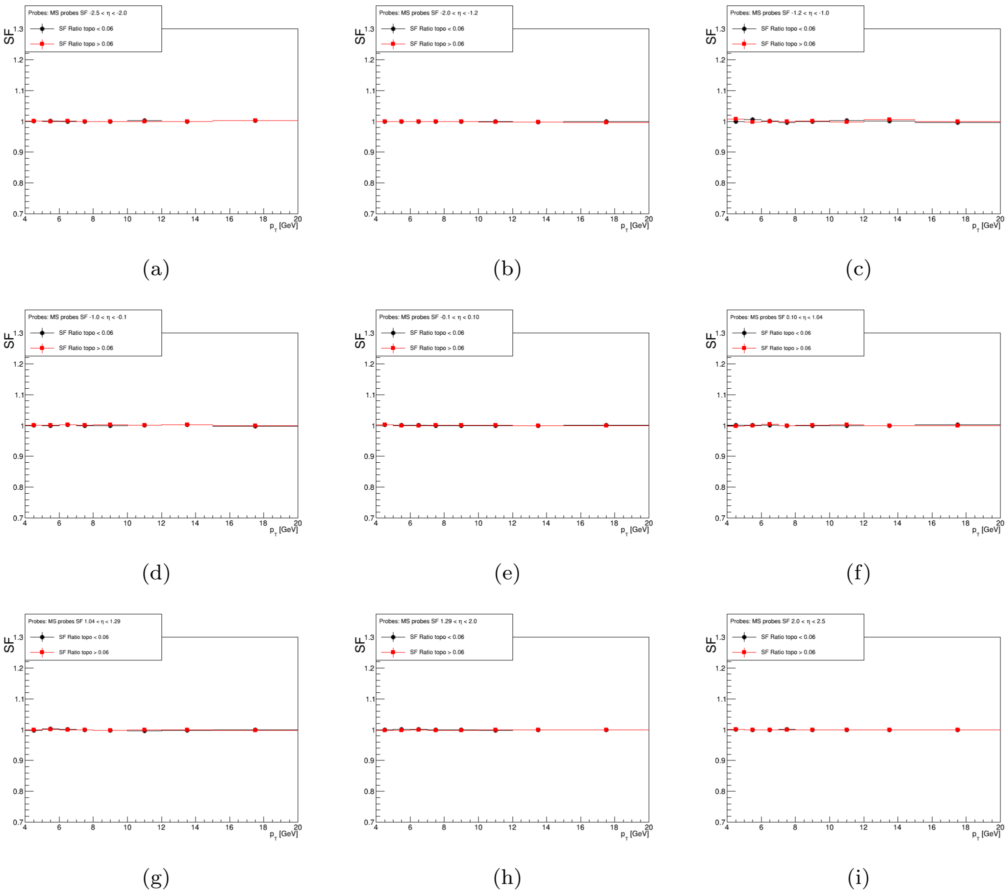

(a) (b) (c)

(d) (e) (f)

(g) (h) (i)

FIGURE A.17: Scale factor of the two different regions of isolation for ID muons: Black: $E_T^{topocone20}/p_T(probe) < 0.06$; Red: $E_T^{topocone20}/p_T(probe) > 0.06$.

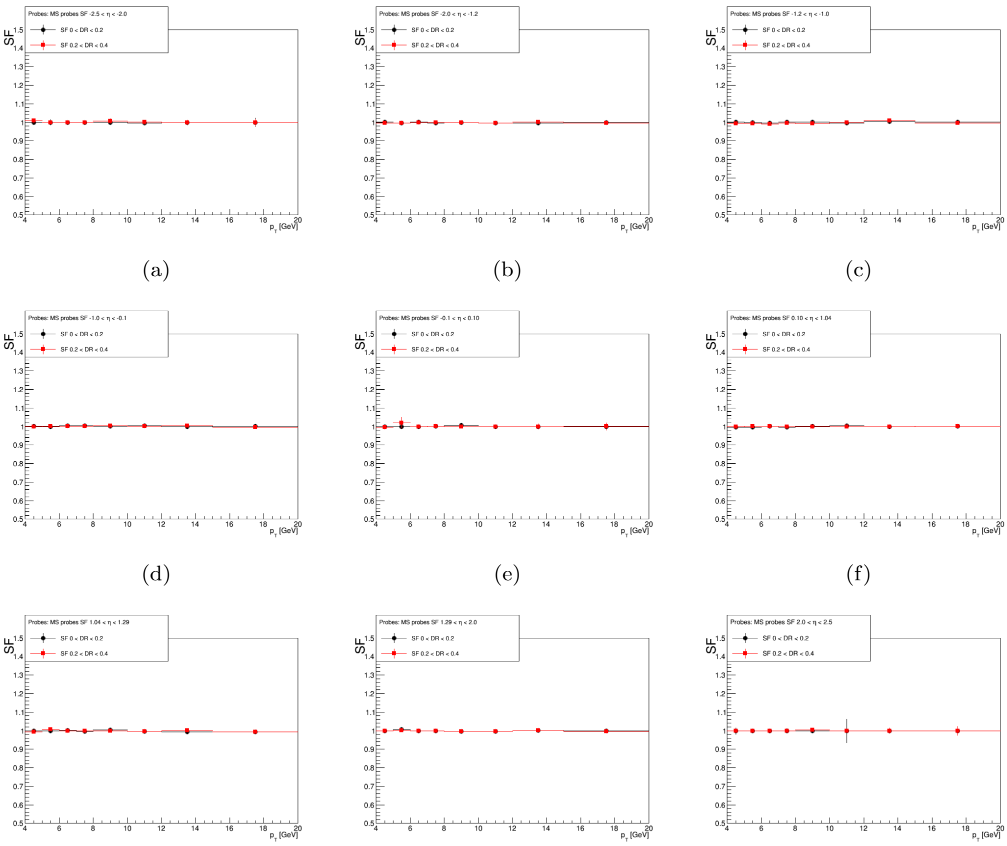

(a) (b) (c)

(d) (e) (f)

(g) (h) (i)

FIGURE A.18: Scale factor of the two different regions of ΔR for ID muons: Black: $0 < \Delta R < 0.2$; Red: $0.2 < \Delta R < 0.4$.

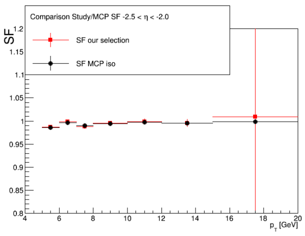

(a)

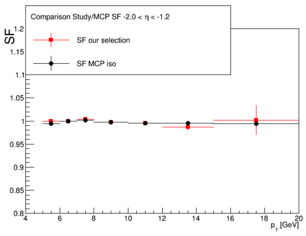

(b)

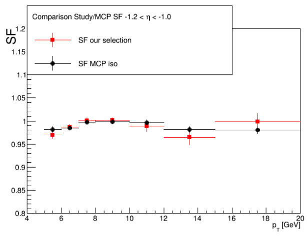

(c)

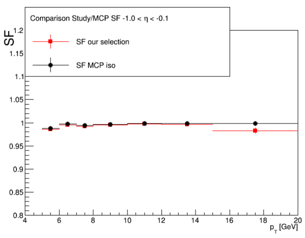

(d)

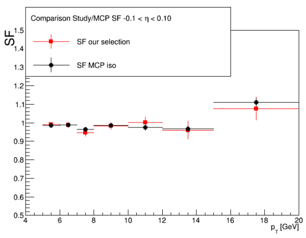

(e)

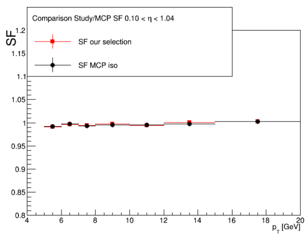

(f)

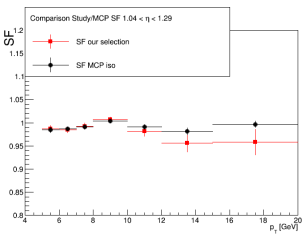

(g)

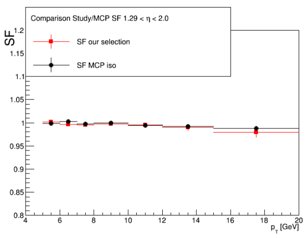

(h)

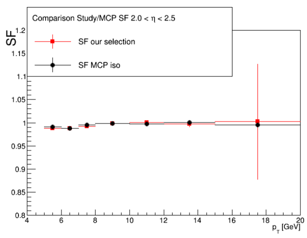

(i)

FIGURE A.19: Comparison between the SFs of the region $p_T^{varcone30}/p_T(probe) < 0.06$ (red) and the official MCP SFs (black).

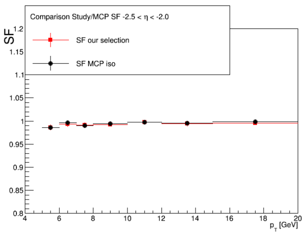

(a)

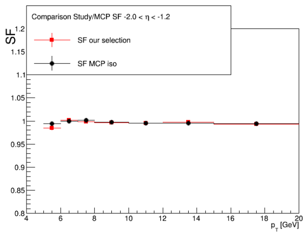

(b)

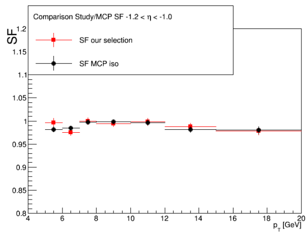

(c)

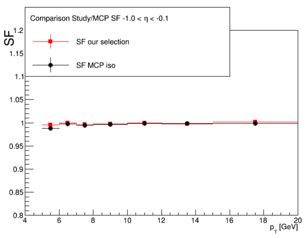

(d)

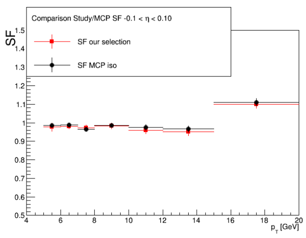

(e)

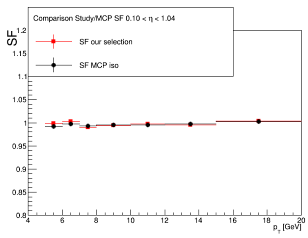

(f)

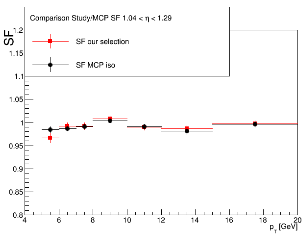

(g)

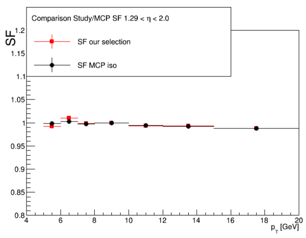

(h)

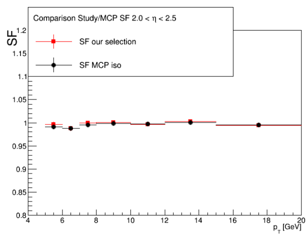

(i)

FIGURE A.20: Comparison between the SFs of the region $p_T^{varcone30}/p_T(probe) > 0.06$ (red) and the official MCP SFs (black).

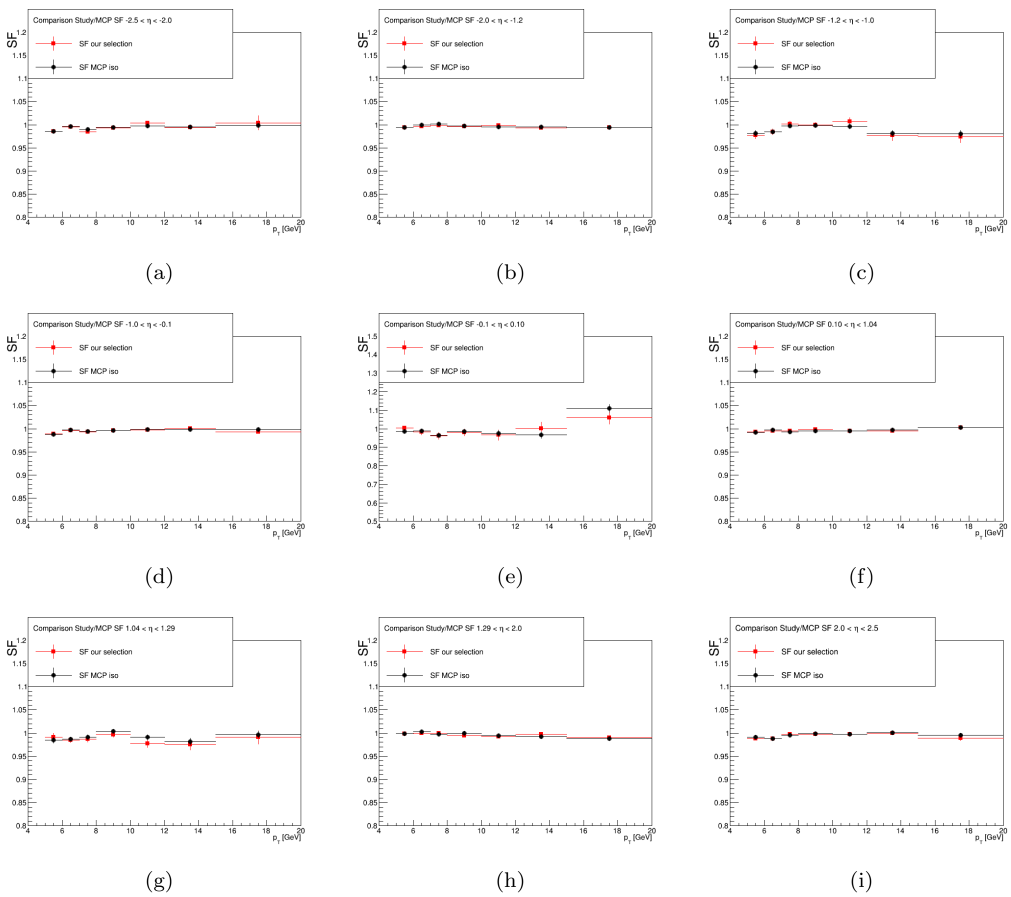

FIGURE A.21: Comparison between the SFs of the region $E_T^{topocone20}/p_T(probe) < 0.06$ (red) and the official MCP SFs (black).

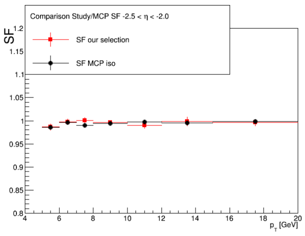

(a)

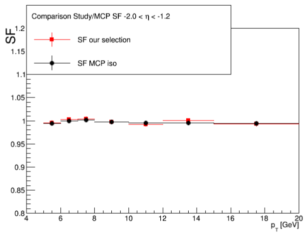

(b)

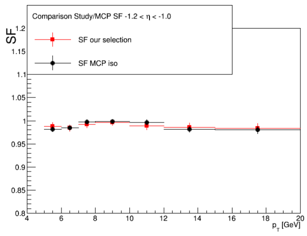

(c)

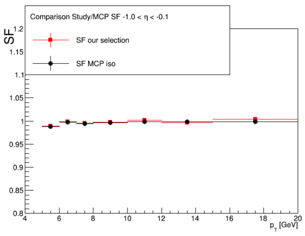

(d)

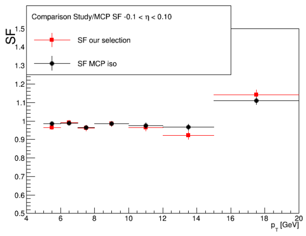

(e)

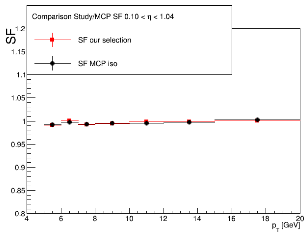

(f)

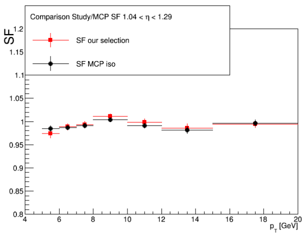

(g)

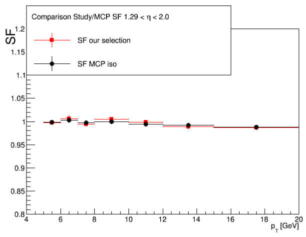

(h)

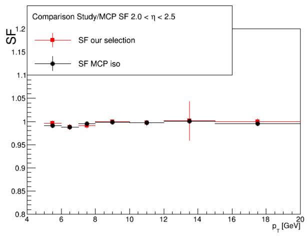

(i)

FIGURE A.22: Comparison between the SFs of the region $E_T^{topocone20}/p_T(probe) > 0.06$ (red) and the official MCP SFs (black).

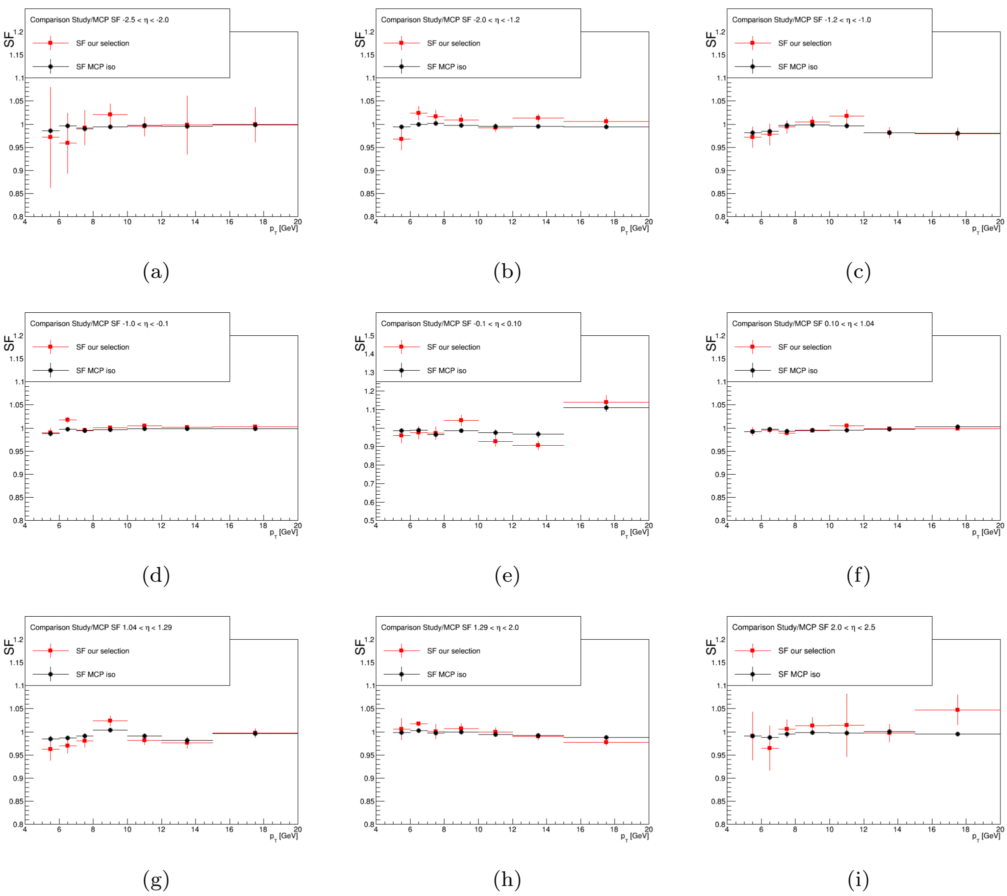

FIGURE A.23: Comparison between the SFs of the region $0 < \Delta R < 0.2$ (red) and the official MCP SFs (black).

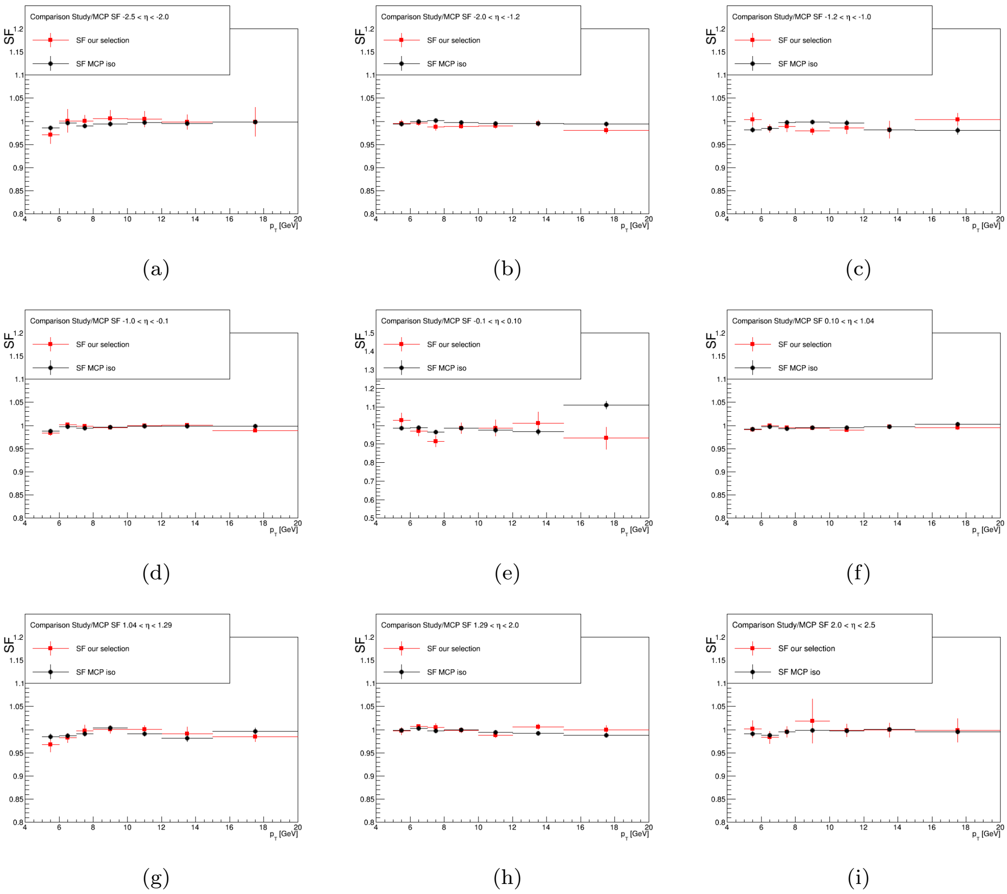

FIGURE A.24: Comparison between the SFs of the region $0.2 < \Delta R < 0.4$ (red) and the official MCP SFs (black).

Appendix B

Electron isolation study

In this appendix will be show the additional electron isolation comparison, discussed in Chapter 5.

B.1 Electron isolation study

In Fig. B.1 is possible to see the efficiency plots about the comparison between different isolation working point, in the *ee-channel*, for the $Z' \rightarrow t\bar{t}$ events. The FCTightTrackOnly has the best efficiency trend and remains flat when the Z' mass rises; the second best working point is FCLoose, but in this case the efficiency decreases with increasing Z' mass; the FCTight working point efficiency rises with increasing the electrons p_T but is not so good, specially for the high Z' masses; the FCHighPtCaloOnly working point is better than the FCTight for the Z' low masses, but the efficiency decrease when the Z' mass is 2 TeV or higher. In Fig. B.2 is possible to see the efficiency plots about the comparison between different isolation working point, in the *eμ-channel*, for the $Z' \rightarrow t\bar{t}$ events. The FCTightTrackOnly has the best efficiency trend and remains flat when the Z' mass rises; the second best working point is FCLoose, but in this case the efficiency decreases with increasing Z' mass, starting around $m_{Z'} = 3$ TeV; the FCTight working point efficiency remains flat when the electrons p_T increases until 1 TeV, but is not so good when the Z' mass increases above this quantity; the FCHighPtCaloOnly working point tend to decrease around 100 GeV of the electron p_T, and is not so good increasing the Z' mass.

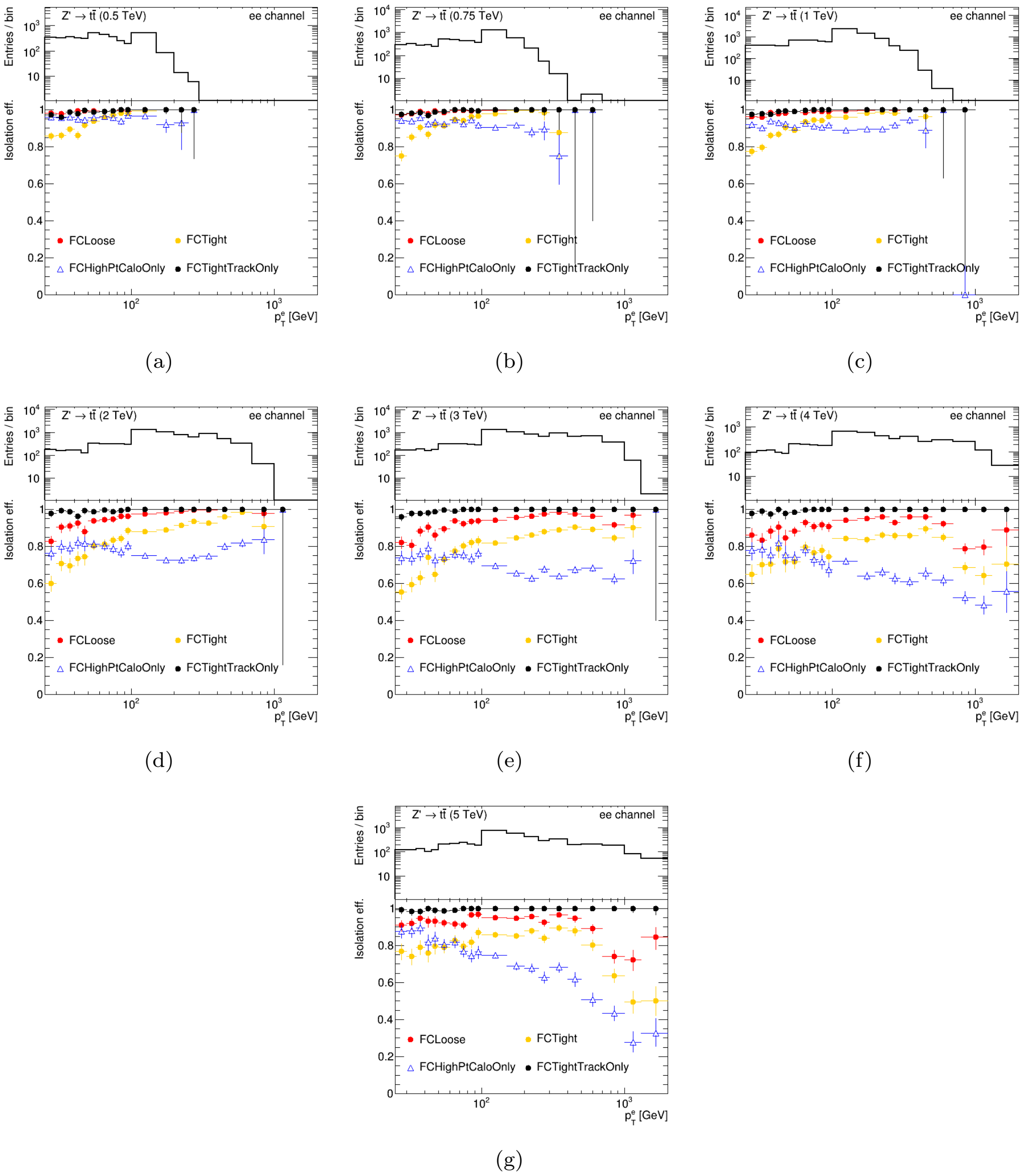

FIGURE B.1: Efficiency plots comparing different electron isolation working point. The comparison is done for different $Z' \to t\bar{t}$ signal samples: Z' with a mass of 500 GeV (a), 750 GeV (b), 1 TeV (c), 2 TeV (d), 3 TeV (e), 4 TeV (f) and 5 TeV (g). The samples are measured in the *ee-channel*.

In Fig. B.3 is possible to see the efficiency plots about the comparison between different isolation working point, in the *ee-channel*, for the $G_{RS} \to t\bar{t}$ events. The

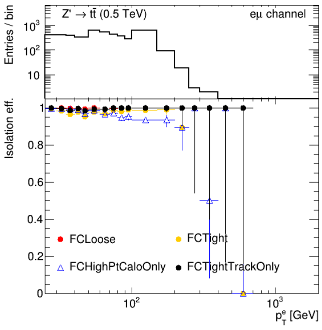

(a)

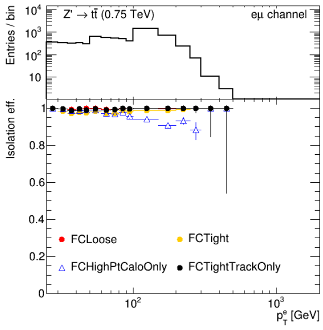

(b)

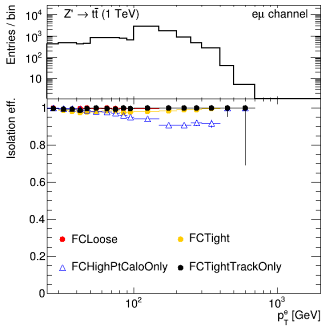

(c)

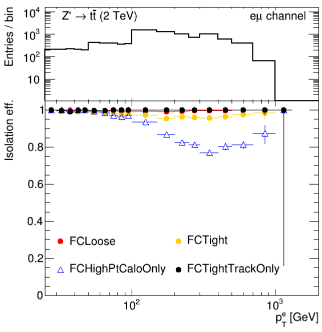

(d)

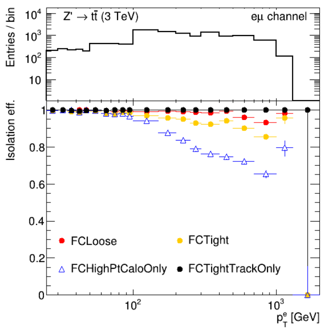

(e)

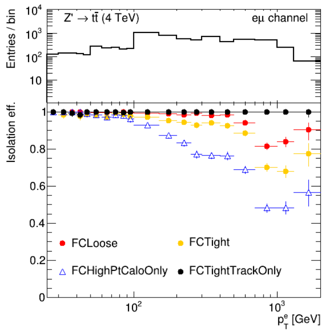

(f)

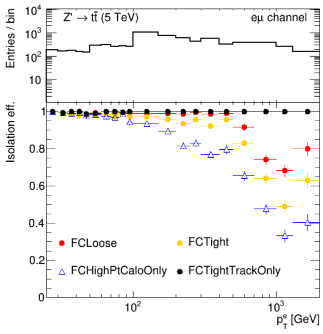

(g)

FIGURE B.2: Efficiency plots comparing different electron isolation working point. The comparison is done for different $Z' \to t\bar{t}$ signal samples: Z' with a mass of 500 GeV (a), 750 GeV (b), 1 TeV (c), 2 TeV (d), 3 TeV (e), 4 TeV (f) and 5 TeV (g). The samples are measured in the *eμ-channel*.

FCTightTrackOnly has the best efficiency trend and remains flat when the graviton mass rises; the second best working point is FCLoose and has a good trend until $m_{G_{RS}} = 750$ GeV; the FCTight working point efficiency is the lowest for low-p_T and increase when the electron transverse momentum rises; the FCHighPtCaloOnly working point is better than the FCTight for the G_{RS} low masses, but the efficiency decrease when the G_{RS} mass is 2 TeV or higher. In Fig. B.4 is possible to see the efficiency plots about the comparison between different isolation working point, in the *eμ-channel*, for the $G_{RS} \to t\bar{t}$ events. The FCTightTrackOnly has the best efficiency trend and remains flat when the G_{RS} mass rises; the second best working point is FCLoose, but in this case the efficiency decreases for $m_{G_{RS}} = 3$ TeV; the FCTight working point efficiency remains flat until $m_{G_{RS}} = 1$ TeV, but is not so good when the G_{RS} mass increases above this quantity and also for high electron transverse momentum; the FCHighPtCaloOnly working point tend to decrease for high electron p_T and for high signal masses.

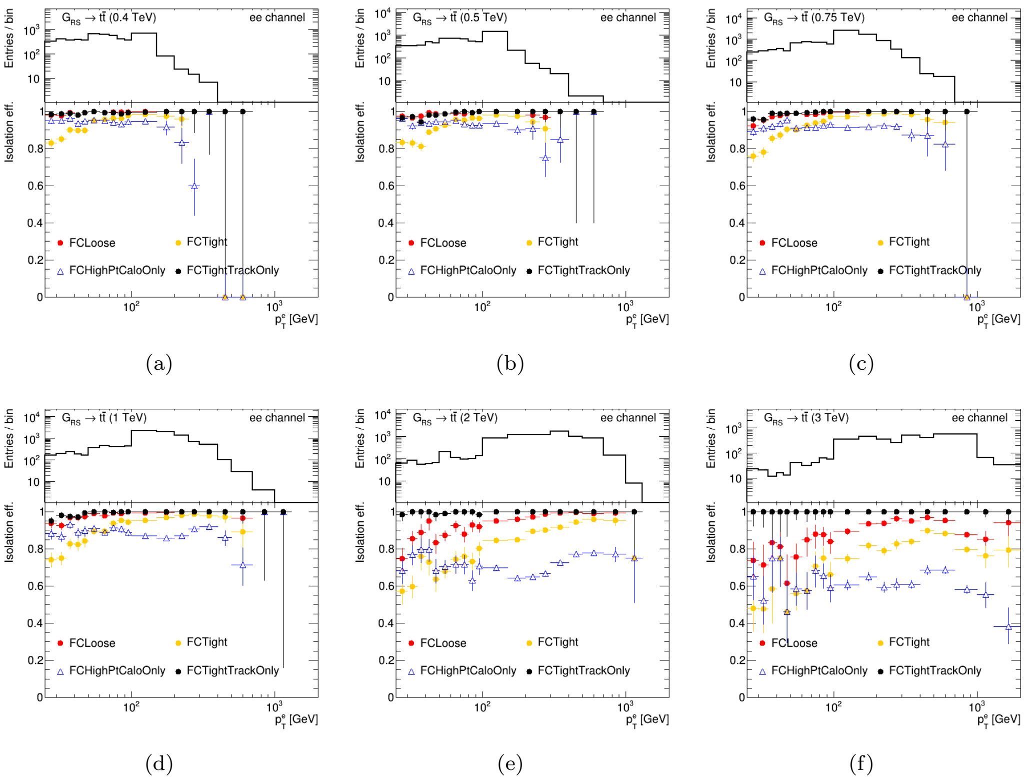

FIGURE B.3: Efficiency plots comparing different electron isolation working point. The comparison is done for different $G_{RS} \to t\bar{t}$ signal samples: graviton with a mass of 400 GeV (a), 500 GeV (b), 750 GeV (c), 1 TeV (d), 2 TeV (e) and 3 TeV (f). The samples are measured in the *ee-channel*.

In Fig. B.5 is possible to see the efficiency plots about the comparison between different isolation working point, in the *ee-channel*, for the $g_{KK} \to t\bar{t}$ events. The FCTightTrackOnly has the best efficiency trend and remains flat when the KK-gluon mass rises; the second best working point is FCLoose and has a good trend until $m_{g_{KK}} = 2.5$ TeV; the FCTight working point efficiency is the lowest for low-p_T

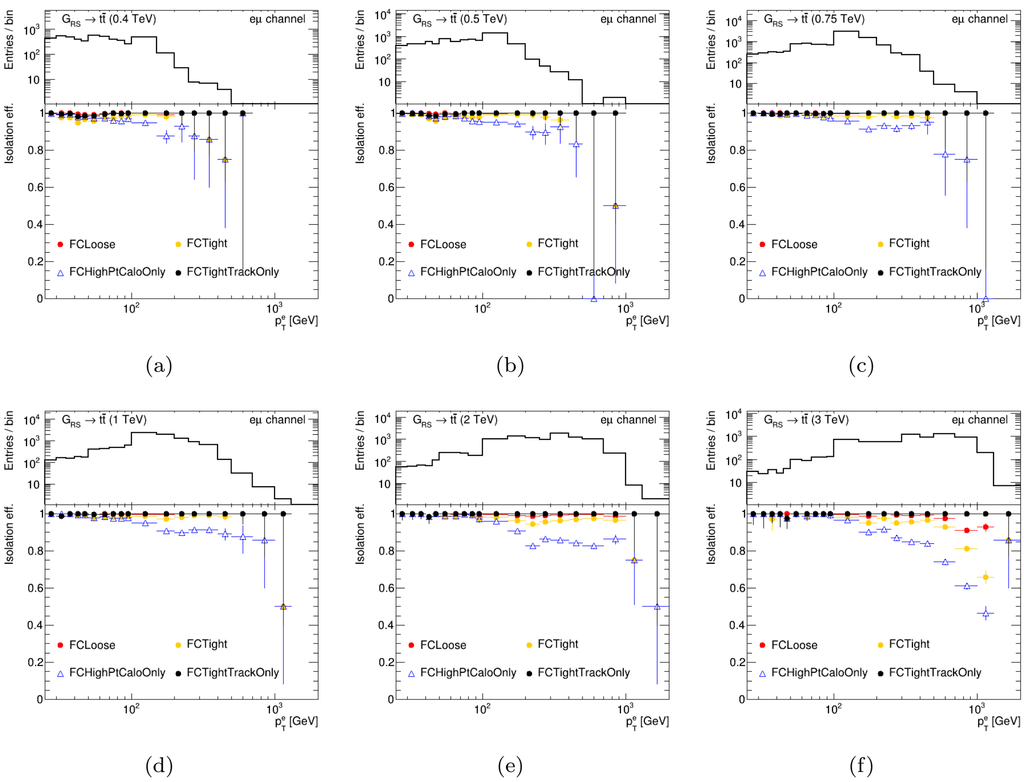

FIGURE B.4: Efficiency plots comparing different electron isolation working point. The comparison is done for different $G_{RS} \to t\bar{t}$ signal samples: graviton with a mass of 400 GeV (a), 500 GeV (b), 750 GeV (c), 1 TeV (d), 2 TeV (e) and 3 TeV (f). The samples are measured in the *eμ-channel*.

and increase when the electron transverse momentum rises; the FCHighPtCaloOnly working point is better than the FCTight for the G_{RS} low masses, but the efficiency decrease when the g_{KK} mass is 2.5 TeV or higher. In Fig. B.6 is possible to see the efficiency plots about the comparison between different isolation working point, in the *eμ-channel*, for the $g_{KK} \to t\bar{t}$ events. The FCTightTrackOnly has the best efficiency trend and remains flat when the g_{KK} mass rises; the second best working point is FCLoose, but in this case the efficiency decreases a little for $m_{g_{KK}} = 3$ TeV; the FCTight working point efficiency remains flat until $m_{g_{KK}} = 1.5$ TeV, but is not so good when the g_{KK} mass increases above this quantity and also for high electron transverse momentum; the FCHighPtCaloOnly working point tend to decrease for high electron p_T and for high signal masses.

B.2 Overlap Removal study

Tab. B.1 shows the samples used for this study.

Fig. B.7 shows the differences between the default configuration and the dilepton analysis configuration, for the subleading electron in the $ee-channel$. It is possible to see a double peak both for electron and signal, the second one is due to the fact that we always match the electron correctly, the first one is due to the fact that there are different effects: first of all, the presence of the jet disturbs the electron identification and therefore there is a loss of efficiency, then the electron-in-jet-4-momentum subtraction for which, even if the jet survives it, causes a recalculation of the ΔR, and therefore the distribution is more complicated than before.
The Fig. B.8 shows the differences between the default configuration and the dilepton analysis configuration, for the subleading muon in the $\mu\mu - channel$.

The Fig. B.10 and Fig. B.12 show the comparison between the two different configuration for the fake leading leptons, in $\mu\mu{-}channel$ and $e\mu{-}channel$, respectively.The same thing can be stated with the subleading leptons shown in Fig. B.9 Fig. B.11 and Fig. B.13.

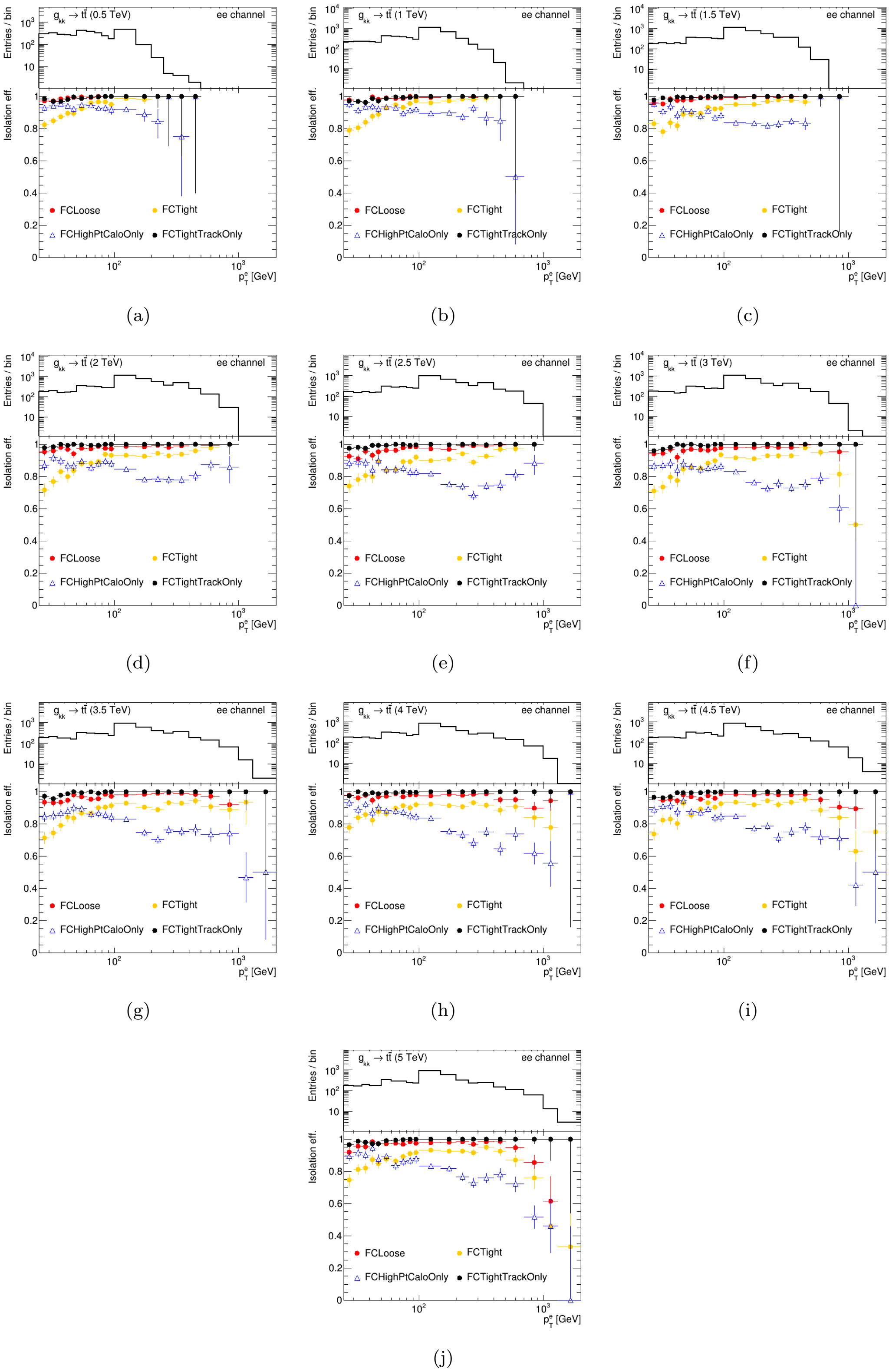

FIGURE B.5: Efficiency plots comparing different electron isolation working point. The comparison is done for different $g_{KK} \to t\bar{t}$ signal samples: Kaluza-Klein gluon with a mass of 500 GeV (a), 1 TeV (b), 1.5 TeV (c), 2 TeV (d), 2.5 TeV (e), 3 TeV (f), 3.5 TeV (g), 4 TeV (h), 4.5 TeV (i) and 5 TeV (j). The samples are measured in the *ee-channel*.

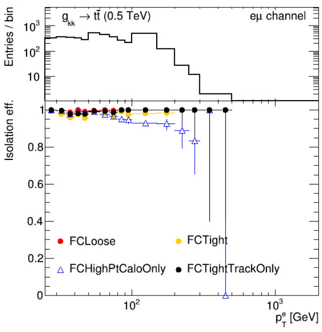

(a)

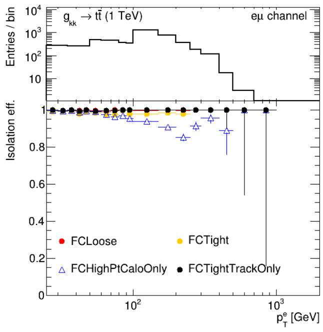

(b)

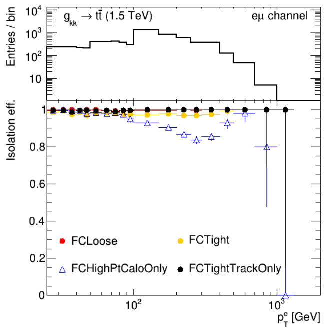

(c)

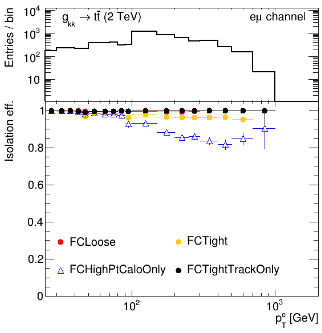

(d)

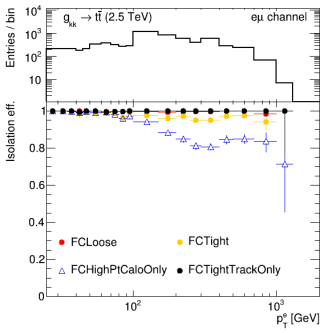

(e)

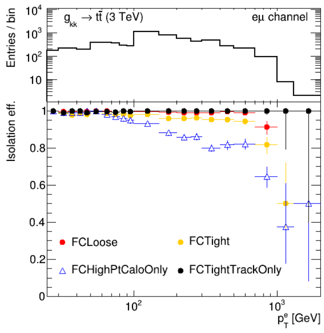

(f)

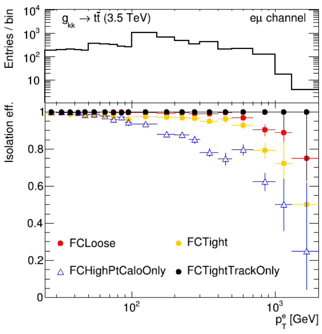

(g)

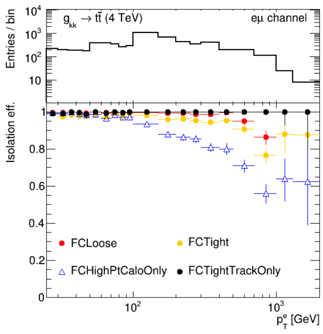

(h)

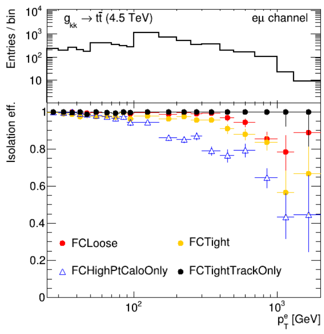

(i)

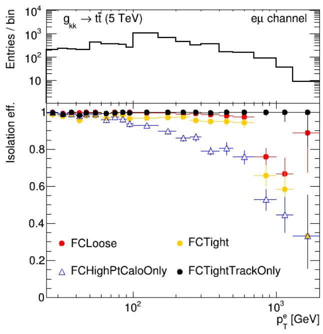

(j)

FIGURE B.6: Efficiency plots comparing different electron isolation working point. The comparison is done for different $g_{KK} \to t\bar{t}$ signal samples: Kaluza-Klein gluon with a mass of 500 GeV (a), 1 TeV (b), 1.5 TeV (c), 2 TeV (d), 2.5 TeV (e), 3 TeV (f), 3.5 TeV (g), 4 TeV (h), 4.5 TeV (i) and 5 TeV (j). The samples are measured in the *eμ-channel*.

Name	Monte Carlo sample
$t\bar{t}$ dilepton	mc16_13TeV.410472.PhPy8EG_A14_ttbar_hdamp258p75_dil.deriv.DAOD_TOPQ1.e6348_e5984_s3126_r9364_r9315_p3761
$t\bar{t}$ fakes	mc16_13TeV.410470.PhPy8EG_A14_ttbar_hdamp258p75_nonallhad.deriv.DAOD_TOPQ1.e6337_e5984_s3126_r9364_r9315_p3832
Z' (3 TeV)	mc16_13TeV.301333.Pythia8EvtGen_A14NNPDF23LO_zprime3000_tt.deriv.DAOD_EXOT4.e3723_s3126_r9364_r9315_p3731

TABLE B.1: List of samples used for the Overlap Removal study.

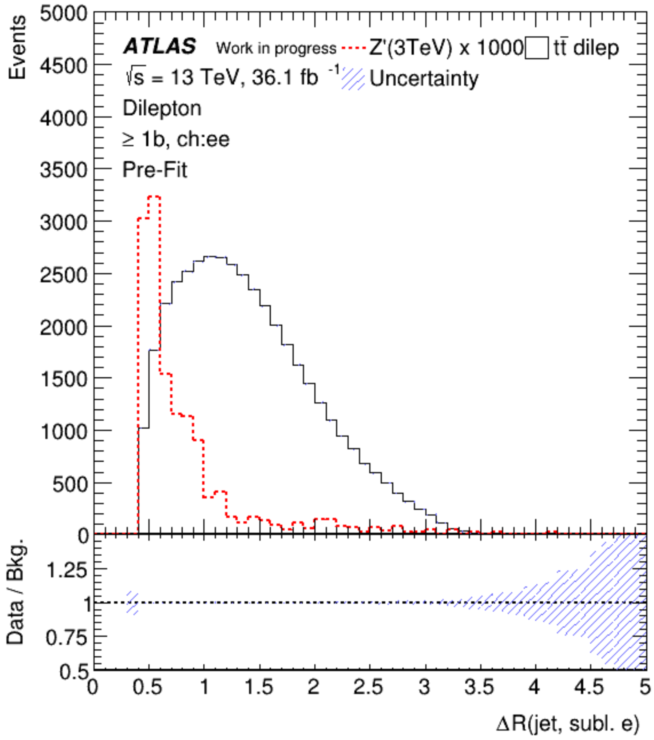

(a)

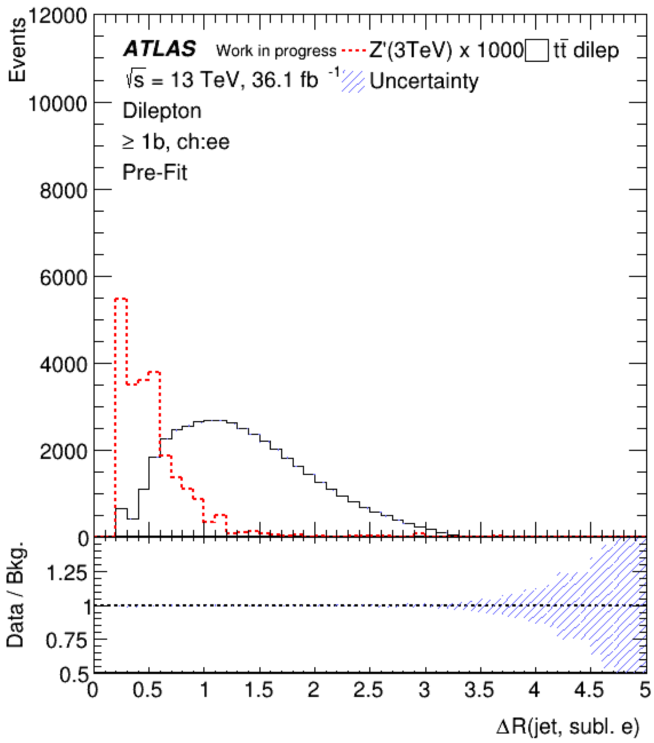

(b)

FIGURE B.7: Comparison between the default configuration (*Gradient* isolation and default OR for electrons) (a) and this analysis configuration (No electron isolation and $Electron-in-Jet-subtraction$ OR for electrons) (b). In white the $t\bar{t}$ dilepton background and in dashed red the signal (Z' with $m_{Z'}$ = 3 TeV). The plots are for $ee-channel$ of the subleading electron. Only statistical uncertainty.

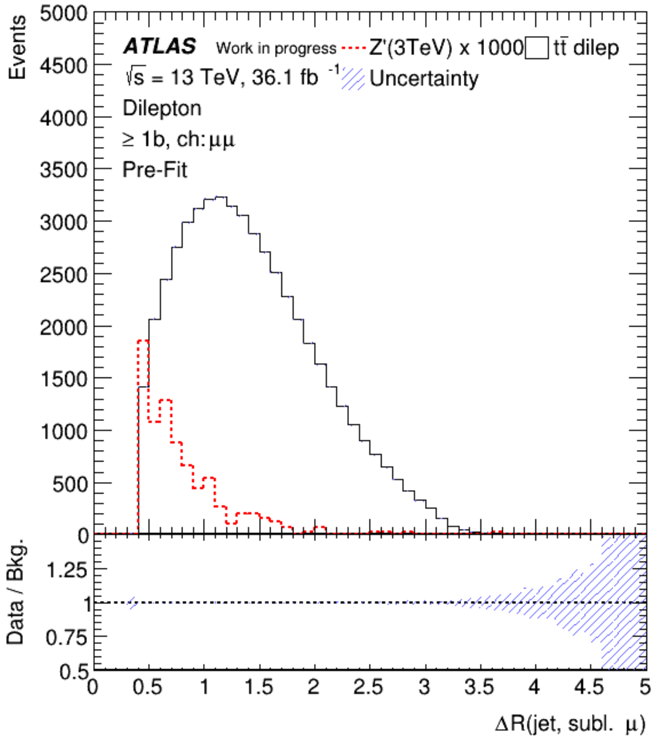

(a)

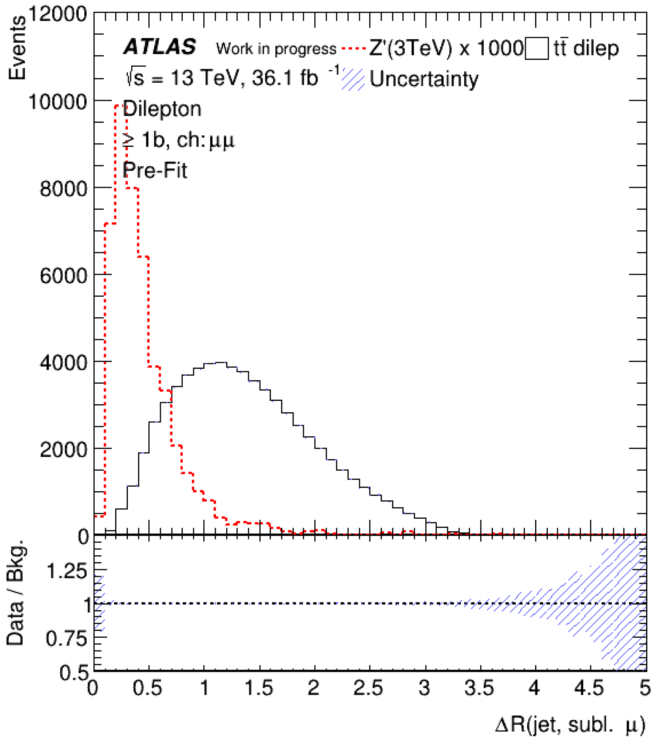

(b)

FIGURE B.8: Comparison between the default configuration (*Gradient* isolation and default OR for muons) (a)and this analysis configuration (*FixedCutTightTrackOnly* muon isolation in addition to *BoostedSlidingDrMu* OR for muons) (b). In white the $t\bar{t}$ dilepton background and in dashed red the signal (Z' with $m_{Z'} = 3$ TeV). The plots are for $\mu\mu - channel$ of the subleading muon. Only statistical uncertainty.

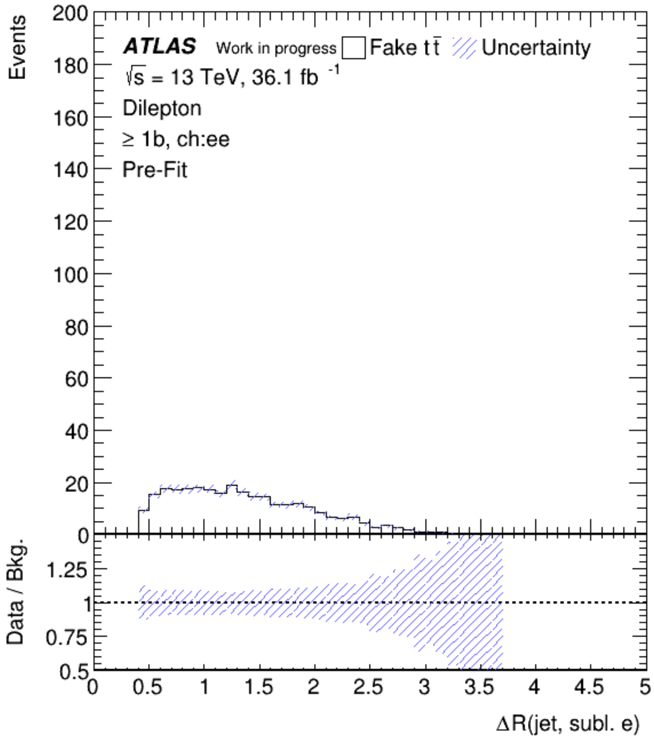

(a)

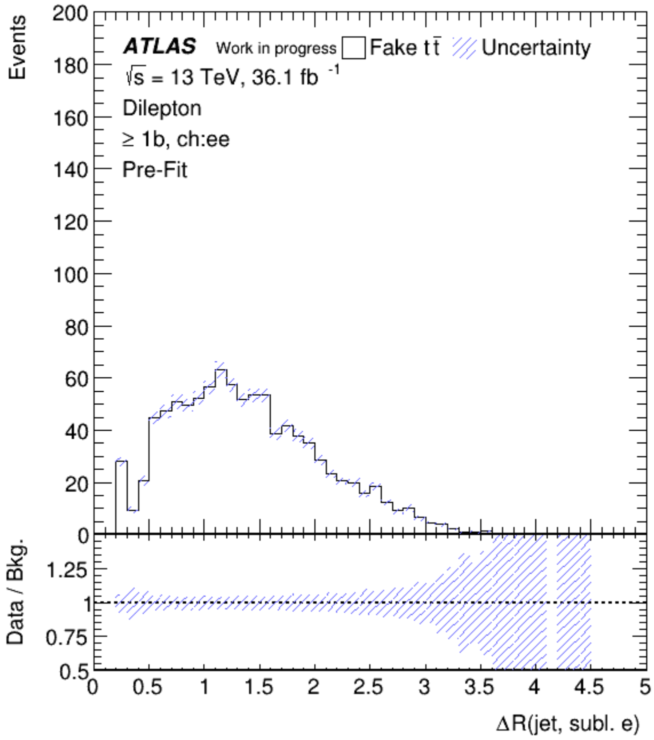

(b)

FIGURE B.9: Comparison between the default configuration (*Gradient* isolation and default OR for electrons) (a) and this analysis configuration (No electron isolation and $Electron-in-Jet-subtraction$ OR for electrons) (b) for fake events. The plots are for $ee-channel$ of the subleading electron. Only statistical uncertainty.

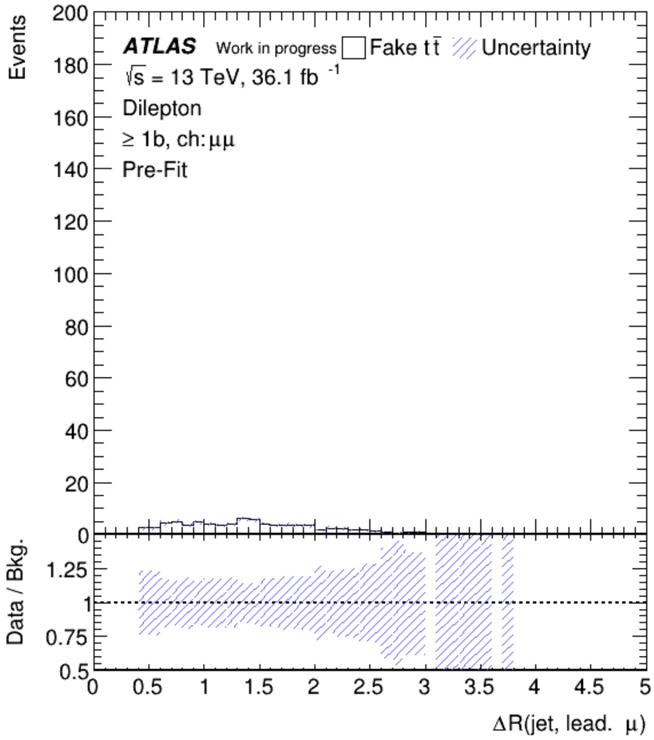

(a)

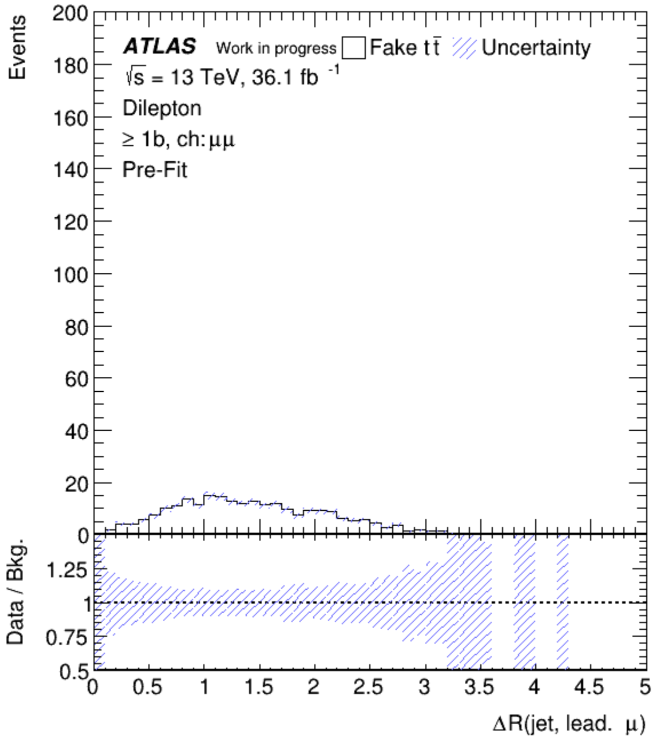

(b)

FIGURE B.10: Comparison between the default configuration (*Gradient* isolation and default OR for muons) (a) and this analysis configuration (*FixedCutTightTrackOnly* muon isolation in addition to *BoostedSlidingDrMu* OR for muons) (b) for fake events. The plots are for $\mu\mu - channel$ of the leading muon. Only statistical uncertainty.

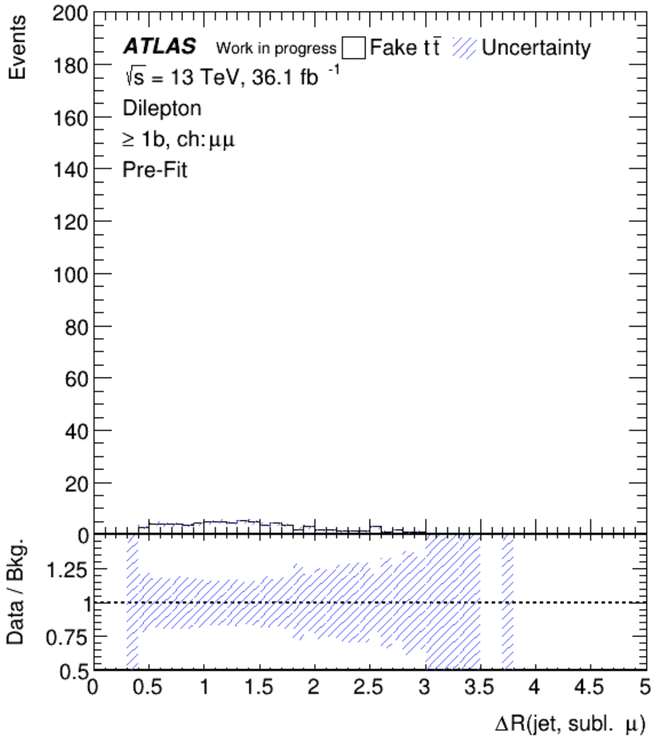

(a)

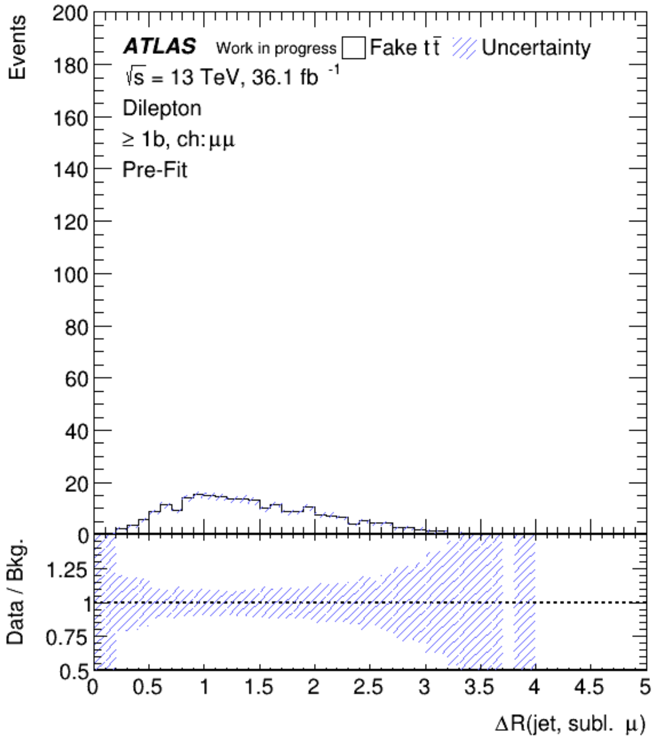

(b)

FIGURE B.11: Comparison between the default configuration (*Gradient* isolation and default OR for muons) (a) and this analysis configuration (*FixedCutTightTrackOnly* muon isolation in addition to *BoostedSlidingDrMu* OR for muons) (b) for fake events. The plots are for $\mu\mu-channel$ of the subleading muon. Only statistical uncertainty.

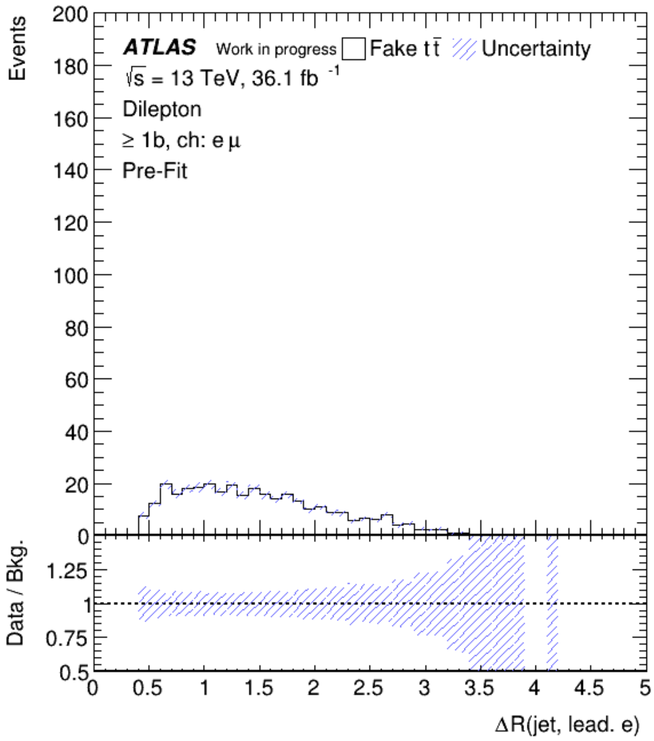

(a)

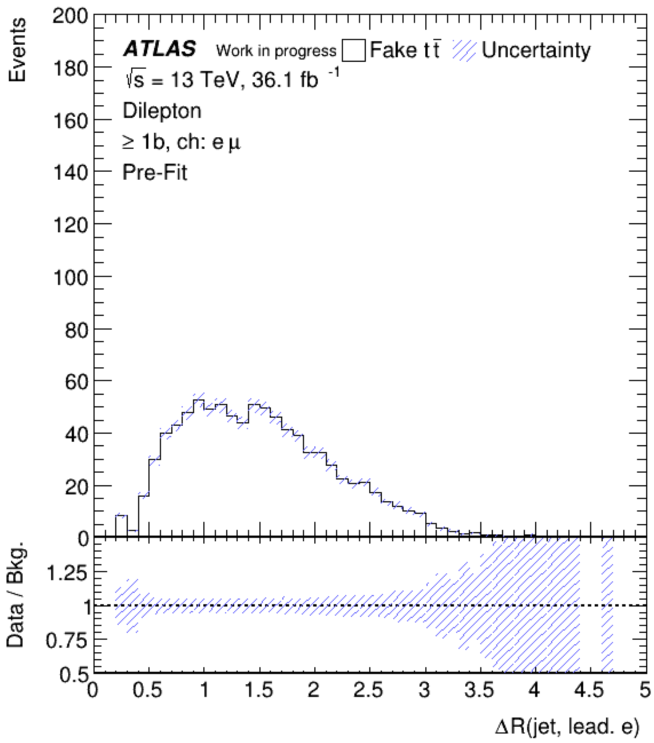

(b)

FIGURE B.12: Comparison between the default configuration (*Gradient* isolation and default OR for both electrons and muons) (a) and this analysis configuration (No electron isolation and *FixedCutTightTrackOnly* muon isolation in addition to $Electron-in-Jet-subtraction$ and $BoostedSlidingDrMu$ for electron and muons, respectively) (b) for fake events. The plots are for the electron in $e\mu-channel$. Only statistical uncertainty.

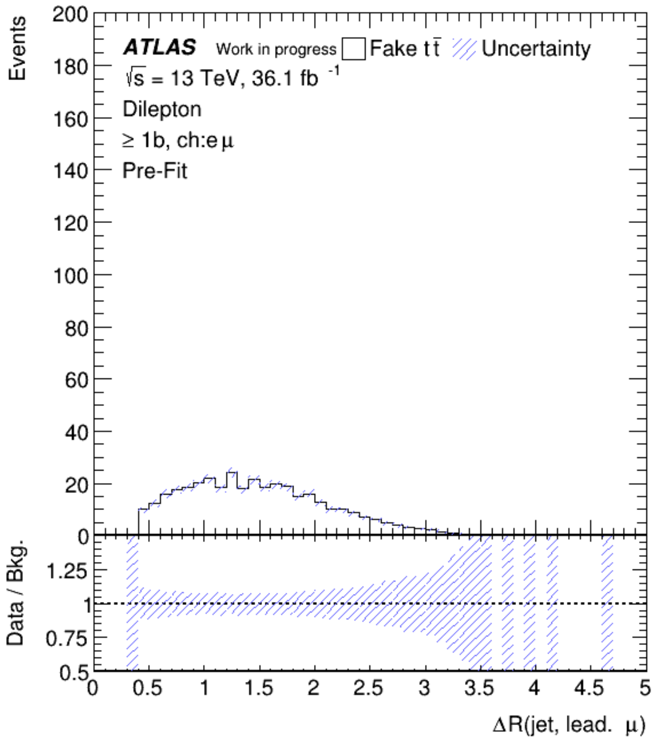

(a)

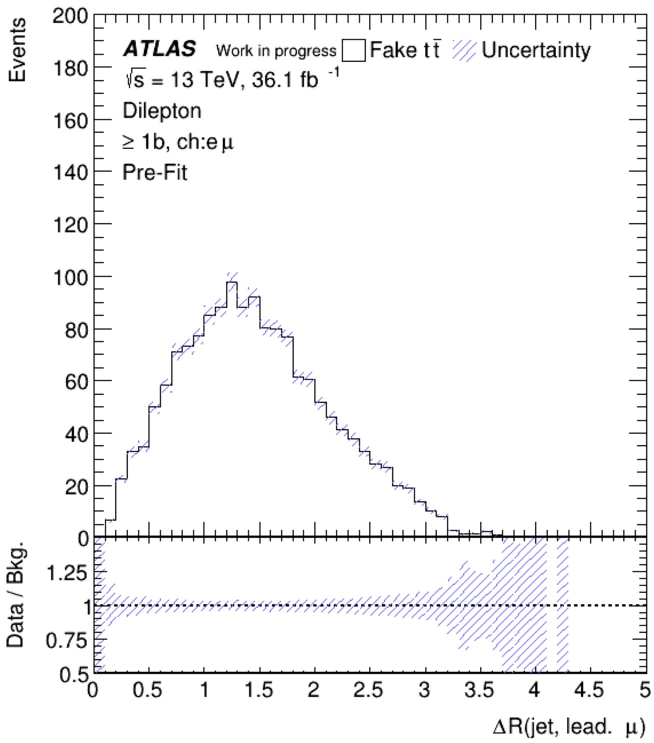

(b)

FIGURE B.13: Comparison between the default configuration (*Gradient* isolation and default OR for both electrons and muons) (a) and this analysis configuration (No electron isolation and *FixedCutTightTrackOnly* muon isolation in addition to $Electron - in - Jet - subtraction$ and $BoostedSlidingDrMu$ for electron and muons, respectively) (b) for fake events. The plots are for the muon in $e\mu - channel$. Only statistical uncertainty.

Appendix C

Search of a BSM resonance in $t\bar{t}$ dilepton final state

In this appendix will be show the additional plots about kinematics, various regions (Control and Signal) that I studied and systematics discussed in Chapter 6.
The backgrounds that contribute in the analysis and there will be see in the next plots are: Z+jets background (orange), SM $t\bar{t}$ dilepton (white), single top (blue), diboson (yellow), $t\bar{t}+V$ (green) and the fakes (that contain W+jets, mis-measured tops and single-top-single-lepton) (purple). Both statistical and systematic errors are taken into account.

Tab. C.1 shows the various single electron triggers used in this analysis setup, while Tab. C.2 shows the different single muon triggers used in this analysis setup. The GRL used for the data samples are listed in Tab. C.3. Tab. C.4, Tab. C.5 and Tab. C.6 show the list of Z', Kaluza-Klein gluon and Randall-Sundrum graviton samples used for this analysis, respectively.

TABLE C.1: List of single lepton triggers used for electrons in $ee - channel$ and $emu - channel$. The electron pass the threshold if $p_T > 27$ GeV.

Channel	2015	2016	2017	2018
$ee - channel$	HLT_e24_lhmedium_L1EM20VH HLT_e60_lhmedium HLT_e120_lhloose	HLT_e26_lhtight_nod0_ivarloose HLT_e60_lhmedium_nod0 HLT_e140_lhloose_nod0	HLT_e26_lhtight_nod0_ivarloose HLT_e60_lhmedium_nod0 HLT_e140_lhloose_nod0	same as 2017
$e\mu - channel$	HLT_e24_lhmedium_L1EM20VH HLT_e60_lhmedium HLT_e120_lhloose	HLT_e26_lhtight_nod0_ivarloose HLT_e60_lhmedium_nod0 HLT_e140_lhloose_nod0	HLT_e26_lhtight_nod0_ivarloose HLT_e60_lhmedium_nod0 HLT_e140_lhloose_nod0	same as 2017

TABLE C.2: List of single lepton triggers used for muons in $\mu\mu - channel$ and $e\mu - channel$. The muon pass the threshold if $p_T > 27$ GeV.

Channel	2015	2016	2017	2018
$\mu\mu - channel$	HLT_mu20_iloose_L1MU15 HLT_mu50	HLT_mu26_ivarmedium HLT_mu50	HLT_mu26_ivarmedium HLT_mu50	same as 2017
$e\mu - channel$	HLT_mu20_iloose_L1MU15 HLT_mu50	HLT_mu26_ivarmedium HLT_mu50	HLT_mu26_ivarmedium HLT_mu50	same as 2017

TABLE C.3: List of Good Run List used for the data samples.

Data sample	Good Run List
2015	physics_25ns_21.0.19.xml
2016	physics_25ns_21.0.19.xml
2017	data17_13TeV.periodAllYear_DetStatus-v99-pro22-01_Unknown_PHYS_StandardGRL_All_Good_25ns_Triggerno17e33prim.xml
2018	data18_13TeV.periodAllYear_DetStatus-v102-pro22-03_Unknown_PHYS_StandardGRL_All_Good_25ns_Triggerno17e33prim.xml

TABLE C.4: List of Z' signal MC samples.

Signal	MC Sample
Z' 0.5 TeV	mc16_13TeV.301323.Pythia8EvtGen_A14NNPDF23LO_zprime500_tt.deriv.DAOD_EXOT4
Z' 0.75 TeV	mc16_13TeV.301324.Pythia8EvtGen_A14NNPDF23LO_zprime750_tt.deriv.DAOD_EXOT4
Z' Z' 1 TeV	mc16_13TeV.301325.Pythia8EvtGen_A14NNPDF23LO_zprime1000_tt.deriv.DAOD_EXOT4
Z' 2 TeV	mc16_13TeV.301329.Pythia8EvtGen_A14NNPDF23LO_zprime2000_tt.deriv.DAOD_EXOT4
Z' 3 TeV	mc16_13TeV.301333.Pythia8EvtGen_A14NNPDF23LO_zprime3000_tt.deriv.DAOD_EXOT4
Z' 4 TeV	mc16_13TeV.301334.Pythia8EvtGen_A14NNPDF23LO_zprime4000_tt.deriv.DAOD_EXOT4

TABLE C.5: List of g_{KK} signal MC samples.

Signal	MC Sample
g_{KK} 0.5 TeV	mc16_13TeV.307522.Pythia8EvtGen_A14NNPDF23LO_KKgluon500_Width30_tt.deriv.DAOD_EXOT4
g_{KK} 1 TeV	mc16_13TeV.307523.Pythia8EvtGen_A14NNPDF23LO_KKgluon1000_Width30_tt.deriv.DAOD_EXOT4
g_{KK} 1.5 TeV	mc16_13TeV.307524.Pythia8EvtGen_A14NNPDF23LO_KKgluon1500_Width30_tt.deriv.DAOD_EXOT4
g_{KK} 2 TeV	mc16_13TeV.307527.Pythia8EvtGen_A14NNPDF23LO_Kkgluon2000_Width30_tt.deriv.DAOD_EXOT4
g_{KK} 2.5 TeV	mc16_13TeV.307528.Pythia8EvtGen_A14NNPDF23LO_KKgluon2500_Width30_tt.deriv.DAOD_EXOT4
g_{KK} 3 TeV	mc16_13TeV.307529.Pythia8EvtGen_A14NNPDF23LO_KKgluon3000_Width30_tt.deriv.DAOD_EXOT4
g_{KK} 3.5 TeV	mc16_13TeV.307530.Pythia8EvtGen_A14NNPDF23LO_KKgluon3500_Width30_tt.deriv.DAOD_EXOT4
g_{KK} 4 TeV	mc16_13TeV.307531.Pythia8EvtGen_A14NNPDF23LO_Kkgluon4000_Width30_tt.deriv.DAOD_EXOT4
g_{KK} 4.5 TeV	mc16_13TeV.307532.Pythia8EvtGen_A14NNPDF23LO_KKgluon4500_Width30_tt.deriv.DAOD_EXOT4

TABLE C.6: List of G signal MC samples.

Signal	MC Sample
G 0.4 TeV	mc16_13TeV.305012.MadGraphPythia8EvtGen_A14NNPDF23LO_RS_G_tt_c10_m0400.deriv.DAOD_EXOT4
G 0.5 TeV	mc16_13TeV.305013.MadGraphPythia8EvtGen_A14NNPDF23LO_RS_G_tt_c10_m0500.deriv.DAOD_EXOT4
G 0.75 TeV	mc16_13TeV.305014.MadGraphPythia8EvtGen_A14NNPDF23LO_RS_G_tt_c10_m0750.deriv.DAOD_EXOT4
G 1 TeV	mc16_13TeV.305015.MadGraphPythia8EvtGen_A14NNPDF23LO_RS_G_tt_c10_m1000.deriv.DAOD_EXOT4
G 2 TeV	mc16_13TeV.305016.MadGraphPythia8EvtGen_A14NNPDF23LO_RS_G_tt_c10_m2000.deriv.DAOD_EXOT4

C.1 System kinematics

In this section the generic kinematics plots are shown.
Fig. C.1 shows the distribution of the sub-leading lepton p_T in $ee - channel$ and $\mu\mu - channel$, respectively.
Fig. C.2 shows the ΔR between the charged sub-leading lepton and its nearest jet in $ee - channel$ and $\mu\mu - channel$, respectively.
Fig. C.3 shows the distribution of the leading jet p_T in $ee - channel$, $\mu\mu - channel$ and $e\mu - channel$, respectively.
Fig. C.4 shows the distribution of the sub-leading jet p_T in $ee-channel$, $\mu\mu-channel$ and $e\mu - channel$, respectively.
Fig. C.5 shows the distribution of the pseudorapidity η for the leading lepton in $ee - channel$, $\mu\mu - channel$ and $e\mu - channel$, respectively.
Fig. C.6 shows the distribution of the pseudorapidity η for the sub-leading lepton in $ee - channel$ and $\mu\mu - channel$, respectively.
Fig. C.7 shows the number of jets in $ee - channel$, $\mu\mu - channel$ and $e\mu - channel$, respectively.
Fig. C.8 shows the number of b-jets in $ee-channel$, $\mu\mu-channel$ and $e\mu-channel$, respectively.
In all plots, it is possible to see a good agreement data/MC. Both statistical and systematic errors are taken into account.

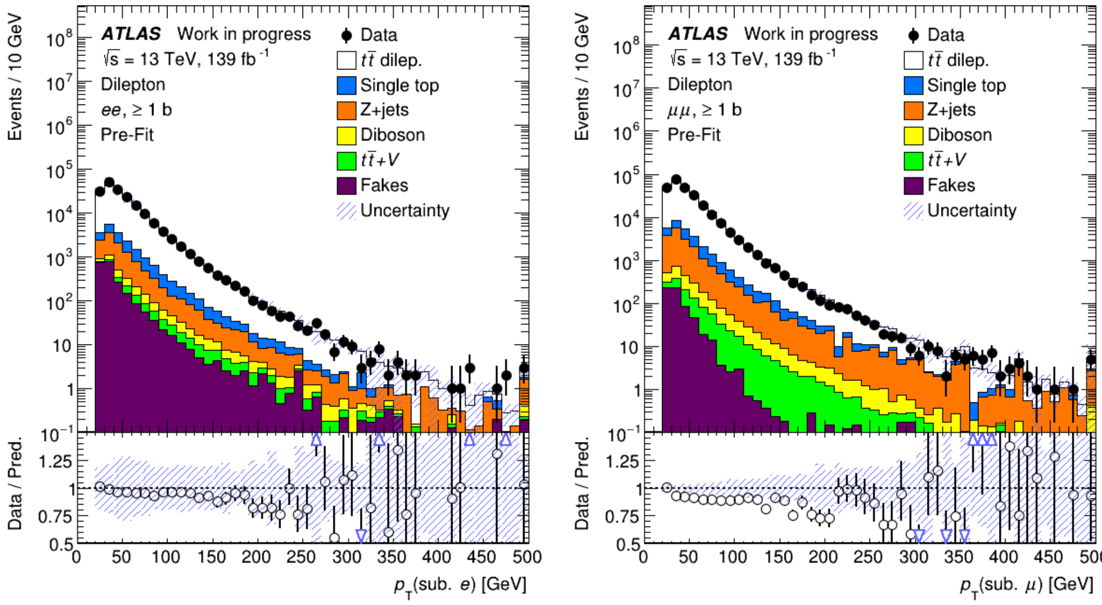

(a) (b)

Figure C.1: Transverse momentum of the sub-leading lepton in $ee - channel$ (a) and $\mu\mu - channel$ (b). Both statistical and systematic errors are taken into account.

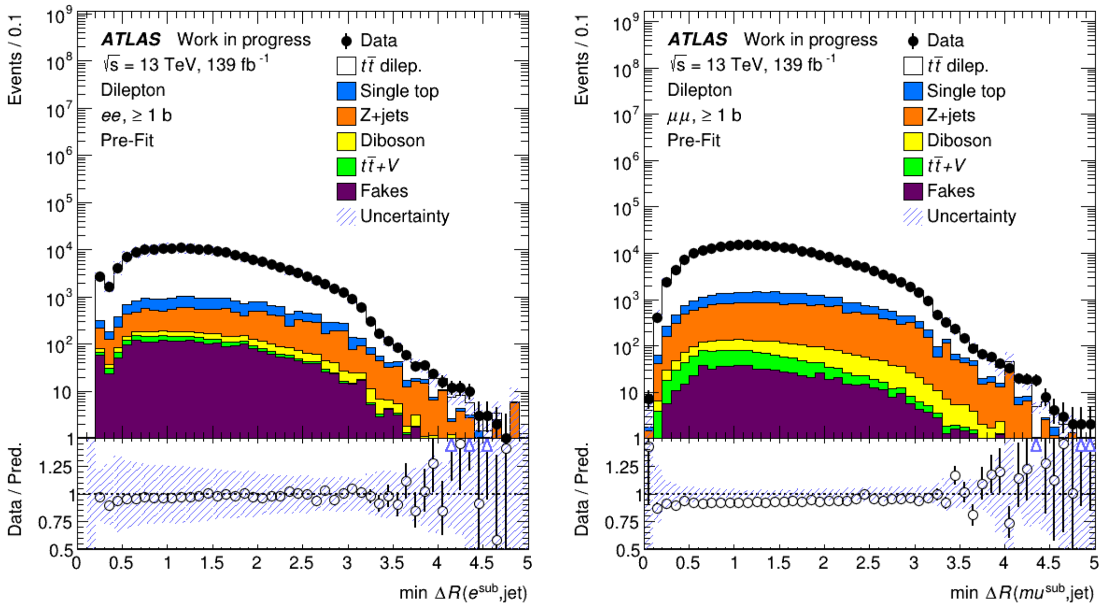

(a) (b)

Figure C.2: ΔR between the charged sub-leading lepton and its nearest jet in $ee - channel$ (a) and $\mu\mu - channel$ (b). Both statistical and systematic errors are taken into account.

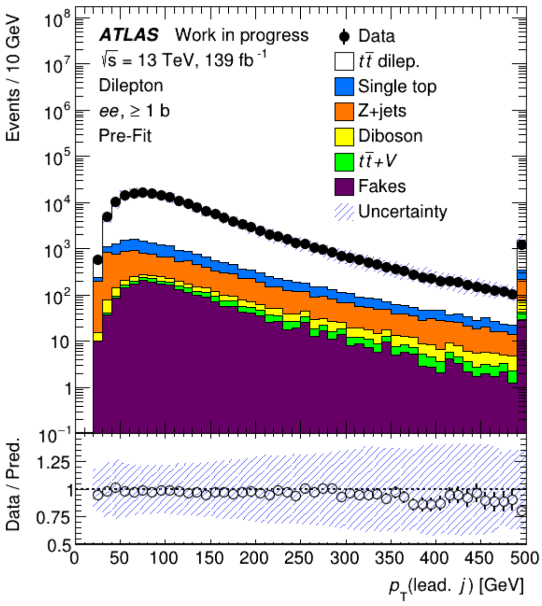

(a)

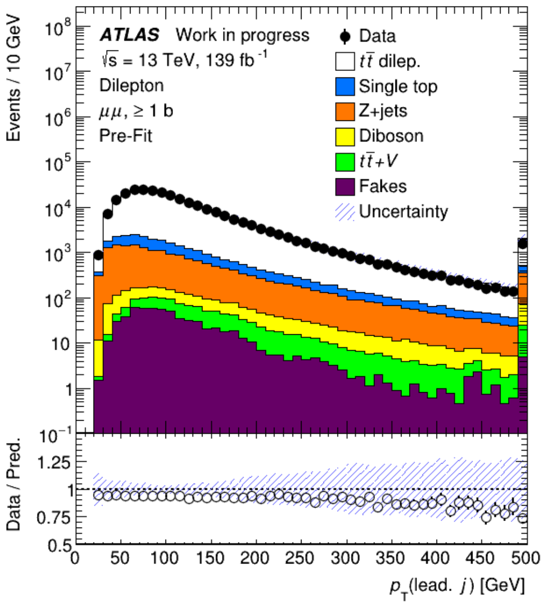

(b)

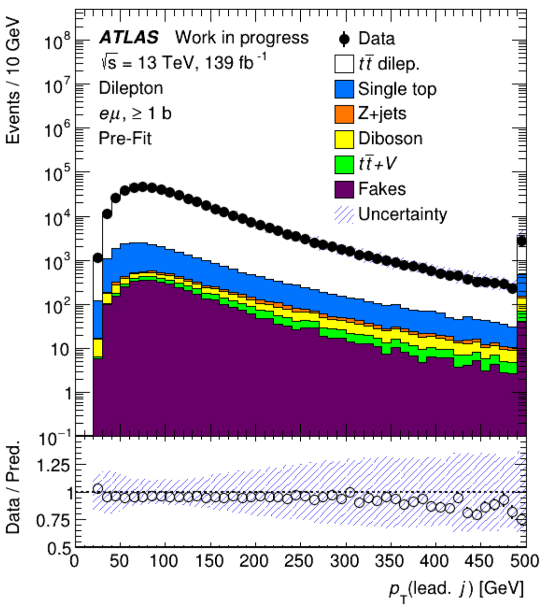

(c)

FIGURE C.3: Transverse momentum of the leading jet in $ee-channel$ (a) $\mu\mu-channel$ (b) and $e\mu-channel$. Both statistical and systematic errors are taken into account.

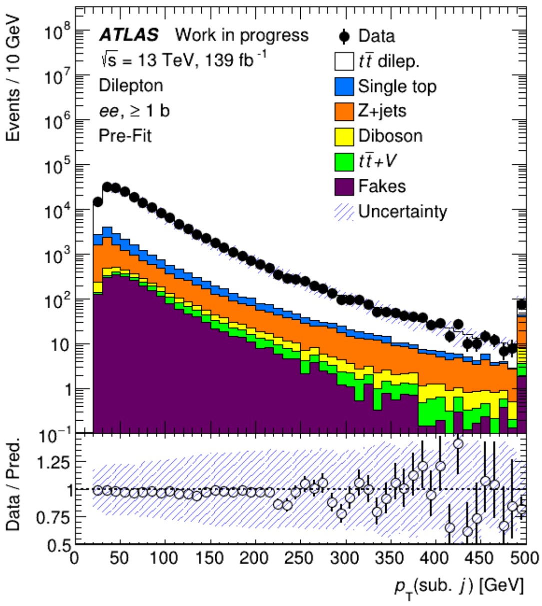

(a)

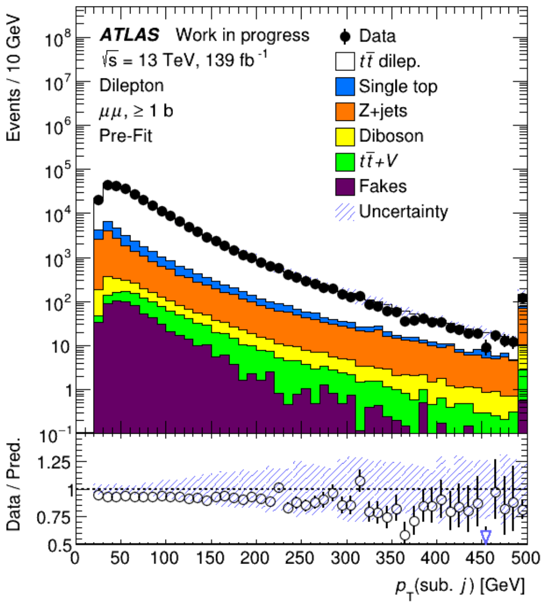

(b)

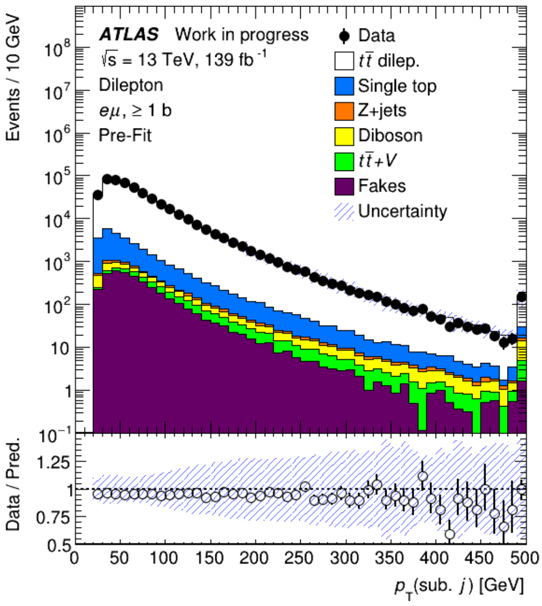

(c)

FIGURE C.4: Transverse momentum of the sub-leading jet in $ee - channel$ (a), $\mu\mu - channel$ (b) and $e\mu - channel$. Both statistical and systematic errors are taken into account.

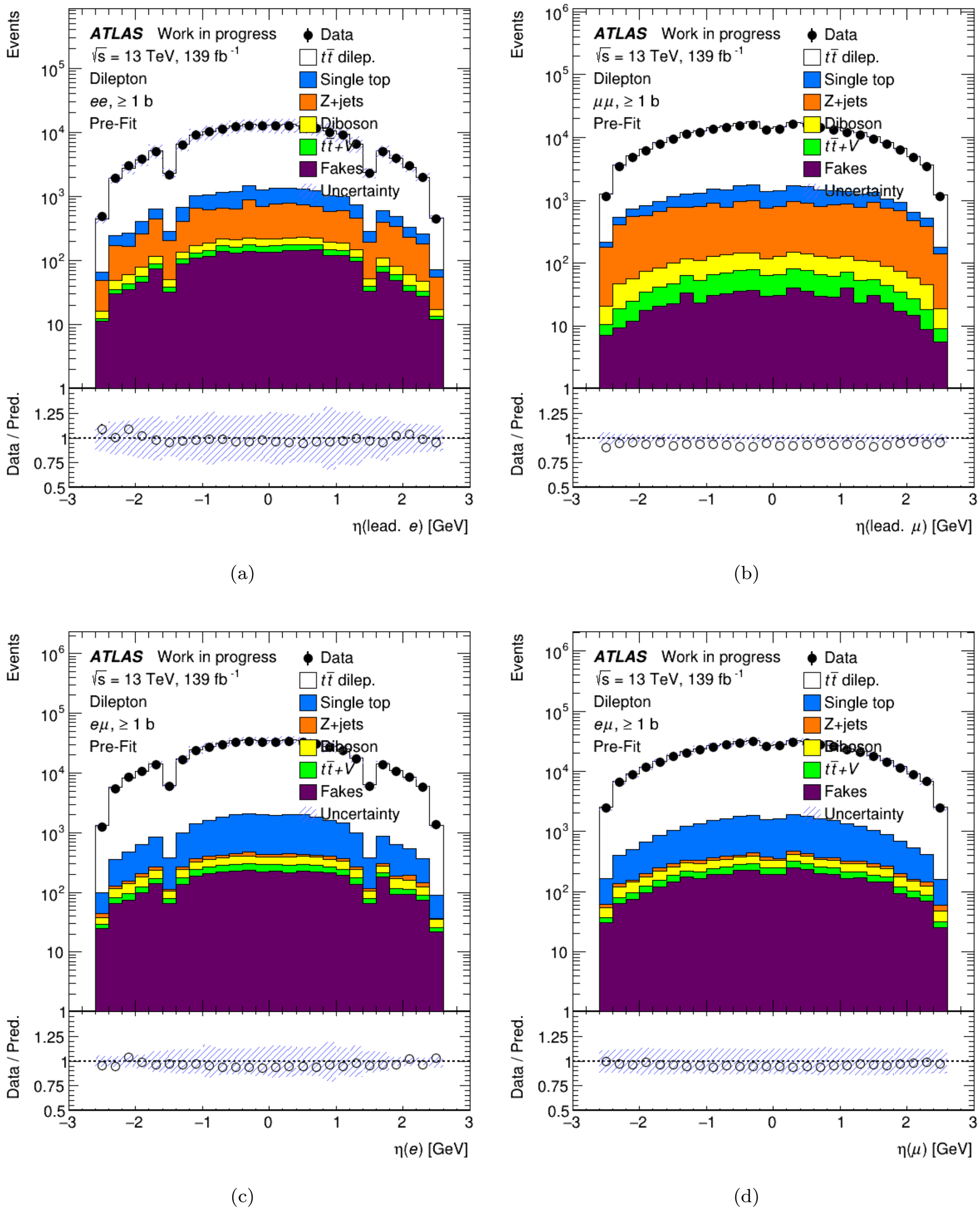

FIGURE C.5: Pseudorapidity η of the leading lepton in $ee-channel$ (a) $\mu\mu-channel$ (b) and $e\mu-channel$: electron (c) and muon(d). Both statistical and systematic errors are taken into account.

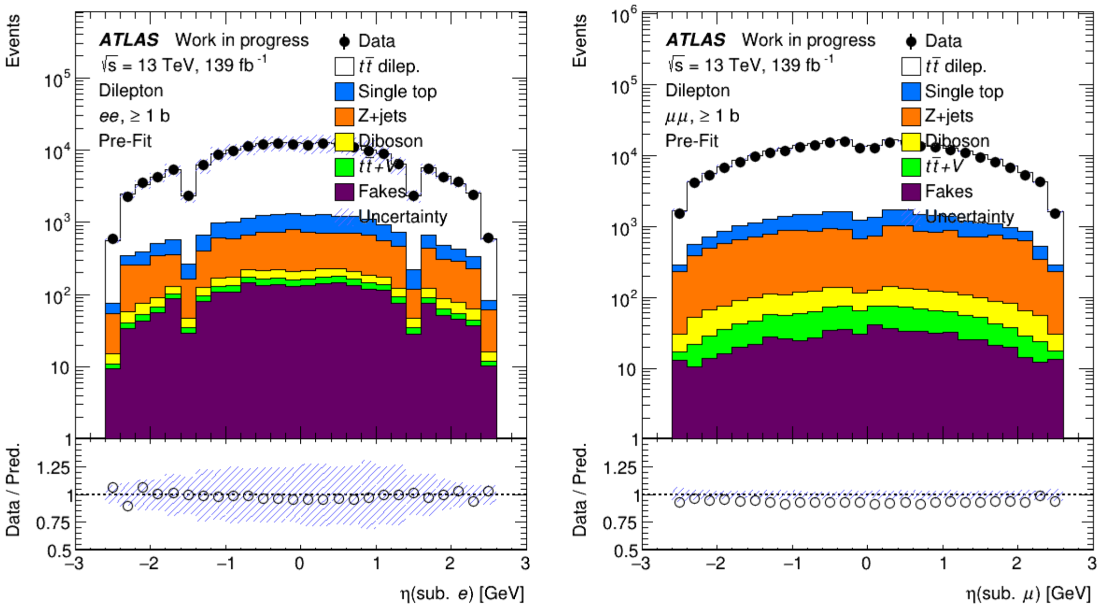

(a)

(b)

FIGURE C.6: Pseudorapidity η of the sub-leading lepton in $ee - channel$ (a) and $\mu\mu - channel$ (b). Both statistical and systematic errors are taken into account.

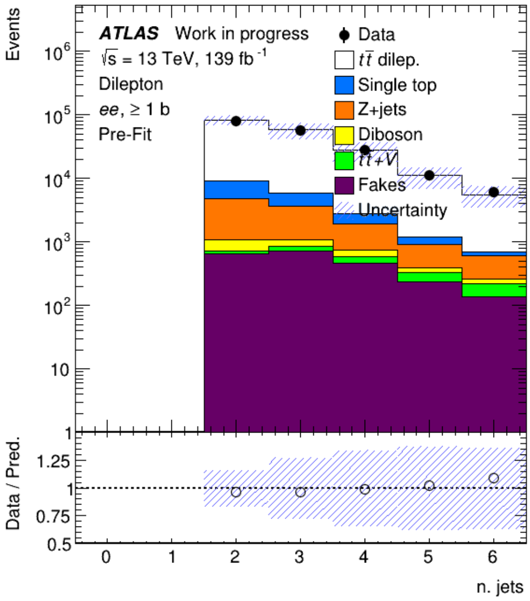

(a)

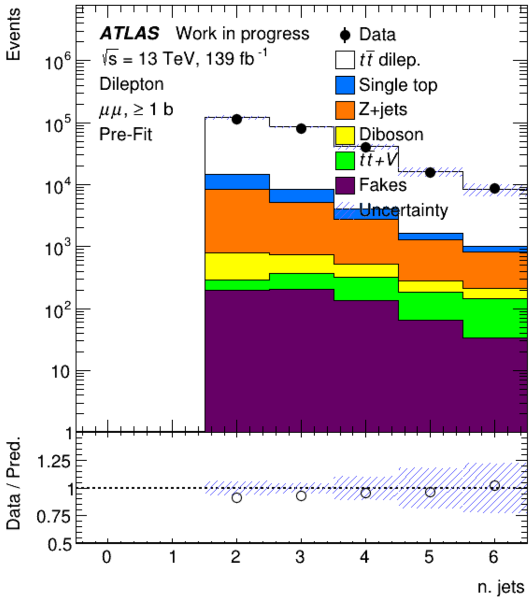

(b)

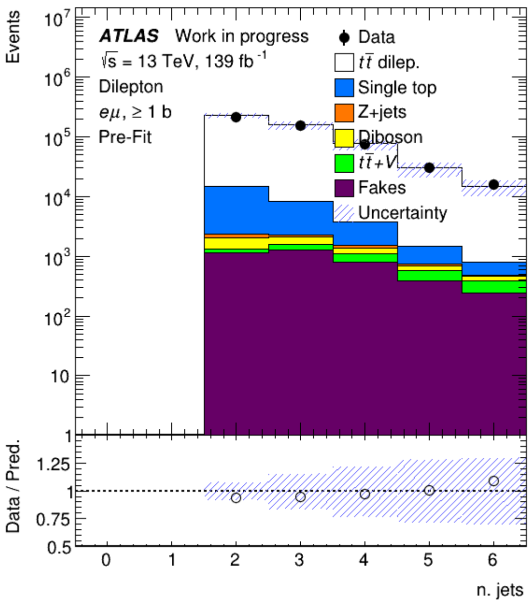

(c)

FIGURE C.7: Number of jets in $ee - channel$ (a), $\mu\mu - channel$ (b) and $e\mu - channel$. Both statistical and systematic errors are taken into account.

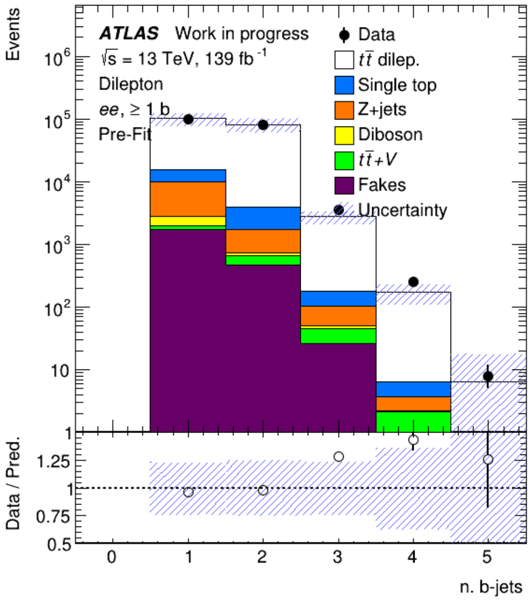

(a)

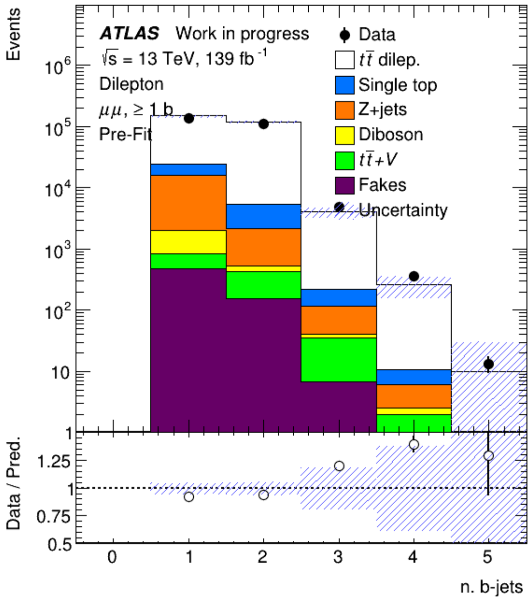

(b)

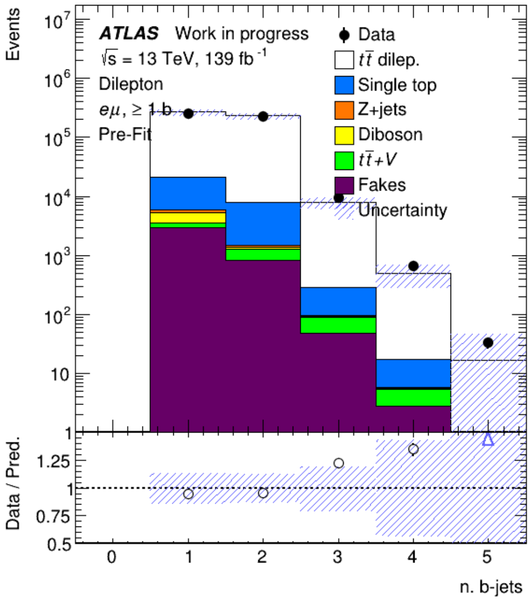

(c)

FIGURE C.8: Number of b-jets in $ee-channel$ (a), $\mu\mu-channel$ (b) and $e\mu-channel$. Both statistical and systematic errors are taken into account.

C.2 Control regions

In this part of section the kinematics variable in CR_Z control region are shown. In these plots is possible to see a trend of over-estimation; this is due to the fact that, at this point, the Z+jets normalization has not yet been done.
Fig. C.9 shows the distribution of the sub-leading lepton p_T in $ee-channel$ and $\mu\mu-channel$, respectively, in CR_Z control region.
Fig. C.10 shows the ΔR between the charged sub-leading lepton and its nearest jet in $ee-channel$ and $\mu\mu-channel$, respectively, in CR_Z control region.
Fig. C.11 shows the distribution of the sub-leading jet p_T in $ee-channel$ and $\mu\mu-channel$, respectively, in CR_Z control region.
Fig. C.12 shows the distribution of the pseudorapidity η for the leading lepton in $ee-channel$ and $\mu\mu-channel$, respectively, in CR_Z control region.
Fig. C.13 shows the distribution of the pseudorapidity η for the sub-leading lepton in $ee-channel$ and $\mu\mu-channel$, respectively, in CR_Z control region.
It is possible to see, in all plots, a good agreement data/MC within the error bars. Both statistical and systematic errors are taken into account.

In this part of section the kinematics variable in CR_{Fake} control region are shown. In these plots is possible to see a trend of over-estimation; this is due to the fact that the statistics is very low.
Fig. C.14 shows the distribution of the sub-leading lepton p_T in $ee-channel$ and $\mu\mu-channel$, respectively, in CR_{Fake} control region.
Fig. C.15 shows the ΔR between the charged sub-leading lepton and its nearest jet in $ee-channel$ and $\mu\mu-channel$, respectively, in CR_{Fake} control region.
Fig. C.16 shows the distribution of the sub-leading jet p_T in $ee-channel$ and $\mu\mu-channel$, respectively, in CR_{Fake} control region.
Fig. C.17 shows the distribution of the pseudorapidity η for the leading lepton in $ee-channel$ and $\mu\mu-channel$, respectively, in CR_{Fake} control region.
Fig. C.18 shows the distribution of the pseudorapidity η for the sub-leading lepton in $ee-channel$ and $\mu\mu-channel$, respectively, in CR_{Fake} control region.

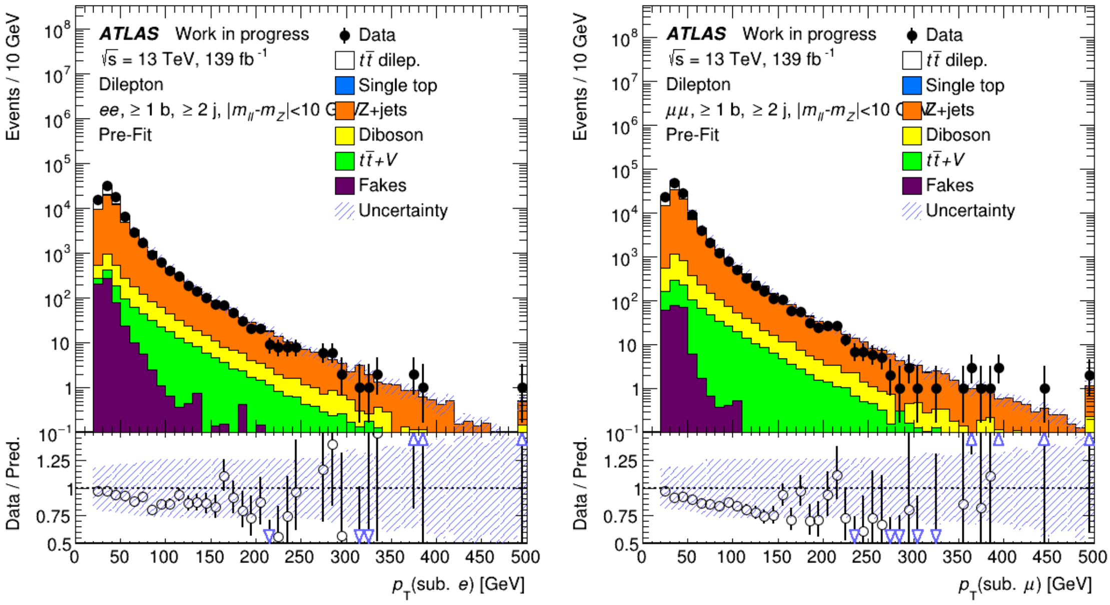

(a) (b)

FIGURE C.9: Transverse momentum of the sub-leading lepton in $ee-channel$ (a) and $\mu\mu-channel$ (b), in CR$_Z$ control region. Both statistical and systematic errors are taken into account.

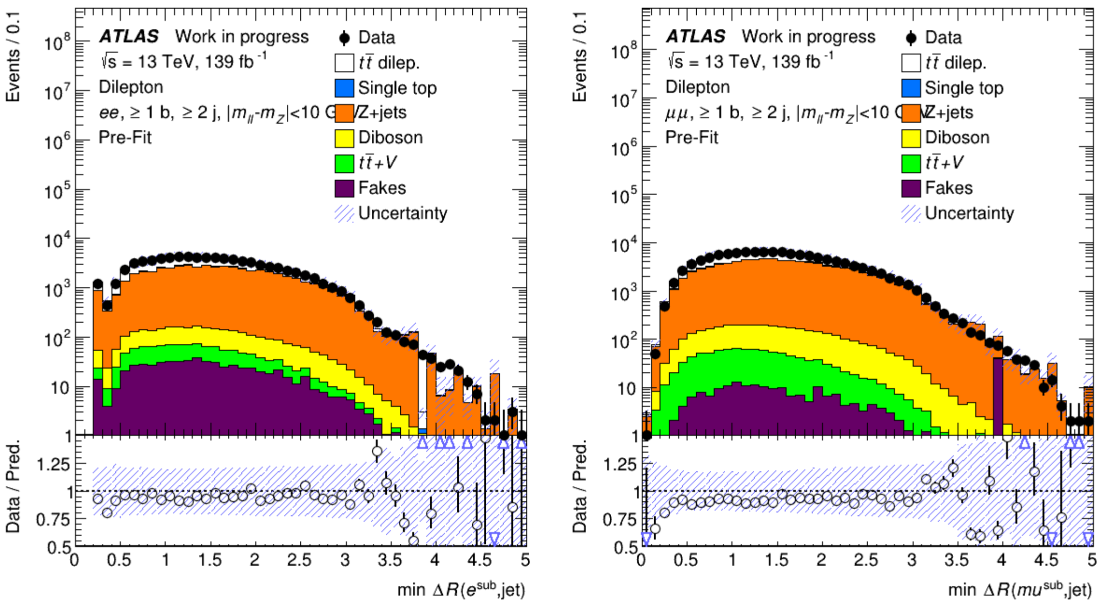

(a) (b)

FIGURE C.10: ΔR between the charged sub-leading lepton and its nearest jet in $ee-channel$ (a) and $\mu\mu-channel$ (b), in CR$_Z$ control region. Both statistical and systematic errors are taken into account.

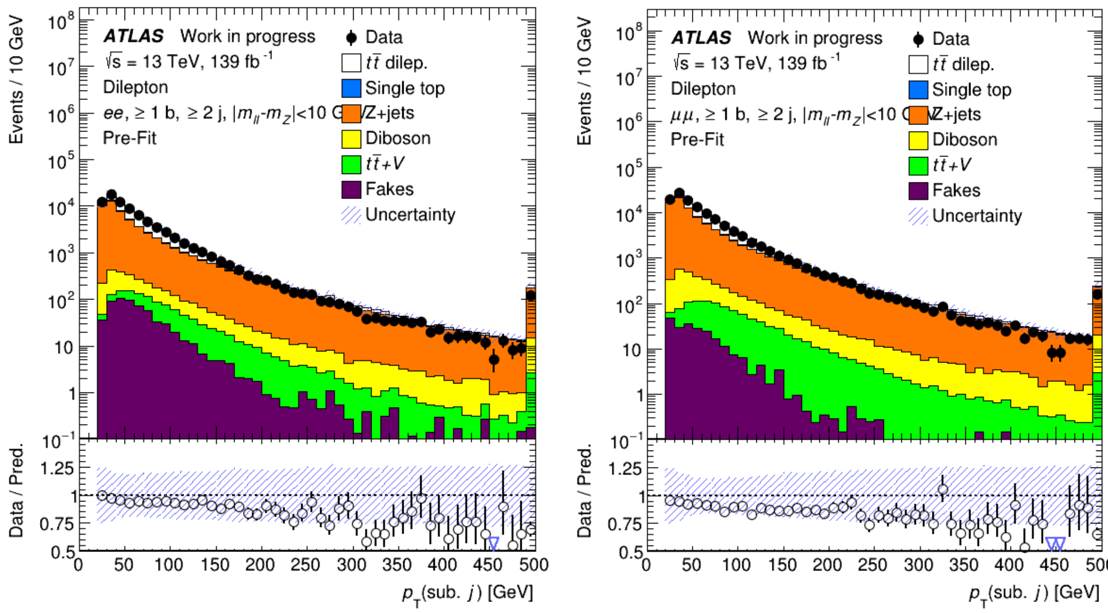

(a) (b)

FIGURE C.11: Transverse momentum of the sub-leading jet in *ee − channel* (a) and $\mu\mu$ − *channel* (b), in CR$_Z$ control region. Both statistical and systematic errors are taken into account.

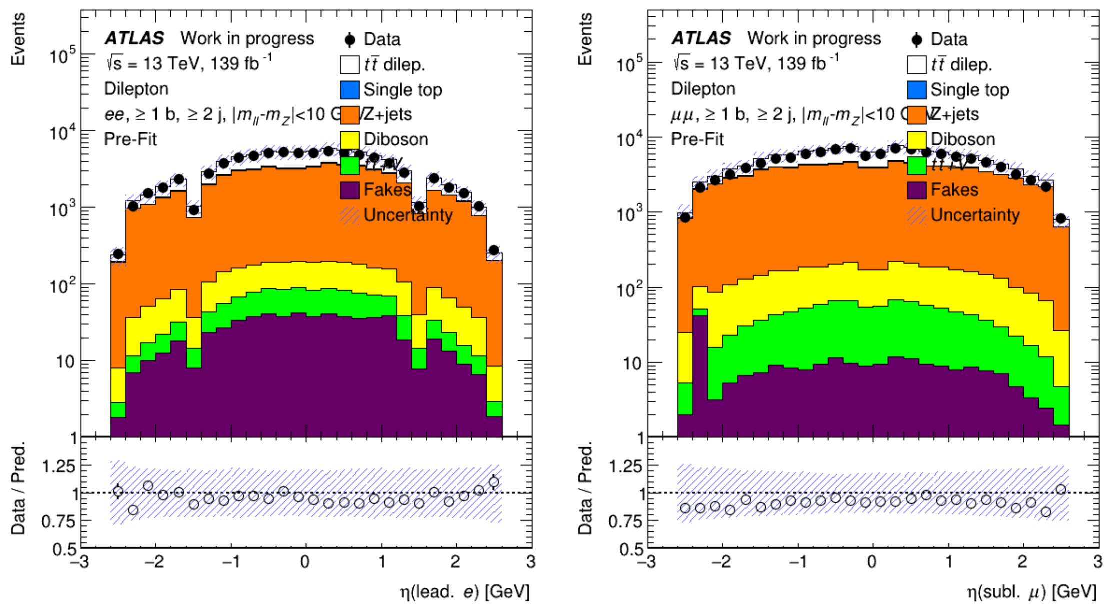

(a) (b)

FIGURE C.12: Pseudorapidity η of the leading lepton in *ee − channel* (a) and $\mu\mu$ − *channel* (b), in CR$_Z$ control region. Both statistical and systematic errors are taken into account.

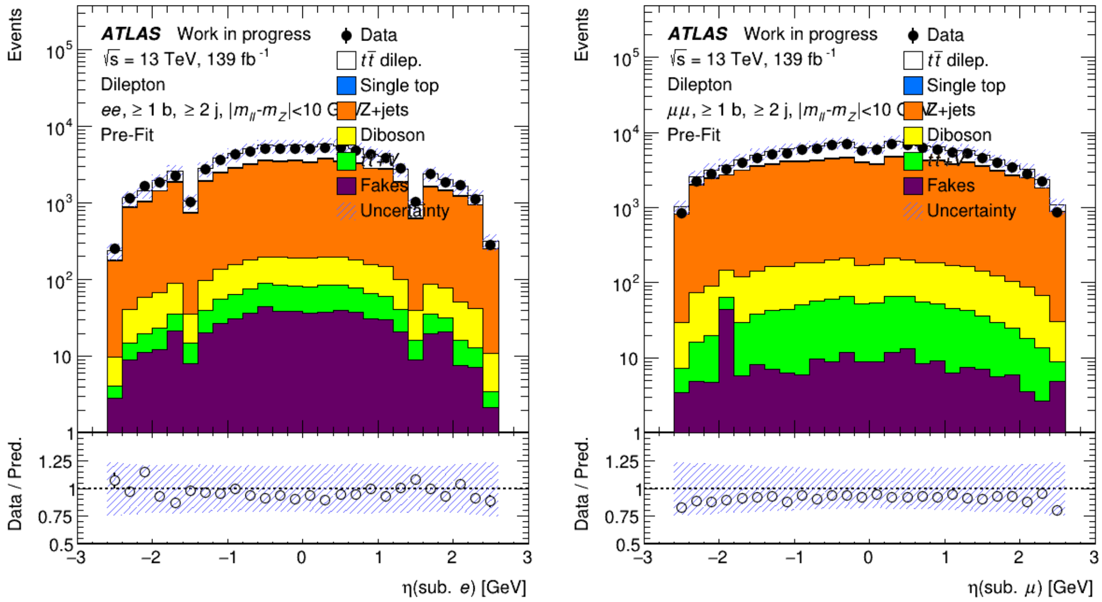

(a) (b)

FIGURE C.13: Pseudorapidity η of the sub-leading lepton in $ee-channel$ (a) and $\mu\mu-channel$ (b), in CR$_Z$ control region. Both statistical and systematic errors are taken into account.

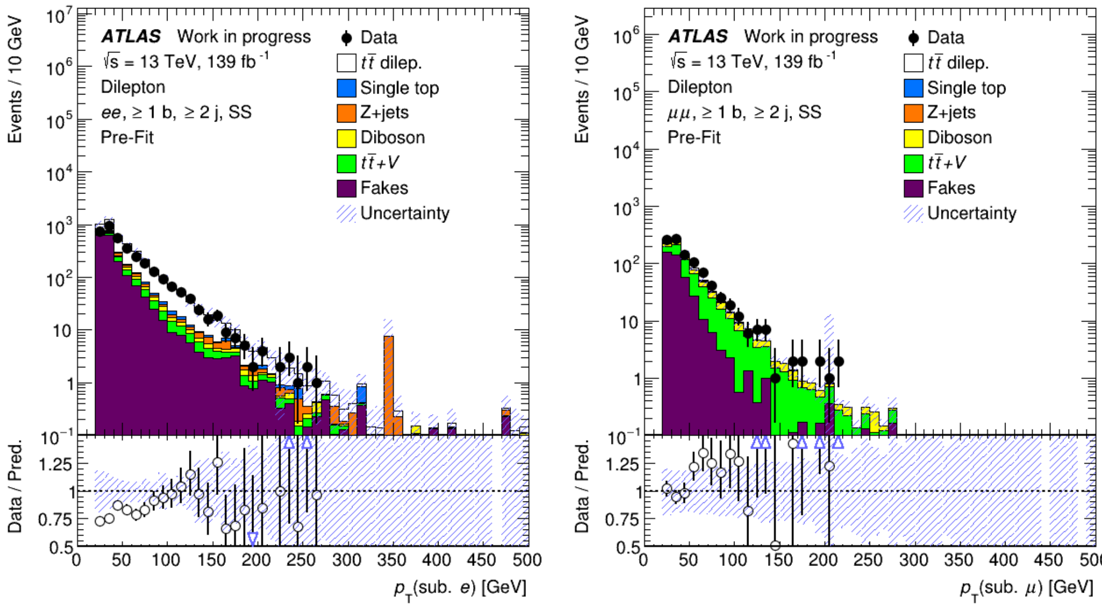

(a) (b)

FIGURE C.14: Transverse momentum of the sub-leading lepton in $ee-channel$ (a) and $\mu\mu-channel$ (b), in CR$_{Fake}$ control region. Both statistical and systematic errors are taken into account.

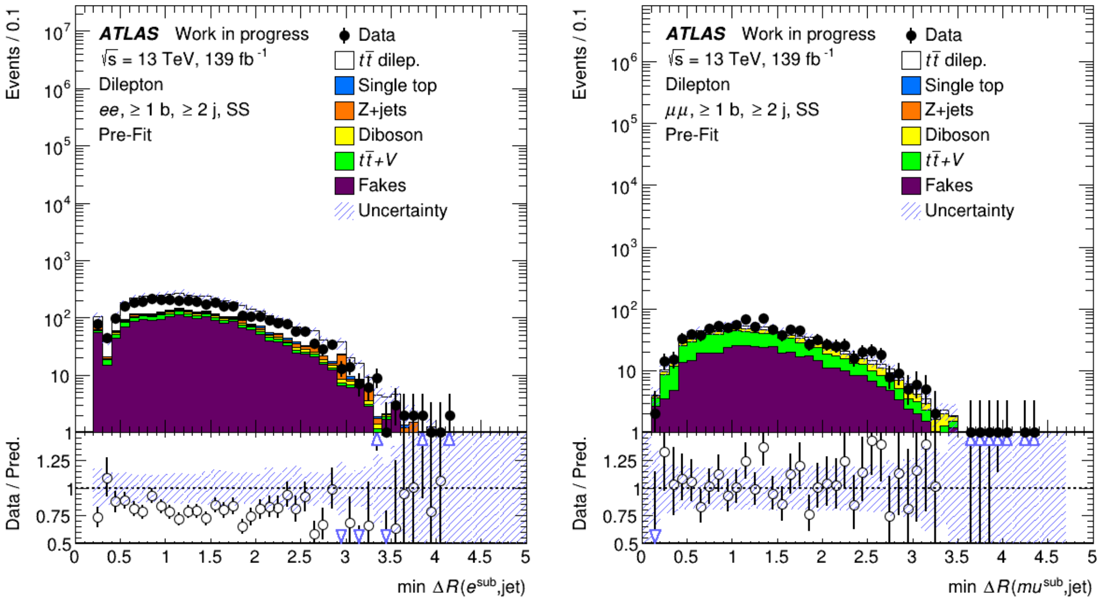

(a) (b)

Figure C.15: ΔR between the charged sub-leading lepton and its nearest jet in $ee-channel$ (a) and $\mu\mu-channel$ (b), in CR$_{Fake}$ control region. Both statistical and systematic errors are taken into account.

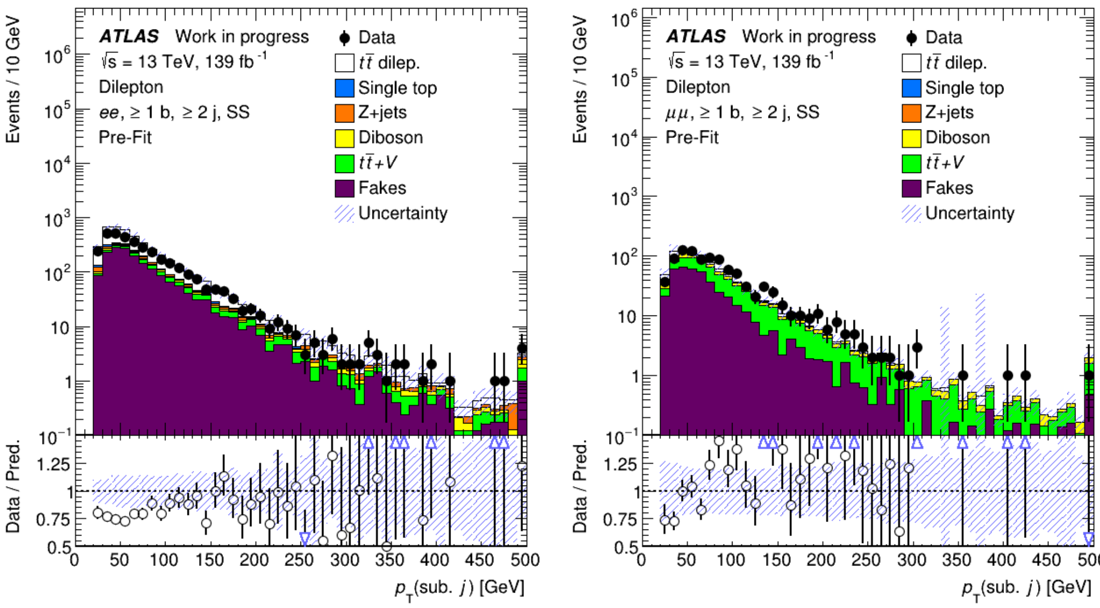

(a) (b)

Figure C.16: Transverse momentum of the sub-leading jet in $ee-channel$ (a) and $\mu\mu-channel$ (b), in CR$_{Fake}$ control region. Both statistical and systematic errors are taken into account.

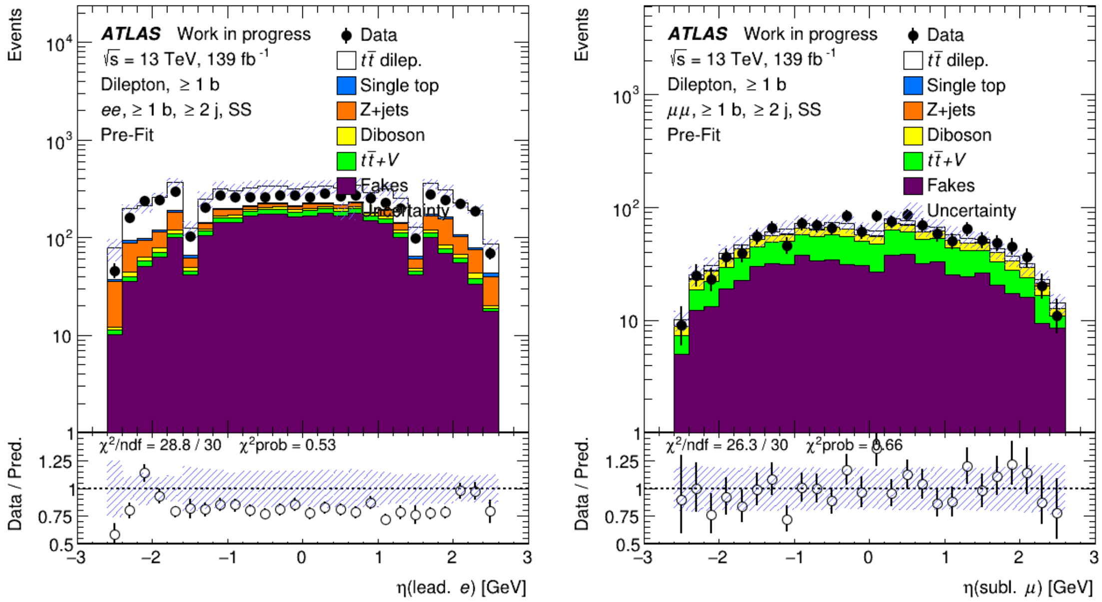

(a) (b)

FIGURE C.17: Pseudorapidity η of the leading lepton in $ee - channel$ (a) and $\mu\mu - channel$ (b), in CR_{Fake} control region. Both statistical and systematic errors are taken into account.

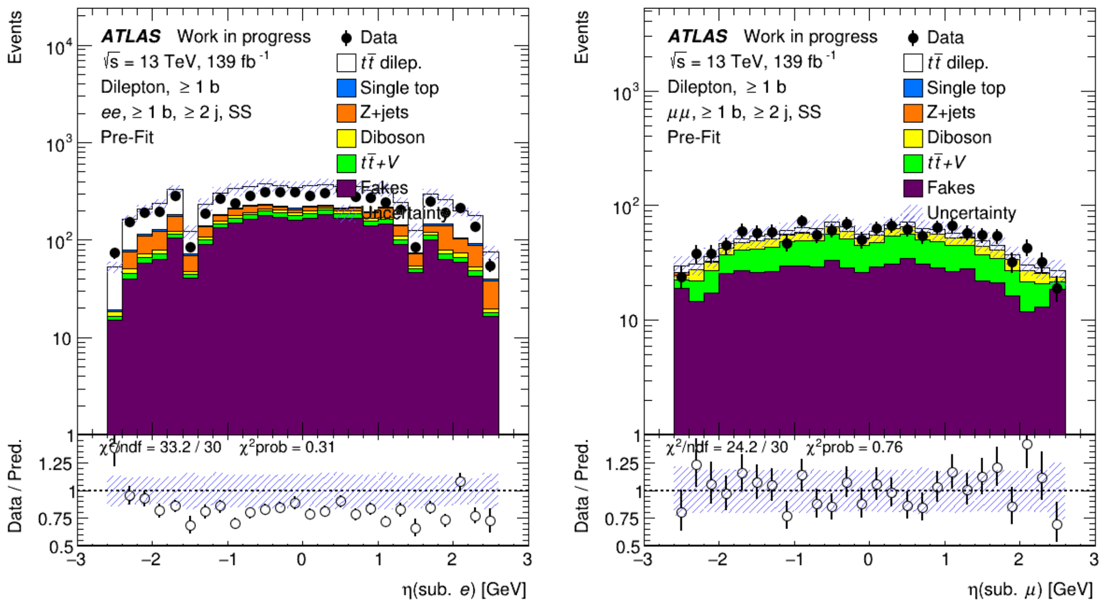

(a) (b)

FIGURE C.18: Pseudorapidity η of the sub-leading lepton in $ee - channel$ (a) and $\mu\mu - channel$ (b), in CR_{Fake} control region. Both statistical and systematic errors are taken into account.

C.3 Signal regions

Here all the 10 bins of invariant mass variable are shown.
Fig. C.19 shows the 10 bins of $m_{t\bar{t}}^{NW}$ invariant mass variable, only simulated samples without data, due to the blinding study.
Fig. C.20 shows the 10 bins of $m\ell\ell bb$ proxy variable, only simulated samples without data, due to the blinding study.
It is possible to see that the systematics errors increase with the rising of the region mass under study. The signal here is the Z' with a mass of 2 TeV and is possible to see that the signal events increase with the rises mass region, as we expected.

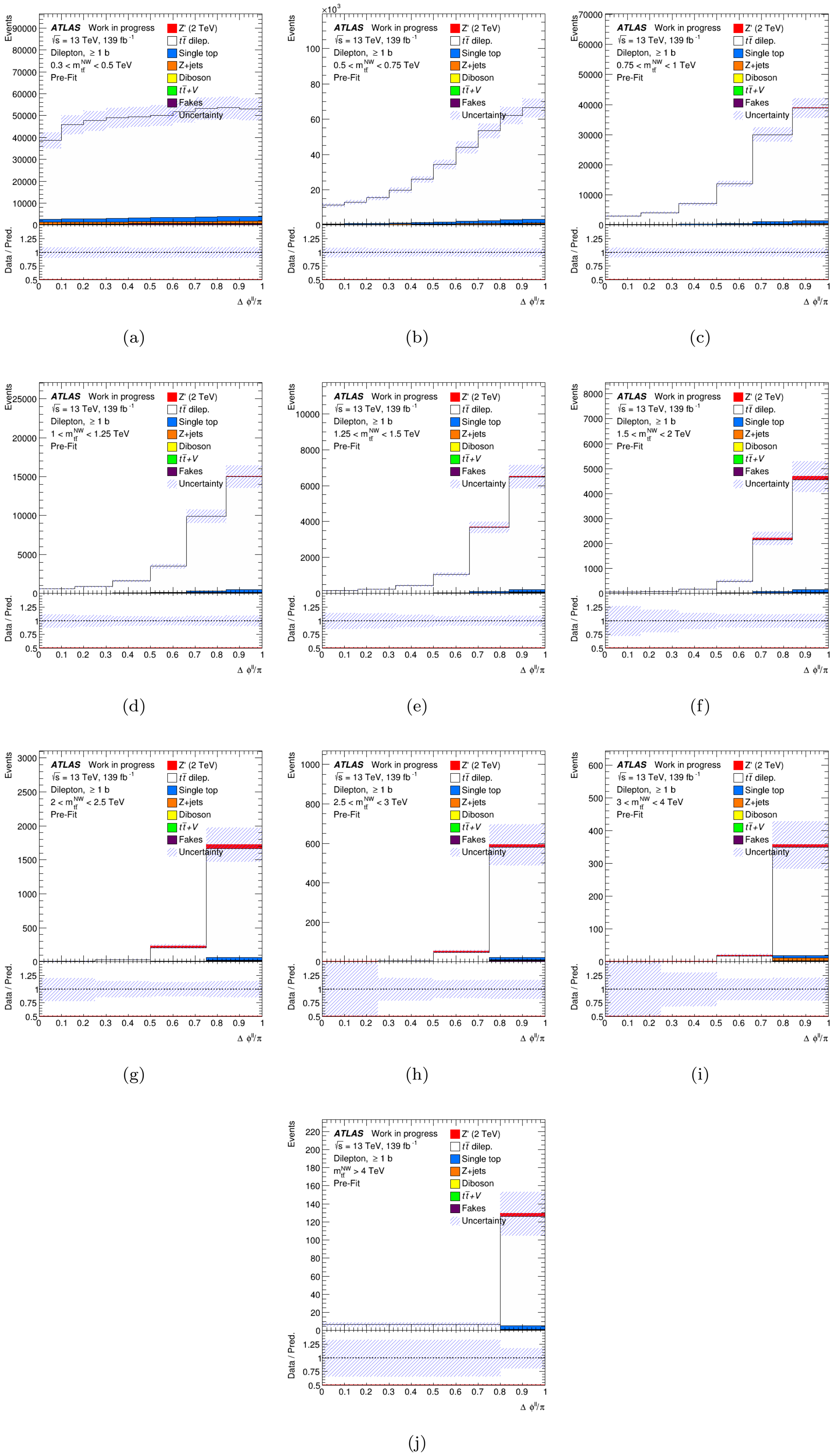

FIGURE C.19: The 10 bins of $m_{t\bar{t}}^{NW}$ invariant mass variable signal region. The signal is Z' with a mass of 2 TeV Errors are MC statistics and systematics.

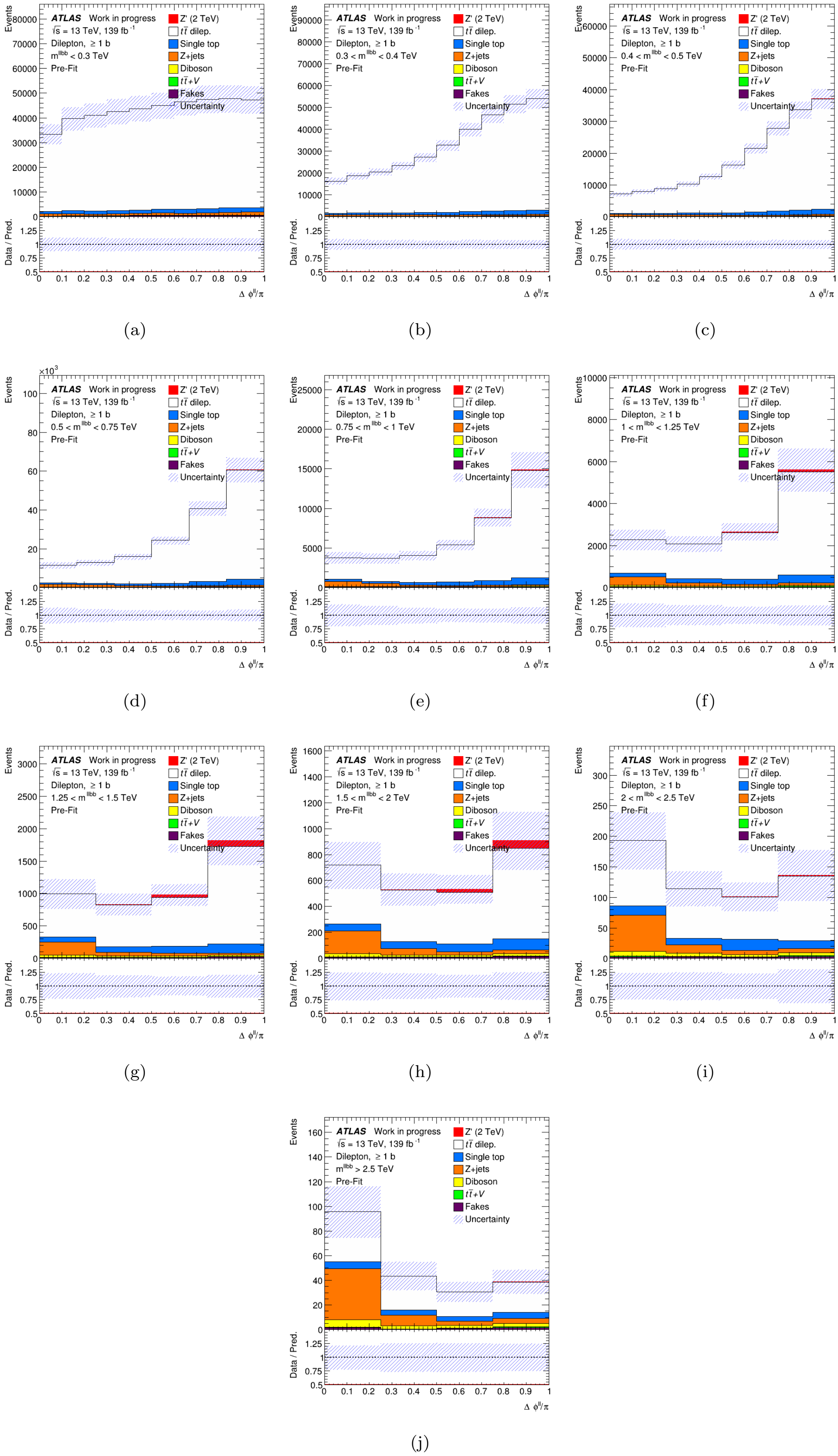

FIGURE C.20: The 10 bins of $m_{\ell\ell bb}$ proxy variable signal region. The signal is Z' with a mass of 2 TeV Errors are MC statistics and systematics.

C.4 Ranking plots and nuisance parameters

In this section all plot regarding the ranking plots and nuisance parameters are shown.
Fig. C.21, Fig. C.22 and Fig. C.23 show the ranking plots of $m_{\ell\ell bb}$ proxy variable in all Z', g_{KK} and G signal mass points, respectively.
Fig. C.24, Fig. C.25 and Fig. C.26 show the ranking plots of $m_{t\bar{t}}^{NW}$ invariant mass variable in all Z', g_{KK} and G signal mass points, respectively.
The empty squares in the plots are the pre-fit systematics and the full squares are the post-fit systematics.

Fig. C.27, Fig. C.28 and Fig. C.29 show the pull of nuisance parameter of $m_{\ell\ell bb}$ proxy variable in all Z', g_{KK} and G signal mass points, respectively.
Fig. C.30, Fig. C.31 and Fig. C.32 show the pull of nuisance parameter of $m_{t\bar{t}}^{NW}$ invariant mass variable in all Z', g_{KK} and G signal mass points, respectively.
The errors are inside the limit significance of the systematics.

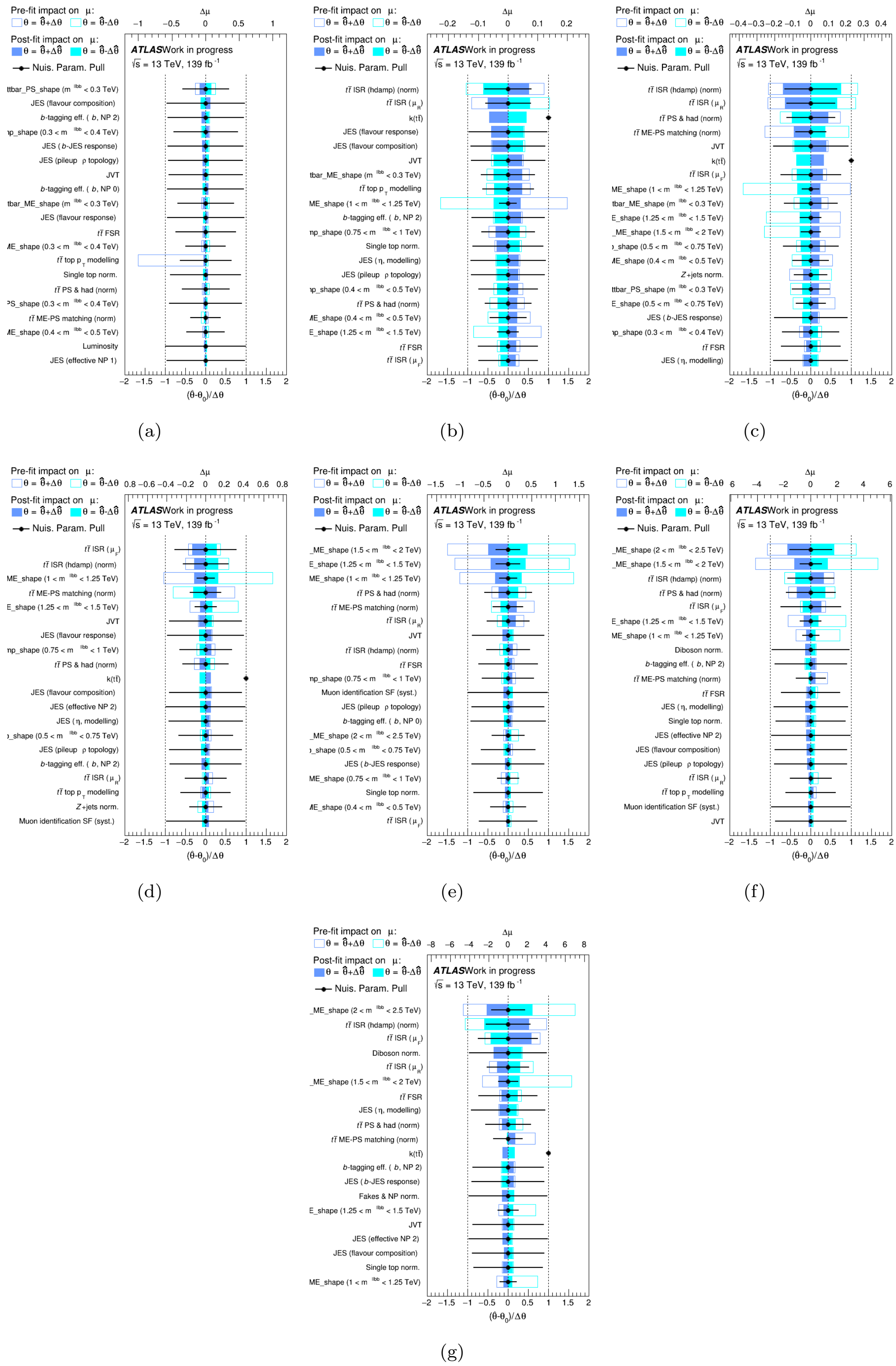

FIGURE C.21: Ranking plots of $m_{\ell\ell bb}$ proxy variable in all seven Z' signal mass: 500 GeV (a), 750 (b), 1 TeV (c), 1.5 TeV (d), 2 TeV (e), 3 TeV (f) and 4 TeV (g).

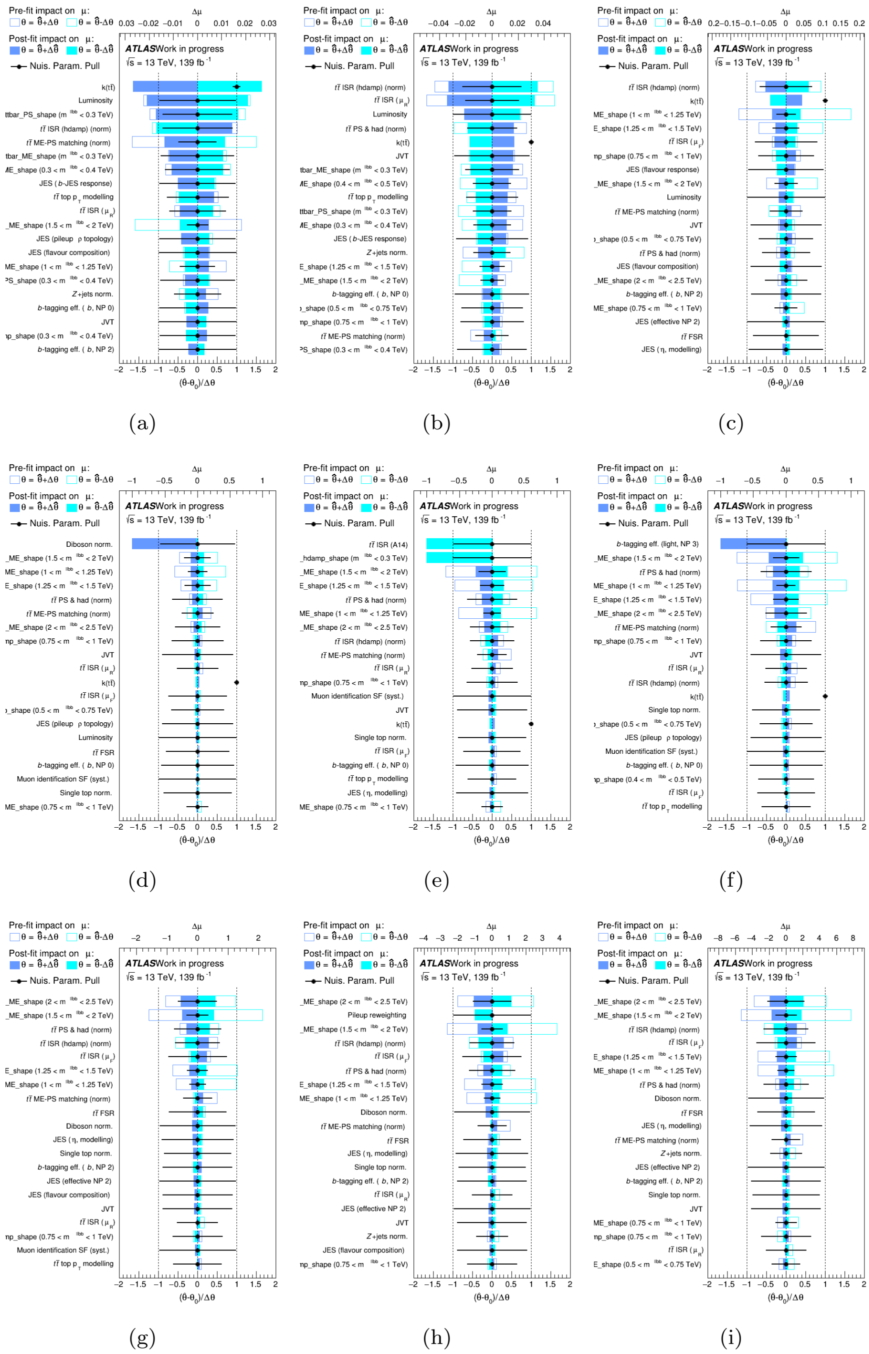

(a) (b) (c)

(d) (e) (f)

(g) (h) (i)

FIGURE C.22: Ranking plots of $m_{\ell\ell bb}$ proxy variable in all nine g_{KK} signal mass: 500 GeV (a), 1 TeV (b), 1.5 TeV (c), 2 TeV (d), 2.5 TeV (e), 3 TeV (f), 3.5 TeV (g), 4 TeV (h), and 4.5 TeV (i).

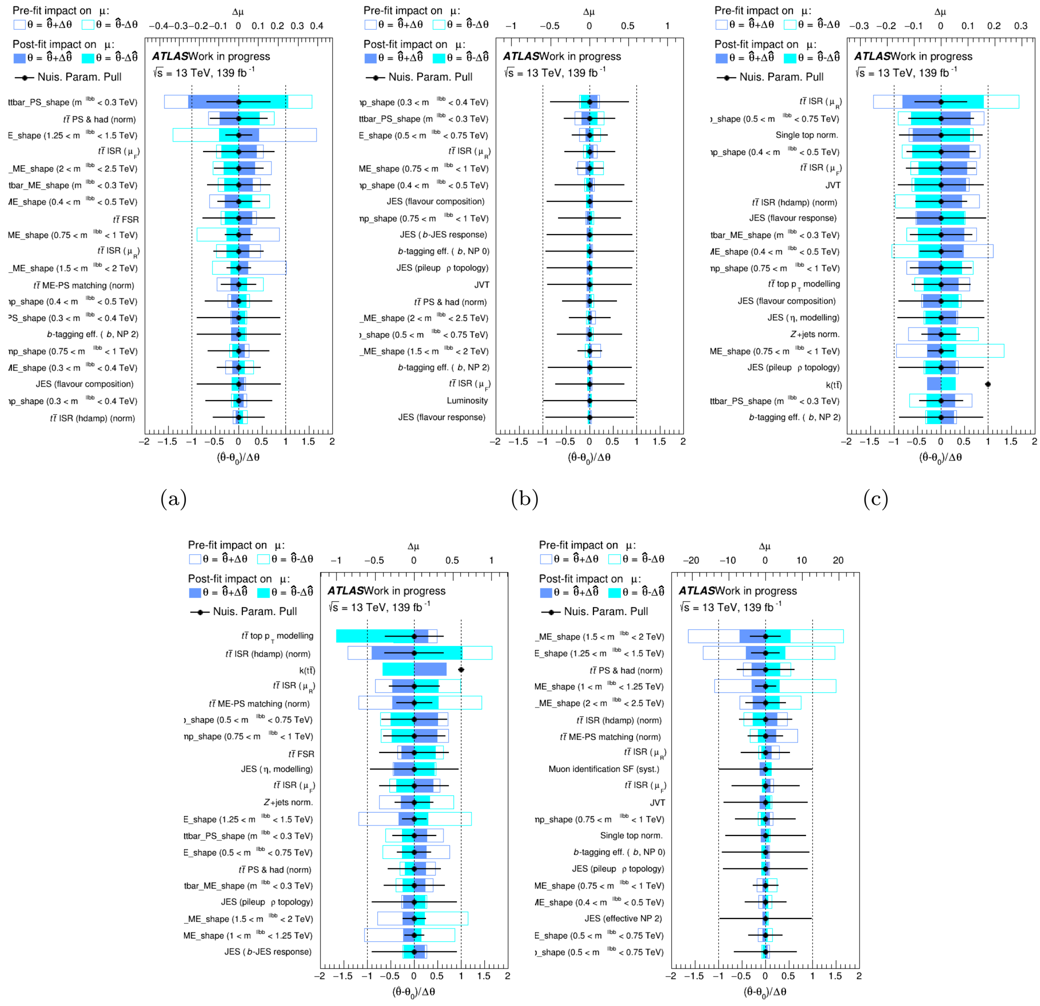

(a) (b) (c)

(d) (e)

FIGURE C.23: Ranking plots of $m_{\ell\ell bb}$ proxy variable in all five G signal mass: 400 GeV (a), 500 (b), 750 GeV (c), 1 TeV (d) and 2 TeV (e).

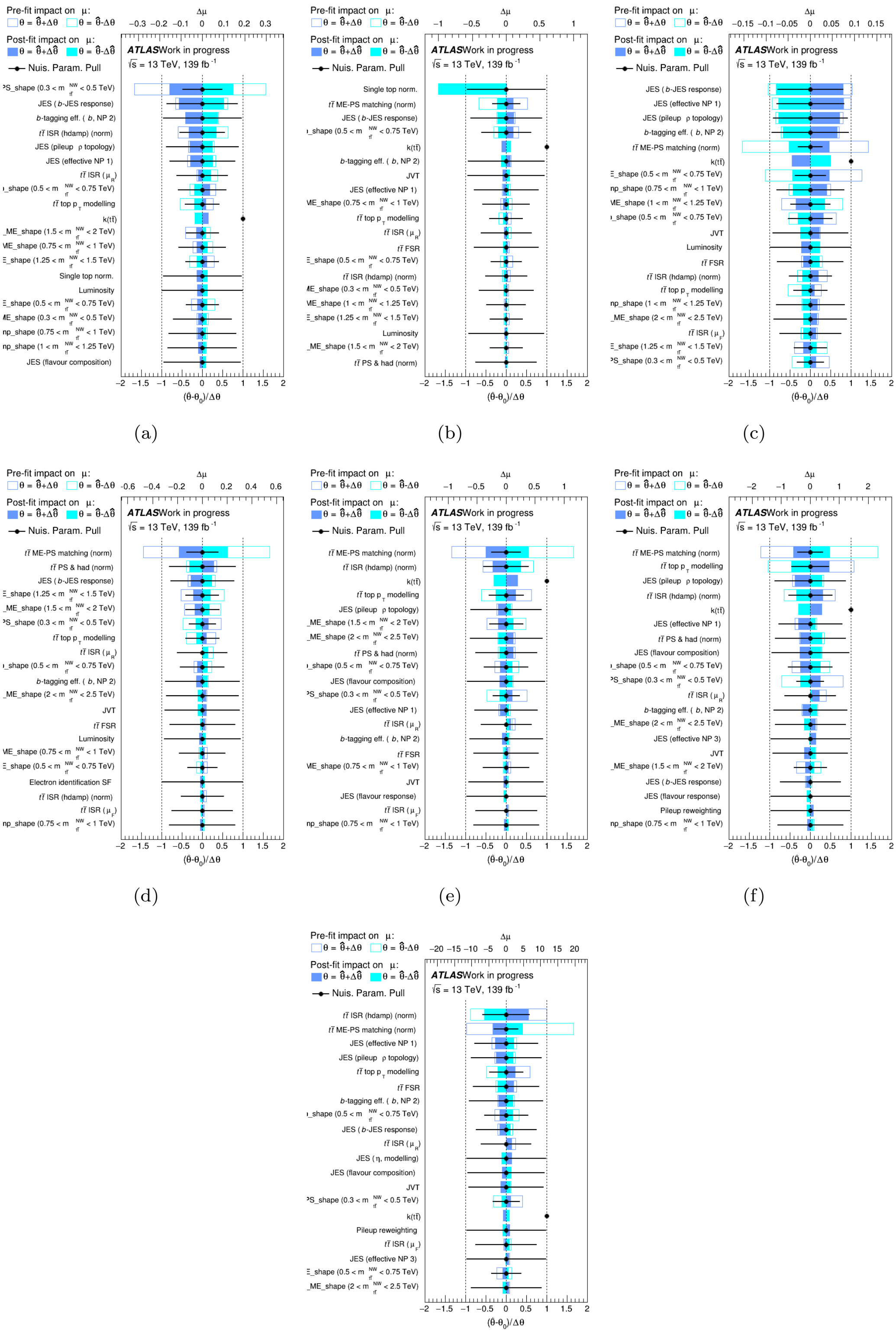

(a) (b) (c)

(d) (e) (f)

(g)

Figure C.24: Ranking plots of $m_{t\bar{t}}^{NW}$ variable in all seven Z' signal mass: 500 GeV (a), 750 (b), 1 TeV (c), 2 TeV (d), 3 TeV (e) and 4 TeV (f).

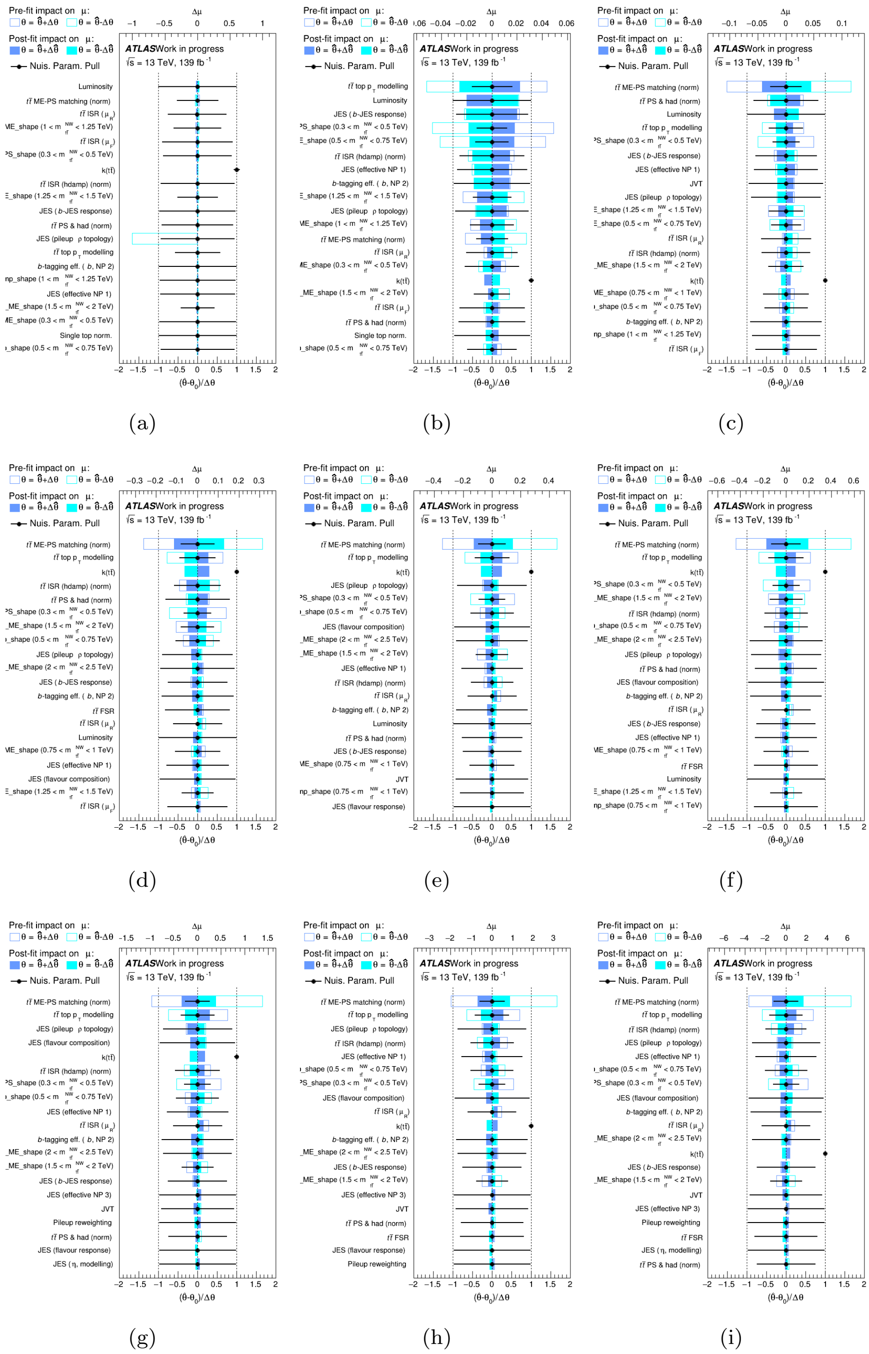

(a) (b) (c)

(d) (e) (f)

(g) (h) (i)

FIGURE C.25: Ranking plots of $m_{t\bar{t}}^{NW}$ variable in all nine g_{KK} signal mass: 500 GeV (a), 1 TeV (b), 1.5 TeV (c), 2 TeV (d), 2.5 TeV (e), 3 TeV (f), 3.5 TeV (g), 4 TeV (h) and 4.5 TeV (i).

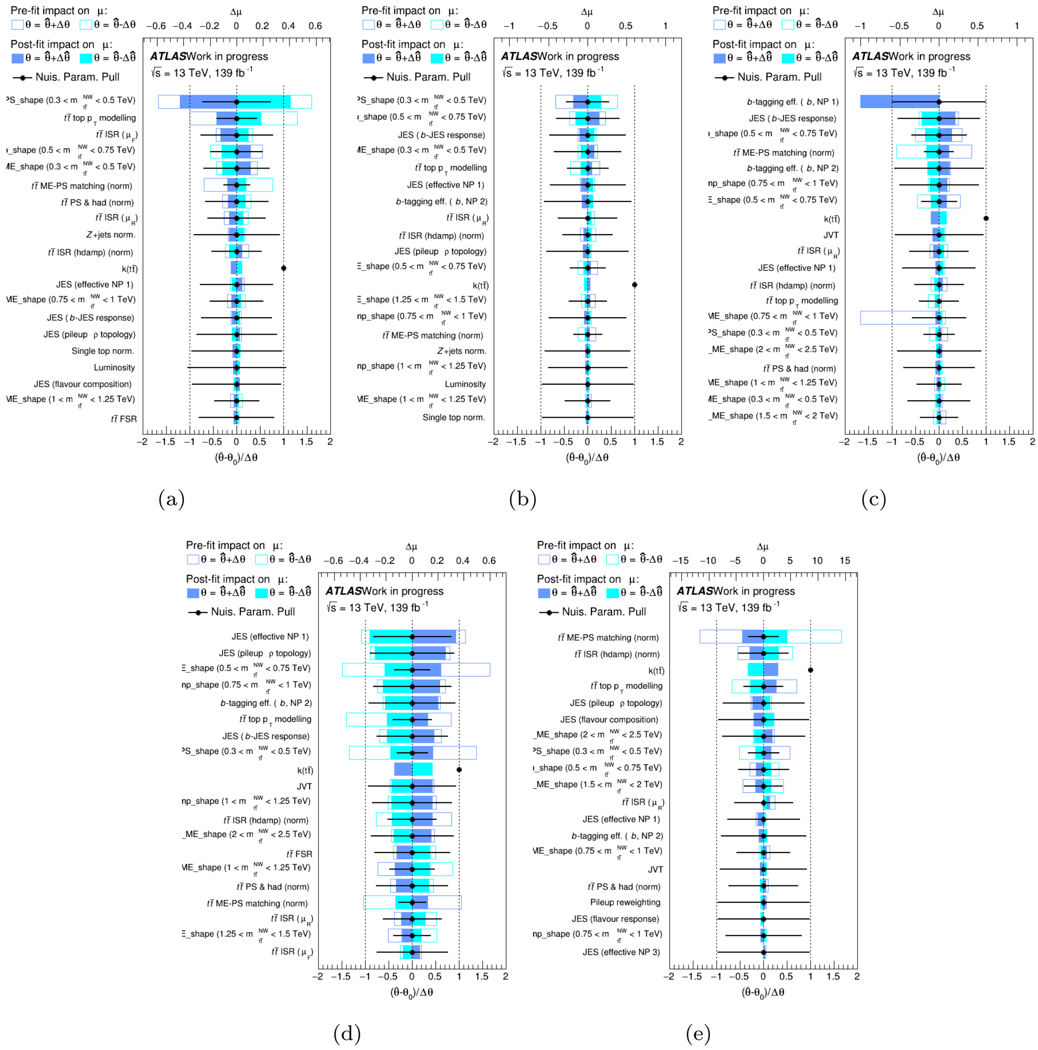

FIGURE C.26: Ranking plots of $m_{t\bar{t}}^{NW}$ variable in all five G signal mass: 400 GeV (a), 500 (b), 750 GeV (c), 1 TeV (d) and 2 TeV (e).

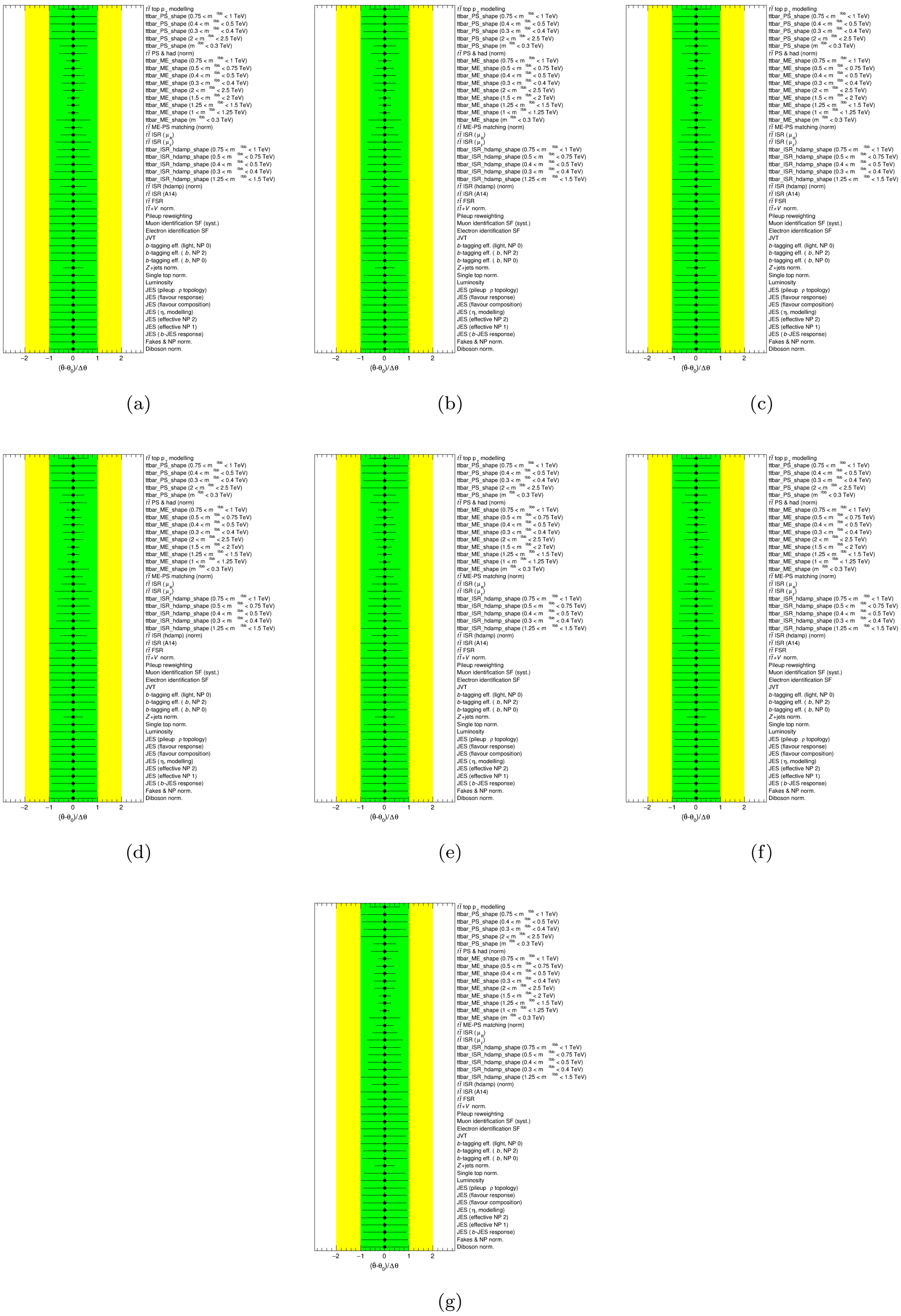

FIGURE C.27: Nuisance parameters of $m_{\ell\ell bb}$ proxy variable in all seven Z' signal mass: 500 GeV (a), 750 (b), 1 TeV (c), 1.5 TeV (d), 2 TeV (e), 3 TeV (f) and 4 TeV (g).

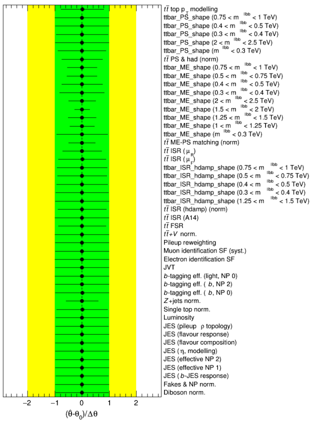

(a)

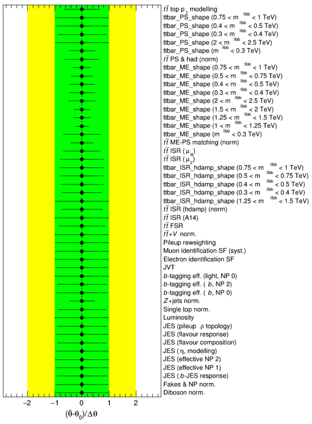

(b)

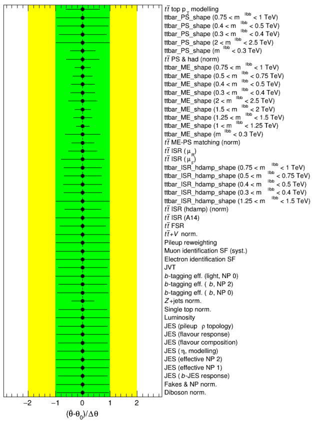

(c)

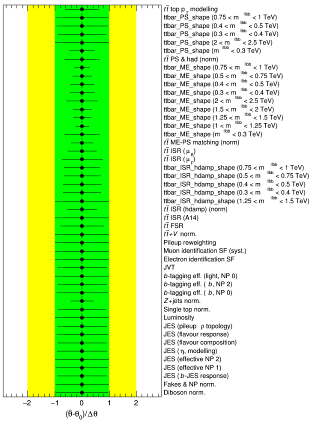

(d)

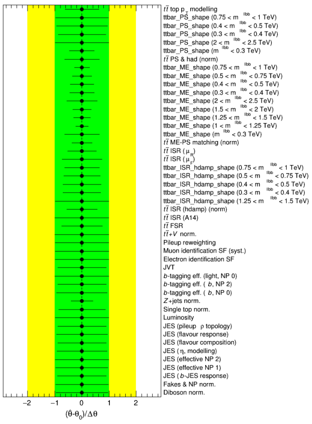

(e)

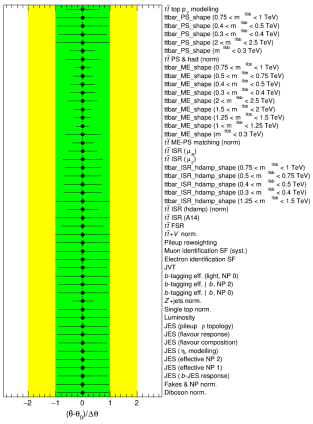

(f)

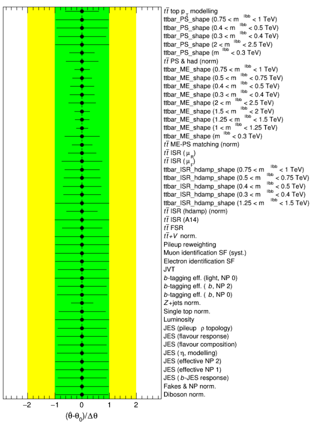

(g)

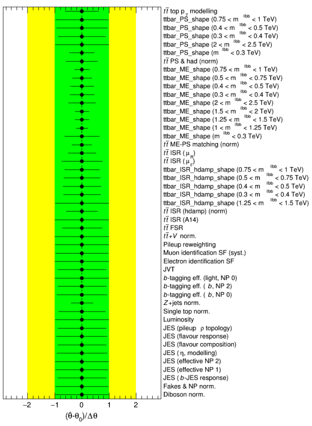

(h)

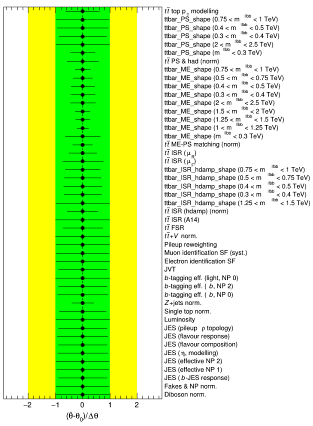

(i)

FIGURE C.28: Nuisance parameters of $m_{\ell\ell bb}$ proxy variable in all nine g_{KK} signal mass: 500 GeV (a), 1 TeV (b), 1.5 TeV (c), 2 TeV (d), 2.5 TeV (e), 3 TeV (f), 3.5 TeV (g), 4 TeV (h), and 4.5 TeV (i).

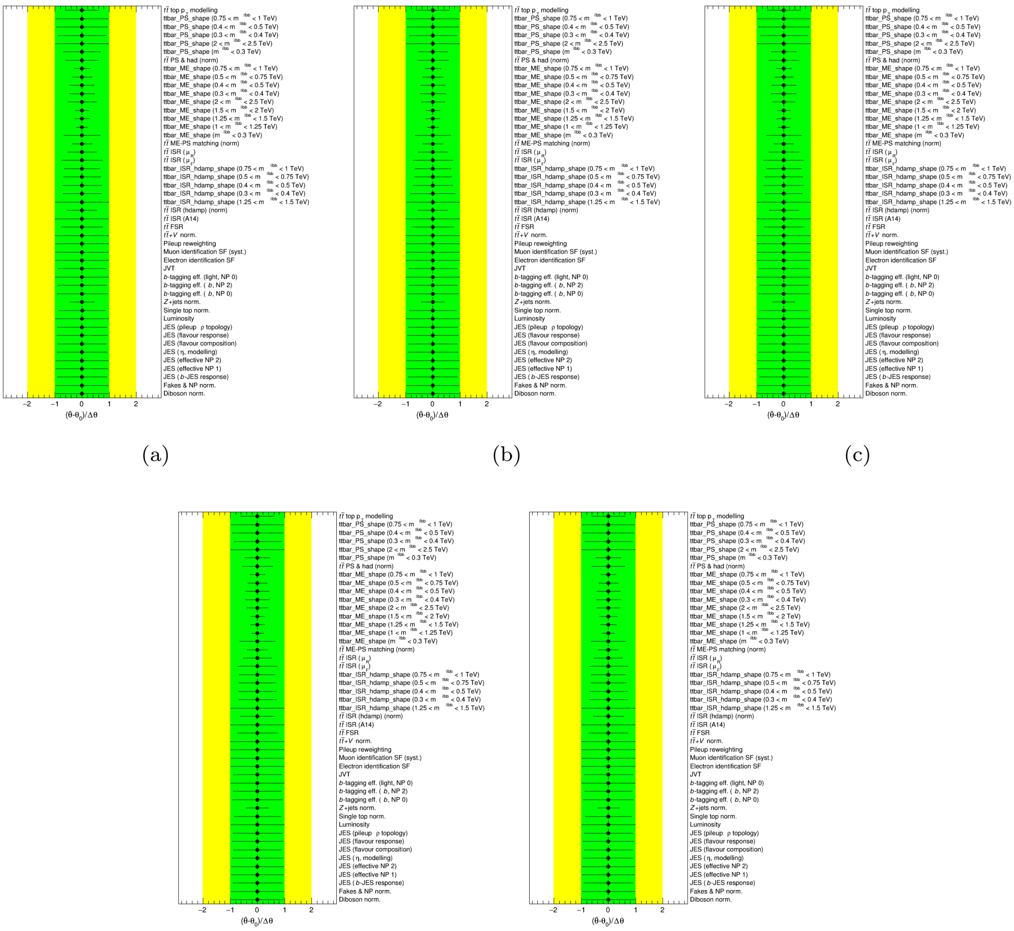

(a) (b) (c)

(d) (e)

FIGURE C.29: Nuisance parameters of $m_{\ell\ell bb}$ proxy variable in all five G signal mass: 400 GeV (a), 500 (b), 750 GeV (c), 1 TeV (d) and 2 TeV (e).

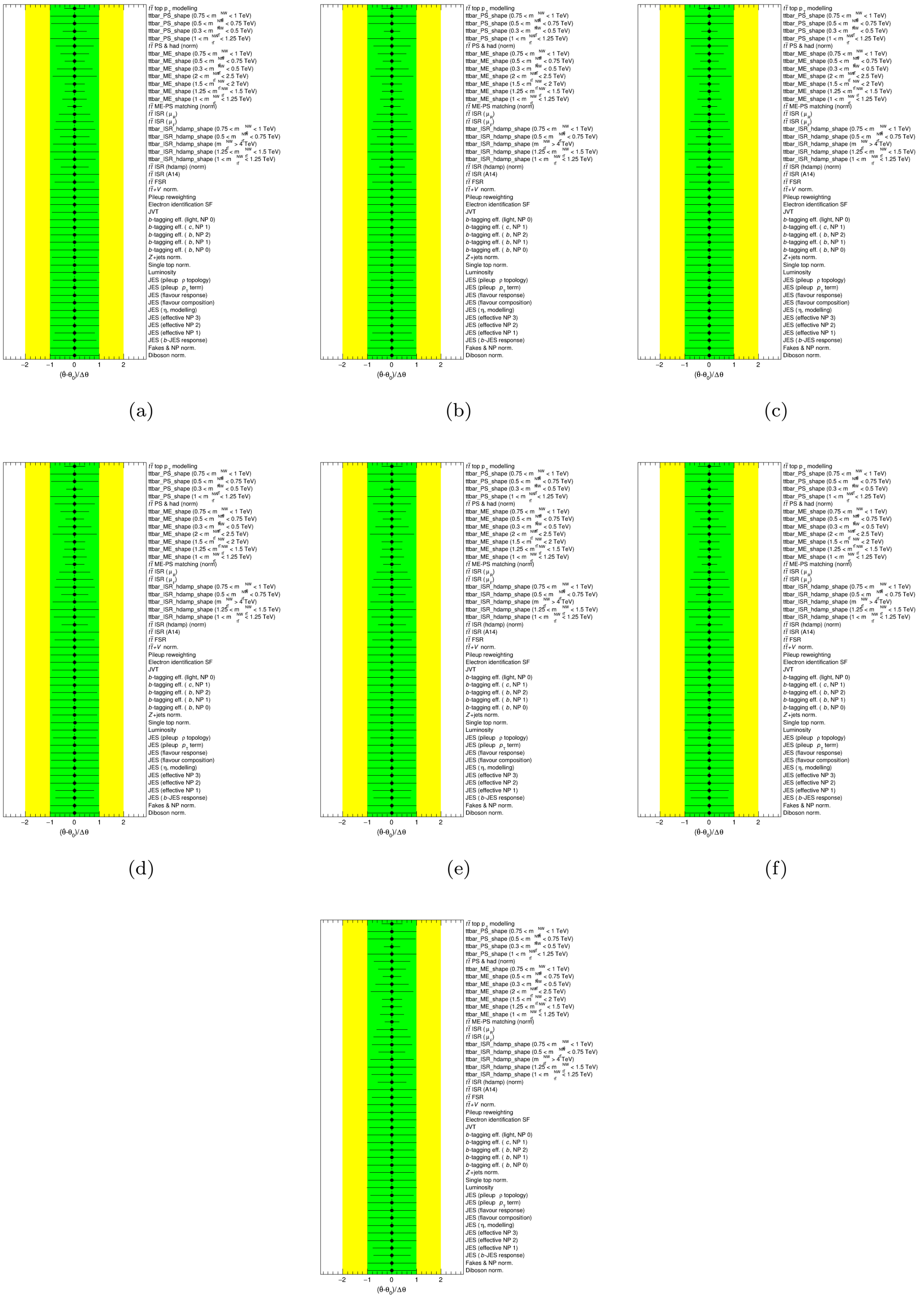

(a) (b) (c) (d) (e) (f) (g)

FIGURE C.30: Nuisance parameters of $m_{t\bar{t}}^{NW}$ variable in all seven Z' signal mass: 500 GeV (a), 750 (b), 1 TeV (c), 2 TeV (d), 3 TeV (e) and 4 TeV (f).

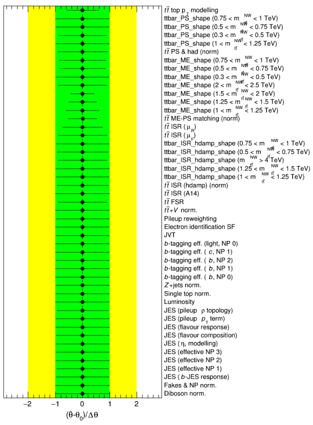

(a)

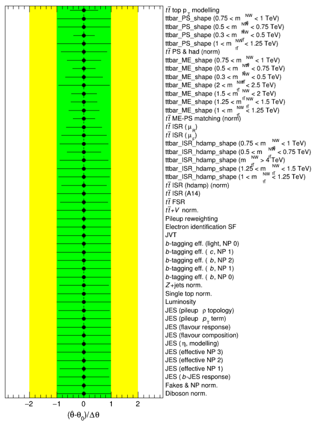

(b)

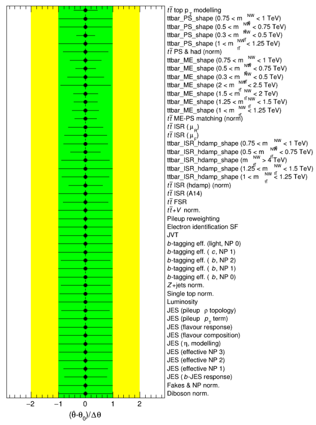

(c)

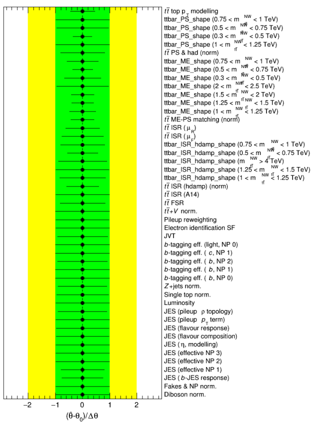

(d)

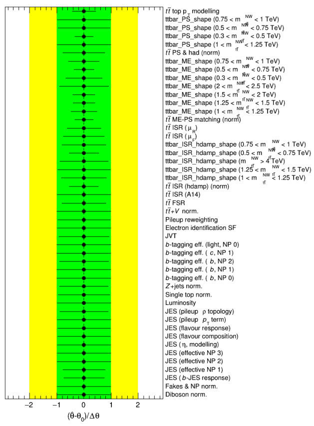

(e)

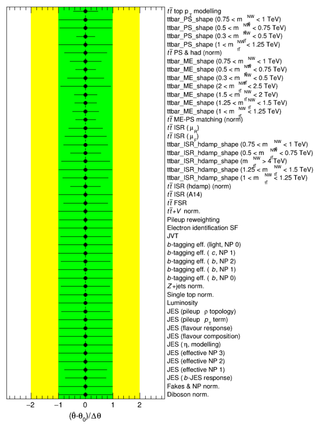

(f)

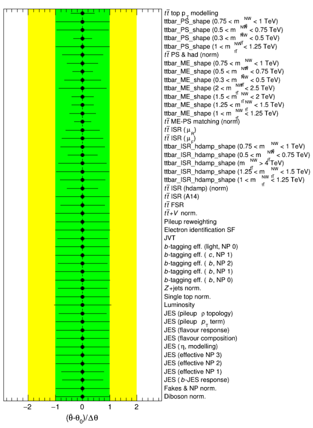

(g)

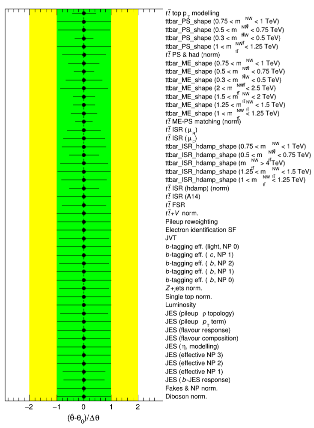

(h)

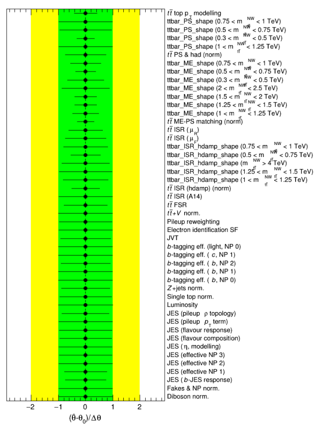

(i)

FIGURE C.31: Nuisance parameters of $m_{t\bar{t}}^{NW}$ variable in all nine g_{KK} signal mass: 500 GeV (a), 1 TeV (b), 1.5 TeV (c), 2 TeV (d), 2.5 TeV (e), 3 TeV (f), 3.5 TeV (g), 4 TeV (h) and 4.5 TeV (i).

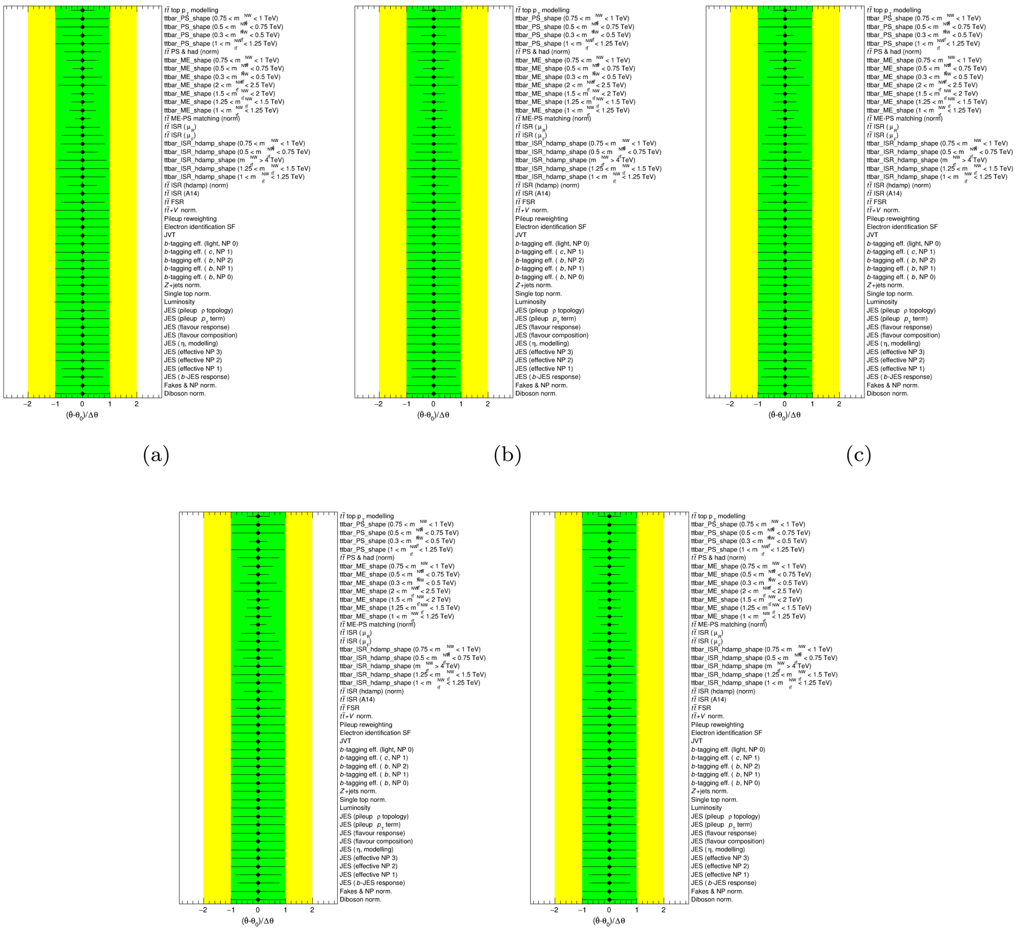

(a) (b) (c)

(d) (e)

FIGURE C.32: Nuisance parameters of $m_{t\bar{t}}^{NW}$ variable in all five G signal mass: 400 GeV (a), 500 (b), 750 GeV (c), 1 TeV (d) and 2 TeV (e).

Bibliography

[1] W.E. Burcham and M. Jobes, "Nuclear and Particle Physics," *Pearson Education*, 1994.

[2] ATLAS Collaboration, "Observation of a new particle in the search for the Standard Model Higgs boson with the ATLAS detector at the LHC," *Physics Letters B V. 716, Issue 1*, 2012.

[3] CMS Collaboration, "Observation of a new boson at a mass of 125 GeV with the CMS experiment at the LHC," *Physics Letters B V. 716, Issue 1*, 2012.

[4] F. Mandl and G. Shaw, "Quantum field theory," *Wiley-Interscience Publication*, 1986.

[5] Englert F. and Brout R., "Broken Symmetry and the Mass of Gauge Vector Mesons," *Physical Review Letters. 13 (9): 321–23*, 1964.

[6] Higgs P., "Broken Symmetries and the Masses of Gauge Bosons," *Physical Review Letters. 13 (16): 508–509*, 1964.

[7] J. Erler and A. Freitas, "Electroweak Model and Constraints on New Physics," *http://pdg.lbl.gov/2019/reviews/rpp2019-rev-standard-model.pdf*, 2018.

[8] Trimble, V., "Existence and nature of dark matter in the universe," *Annual Review of Astronomy and Astrophysics. 25: 425–472*, 1987.

[9] M. C. Gonzalez-Garcia and M. Maltoni, "Phenomenology with Massive Neutrinos," *arXiv:0704.1800*, 2008.

[10] S. Tsujikawa, "Introductory review of cosmic inflation," *arXiv:hep-ph/0304257*, 2003

[11] J. A. Casas, J. R. Espinosa, and I. Hidalgo, "Implications for new physics from fine-tuning arguments. 1) Application to SUSY and seesaw cases," *JHEP, vol. 2004, no. 11*, 2004.

[12] M. Tanabashi et al., "The Review of Particle Physics," *Phys. Rev. D 98, 030001 (2018)*, 2018.

[13] Czakon and Fiedler and Mitov, "The total top quark pair production cross-section at hadron colliders through O(alphaS4)," *Phys. Rev. Lett. 110, 252004*, 2013.

[14] ATLAS Collaboration, "Measurement of the charge asymmetry in top-quark pair production in the lepton-plus-jets final state in pp collision data at sqrt(s)=8 TeV with the ATLAS detector," *Eur. Phys. J. C76, 87 (2016)*, 2017.

[15] ATLAS Collaboration, "Measurements of the charge asymmetry in top-quark pair production in the dilepton final state at sqrt(s)=8 TeV with the ATLAS detector," *Phys. Rev. D94, 032006 (2016)*, 2016.

[16] CMS Collaboration, "Measurement of the charge asymmetry in top quark pair production in pp collisions at sqrt(s)= 8 TeV using a template method," *Phys. Rev. D93, 034014 (2016)*, 2016.

[17] G. Mahlonm and S.J. Parke, "Spin Correlation Effects in Top Quark Pair Production at the LHC," *Phys. Rev. D81, 074024 (2010)*, 2010.

[18] ATLAS Collaboration, "Measurements of top-quark pair spin correlations in the eμ channel at sqrt(s)= 13 TeV using pp collisions in the ATLAS detector," *arXiv:1903.07570v2*, 2020.

[19] P. Langacker, "The Physics of Hevay Z0 Gauge Boson," *Rev. Mod. Phys.*, 2009.

[20] D. London and J.L. Rosner, "Extra Gauge Bosono in E(6)," *Proceedings, 23rd International Conference on High Energy Physics*, 1986.

[21] ATLAS Collaboration, "Search for high-mass new phenomena in the dilepton final state using proton–proton collisions at sqrt(s) = 13 TeV with the ATLAS detector," *ATL-COM-PHYS-2016-1404*, 2017.

[22] CDF Collaboration, "Search for High Mass Resonances Decaying to Muon Pairs in sqrt(s)= 1.96 TeV ppbar Collisions," *arXiv:1101.4578*, 2011.

[23] P. Langacker, "Z' Physics at the LHC," *arXiv:0911.4294*, 2009.

[24] Robert M. Harris, Christopher T. Hill, Stephen J. Parke, "Cross Section for Topcolor Z' decaying to top-antitop," *arXiv:hep-ph/9911288*, 1999.

[25] CMS Collaboration, "Search for resonant ttbar production in proton-proton collisions at sqrt(s) = 13 TeV," *arXiv:1810.05905*, 2019.

[26] L. Randall and R. Sundrum, "A Large Mass Hierarchy from a Small Extra Dimension," *arXiv:hep-ph/9905221*, 1999.

[27] ATLAS Collaboration, "Search for heavy ZZ resonances in the $\ell^+\ell^-\ell^+\ell^-$ and $\ell^+\ell^-\nu^+n\bar{u}$ final states using proton–proton collisions at $sqrts$ = 13 TeV with the ATLAS detector," *ATLAS-CONF-2017-058*, 2017.

[28] ATLAS Collaboration, "Search for WW/WZ resonance production in $\ell\nu$qq final states in pp collisions at $\sqrt{s}$ = 13 TeV with the ATLAS detector," *ATLAS-CONF-2017-051*, 2017.

[29] ATLAS Collaboration, "Search for heavy particles decaying into top-quark pairs using lepton-plus-jets events in proton–proton collisions at sqrt(s)= 13 TeV with the ATLAS detector," *arXiv:1804.10823*, 2018.

[30] B. Lillie and L. Randall and L.T. Wang, "The Bulk RS KK-gluon at the LHC," *arXiv:hep-ph/0701166*, 2007.

[31] ATLAS Collaboration, "A Search for ttbar Resonances in the Dilepton Channel in 1.04/fb of pp Collisions at sqrt(s) = 7 TeV," *ATLAS-CONF-2011-123*, 2011.

[32] L. Evans and P. Bryant, "LHC Machine," *JINST 3 S08001*, 2008.

[33] ATLAS Collaboration, "The ATLAS Experiment at the CERN Large Hadron Collider," *JINST 3 S08003*, 2008.

[34] CMS Collaboration, "The CMS experiment at the CERN LHC," *JINST 3 S08004*, 2008.

[35] LHCb Collaboration, "The LHCb Detector at the LHC," *JINST 3 S08005*, 2008.

[36] ALICE Collaboration, "The ALICE experiment at the CERN LHC," *JINST 3 S08002*, 2008.

[37] B.J. Gallop, "ATLAS SCT Readout and Barrel Macro-Assembly Testing and Design of MAPS Test Structure," *CERN-THESIS-2005-107*, 2005.

[38] M. Capeans and G. Darbo, et al., "ATLAS Insertable B-Layer Technical Design Report," *ATLAS-TDR-19*, 2010.

[39] ATLAS Collaboration, "ATLAS pixel detector: Technical Design Report," *CERN/LHCC, vol. 98*, 1998.

[40] P.J. Bell, "Constraints on Anomalous Quartic Gauge Boson Coupling at OPAL and the System Test of the ATLAS Barrel SCT," *https://cds.cern.ch/record/2137998?ln=en*, 2003.

[41] ATLAS Collaboration, "ATLAS Tile Calorimeter: Technical Design Report," *Technical Design Report ATLAS. CERN*, 1996.

[42] T. Cornelissen, "Concepts, Design and Implementation of the ATLAS New Tracking (NEWT)," *ATL-COM-SOFT-2007-002*, 2007.

[43] G. Piacquadio, "Primary vertex reconstruction in the ATLAS experiment at LHC," *J. Phys. Conf. Ser.*, 2008.

[44] ATLAS Collaboration, "ATLAS Liquid Argon Calorimeter: Technical Design Report," *Technical Design Report ATLAS. CERN*, 1996.

[45] ATLAS Collaboration, "ATLAS Tile Calorimeter: Technical Design Report," *Technical Design Report ATLAS. CERN*, 1996.

[46] N. Somi, "ATLAS Forward Detectors and Physics," *arXiv: 1006.5426*, 2010.

[47] ATLAS Collaboration, "ATLAS Trigger Performance Status Report," *CERN/LHCC, pp. 98–15*, 1998.

[48] ATLAS Collaboration, "ATLAS high-level trigger, data acquisition and controls: Technical Design Report," *Technical Design Report ATLAS. CERN*, 2003.

[49] ATLAS Collaboration, "Jet Calibration and Systematic Uncertainties for Jets Reconstructed in the ATLAS Detector at sqrt(s) = 13 TeV," *ATL-PHYS-PUB-2015-015*, 2015.

[50] ATLAS Collaboration, "Measurement of the tau lepton reconstruction and identification performance in the ATLAS experiment using pp collisions at sqrt(s)=13 TeV," *ATLAS-CONF-2017-029*, 2017.

[51] ATLAS Collaboration, "Electron efficiency measurements with the ATLAS detector using the 2015 LHC proton-proton collision data," *ATLAS-CONF-2016-024*, 2016.

[52] ATLAS Collaboration, "Calorimeter clustering algorithms: description and performance," *ATL-COM-LARG-2008-003*, 2008.

[53] ATLAS Collaboration, "Expected Performance of the ATLAS Experiment: Detector, Trigger and Physics," *arXiv:0901.0512*, 2008.

[54] R. Frühwirth, "A Gaussian-mixture approximation of the Bethe-Heitler model of electron energy loss by bremsstrahlung," *Computer physics communications, vol. 154*, 2003.

[55] ATLAS Collaboration, "Electron performance measurements with the ATLAS detector using the 2010 LHC proton-proton collision data," *The E.P.J. C, vol. 72*, 2012.

[56] ATLAS Collaboration, "Electron reconstruction and identification in the ATLAS experiment using the 2015 and 2016 LHC proton-proton collision data at $sqrts$ = 13 TeV," *arXiv:1902.04655*, 2019.

[57] ATLAS Collaboration, "Topological cell clustering in the ATLAS calorimeters and its performance in LHC Run 1," *arXiv:1603.02934*, 2017.

[58] M. Cacciari and G. P. Salam and G. Soyez, "The anti-kt jet clustering algorithm," *JHEP 04 (2008) 063*, 2008.

[59] ATLAS Collaboration, "Optimisation of the ATLAS b-tagging performance for the 2016 LHC Run," *ATL-PHYS-PUB-2016-012*, 2016.

[60] ATLAS Collaboration, "Tagging and suppression of pileup jets with the ATLAS detector," *ATLAS-CONF-2014-018*, 2014.

[61] ATLAS Collaboration, "Performance of missing transverse momentum reconstruction with the ATLAS detector in the first proton-proton collisions at sqrt(s) = 13 TeV," *ATL-PHYS-PUB-2015-027*, 2015.

[62] A. Buckley et al., "General-purpose event generators for LHC physics," *arXiv:1101.2599*, 2011.

[63] S. Frixione and P.Nason and C. Oleari, "Matching NLO QCD computations with Parton Shower simulations: the POWHEG method," *arXiv:0709.2092*, 2007.

[64] J. Alwall et al., "The automated computation of tree-level and next-to-leading order differential cross sections, and their matching to parton shower simulations," *JHEP, vol. 07, p. 079*, 2014.

[65] J. Bellm, et al., "Herwig 7.0 / Herwig++ 3.0 Release Note," *arXiv:1512.01178*, 2020.

[66] T. Gleisberg et al., "Event generation with SHERPA 1.1," *arXiv:0811.4622*, 2009.

[67] T. Sjostrand and S. Mreuna and P.Z. Skands, "A brief introduction to PYTHIA 8.1," *arXiv:10710.3820*, 2008.

[68] ATLAS Collaboration, "Muon reconstruction performance of the ATLAS detector in proton-proton collision data at sqrts=13TeV," *https://arxiv.org/pdf/1603.05598.pdf*, 2016.

[69] ATLAS collaboration, "Measurement of the muon reconstruction performance of the ATLAS detector using 2011 and 2012 LHC proton-proton collision data," *arXiv:1407.3935*, 2014.

[70] ATLAS Collaboration, "Jet energy measurement with the ATLAS detector in proton-proton collisions at sqrt(s) = 7 TeV," *https://arxiv.org/abs/1112.6426*, 2011.

[71] Frixione et al., "Single-top hadroproduction in association with a W boson," *arXiv:0805.3067*, 2008.

[72] ATLAS Collaboration, "Recommendations of the Physics Objects and Analysis Harmonisation Study Groups 2014," *ATL-COM-PHYS-2014-451*, 2015.

[73] ATLAS Collaboration, "Search for heavy particles decaying into top-quark pair in the fully hadronic final state in pp collisions at sqrt(s)= 13 TeV with the ATLAS detector," *arXiv:1902.10077*, 2019.

[74] ATLAS Collaboration, "Jet energy scale and its systematic uncertainty in proton-proton collisions at sqrt(s)=7 TeV in ATLAS 2010 data," *ATLAS-CONF-2011-032*, 2010.

[75] D0 Collaboration, "Measurement of the Top Quark Mass Using Dilepton Events," *arXiv:hep-ex/9706014*, 1997.

[76] ATLAS Collaboration, "Performance of missing transverse momentum reconstruction with the ATLAS detector using proton-proton collisions at sqrt(s) = 13 TeV," *arXiv:1802.08168*, 2018.

[77] M. Czakon et al., "Top-pair production at the LHC through NNLO QCD and NLO EW," *arXiv:1705.04105*, 2017.

[78] Cowan, "Asymptotic formulae for likelihood-based tests of new physics," *The European Physical Journal C-Particles and Fields*, 2011.

[79] ATLAS Collaboration, "Luminosity determination in pp collisions at $\sqrt{s}$= 13 TeV using the ATLAS detector at the LHC," *ATLAS-CONF-2019-021*, 2019.